Studies on supramolecular photochirogenesis mediated by synthetic antibody and chiral silica-organic hybrid nanoribbons

Wijak Yospanya

To cite this version:

Wijak Yospanya. Studies on supramolecular photochirogenesis mediated by synthetic antibody and chiral silica-organic hybrid nanoribbons. Organic chemistry. Université de Bordeaux; Tōhoku Daigaku (Sendai, Japon), 2020. English. NNT : 2020BORD0088 . tel-02985185

HAL Id: tel-02985185
https://theses.hal.science/tel-02985185
Submitted on 2 Nov 2020

THESIS UNDER DOUBLE-DEGREE AGREEMENT

To Obtain
DOCTORAL DEGREE IN CHEMISTRY

of
UNIVERSITY OF BORDEAUX
DOCTORAL SCHOOL OF CHEMICAL SCIENCES
and
TOHOKU UNIVERSITY
GRADUATE SCHOOL OF SCIENCE, DEPARTMENT OF CHEMISTRY

by
Wijak YOSPANYA

STUDIES ON SUPRAMOLECULAR PHOTOCHIROGENESIS MEDIATED BY SYNTHETIC ANTIBODY AND CHIRAL SILICA-ORGANIC HYBRID NANORIBBONS

ÉTUDES SUR LA PHOTOCHIROGENÈSE SUPRAMOLÉCULAIRE EN UTILISANT UN ANTICORPS SYNTHÉTIQUE ET DES NANORUBANS D'HYBRIDES (SILICE-ORGANIQUE) CHIRAUX

Under Supervision of
Dr. Takehiko WADA and Dr. Reiko ODA

Defended on 3 August 2020

Jury Members

Dr. Kazushi KINBARA	Professor, Tokyo Institute of Technology	President / Reviewer
Dr. Gaku FUKUHARA	Associate Professor, Tokyo Institute of Technology	Reviewer
Dr. Takehiko WADA	Professor, Tohoku University	Thesis Supervisor
Dr. Reiko ODA	Research Director, CNRS	Thesis Supervisor

Titre : Etudes sur la photochirogenèse supramoléculaire en utilisant un anticorps synthétique et des nanorubans d'hybrides (silice-organique) chiraux

Résumé : Dû à l'augmentation de la demande de nouveaux matériaux chiraux, la préparation de molécules chirales est actuellement l'un des domaines les plus essentiels de la chimie synthèse chimique. La photoréaction supramoléculaire est une stratégie efficace de photoréaction régio- et énantio-sélective qui permet d'éviter le problème de la courte durée de vie de l'état excité de la molécule clé-intermédiaire, ainsi que des faibles interactions dues aux états excités. Cette thèse décrit, la photocyclodimérisation supramoléculaire du 2-anthracènecarboxylate à l'aide de deux procédés différents dans l'eau. Dans une solution aqueuse de molécules, moins de 25% de dimères tête-à-tête (HH) sont formés. Cependant, avec les nanorubans hybrides (organique-silice) chiraux comme template, on 97% de dimères HH sont obtenus. Les anticorps synthétiques sélectionnés pour leur reconnaissance des dimères HH, ont également conduit à 92% de dimères HH avec un excès énantiomérique de 48% pour le dimère HH chiral.

Mots clés : chimie supramoléculaire, photochimie, chiralité, anticorps, nanostructure, anthracène

---

Title : Studies on supramolecular photochirogenesis mediated by synthetic antibody and chiral silica-organic hybrid nanoribbons.

Abstract : As the demand of chiral material increases, synthesis of chiral molecules is one of the most essential fields in chemistry. Supramolecular photoreaction is a powerful strategy for regio- and enantio-selective photoreaction to overcome the short-lifetime excited state key-intermediate molecule and weak interactions in the excited state issues. In this thesis, the supramolecular photocyclodimerization of 2-anthracenecarboxylate mediated by two different media in water are reported. Molecular solution in bulk water, less than 25 % of head-to-head (HH) dimers are produced due to the electronic repulsion of carboxylate. However, using the chiral silica-organic hybrid nanoribbons as dimerization template, 97 % HH dimers were observed with increased reaction rate. The synthetic antibodies, selected by the HH dimer recognition, also gave 92 % HH dimers and 48 % ee of a chiral HH dimer. The intensive studies, such as the binding kinetics and the effects of external factors, will be discussed.

Keywords : supramolecular chemistry, photochemistry, chirality, antibody, nanostructure, anthracene

---

Unité de recherche

CBMN CNRS-UMR5248 - CNRS/UB
IECB, 2, rue Robert Escarpit, 33607 Pessac, France

PREFACE

This study has been carried out under the supervision of Professor Takehiko Wada at The Institute of Multidisciplinary Research for Advanced Materials and The Department of Chemistry, Graduate School of Science, Tohoku University, Japan, and Professor Reiko Oda at The Institute of Chemistry and Biology of Membranes and Nano-objects, CNRS UMR 5248, University of Bordeaux, France from October 2017 to July 2020.

The objective of the thesis is to investigate and utilize the synthetic antibody and chiral silica-organic hybrid nanoribbons for supramolecular asymmetric regio- and enantioselective photochemical reaction as the alternative chiral supramolecular hosts. Not only regioselectivity and enantioselectivity but also interactions, chirality inductions, stabilities, irradiation conditions and the other related topics will be demonstrated and discussed, which can be generally useful information for similar systems. In addition, the interdisciplinary of this research, composed of chirality, photochemistry, supramolecular chemistry, protein engineering and nanomaterial, makes this research a unique topic.

The author hopes that the experimental results and discussions in this thesis will contribute to further development of chiral supramolecular photochemistry.

Wijak YOSPANYA

Department of Chemistry, Graduate School of Science

Tohoku University, Sendai, Japan

Doctoral School of Chemical Science

University of Bordeaux, Bordeaux, France

August 2020

ABSTRACT

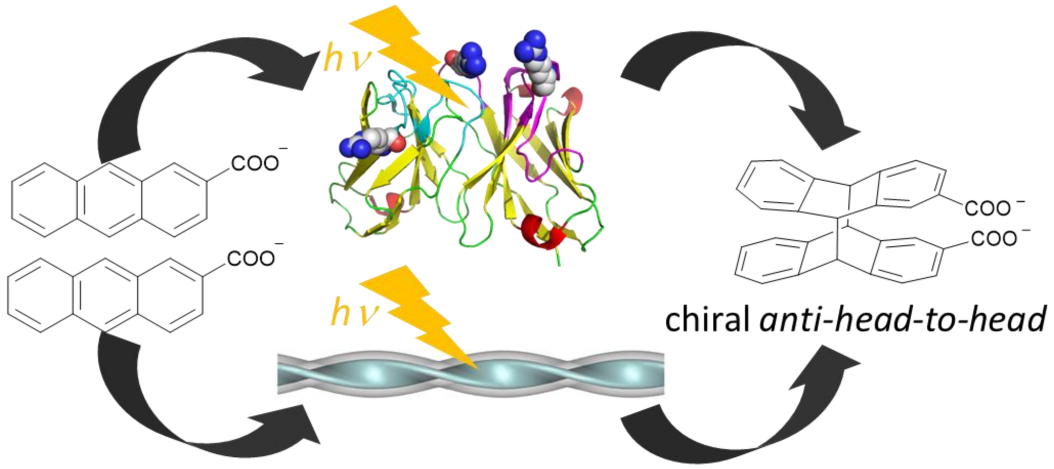

The photochemical approaches to asymmetric synthesis have several unique, inherent advantages over the thermal counterparts, since photochemical reaction proceeds through the electronically excited state and often provides strained and/or thermally difficult-to-accessible products of unique structures in a single step. However, major drawbacks of photochemical reactions, such as the short lifetime of the excited-state molecules, make them difficult to control. Previously reported, the supramolecular asymmetric photocyclodimerization of 2-antharcenecarboxylate using mammalian serum albumins as chiral reaction media favor the *syn-head-to-tail* dimer with high product distribution of 77 % with 97 % enantiomeric excess (ee). However, in general, it is difficult to obtain *head-to-head* dimers in aqueous solution due to the steric hindrance and electronic repulsion between carboxylate groups.

Here, the supramolecular photocyclodimerization of 2-anthracenecarboxylate mediated by two different chiral media in water are reported. The chiral silica-organic hybrid nanoribbons, gemini-surfactant double-bilayer structure covered with silica network, can generate a complete *head-to-head* regioselective photosynthesis of 2-anthracenecarboxylate dimers even at room temperature. The synthetic single-chain antibody (scFv) can also be used for enantioselective of *anti-head-to-head* 2-anthracenecarboxylate dimer with 48 % ee and more than 90 % *head-to-head* regioselectivity.

The chiral organic-silica hybrid nanoribbons were synthesized from the self-assemblies of gemini surfactants and silica transcription. First, the gemini 16-2-16 L- or D-tartrate surfactants were synthesized. Their self-assemblies in water yield twisted nanostructures with specific handedness depending on the enantiomer of tartrate. Then, they were transcribed using tetraethyl orthosilicate giving the chiral silica outer layer while still retaining the organized organic structure inside, called silica-organic hybrid nanoribbons.

The hybrid nanoribbons could maintain the chiral assembly of gemini even after exchanging tartrate counter anions with achiral anions, and this assembly can in turn induce chirality to these anions, such as methyl orange. In this work, tartrate was exchanged with 2-anthracenecarboxylate, which also showed the exceptional induced CD signals (g-factor -6×10^{-3} and 7×10^{-3} for L-hybrid nanoribbons). The efficiency and the stability of the chirality induction strongly depend on temperature, time, and the ratios of 2-anthracenecarboxylate to gemini surfactant inside hybrid nanoribbons. Using different spectroscopic techniques (CD, VCD, IR, NMR and Fluorescence), the organization of 2-anthracenecarboxylate inside the nanoribbons were studied. The photocyclodimerization of 2-anthracenecarboxylate inside the nanoribbons showed more than 97 % selectivity to the *head-to-head* dimers with similar ratio between *anti-* and *syn-*isomers.

Toward tailor-made chiral biomolecular hosts, synthetic single-chain antibody (scFv) prepared by a conventional phage display technique was used as an alternative biomolecular chiral media. The ligand in phage display was *syn-head-to-head* dimer linked to polyethylene glycol spacer and biotin with amide bonds. The phage display protocol is reported, and the best antibody candidate was expressed in *E. coli*. Together with the optimization of photochemical reaction conditions, the photocyclodimerization of 2-anthracenecarboxylate in the antibody cavity yielded *head-to-head* dimers up to 92 % with 48 % ee for *anti-head-to-head* dimer.

Although the synthesis of *anti-head-to-head* dimer was promoted, the undesired *syn-head-to-head* dimer was also observed with high distribution. After analysing the structure derived from the sequence of antibody, the new design of the ligand for phage display technique is proposed, which includes the new design of anthracene heterodimer, changing the directions of carboxylate groups and removing amide bond. The synthesis and separation of 2-anthracenecarboxylic acid and 6-hydroxy-2-anthracenecarboxylic acid hetero dimer, a new dimer for ligand in phage display technique, is reported.

In conclusion, the applications of silica-organic hybrid nanoribbons and synthetic antibody for the supramolecular regio- and enantioselective [4+4] photocyclodimerization of 2-anthracenecarboxylate were demonstrated.

要約

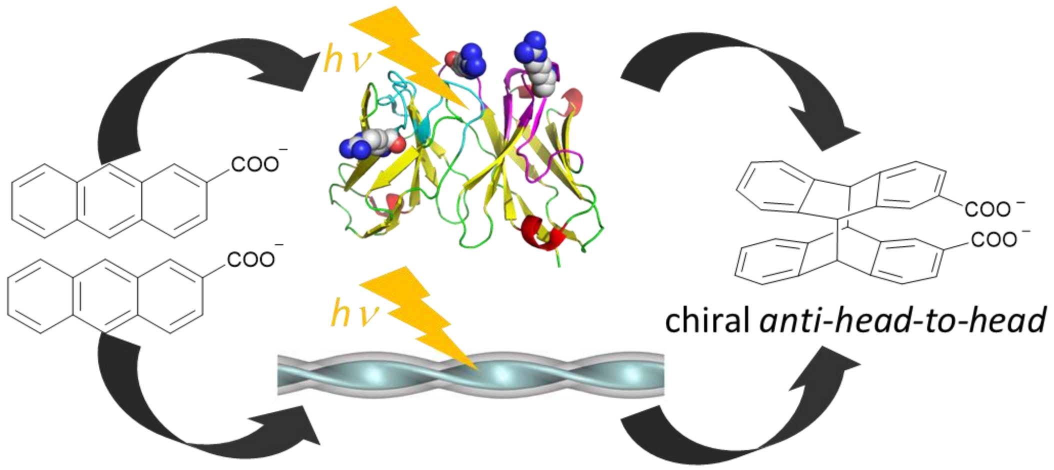

不斉光合成は、熱的反応では多段階を必要とする、或いは合成困難な歪みの高い化合物を一段階で合成可能といった利点を有し、有機化学において極めて重要な研究分野である。しかし、光反応の鍵中間体である励起状態はその寿命が短く、また相互作用も弱いことから反応の制御は困難とされている。これまでに、哺乳類の血清アルブミンをキラル反応場として使用した 2-アントラセンカルボキシレートの超分子非対称光二量化は、77%と 97%ee で *syn-head-to-tail* 二量体を生成することが報告されているが、一般に、カルボン酸塩の電子反発力や立体障害により、水中で *head-to-head* 二量体を得るのは困難と見做されきた。

本博士論文では、水中の 2 つの異なる媒体によって媒介される 2-アントラセンカルボキシレートの超分子光二量化反応について報告する。まず、水中で二重二分子膜の界面活性剤組織を内側に、シリカ壁を外側に持つキラルな有機-シリカ複合ナノリボン構造体を用いて、室温においても AC 二量体の優れた位置選択的光合成を達成した。また、合成一本鎖抗体（scFv）は、48%ee および 90%以上の *head-to-head* の位置選択性を備えた *anti-head-to-head* の AC 二量体のエナンチオ選択性を達成した。

有機-シリカ複合ナノリボン構造体は、界面活性剤の自己組織化とシリカの複合化により合成した。初めに、ジェミニ型 L-または D-酒石酸塩界面活性剤を合成し、水中での自己組織化により、酒石酸塩の鏡像異性体キラリティーに依存し、特定の巻き方向を持つ、ねじれた配向を有する螺旋状ナノ構造体を形成した。次に、キラル有機テンプレートを用いたテトラエトキシシランのソル-ゲル法により、ハイブリッド有機シリカナノリボンと呼ばれる内部の組織化された有機構造を保持しながら、キラルシリカの外層を形成した。

複合ナノ構造体は、酒石酸対アニオンをアキラルアニオンと交換した後でもジェミニの螺旋キラル構造を維持でき、このキラル構造は、メチルオレンジといったアニオン化合物にキラリティーを転写できる。本研究では、酒石酸塩を 2-アントラセンカルボキシレートと交換することで、2-アントラセンカルボキシレートも強力な誘起 CD ピークを示し（L ハイブリッドナノリボンの g-factor : -6×10^{-3} と 7×10^{-3}）、キラリティー誘導の効率と安定性は、ハイブリッドナノリボン内の AC とジェミニ界面活性剤の化学量論比、温度、および時間に大きく依存することが分かった。さまざまな分光法（CD、VCD、IR、NMR、蛍光）を使用してナノ構造内の 2-アントラセンカルボキシレートの組織化を検討し、ナノ構造内での 2-アントラセンカルボキシレートの光二量化では、*anti* 異性体と *syn* 異性体の比率が同程度で、97%以上の極めて高い選択性で、*head-to-head* 型二量体が得られる事を明らかとした。

より一般的な戦略として、従来のファージディスプレイ技術によって調製された人工一本鎖抗体（scFv）を、生体分子キラル反応場とした超分子不斉合成を検討した。ファージディスプレイにおけるリガンドは、スペーサーとしてポリエチレングリコール、およびアミド結合を有するビオチンに連結された *syn-head-to-head* の AC 二量体（ACD3）を使用した。ファージディスプレイ法を用い、ADC3 に対する選択性の最も優れた抗体を選択し、その遺伝子配列を確定後、遺伝子工学手法を駆使し大腸菌で目的抗体を発現可能であることを確認した。光反応条件の最適化と合わせて、抗体認識表面での 2-アントラセンカルボキシレートの光二量化により、最大 92%の *head-to-head* の二量体が得られ、*anti-head-to-head* の二量体については 48%ee だった。

Anti-head-to-head 二量体の合成が促進された一方、目的とは異なる *syn-head-to-head* の二量体も高い割合で得られた。抗体の配列に由来する構造の分析後、新しい方向とカルボン酸基の数、およびアミド結合の除去を含む、ファージディスプレイ技術のためのリガンドの新設計を提案し、ファージディスプレイ技術におけるリガンドの新しい二量体である、2-アントラセンカルボキシレートと 6-ヒドロキシ-2-アントラセンカルボン酸ヘテロ二量体の合成と単離を達成した。

以上、2-アントラセンカルボキシレートの超分子不斉[4 + 4]光二量化をベンチマーク的光反応として、ハイブリッドシリカ-有機ナノリボンおよび人工抗体が有効に機能することを明らかとした。

RESUME

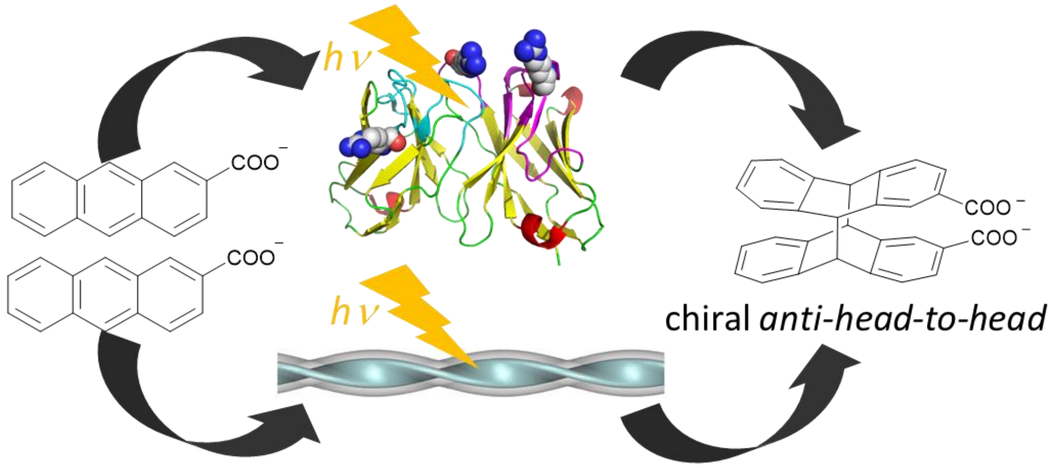

Récemment, la photosynthèse supramoléculaire régio- et énantiosélective a été l'un des domaines de recherche importants en chimie organique, en raison de ses nombreux avantages uniques, tels que la possibilité de synthétiser en une seule étape des produits contraints et/ou thermiquement difficiles d'accès. Cependant, les inconvénients majeurs des réactions photochimique, tels que la faiblesse des interactions et la courte durée de vie à l'état excité, peuvent rendre le contrôle des réactions plus difficiles. Dans notre groupe, il a été montré que la photocyclodimérisation supramoléculaire asymétrique du 2-antharcenecarboxylate (AC) en utilisant des albumines sériques de mammifères comme milieu réactionnel chiral favorise la formation du dimère tête-à-queue *syn* avec un rendement de 77 % et 97 % excès énantiomérique. Cependant, il généralement difficile d'obtenir des dimères tête-à- tête dans l'eau à cause de la répulsion électronique des groupes carboxylates.

Cette thèse décrit la photocyclodimérisation supramoléculaire du 2-anthracènecarboxylate à l'aide de deux procédés différents dans l'eau. Les nanorubans hybrides (organique-silice) chiraux formés par organisation supramoléculaire des tensioactifs en double bicouche à l'intérieur d'une paroi externe de silice, sont utilisés efficacement pour la photosynthèse régiosélective complète des dimères 2-anthracènecarboxylate, même à température ambiante. L'anticorps synthétique à chaîne unique (scFv) a également montré son efficacité pour la photosynthèse énantiosélective de dimères 2-anthracènecarboxylate tête-à-tête *anti* avec 48% d'excès énantiomériques et plus de 90% de régiosélectivité.

Les nanorubans hybrides (silice-organique) chiraux ont été préparés par auto-assemblages de tensioactifs suivis d'une transcription par de la silice. Tout d'abord, les

tensioactifs gemini ayant comme contre ion du L- ou D-tartrate ont été synthétisés. Leurs auto-assemblages dans l'eau conduit à la formation de nanostructures torsadées dont le sens de rotation dépend de l'énantiomère L- ou D-tartrate utilisé. La transcription des nanostructures organiques obtenues à l'aide d'orthosilicate de tétraéthyle conduit à une nanostructure hybride composée d'une couche chirale externe de silice à l'intérieur de laquelle l'organisation supramoléculaire des tensioactifs est maintenue, et que nous avions nommée « nanorubans hybride organique-silice ».

Cet assemblage des nanofibres hybrides permet de conserver l'organisation chirale des surfactants géminés même après avoir échangé les contre-anions tartrate par d'autres anions achiraux. L'organisation chirale de ces hybrides peut ensuite induire la chiralité sur des anions achiraux comme le méthyl orange. Dans ce travail, le tartrate a été échangé par le 2-anthracènecarboxylate, et ces assemblages à base de 2-anthracènecarboxylate ont montré de forts signaux en CD induits, avec des facteurs g de -6×10^{-3} et 7×10^{-3} pour L-nanorubans hybrides. L'efficacité et la stabilité de cette induction de chiralité dépend fortement du rapport stoechiométrique entre l'anion 2-anthracènecarboxylate et le surfactant gemini à l'intérieur des nanorubans hybrides, de la température et du temps de réaction. L'organisation du 2-anthracènecarboxylate à l'intérieur des nanostructures a été étudiée par différentes techniques de spectroscopie telles que le CD, VCD, IR, RMN et Fluorescence. La photocyclodimérisation du 2-anthracènecarboxylate à l'intérieur des nanostructures hybrides a montré une sélectivité de plus de 97 % pour les dimères tête-à-tête, et un rapport similaire pour les isomères *anti* et *syn*.

Comme stratégie plus générale, un anticorps synthétique à chaîne unique (scFv) préparé par la technique de « phage display » a été utilisé comme milieu biomoléculaire chiral alternatif. Le ligand dans le « phage display » était un dimère tête-à-tête *anti* lié à un espaceur polyéthylène glycol et à la biotine par liaisons amides. Le protocole du « phage display » est également décrit. Nous avions montré que le meilleur anticorps a été exprimé dans E. coli. Parallèlement à l'optimisation des conditions de réaction photochimique, la photocyclodimérisation de l'AC dans la cavité de l'anticorps a conduit à 92% de dimères tête-à-tête *anti* avec 48 % d'*ee.*

Bien que le dimère tête-à-tête *anti* ait été favorablement obtenu, l’isomère tête-à-tête *syn* indésirable a été également significativement obtenu. Après l'analyse de la structure dérivée de la séquence d'anticorps, une nouvelle structure du ligand adaptée à la technique de « phage display » a été proposée. Elle tient en compte la géométrie et le nombre des groupes carboxylates, et élimine les liaisons amides. Ainsi, pour la synthèse et la séparation de 2-anthracènecarboxylate et de l'acide 6-hydroxy-2-anthracènecarboxylique, un nouveau ligand dimère pour la technique de phase display est décrit.

En conclusion, lors de ce travail, nous avions réussi le régio- et énantiosélective photocyclodimérisation [4+4] supramoléculaire de 2-anthracènecarboxylate à l’aide de nanorubans hybrides organique-silice et d’un anticorps synthétique.

LIST OF ABBREVIATION

% v	% volume
% w	% weight
× g	Centrifugation Force in Earth Gravitation Force Unit ($9.8\ m/s^2$)
°C	Degree Celsius
1-AC	1-Anthracenecarboxylate or 1-Anthracenecarboxylic Acid
9-AC	9-Anthracenecarboxylate or 9-Anthracenecarboxylic Acid
AB	2-Anthraceneboronate or 2-Anthraceneboronic Acid
AC	2-Anthracenecarboxylate or 2-Anthracenecarboxylic Acid
AC*	Electronically Excited 2-Anthracenecarboxylate
AC-Chd	(2-*trans*-Hydroxycyclohexyl)-2-anthroate
AC-Chd-MAC	*trans*-1,2-Cyclohexanediyl 1-(6-Methoxy-2-anthroate)-2-(2-anthroate)
ACD	2-Anthracenecarboxylate Dimer
ACD1	*anti-head-to-tail* 2-Anthracenecarboxylate Dimer
ACD2	*syn-head-to-tail* 2-Anthracenecarboxylate Dimer
ACD3	*anti-head-to-head* 2-Anthracenecarboxylate Dimer
ACD4	*syn-head-to-head* 2-Anthracenecarboxylate Dimer
AC-HAC dimer3	2-Anthracenecarboxylic Acid and 6-Hydroxy-2-anthracenecarboxylic Acid *anti-head-to-head* Heterodimer
aq	Aqueous Solution
ASO	9,10-Dimethylanthracene-2-sulfonate
CD	Circular Dichroism Spectroscopy
CDR	Complementarity-Determining Regions
Chd	*trans*-1,2-Cyclohexanediol
Chd(AC-HAC dimer3)	*trans*-1,2-Cyclohexanediyl 6-Hydroxy-2-anthroate 2-Anthroate *anti-head-to-head* Heterodimer
CPL	Circularly Polarized Luminescence Spectroscopy
d	Day
D-hybrid nanohelices	Silica-Organic Hybrid Nanohelices of Gemini 16-2-16 D-Tartrate
D-hybrid nanoribbons	Silica-Organic Hybrid Nanoribbons of Gemini 16-2-16 D-Tartrate
D-hybrid nanostructures	Silica-Organic Hybrid Nanostructures of Gemini 16-2-16 D-Tartrate
Dimethyl(AC-HAC dimer3)	Methyl 6-Hydroxy-2-anthroate Methyl 2-Anthroate *anti-head-to-head* Heterodimer
DMAP	4-Dimethylaminopyridine
DMF	Dimethylformamide
DMSO	Dimethyl Sulfoxide

DNA	Deoxyribonucleic Acid
E. coli	*Escherichia coli*
EDC·HCl	1-Ethyl-3-(3-dimethylaminopropyl)carbodiimide Hydrochloride
EDTA	Ethylenediaminetetraacetic Acid
ee	Enantiomeric Excess
ELISA	Enzyme-Linked Immunosorbent Assay
eq	Equivalence
ESI-QTOF	Electrospray Ionization Quadrupole Time-of-Flight (Mass Spectroscopy)
ESI-TOFMS	Electrospray Ionization Time-of-Flight Mass Spectroscopy
EtSH	Ethanethiol
ε	Molar Extinction Coefficient
g	Gram
h	Hour
HAC	6-Hydroxy-2-anthracenecarboxylic Acid
HOBt	Hydroxybenzotriazole
HPLC	High Performance Liquid Chromatography
HT	High Tension
Hybrid nanohelices	Silica-Organic Hybrid Nanohelices of Gemini 16-2-16 Tartrate
Hybrid nanoribbons	Silica-Organic Hybrid Nanoribbons of Gemini 16-2-16 Tartrate
Hybrid nanostructures	Silica-Organic Hybrid Nanostructures of Gemini 16-2-16 Tartrate
I_{FL}	Fluorescence Intensity
IPTG	Isopropyl β-D-1-Thiogalactopyranoside
LED	Light-Emitting Diode
L-hybrid nanohelices	Silica-Organic Hybrid Nanohelices of Gemini 16-2-16 L-Tartrate
L-hybrid nanoribbons	Silica-Organic Hybrid Nanoribbons of Gemini 16-2-16 L-Tartrate
L-hybrid nanostructures	Silica-Organic Hybrid Nanostructures of Gemini 16-2-16 L-Tartrate
M	Molar
MAC	6-Methoxy-2-anthracenecarboxylic Acid
MALDI-TOF	Matrix-Assisted Laser Desorption Ionization Time-of-Flight (Mass Spectroscopy)
mdeg	Millidegree
min	Minute
MS	Mass Spectroscopy
NC	2-Naphthanlenecarboxylic Acid
NDC	2,3-Naphthalenedicarboxylic Acid
nm	Nanometer
NMP	*N*-Methyl-2-pyrrolidone

NMR	Nuclear Magnetic Resonance Spectroscopy
OD	Optical Density
PCR	Polymerase Chain Reaction
RP-HPLC	Reversed-Phase High Performance Liquid Chromatography
rt	Room Temperature
s	Second
scFv Antibody	Single-Chain Fv Antibody
SDS-PAGE	Sodium Dodecyl Sulfate Polyacrylamide Gel Electrophoresis
sH_2O	Sterilized Water
t	Time
TBE	Tris/Borate/EDTA Buffer
TBHP	*tert*-Butyl Hydroperoxide
TBS	Tris HCl 20 mM Buffer Containing NaCl 150 mM
TBST	Tris HCl 20 mM Buffer Containing NaCl 150 mM and Tween-20
TEM	Transmission Electron Microscopy
TEOS	Tetraethyl Orthosilicate
TFA	Trifluoroacetic Acid
THF	Tetrahydrofuran
TIPS	Triisopropylsilane
TLC	Thin-Layer Chromatography
Tris	2-Amino-2-hydroxymethyl-propane-1,3-diol
UV	Ultraviolet
UV-Vis	Ultraviolet-Visible Spectroscopy
W	Watt

TABLE OF CONTENT

CHAPTER 3: SUPRAMOLECULAR REGIO- AND ENANTIOSELECTIVE [4+4] PHOTOCYCLODIMERIZATION OF 2-ANTHRACENECARBOXYLATE USING SYNTHETIC ANTIBODY OBTAINED FROM PHAGE DISPLAY TECHNIQUE **65**

CHAPTER 1: GENERAL INTRODUCTION AND LITERATURE REVIEW

1.1 Chirality

Chirality is a property of structure having mirror image that cannot be superimposed to itself. Such isomer is called stereoisomer and each individual is called enantiomer.[1] The most common example would be biological appendages, such as our left and right hands. This observation has been with mankind since the origin, but never received much attention, although found in daily basis, because they are usually in pairs.

Scientists, such as Faraday, discovered the rotation of polarized light passing through some certain media, but the ideas of enantiomers were mixed up with the influence of external magnetic field.[2] In 1848, Pasteur isolated crystal of sodium ammonium L- and D-tartrate and discovered that they can rotate polarized light to the opposite direction with the same magnitude (dextrorotatory and levorotatory).[3] Moreover, in 1858, he found that the fermentation of D-tartaric acid is significantly more efficient than L-isomer. By using racemic mixture of tartaric acid for fermentation, D-tartaric acid is consumed while L-tartaric acid stays intact, the first evidence of biological chiral selectivity.[4–6]

Later, van't Hoff[7] and Le Bel[8] introduced the idea of carbon atom having 4 different bonds in tetrahedral structure as an original source of chirality. Any molecules having this asymmetry, in isolated of mirror-image structure, will be optically active, defining the terminology "optical isomers."[9] In, 1886 Piutti isolated D-asparagine and discovered that it has a sweet taste while L-asparagine has no taste,[10] which inspired the research on taste and stereochemistry until now.[11–14] Fischer, in 1891, discovered that sugars in nature are in the same isomer, defined with his notations as D configutations.[15,16]

Figure 1-1. (a) Examples of chirality in different scales (DNA and stair pictures from Pixabay, hands and tower photos from Unsplash, and galaxy photo from NASA), and (b) Snail species with different chirality (sinistral *Busycon pulleyi* and dextral *Fusinus salisbury*) and a species with chiral dimorphism (*Amphidromus perversus*). (reprinted from ref 19 with permission from Springer Nature)

Even though this thesis focuses on only molecular-level chirality, it is important to address that chirality in living organisms are not only in molecular level but also anatomy level. Simple as it sounds, the normal position of human heart to the left of the body is one of them. There are also other visible examples such as helical parts of plant growing in certain handedness induced by twisted cells,[17] or more than 90 % of snail taxa having dextral shells.[18,19] (Figure 1-1 b) Every specific chirality in anatomy level comes from the assemblies of small chiral units such as cells. Moreover, the existence of chirality can be found in large scale in the universe, such as the shapes of galaxies and circularly polarized light produced by reflection nebulae.[20] Chirality-inspired design and architecture are also abundant in human civilizations. (Figure 1-1 a)

1.1.1 **Notations**

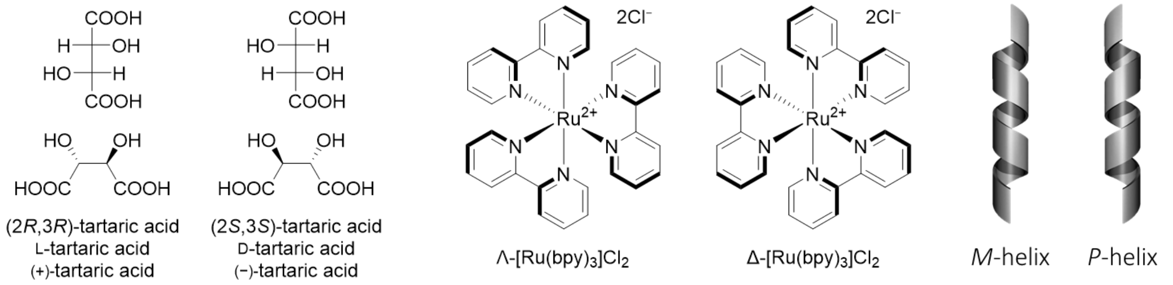

Figure 1-2. Examples of notations for enantiomers.

There are different notations for enantiomers depending on types of enantiomer and differentiating properties. (Figure 1-2) The (+)- and (−)- notations, the original nomenclature, are defined by the ability to rotate the plane polarized light ((+) for dextrorotatory or clockwise rotation, and (−) for levorotatory or counterclockwise rotation). It was the most convenient notation because it directly relates to the experimental results, but the molecules having multiple chiral points are not suitable for these notations because the rotation can be different depending on wavelength. Therefore, the notations based on molecular structures are more popular nowadays.

For the basic point chirality such as sp^3 carbon with all different substitutions, S and R-configuration is separated by the actual positions of connected atoms. If there are multiple chiral points, all are designated. For biomolecules, L- and D- are designated based on Fischer projection such as D-glucose and L-arginine which are natural carbohydrate and amino acid.[15,16] For planar or helical chirality, *P*- and *M*- are used to identify the right- and left-handed rotations. For octahedral metal complex, Δ and Λ are used to distinguish the orientation of ligands encapsulating metal ions such as in the case of $Ru(bpy)_3Cl_2$.[21]

With the advancement of technologies, various techniques have been developed to identify chirality in different levels. For examples, computational calculation is used to determine the absolute configurations of chiral molecules,[22,23] electron diffractions are used to determine the absolute configurations of organic nanocrystals,[24] and scanning electron microscope can be used to identify the patterns of nanostructures.

1.1.2 **Optical Activity**

In the early discovery of chirality, the optical activity was used to define two different enantiomers. The (+)- and (−)- or *d*- and *l*-isomers are defined from the directions of rotated linear polarized light to clockwise or counterclockwise, called optical rotation (OR). It is actually the results of circular birefringence, the velocity difference between circularly polarized light through the chiral media causing the phase difference.

Circular dichroism (CD) is the difference between the absorption of opposite circularly polarized light. Nowadays, CD is more popular technique than OR because only small amount of sample is needed for the measurement. CD can be defined as

$$\Delta \mathrm{A} = \mathrm{A}_{\mathrm{RCPL}} - \mathrm{A}_{\mathrm{LCPL}}$$

$$\Delta \varepsilon = \varepsilon_{\mathrm{RCPL}} - \varepsilon_{\mathrm{LCPL}}$$

When $\mathrm{A}_{\mathrm{RCPL}}$ and $\mathrm{A}_{\mathrm{LCPL}}$ are the absorption of right- and left-handed circularly polarized light, and the same to molar circular dichroism (Δε). Similar to molar extinction coefficient, molar circular dichroism is a unique character of each chiral molecules, and enantiomers will always have the same Δε with the opposite sign.

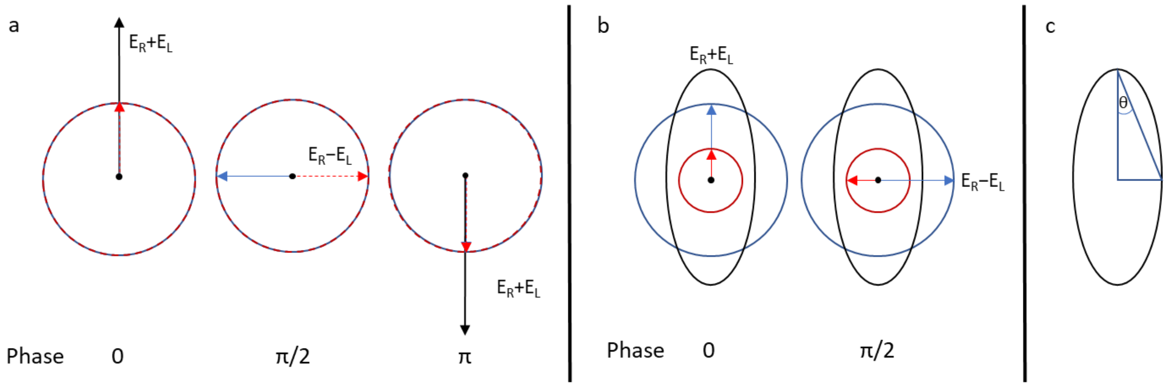

Figure 1-3. (a) Summation of left- and right-handed cicularly polarized light at the same phase with the same amplitude is linearly polarized light, but (b) different amplitude will give elliptical polarized light, and (c) definition of θ for CD measurement.

Normally, the measurement of CD is ellipticity (θ). The physical meaning of this ellipticity is the summations of right- and left-handed circularly polarized light in the same phase after passing through the sample. (Figure 1-3 b and c) θ can be defined as

$$\tan(\theta) = \frac{\mathrm{E}_{\mathrm{RCPL}} - \mathrm{E}_{\mathrm{LCPL}}}{\mathrm{E}_{\mathrm{RCPL}} + \mathrm{E}_{\mathrm{LCPL}}}$$

When E is the electric field for each circularly polarized light. From this equation and approximation that θ is very small and ΔA << 1, the relation between θ and ΔA can be derived as

$$\theta = \Delta \mathrm{A}(\frac{\ln 10}{4}) \tag{1-1}$$

In equation (1-1), θ is in radians, but θ is usually small, so that the unit mdeg is used in general.

$$\theta\ (\mathrm{mdeg}) = \Delta \mathrm{A}\left(\frac{\ln 10}{4}\right)\left(\frac{360 \cdot 1000}{2\pi}\right)$$

$$\theta\ (\mathrm{mdeg}) \approx 32980 \Delta \mathrm{A}$$

Kuhn's dissymmetry factor (g factor) is a dimensionless value showing the dissymmetry of the system. The higher dissymmetry gives the higher absolute g factor (positive and negative sign indicate the opposite dissymmetry). For CD, g factor is defined by ΔA/A (from –2 to 2), which means it is independent to concentration, path length or the absolute absorptivity. It only indicates the proportions of anisotropic absorption to the total absorption. If g factor is ±2, only one circularly polarized light is absorbed. If g factor is 0, there is no difference between the absorption of both circularly polarized light. The g factor can be obtained from θ and absorption as follow.

$$\mathrm{g} = \frac{\theta\ (\mathrm{mdeg})}{\mathrm{A} \cdot 32980} \qquad (1\text{-}2)$$

In addition, g factor can be used to compare dissymmetry among different systems.[25,26]

However, as shown in Figure 1-3 a, the linearly polarized light can be considered as a summation of opposite-direction circularly polarized lights with the same amplitude at the same phase. Meaning, linear dichroism (LD) can affect the CD measurement. The main difference is that CD is independent to the measurement directions, while rotating sample will severely affect LD. In the case of solution, the chiral molecules have high degree of rotations and diffusion. Therefore, LD is negligible. However, in the solid or aggregation states, the alignment in certain directions can induce LD. In chapter 2, which is related to the chirality of nanostructures, every CD measurement was carefully checked that LD was low enough to be negligible.[27]

There are other optical activities of chiral molecules which are not discussed in this work. For examples, circularly polarized luminescence (CPL) is a phenomenon that the chiral chromophores, excited by nonpolarized light, emit circularly polarized light,[25,28,29] or magneto-chiral dichroism (MChD) is the change in the light absorption of chiral molecules depending on magnetic field directions.[30,31]

1.1.3 **Producing Enantiopure Chiral Compounds**

As living organisms composed of homochirality,[20] different enantiomers can have different outcomes when applied to biological system, especially to human. Thus, the demand of enantiopure chiral molecules is in various fields such as foods,[32–34] agricultures[35] and the most important field, pharmaceuticals. Since the thalidomide tragedy in 1961,[36,37] serious attentions in chirality of drugs drastically increased the demand of enantiopure materials not only as drugs themselves but also as components in synthesis and purification procedures.[38] In addition, optical active properties of chiral molecules lead to possible fabrication of functional materials,[39–47] enantioselective binding properties were utilized in biosensors,[48–51] and many other research fields were developed based on the unique properties of chiral molecules.[52]

Despite the endless demand, syntheses of enantiopure chiral molecules are challenging because enantiomers are mirror images, impossible to selectively obtain by fundamental synthesis. There are several methods to produce enantiopure chiral molecules. The majority of commercially available enantiopure chiral molecules are synthesized from homochiral natural products as starting materials. Even so, the stereocontrolled synthetic pathway must be carefully planned to maintain chirality throughout the syntheses.[53–55] Different steps can induce isomerization or loose the chirality, such as eliminations of sp^3 carbon to sp^2.

Another method is the separations after syntheses. For examples, the racemic mixture can be converted to diastereomers, causing the difference in fundamental properties such as solubility; therefore, they can be easily isolated.[56–59] Also, different apparatus modified by chiral molecules,[60] such as chiral column chromatography,[61] can also be used. This approach is the most widely used in preparative scales.[62] This field is still one of the most active research in chirality, and alternative techniques, such as capillary electrophoresis,[63–65] adsorption on metal-organic framework[66] and anisotropic crystallization,[67–69] are vastly proposed. Still, there are several drawbacks such as additional reactions, additional purifications, and the loss of half of the synthesized compounds.

The final method is to use chiral templates or chiral catalysts.[38,70] Chiral catalyst is the only way to increase the number of chiral molecules in the total system, called asymmetric synthesis. The recyclable chiral templates also have similar properties. Supramolecular chiral hosts and chiral metal complexes are intensely developed for this purpose. Griesbeck and Meierhenich categorized asymmetric photochemistry to photochemistry in isotropic media (supramolecular directivity in solution, sensitized enantioselectivity and chiral memory), photochemistry in anisotropic media (solid-state and zeolites) and absolute photochemistry (magneto chirality and asymmetric photolysis using circularly polarized light).[71] This challenge inspired regio- and enantioselectivity in this thesis.

To indicate the purity of chiral molecules, % enantiomeric excess (ee) can be used as an indication. Enantiomeric excess is defined as

$$\%\ \mathrm{ee} = \frac{\text{Difference of amount between enantiomers}}{\text{Sum of amount of enantiomers}} \times 100\% \tag{1-3}$$

0 % ee means racemic mixture, and 100 % ee means pure enantiomer. Positive and negative signs are used to differentiate enantiomers. Similarly, diastereomeric excess is calculated using equation (1-3) but using amount of diastereomers instead of enatiomers. % ee can be determined by different technique, such as HPLC, CD and other chiral separation methods.

1.2 Photochemical Reaction

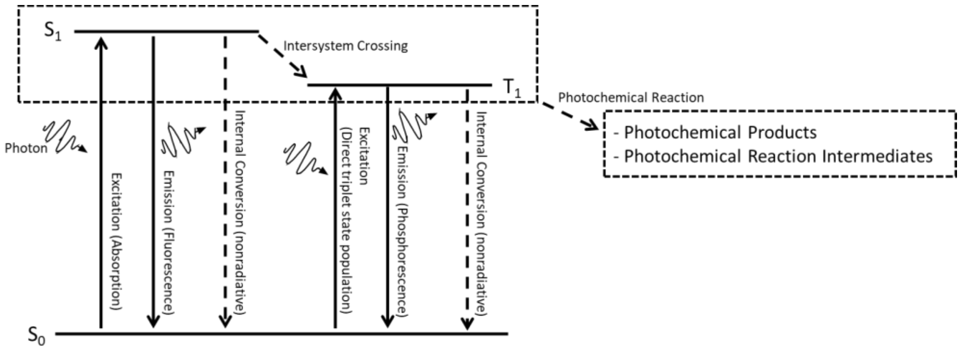

Figure 1-4. Simplified Jablonski diagram including ground state (S_0), first singlet excited state (S_1), first triplet excited state (T_1) and photochemical reaction. The solid-line and dashed arrows indicate radiative and nonradiative processes, respectively.

Photochemical reaction, a filed in photochemistry, is defined as reaction driven by light or photochemical process.[72] The simplified Jablonski diagram, named after Aleksander Jabłoński,[73] (Figure 1-4) shows the starting point when electron is excited by light (photon) and promoted to excited state. In this state, the energy of electron increases significantly, allowing the synthesis of wide variety of compounds even with higher free energy, such as strained and multi-cycle products, which is difficult by ground-state electron of thermal reactions.[74]

However, higher energy comes with less stability. Electronically excited state is finite, and the life time is very short. For example, fluorescence lifetime of anthracene is 10^{-8} to 10^{-9} s. Other relaxation pathways, such as emissions and internal conversions, are competing against photochemical reactions. Therefore, controlling photochemical reaction is crucial in practical and preparative-scale applications. Nevertheless, different photochemical reactions, especially organic photochemistry, have been reported with more understanding over the last decades, giving the bright future to applications of photochemical reaction.[75]

1.2.1 **Cycloaddition Reactions**

There are numerous discovered photochemical reaction and photobiological processes, and most of them are not possible by thermal reactions.[76] Cycloaddition, formation of σ bond from excited π electrons, is a good case study. This reaction, also known as Diels-Alder reactions,[77] is very useful to create rings in a single step even between separated molecules. In thermal reaction, [4+2] cycloaddition occurs simply by heating. However, [2+2] and [4+4] cycloaddition does not occur via thermal reaction.

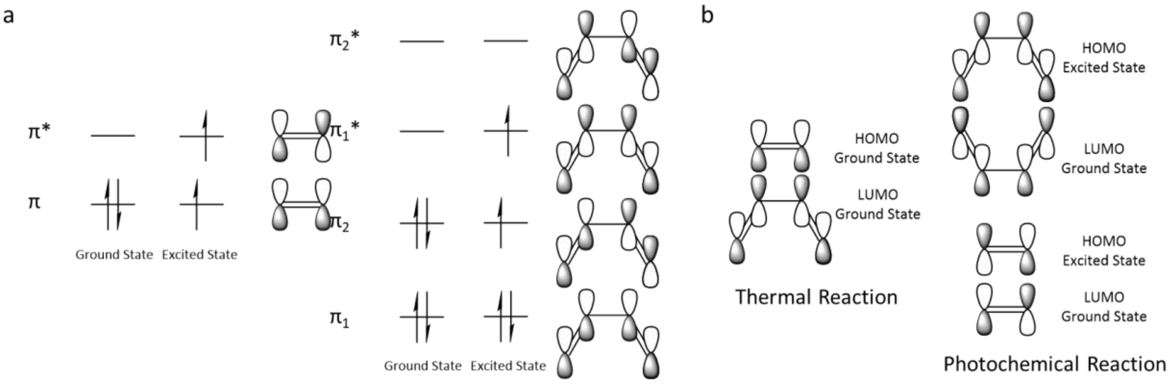

Figure 1-5. (a) π molecular orbitals of ethylene and 1,3-butadiene, and (b) suprafacial orientation for cycloaddition. [4+2] cycloaddition can occur when both reactants are in ground state, but [4+4] and [2+2] cycloadditions require one excited reactant to proceed.

The prediction can be explained by conjugated π molecular orbitals. (Figure 1-5 a) In electrolytic reactions, electron from HOMO of one reactant is donated to the LUMO of the other. Therefore, terminal π orbitals HOMO of one reactant must have the same face (suprafacial) as LUMO of the other. As a result, [4+2] cycloaddition is possible in ground state, while electron of one reactant must be excited from π to π^* orbital for [2+2] and [4+4] cycloaddition.[78] (Figure 1-5 b) Cyclobutane can be synthesized from 2 alkenes, 8-membered rings can be synthesized from butadiene derivatives, and other multi-cycles compound can be synthesized via photocycloadditions.[79,80] Together with thermal reaction, [2+2], [4+2], [4+4], and other cycloadditions can be achieved.

1.2.2 [4+4] Photocyclodimerization of Anthracene

One of the first discovered photochemical reactions is [4+4] photocyclodimerization of anthracene in benzene by Fritzsche in 1866.[81] He reported that when he kept the anthracene solution in benzene under sunlight, the white precipitate having different color, solubility and melting point was formed.[82] After that, the photochemistry has grown into different fields, but relatively unsatisfactory due to the lack of understanding in quantum chemistry at that time.[83]

Soon, the structure of anthracene dimer and different mechanisms were proposed, including not only anthracene but also 9-substituted derivatives.[84,85] The singlet state is accepted as a pathway of [4+4] photocyclodimerization of anthracene. However, the fluorescence emission, oxidation, excimer formation and triplet-triplet annihilation cause the mechanism to be complicated.[86] The excimer is expected to be the transition state, which is different from [2+2] photocycloaddition that is known to proceed through radical reactions.[87] Despite the fact that it has been discovered over a century, new insights of [4+4] photocycloadditions are continuously reported.[82,88–94]

The dissociation of anthracene dimers back to monomers can be achieved by thermal and photochemical processes, which has been utilized in different research fields such as energy storage,[95,96] photo responsive materials[97–99] and data storage.[100,101] On the other hand, few have utilized anthracene derivative dimers as synthesis building blocks or catalysts.[102–105]

Due to the short lifetime and only weak interactions associated in the electronically excited states, intermolecular photochemical reactions are not efficient at low concentration and difficult to control. Similarly, anthracene dimerization efficiency significantly depends on concentrations and diffusions.[106–108] Controlling selective [4+4] photocyclodimerization of anthracene derivatives is still not practical.

1.2.3 Sustainable Chemistry

Sustainable Chemistry (or Green Chemistry) is a chemistry research with the aim to reduce the toxicity and waste from the chemical process, especially the synthesis. Some examples include replacing the solvent to less toxic one such as water or alcohol, reducing synthesis and purification step or one-pot synthesis, avoiding rare or toxic metal catalysts, and designing the recyclable systems. Because photochemical reactions use light as an energy source, they are related to sustainable chemistry most of the time, not to mention the light energy harvesting systems which is the future solution for the energy crisis of mankind. Therefore, many researches have been devoted to the development of visible-light driven and nontoxic photochemical reactions.[109–113]

In this work, the photochemical reaction was developed with the idea of sustainable chemistry. The water was used as a main solvent for conducting photochemical reactions. The synthetic antibody, a biodegradable protein, was obtained from animal-free experiments and produced from bacteria. The chiral silica-organic hybrid nanoribbons are easy to handle at room temperature in water, easy to synthesize, and possibly recyclable templates. Finally, the arrangement of starting compounds was expected to increase the reaction efficiency, reducing energy and time of photoirradiation.

1.3 Supramolecular Chemistry

Supramolecular chemistry is the chemistry of the intermolecular bond based on weak (noncovalent) interactions.[114] This concept has been introduced in 80s, but the growth is remarkable. The weak interactions allow the reversibility and easily manipulated binding. This property makes supramolecular chemistry a promising approach in different fields such as functional materials,[115,116] sensors,[117–119] purifications, and reaction control.[120–122] This thesis incorporates the use of synthetic antibody and chiral silica-organic hybrid nanoribbons as chiral templates for photochemical reaction.

1.3.1 **Supramolecular Chirality Induction, Chirality Transfer and Asymmetric Synthesis**

Chirality induction is the method to induce chiral properties, mostly optical activity, to achiral molecules. Achiral molecules can exhibit chiral properties under anisotropic influences including chiral organizations or polarization from chiral environment.[123–125] The chirality inducers can be referred as chiral templates or chiral hosts. The supramolecular chirality inductions can be achieved without chemical modification of original achiral molecules, so that the new design or synthesis are not needed, and other physical properties do not change much. Moreover, the chirality induction system can be applied to different achiral molecules with similar structures with minimum optimization.[124] Chirality transfer is similar as chirality induction, but the induction is more permanent. The induced chiral property must remain even after dissociated from the chiral templates through different mechanisms such as isomerization, asymmetric synthesis or asymmetric degradation.[126–130]

Asymmetric synthesis, previously mentioned in “Producing Enantiopure Chiral Molecules” is defined as a synthesis that breaks the symmetry of the products.[71] The major product of any reactions depending on different factors such as transition states, intermediates, stability and energy level of products. However, enantiomers, without any chiral influence, going through the same path and have the same energy level. Therefore, the racemic mixture (symmetric product) is usually produced. To break this symmetry, chiral molecules can be used as chiral sources to differentiate the reactions pathway or final free energy of the products, making one enantiomer more favorable than the other. It is one of the most widely used methods to produce one enantiopure chiral compounds.[131–133]

Because antibody is naturally homochiral, many studies utilized antibodies, both wild and synthetic, as chiral templates or even catalysts.[134–137] However, only few cases have reported the use of antibody in asymmetric photochemical reactions.[138–141] Likewise, there are numerous reports on using chiral self-assembled systems as supramolecular chiral templates in different reactions, but relatively less reports utilize them for asymmetric photochemical reactions.[142–145] In addition, self-assemblies of amphiphiles, driven by hydrophilic and hydrophobic interactions such as micelles and bilayers, are less efficient than others because the they are relatively dynamics. Consequently, it is difficult to use as a rigid template. Therefore, in this thesis, synthetic antibody and hybrid gemini-type surfactant were utilized as chiral templates for regio- and enantioselective photochemical reactions.

1.3.2 Catalytic Antibody

Antibody has known to have specific binding sites for different organic molecules, and different types of antibodies can be generated, a basis of immune system, inside living organisms from the stimulation of different antigens. The variety of these sites is suitable for the design of selective catalysts.[146,147] Therefore, catalytic antibody is one of the most versatile catalytic biomolecules.[134]

Catalytic antibodies can be obtained from hybridoma technique, which is usually used to obtain therapeutic antibodies with high binding affinity to certain antigens.[148] The molecule that resembled the transition state of the reaction is used as a target for antibody binding. This molecule is usually conjugated to some proteins and injected to animals. The myeloma cells are fused with the extracted spleen cells of animal, and monoclonal antibodies can be harvested from growing hybridoma cells. The antibody candidates are screened for the best results, and they can be harvested repeatedly by growing hybridoma clones.[149,150]

Another method is to conduct the mutation on the antibody. With this method, it is the most direct approach for constructing the desired reaction sites.[151–153] The problem is this technique requires meticulous design of reaction-site architect, careful selection of antibody, the complete knowledge and experience on mutation regions, and the ability to predict the tertiary structure of antibodies. On the other hand, there has been some development on computational design and random mutagenesis evolution for enzymes, which can be a future for mutation technique.[136,154]

The recent advancement led to the phage display technique. The protein library with random sequences are generated and stored in the form of vectors in phage particles. The target molecules are attached to biotin with some linker such as polyethylene glycol (PEG). The phage library can be mixed with this modified target molecules *in vitro*, and the phages with proteins bound to the target molecules are isolated using streptavidin, bound to biotin, on surface of paramagnetic beads. The bound phages are infected to *Escherichia coli* (*E. coli*) for reproduction, and the panning can be repeated as preferred (usually 3 - 6 rounds). After screening the candidates, the information of desired protein can be obtained from vector in infected *E. coli* cells. Using genetic engineering methods to transform this gene to *E. coli*, the desired protein can be produced from bacteria.

This technique was first used for peptide therapeutics. The antibody, however, is more complicated to be fully expressed in *E. coli*. Tomlinson *et al.* succeeded in expressing full human single-chain (sc) Fv antibody in *E. coli*, the breakthrough of antibody phage display library. For Tomlinson I and J libraries, the random sequences give more than 10^9 variety of antibodies, which is obviously less than hybridoma technique. On the other hand, besides the animal-free and faster procedure, the sequence of antibody can be obtained. Together with the known structure, the models of synthetic antibody can be constructed with high accuracy.

1.3.3 Chiral Self-Assembly of Amphiphile

Amphiphile, the molecule containing hydrophilic and hydrophobic parts, always has significant influence in self-assembly field.[155] The wide variety of building blocks, relatively simple synthesis and the possible use in both hydrophilic and hydrophobic solvents increase the variety of application. In addition, the ability to form different self-assembled structures make amphiphile a forerunner in bottom-up synthesis of nanotechnology.[156,157]

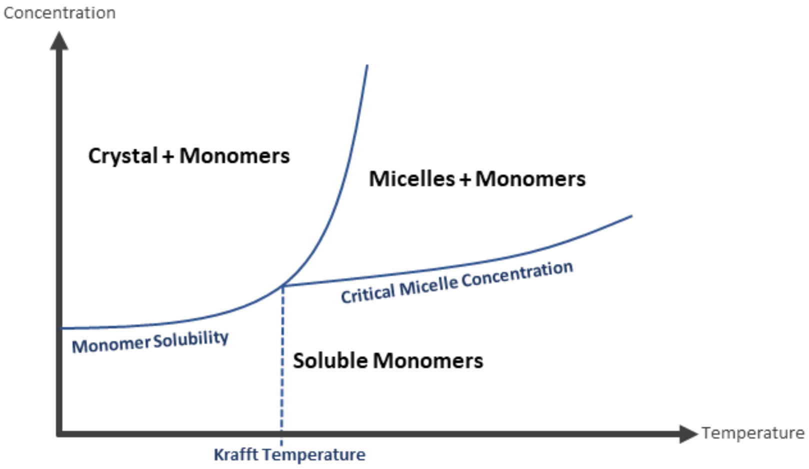

Figure 1-6. Simplified graph showing temperature-solubility relations of typical ionic surfactant.

The important parameter for self-assemblies of amphiphiles or surfactants is Krafft temperature (T_K) and critical micelle concentration (CMC). (Figure 1-6) CMC is defined as the concentration that surfactant monomers start to form micelles, beyond CMC, self-assemblies occur. T_K is defined as a temperature exhibiting discontinuous increase of solubility. Based on this information, the self-assemblies of amphiphiles in different crystalline structures and micelles can be manipulated by changing concentration and temperature. It is possible to form homogeneous crystalline structures by heating the solid amphiphile to micellar or soluble domains and cooling down.[158] For ionic surfactants, T_K and CMC strongly depend on the lengths of hydrophobic chain and the nature of counterions.[159–161]

The self-assembly of chiral molecules can sometimes lead to chiral mesoscopic structures such as chiral patterning or helical structure in nano- to micrometer scales.[162–164] The use of gemini surfactant is particularly interesting in the field. The term "gemini" was introduced in 1991 for surfactant having a pair of hydrocarbon chains and ionic groups, where the two ionic groups are linked by a covalent linker.[165–167] There are different reports on making twisted nanostructure from chiral gemini surfactants.[168–172]

In the group of Oda, there have been several reports related to chiral self-assembly from ionic gemini surfactants directed by chiral cations since over 2 decades.[169,173–178] The properties of surfactants influenced by hydrocarbon chains and counterions were studied.[159,179] Moreover, the structure of self-assembly in molecular level and parameters affecting morphologies were elucidated,[176,180–183] establishing standard and reproducible procedure for preparing twisted nanoribbons and helices in water and organic solvents.

Furthermore, not only the morphology of twisted nanoribbons but also the chirality induction and chiral memory in stable materials were developed. The chiral morphology (and even molecular chirality) can be transferred to silica nanostructure via sol-gel transcription.[184] In a suitable condition, homogeneous chiral silica nanofibers can be synthesized in water.[185,186] The twisted silica nanofibers exhibit chirality in molecular level and possess enantioselective property.[187,188] They can also be used as a chiral template in chirality induction of polyoxometalates for organic synthesis purpose and gold nanoparticles for circular dichroism in visible region.[189–192] Alignment of silica nanofibers were also developed, expanding application to solid state. [193,194]

Recently, the new paradigm of using silica nanofibers having surfactant inside, called hybrid nanofibers, was explored. Interestingly, the silica walls conserve chirality of gemini self-assemblies even after exchanging chiral counterions to achiral ones. In addition, the inversed chirality induction from gemini self-assemblies (chirally arranged achiral molecules) to achiral counterions occurs.[195–197]

Even though chiral self-assemblies have been used as templates in different asymmetric reactions,[198] the surfactant self-assemblies are dynamic structures; therefore, they are difficult to use as reaction templates. However, the silica walls of hybrid nanofibers were proved to maintain the chiral assemblies of gemini while offering them suspendability in aqueous media. Thus, utilizing silica-organic hybrid nanoribbons as chiral supramolecular template for photochemical reaction is one objective of this thesis.

1.4 Selective [4+4] Photocyclodimerization of Anthracene Derivatives

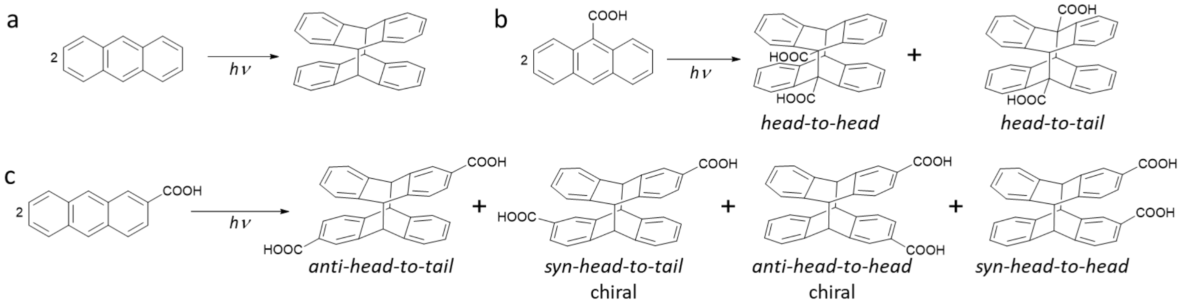

Figure 1-7. Photocyclodimerization products of (a) anthracene, (b) 9-anthracenecarboxylic acid and (c) 2-anthracenecarboxylic acid. In the case of single substitution, only 1- or 2-substituted anthracene will yiled 2 chiral dimers.

[4+4] Photocyclodimerization of anthracene simply gives one dimer as a product. However, anthracene derivatives can have different regio isomers and enantiomers depending on the orientation of anthracenes. (Figure 1-7) There are different attempts to the regio- and enantioselective syntheses of anthracene derivative dimers.

1.4.1 Solid State Photocyclodimerization

The distinct organization of organic molecules in crystal has been vastly utilized for photochemical reactions dated back to pioneer works in 1970s.[199–201] The organization of anthracene molecules in crystal based on aromatic interactions, so that anthracene molecules are usually in face-to-face alignment, which is preferable for photocyclodimerization. In crystal, not only the appropriate distance between anthracene molecules but also the lattice change after reactions are essential for the reaction to proceed. Salzillo and Brillante categorized photocyclodimerization of anthracene derivatives to topochemical, non-topochemical and reversible photocyclodimerization.[202]

Topochemical photocyclodimerization is the case that the products correspond to the original orientation of monomers such as photocyclodimerization of 9-methylanthracene.[203] Moreover, the original orientation can be manipulated in different ways. The co-crystals of anthracene, such as 9-(methylaminomethyl)anthracene and silver(I) complex, and azaanthracene and HCl, could also promote the usually unfavorable photocyclodimerization in solids with absolute regioselectivity.[204,205] Similarly, enantioselective [4+4] photocycloaddition of anthracene and naphthalene can be induced by chiral linker, giving up to 100 % ee.[206]

Non-topochemical photodimerization, however, is more complicated system that the dimer products are not related to the orientation of the original anthracene crystal structure. In the case of β-9-anthracenecarboxylic acid crystal, it can form three different products, and the lattice becomes more disorder with photoirradiation.[207] 9-cyanoantracene and 9-anthraldehyde gives *head-to-tail* dimer even though the crystal structure favors *head-to-head*.[208] The formation of stable but non-favored dimer in solid-state originates from the defects in crystal. The monomer in the crystal will be shifted to defective sites and turn to *head-to-tail* orientations.[209]

Reversible photodimerization is the case when dimerization proceeds but not complete, so the dimers will dissociate back to monomer after some time even without irradiation or heating. For example, α-9-anthracenecarboxylic acid crystal, which dimerizes quickly in solution to *head-to-tail* dimer,[210] can be dimerized to give meta-stable *head-to-head* dimer, but it will turn back to monomer after stop irradiation and kept in the dark. Contradictory, the crystallization of *head-to-tail* dimer from solution state showed solvent molecules incorporated inside the crystal lattice,[211] so that it is not possible to make pure crystal of 9-anthracenecarboxylic acid that favors *head-to-tail* dimerization.

On the other hand, the changes of lattice positions in crystals, even topochemical photocyclodimerization, were utilized as a driving force for mechanical motions of anthracene crystals, called photosalient behavior. [212–214] Similarly, this mechanical force can also be used as a driving force of dimerization or dissociation.[92,93,215–217]

Still, the drawback of photoirradiation to the crystal is the limitations of anthracene orientation in crystal lattice.

1.4.2 **Supramolecular Photocyclodimerization Using Cyclodextrin**

Cyclodextrin is known to be a good host for different hydrophobic molecules and can enhance intermolecular reactions such as Diels-Alder reactions.[218] With different sizes and modifications, the guest can be selected, and the orientation inside the cavity can be manipulated. Moreover, the monomer of cyclodextrin is saccharide, providing chiral cavity for any guest molecules. It houses aromatic molecules such as naphthalene, anthracene and pyrene.

Tamaki *et al.* discovered that the cavity of γ-cyclodextrin is suitable for inclusion of 2 anthracene molecules, which accelerate photodimerization and induce *head-to-tail* regioselectivity, or even sensitization.[219–221] β-cyclodextrin can also form 2 : 2 complex with anthracene that allow different selectivity of dimer products.[222] The major photocyclodimerization products of 2-substituted anthracene obtained from cyclodextrins are *head-to-tail* dimers.

Later, Inoue and col. continued this work focusing on not only regioselectivity but also enantioselectivity of 2-anthracenecarboxylate in γ-cyclodextrin. *syn-head-to-tail* dimer is produced up to 45 % product distribution and 32 % ee.[223] Significant improvements from modifying cyclodextrin and controlling external factors were reported.[224–232] By capped γ-cyclodextrin, ee can be improved to 71 % and 58 % of the antipodal enantiomer.[225,226] Diguanidino-γ-cyclodextrin can produce *anti-head-to-head* dimer with 72 % product distribution and 86 % ee, and 46 % product distribution with 64 % ee of antipodal enantiomer in different solvents, which is opposite to the native γ-cyclodextrin.[233]

The linked β-cyclodextrin, despite the complicated synthesis, can induce absolute enantiopure *syn-head-to-tail* 2-anthracenecarboxylate dimer in certain conditions and generate 5,8:9',10'-cyclodimers (slipped dimers) in another condition.[234,235]

The host molecules providing similar cavity, such as cucurbit[*n*]uril, were also utilized for photocyclodimerization.[236] Cucurbit[*8*]uril and cucurbit[*10*]uril can promoted the photodimerization of 9-substituted anthracenes,[237] and the cucurbit[*8*]uril showed complete *head-to-head* regioselectivity of cyclodextrin-appended 2-anthracenecarboxylate.[238]

1- and 9-anthracenecarboxylic acid, on the other hand, could not form 2 : 1 complex with γ-cyclodextrin.[219] In addition, enantioselectivity and promotion of photocyclodimerization of 2-hydroxyanthracene is much lower.[239] Hence, the substitution to anthracene is crucial for photocyclodimerization in confined media, the limitation of cyclodextrins.

1.4.3 Supramolecular Photocyclodimerization Using Serum Albumin

With natural chirality, protein is the most abundant class of chiral molecules. Enzymes catalyze reactions in living organisms with an absolute enantioselectivity. Together with variety of amino acid residues, including artificial ones, and the different secondary, tertiary and quaternary structures, numerous utilizations of proteins in photochemical reactions have been reported.[240–243]

Serum albumins (SAs), the most abundant serum protein in mammals, were utilized as chiral hosts for supramolecular [4+4] photochirogenesis of 2-anthracenecarboxylate, pioneer work from Wada and col. Different SAs catalyze different products.[244–246] Mostly, they are suitable for synthesizing *head-to-tail* dimers. For examples, canine SA (CSA) yields *syn-head-to-head* dimer with 97 % ee with 77 % product distribution, while porcine SA (PSA) yields 89 % ee of antipodal enantiomer with 69 % product distribution. Moderate ee and product distribution of *head-to-head* dimers were also reported in bovine and sheep SA (BSA and SSA).

Due to multiple binding sites for anthracene derivatives, the variety of products and inactive bound anthracene monomers were found. But the thorough investigation is difficult due to the limitations of information. For instant, BSA crystal structure was just reported in the last decade.[247] Therefore, much attention was devoted to human SA (HSA) having well studied structure and binding sites.[248,249] The studies included photophysical properties of 2-anthracenecarboxylate-HSA complex,[250–252] the photoirradiation in catalytical manner[253] with the details of binding sites,[252,254] and specific mutations to accelerate the reaction.[255]

Still, the limitation of using wild type protein is the unpredictable outcomes of both product distributions and ee, the multiple binding sites and limited information for further improvement.

1.4.4 **Supramolecular Photocyclodimerization Using Other Media**

There are still countless reports on manipulating [4+4] photocyclodimerization of anthracene. Some other selections are introduced in this session. Metastable liquid crystal can align 2-anthracenecarboxylate methyl ester in *head-to-head* orientation and give more than 75 % *syn-head-to-head* dimer with more than 85 % ee.[256] The combination of cucurbit[*8*]uril and chiral ionic liquid also induced 41 % ee of *syn-head-to-tail*,[257] and 91 % *head-to-head* dimers in aqueous solution.[258] The nano helices of silver and copper provide proper surface for regio- and enantioselective photocyclodimerization of AC. Immobilizing AC on the surface and irradiate by light after drying yields absolute *head-to-head* AC dimer with detectable ee.[259] The hydrogen-bonding templates were also used for synthesizing anthracene and 2-anthracenecarboxylic acid cross dimer,[260] and regio- and enantioselective synthesis of 2,6-anthracenedicarboxylic acid dimer up to 55 % ee.[261] Prolinol was also used as hydrogen-bonding template, forming 2 : 2 complex giving exclusively *head-to-head* dimers with 72 % ee as the products at low temperature.[262,263] Directly linking 2 anthracene molecules with chiral linkers, although it is not supramolecular chemistry approaches, can yield close to absolute regio- and enantioselectivity of *anti-head-to-head* dimer.[264–267] Chiral organogel was used as a *head-to-head* regioselective media with detectable ee.[268] Chiral self-assisted amidine-carboxylate template consisted of anthracene can form double-helix structure. Photoirradiation yielded up to 99% ee.[269,270] There are also other host biomolecules utilized for this reaction, such as Insulin fibril superstructure and prefoldin protein.[271,272] Dual amylose-cyclodextrin showed an interesting result in switching between enantiomers of *anti-head-to-head* dimer at different temperature (−10 % to +10 % ee).[273] The regioselective photocyclodimerization of 9-substituted anthracene, even without enantio-selectivity, using micelles and Nafion membrane are pioneer works in the field of utilizing surfactant self-assemblies as photochemical reaction media.[210,274,275]

CHAPTER 2: SUPRAMOLECULAR CHIRALITY INDUCTION AND REGIOSELECTIVE [4+4] PHOTOCYCLODIMERIZATION OF 2-ANTHRACENECARBOXYLATE USING CHIRAL SILICA-ORGANIC HYBRID NANORIBBONS

2.1 Objective

The objective of this chapter is to utilize chiral silica-organic hybrid nanostructures as the supramolecular hosts in [4+4] photocyclodimerization of AC in water. The synthesis and stability of the chiral silica-organic hybrid nanostructures are discussed. The induced chirality, organization, exchange kinetics and stability of AC (and the other molecules) are explained. Finally, the results of photocyclodimerization of AC in chiral silica-organic hybrid nanostructures are reported.

2.2 Introduction

Chiral supramolecular self-assemblies received much attention nowadays because the fabrication though bottom-up approach can be easily manipulated depending on the basic building blocks.[167] The chiral properties of self-assembled systems are widely utilized directly as chiral materials and indirectly as chirality inducers or reaction templates.[167,171]

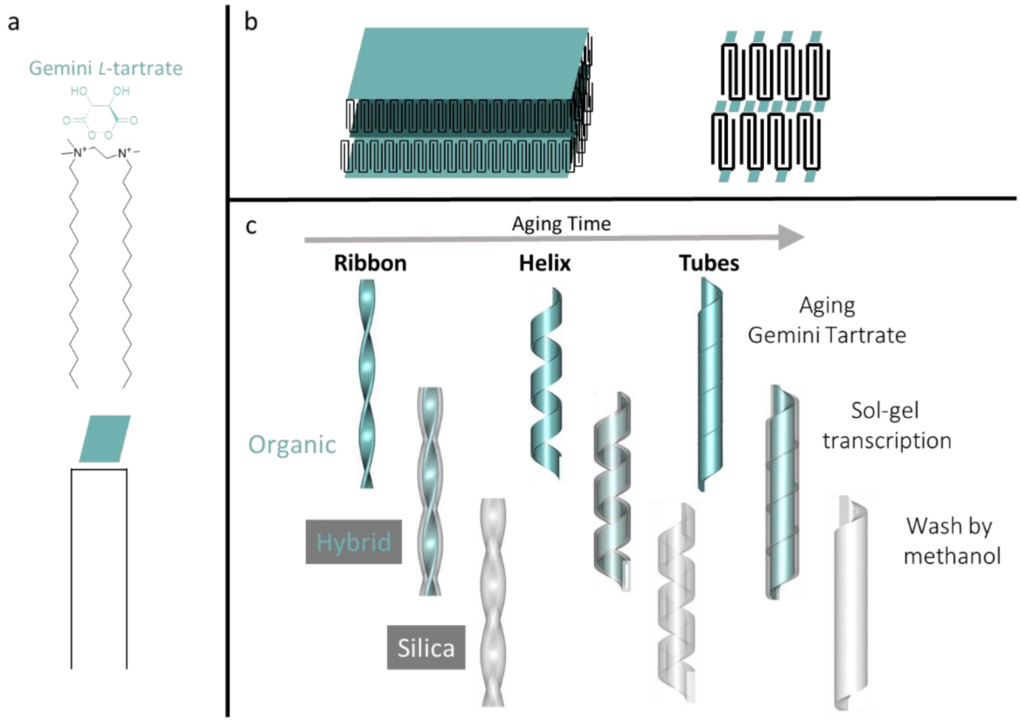

Figure 2-1. (a) Structure and figure representation of gemini L-tartrate, (b) the 3D and cross-section structure of self-assemblied double-bilayer of gemini tartrate, (c) the nano-scale morphologies (left to right: ribbon, helix and tube) and classes (top to bottom: organic, hybrid and silica) of chiral twisted nanostructures.

In 1998, Oda *et al.* reported the formation of chiral twisted nanostructures in the form of hydrogel from previously reported gemini surfactant in the presence of chiral counterions such as tartrate.[173] The formation of chiral supramolecular self-assembled organic nanostructures from *N,N'*-dihexadecyl-*N,N,N',N'*-tetramethylethylene diammonium tartrate (hereafter mentioned as gemini tartrate, Figure 2-1 a) has been investigated. The self-assembled double-bilayer of gemini L- or

D-tartrate surfactants show the nano-scale chiral morphologies: twisted ribbon (Gaussian curvature), helix (cylindrical curvature) and tube. (Figure 2-1 b and c) The control on the formation of each morphology is well established, mostly based on time, temperature and concentration.[169,181,183]

In order to make such self-assembled structures to more robust nano-objects, silica transcription procedure using tetraethyl orthosilicate condensation was developed to imprint and transfer the chiral helical morphology to silica nanostructures.[187] (Figure 2-1 c) After removing the gemini tartrate by washing with hot methanol, the silica nanostructures can be used as a chiral template for chirality induction of other materials, such as gold nanoparticles,[191–193] chromophores[276] and polyoxometalates[189,190] in both solid and suspension forms. Polyoxometalate-grafted silica helices were used as a heterogeneous catalyst for a selective oxidation of sulfides.[189,190]

It was also shown that chiral silica-organic hybrid nanostructures before removing the gemini tartrate (hereafter refer as hybrid nanostructures, Figure 2-1 c) form stable host for anions in suspension. Chiral supramolecular assemblies of gemini tartrate was kept in the silica wall after transcription. The chiral silica-organic hybrid nanoribbons and nanohelices (hereafter called hybrid nanoribbons and hybrid nanohelices) could be synthesized with slightly modified protocols. The silica walls, covering the surfactant self-assemblies, have the ability to sustain the chiral assemblies of gemini even the tartrate, the only chiral molecule, was exchanged by other counterions. Moreover, the memorized chirality of gemini structure can be used to induce the chirality to the other counterions such as halides and sulfonate dyes.[195–197]

Inspired from these results, we attempted to use the synthesized hybrid nanoribbons and hybrid nanohelices as chiral templates for entrapping the AC in aqueous solution and for the chirality induction to the co-organized AC with gemini in the chiral nano space within the hybrid nanoribbons. The AC organization, binding and stability will be discussed. The supramolecular regioselective photocyclodimerization of AC are demonstrated as the first attempt to use hybrid nanoribbons as a supramolecular host for isomer-selective photochemical reaction. As gemini tartrate has low UV absorption below 240 nm, hybrid nanostructure can be used in variety of photoreactions without competitive photoabsorption or photodecomposition. The length of the gemini hydrocarbon chains and spacer are also tunable. These cause hybrid nanostructures to be a potential supramolecular host for various photochemical reactions.

2.3 Synthesis of Chiral Silica-Organic Hybrid Nanoribbons

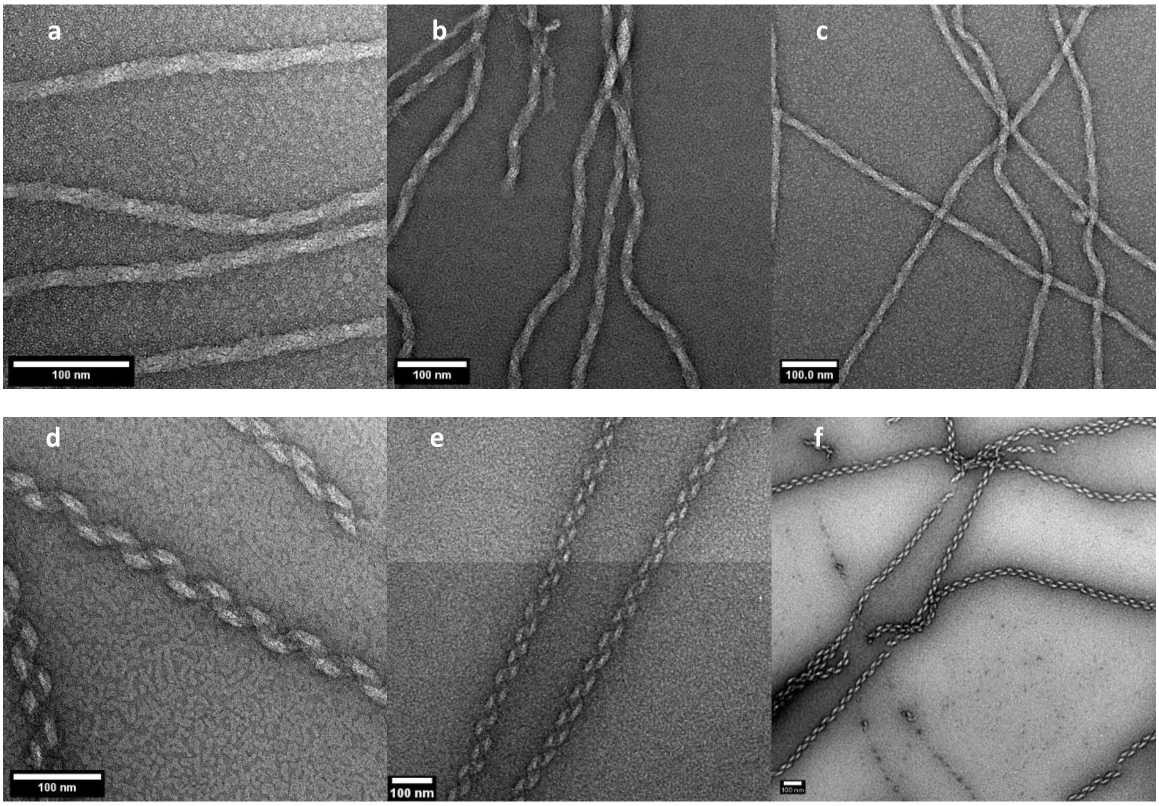

Figure 2-3. TEM images of (a-c) organic nanoribbons and (d-f) organic nanohelices with negative staining by uranyl acetate. All scale bars are 100 nm.

The chiral supramolecular self-assembled organic nanoribbons or nanohelices from gemini tartrate were obtained following the reported protocols.[183,186] (see experimental procedure session for the details of the monomer synthesis and self-assembled formation) The formation of the desired structure was confirmed by TEM with negative staining of uranyl acetate. (Figure 2-3) In this state, surfactants formed twisted double-bilayer solely from the thermodynamics effect of cooling. Therefore, their organization can be easily disturbed by heat or other additives.

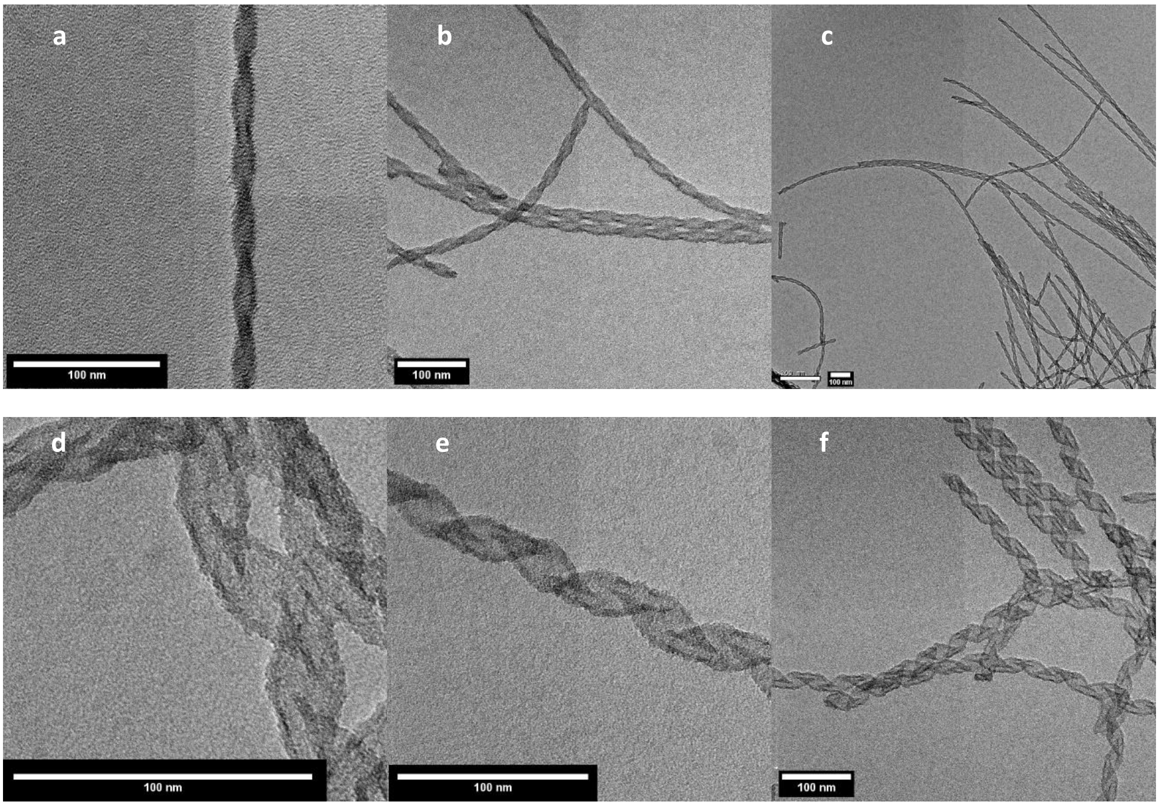

Figure 2-4. The TEM images of (a-c) hybrid nanoribbons and (d-f) nanohelices. All scale bars are 100 nm.

The hybrid nanostructures were synthesized as previously reported,[186] and the morphology of the nanostructures were confirmed by TEM (Figure 2-4). Due to the high contrast of silica, staining was not necessary. Although both nanoribbons and nanohelices were synthesized, the experiments in this chapter mainly focused on nanoribbons because of the synthetic simplicity. Also, the pre-hydrolysis and transcription times used in this work are shorter than in the previous report to minimize the formation of silica particles not associated to the nanoribbons.

While the morphology of these nanostructures can be observed at nanometer scale as transmission images with TEM (no information on the handedness), only small part of suspension can be observed at a time. Therefore, it is difficult to quantitatively establish the standard for the hybrid nanostructure stocks synthesized independently. In addition, only the silica component on the outside can be seen, while the surfactant self-assemblies inside hybrid nanostructures are not visible.

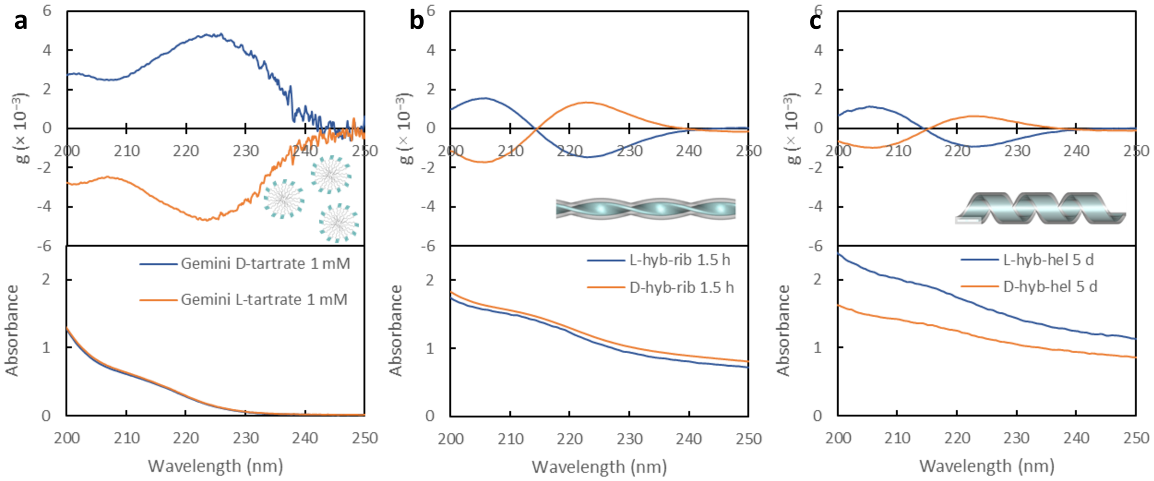

Figure 2-5. g-factors and UV-Vis absorption spectra of (a) gemini tartrate at 70 °C, (b) hybrid nanoribbons aging 1.5 h at 20 °C and (c) hybrid nanohelices aging 5 d at 20 °C.

On the other hand, CD, giving the information on the cooperative chirality from self-assembly *versus* molecular chirality, is a simpler and faster way to determine the average chirality information in the overall suspension stock. Indeed, as shown in Figure 2-5. The CDs of hybrid nanostructures are different from gemini tartrate forming micellar structure. (The Krafft temperature of gemini 16-2-16 tartrate is lower than 60°C.) Finally, the g-factor of hybrid ribbons (absolute maximum about 1.5×10^{-3}) and hybrid helices (absolute maximum about 1.0×10^{-3}) were estimated. To standardize hybrid nanostructures, the samples with g-factor 20 % different from these values were not used in any experiments.

The scattering from the hybrid nanostructures due to the high refractive index of silica and the aggregation formation causes the artefact on the measurements of UV-Vis and the determination of g-factor. The aggregation, in this case, can be divided to 2 main categories: micro aggregation (surfactant double-bilayer assemblies and silica networks) and macro aggregation (the entanglement among nanostructures). Usually, Mie scattering and Rayleigh scattering are used to fit and remove the scattering pattern of micro aggregations.[277] However, the sizes and shapes of the nanostructures are not applicable to estimate the scattering in this work. Another way is to use standard silica particles to obtain scattering pattern, but commercially available silica particle standards are mostly in spherical shapes. Moreover, the macro aggregation is not uniform, increasing the distribution of light-scattering particles. Thus, the approximation of scattering profile is not applicable with the information in the present study.

Indeed, while the scattering of silica and gemini can be removed by subtracting the scattering of chloride-exchanged hybrid nanostructures, which do not have any absorption at the wavelength longer than 200 nm, the scattering due to the molecular aggregation of gemini tartrate still remains. In addition, the macro aggregation of chloride-exchange hybrid nanostructures can be completely different than the original gemini-tartrate hybrid nanostructures due to the heavy centrifugation. Therefore, the scattering was kept as a part of the system.

After every synthesis of hybrid nanoribbons stock, CD and TEM were used to confirm the consistency. The concentration of hybrid nanoribbons and nanohelices were calculated from the lyophilized sample based on the previously reported calculated and empirical results.[197]

2.4 Supramolecular Chirality Induction of 2-Anthracenecarboxylate by Chiral Silica-Organic Hybrid Nanoribbons

2.4.1 CD Induction of AC from Hybrid Nanoribbons

The AC stock solution in NaOH 10 mM (aq, pH < 8.5) and the hybrid nanoribbons stock solution in water were mixed and diluted by water to the desired concentration. The mixture was incubated on roller mixer at 20 °C overnight in the dark to any prevent photobleaching.

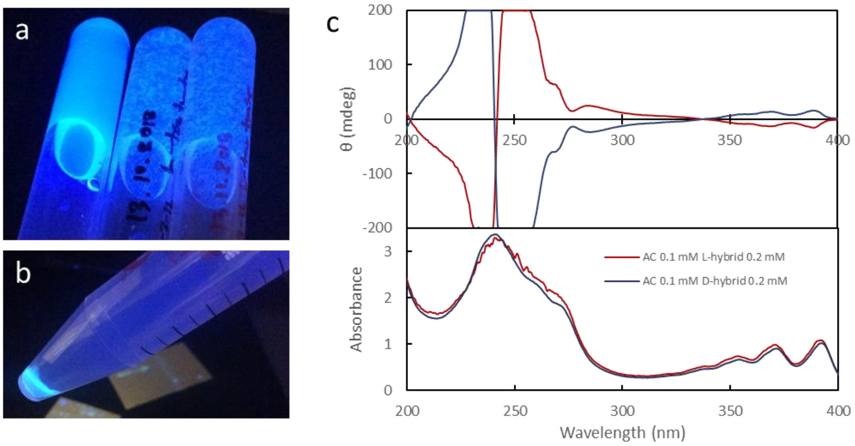

Figure 2-6. (a) Photo of AC in aqueous solution, AC in D-hybrid nanoribbons suspension and AC in L-hybrid nanoribbons suspension (from left to right, observed under 352 nm light), (b) photo AC in L-hybrid nanoribbons suspension after centrifugation (pbserved under 352 nm light), and (c) CD and UV-Vis absorption spectra of AC-exchanged hybrid nanoribbons ([AC] : [hybrid nanoribbons] 100 µM: 200 µM) after 20 h at 20 °C.

Figure 2-6 a and b clearly show the incorporation of AC molecules in the hybrid nanoribbons suspension. This corresponds to the exchange between anions previously reported, in this case AC and tartrate.[196,197,278] The AC-exchanged hybrid nanoribbons showed distinctive induced CD throughout the absorption spectrum. (Figure 2-6 c)

The CD of tartrate at 210-240 nm is negligible in these spectra because the induced CD of AC is much higher than tartaric acid or gemini tartrate in hybrid nanoribbons (absolute maximum less than 20 mdeg for tartaric acid 200 µM). Also, gemini tartrate and tartaric acid do not show absorption peaks longer than 240 nm, which means the CD signal from 240 nm to 400 nm belongs solely to AC.

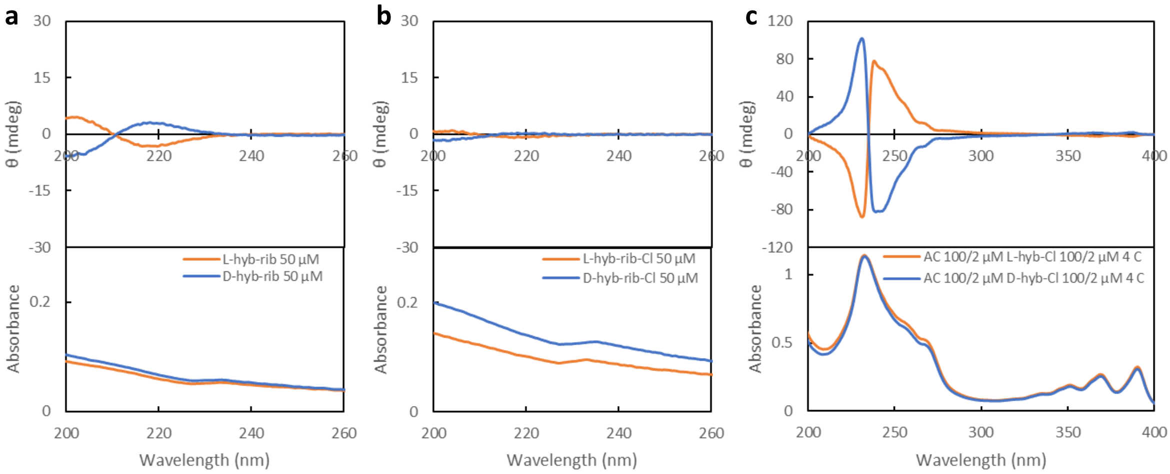

Figure 2-7. CD and UV-Vis absorption spectra of (a) hybrid nanoribbons 50 µM, (b) chloride-exchanged hybrid nanoribbons 50 µM, and (c) mixture of AC 100 µM and chloride-exchanged hybrid nanoribbons 100 µM diluted by half (final concentration [AC] = [chloride-exchanged hybrid nanoribbons] = 50 µM).

We then performed the AC exchange through gemini chloride. First, the hybrid nanoribbons (Figure 2-7 a) were washed by KCl solution until complete substitution, producing chloride-exchanged hybrid nanoribbons.[197] The substitution was followed by CD spectra. Because chloride does not have absorption at the wavelength longer than 200 nm, the diminished CD signal (Figure 2-7 b) implies the complete exchange of tartrate with chloride.

Without tartrate, the UV-Vis absorption spectra should decrease. In contrast, the scattering profiles greatly increased, indicating more aggregated suspension. The washing protocols consist of centrifugation, which could be the main reason for this elevated aggregation. Thus, the chloride-exchanged hybrid nanoribbons were sonicated by probe sonicator again to reduce the aggregation. In addition, the concentration was measured again by lyophilization, avoiding any errors from the loss of hybrid nanoribbons during washing procedure.

Then, AC was added to the chloride-exchanged hybrid nanoribbons. As a result, the CD spectra (Figure 2-7 c) are similar to those obtained from AC mixture with the original gemini-tartrate hybrid nanoribbons. This not only confirm the assumption that the observed induced CD signals belong to AC but also clarify that the chirality of AC is induced by memorized chirality of gemini supramolecular assemblies, not the chiral tartrate molecules. However, there are some difference in the CD spectra possibly due to the properties of tartrate and chloride. The tartrate is dianion, while chloride is monoanion, and the tartrate has stronger interactions to gemini than chloride. The effects of the starting anions will be discussed later in this chapter.

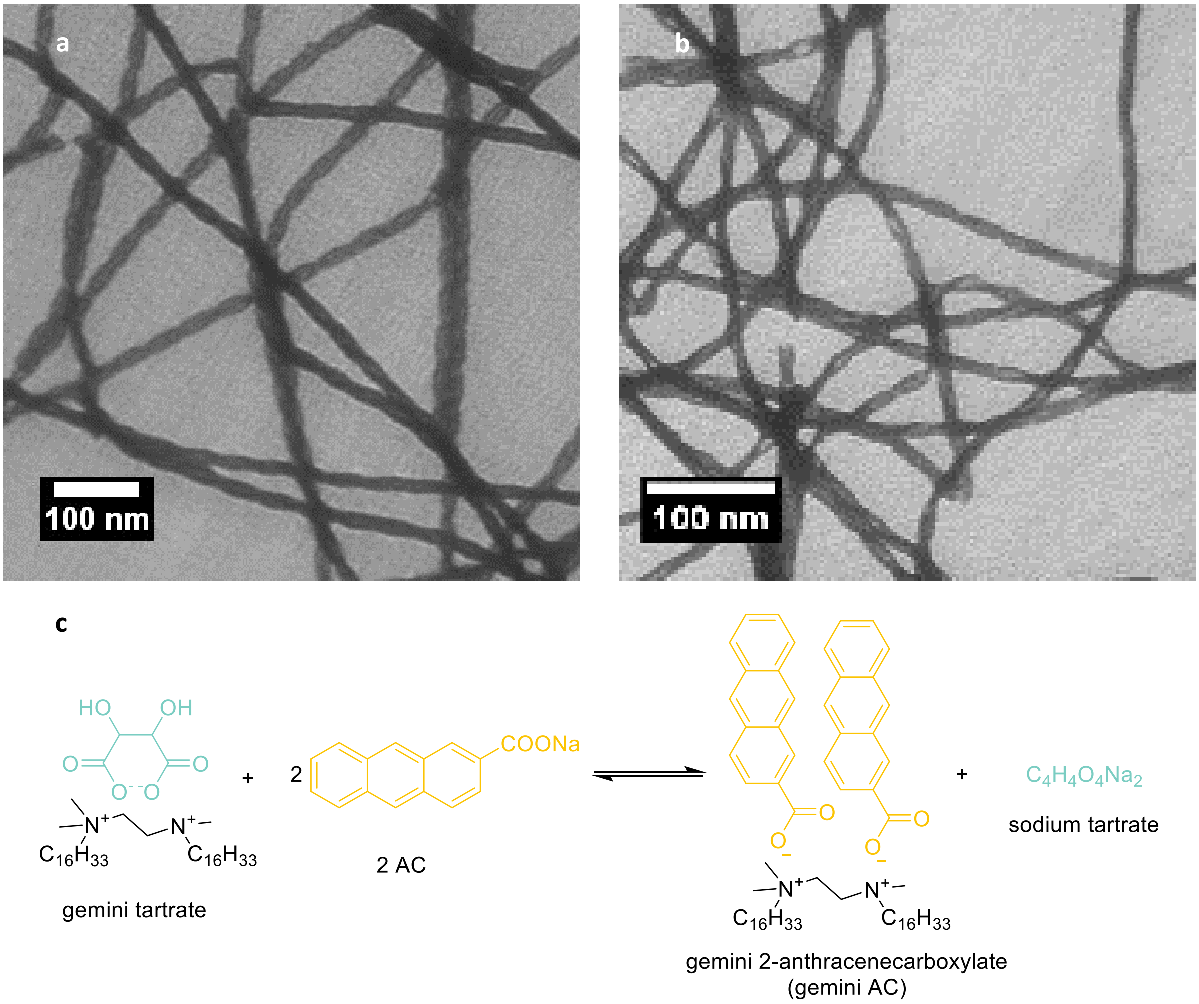

Figure 2-8. TEM images of L-hybrid nanoribbons (a) before and (b) after adding AC ([AC] : [hybrid nanoribbons] 100 µM: 200 µM) for 3 d at 20 °C, and (c) stoichiometry of AC-tartrate anion exchange.

From the TEM images (Figure 2-8 a and b), the silica morphologies of hybrid nanoribbons changed after adding AC. The less consistent twisted structures indicated the perturbation of both organic and silica structures. This change is reasonable considering the size of AC and tartrate. Stoichiometry of AC to tartrate is 2 to 1 because tartrate is dianion, but AC is monoanion. (Figure 2-8 c) Although the absolute organization of AC is not known, the molecular size of AC is larger than tartaric acid. From the molar mass and density (predicted by ACD/Labs Percepta Platform), the molecular size of AC and tartaric acid are 284 and 131 Å^3. Therefore, 4 times increase in size is expected, which can perturb both gemini supramolecular assemblies and silica wall.

The AC incorporation was induced by the presence of cationic gemini in the hybrid nanoribbons. Therefore, negative control was conducted using silica nanoribbons. Although there is a report that 2,6-dihydroxyanthracene can be adsorbed on the surface of silica nanohelices,[279] AC, as expected, did not aggregate when mixing with the silica nanoribbons, and CD i+=nduction was not observed, supporting the presumption that the aggregation and chirality induction of AC molecules come from the interactions to the gemini assemblies. (Appendix)

2.4.2 Time-dependent CD of AC-exchanged hybrid nanoribbons

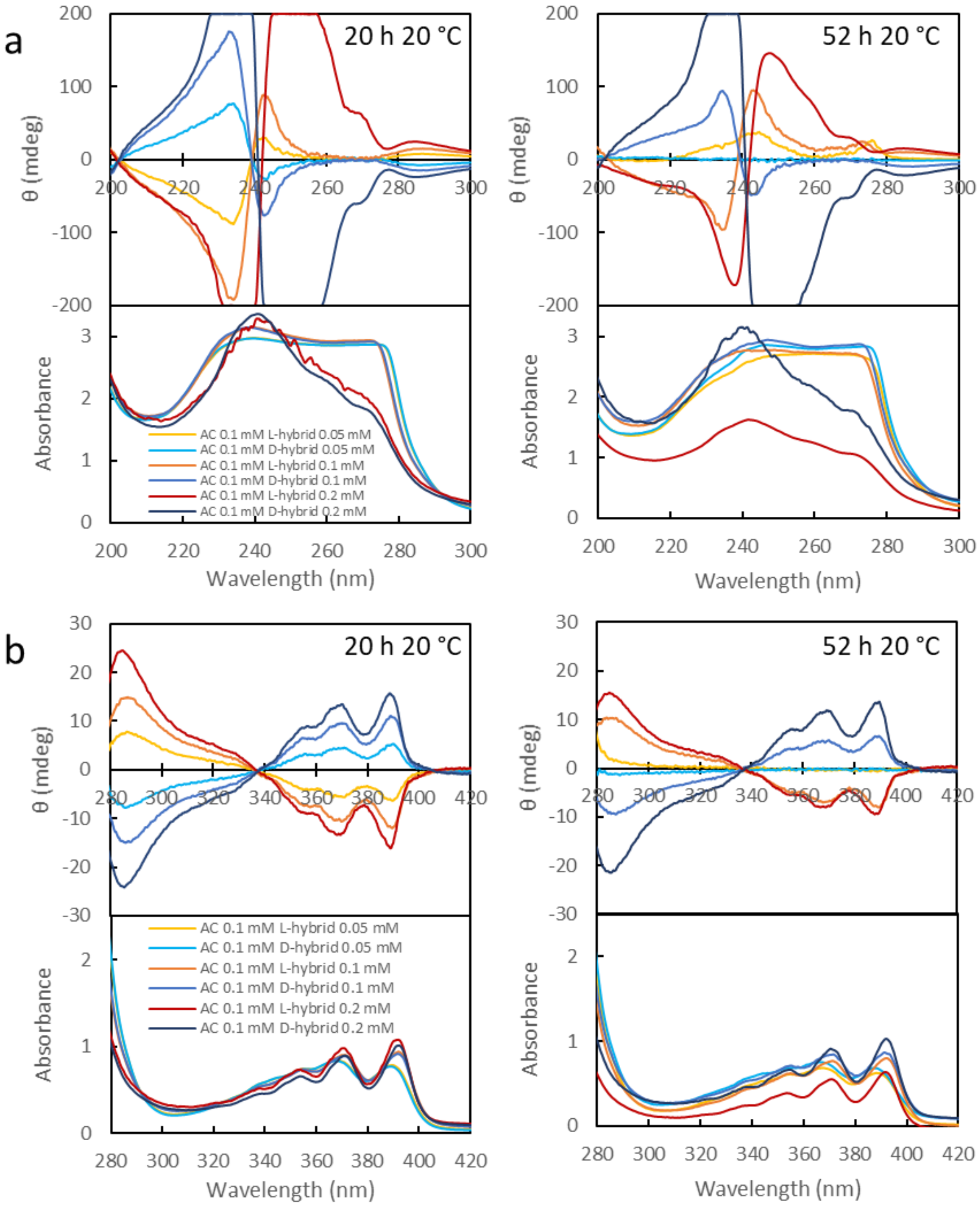

Figure 2-9. CD and UV-Vis absorption spectra of AC-exchanged hybrid nanoribbons ([AC] = 100 µM, [hybrid nanoribbons] = 50, 100 and 200 µM) incubated at 20 °C for 20 h and 52 h in (a) 200 - 300 nm and (b) 280 - 420 nm ranges. The abnormal CD intensity at 220-260 nm is due to the saturation of the detector (HT > 600 V).

Although the preliminary results show distinctive induced CDs, they are not stable over time. The AC-exchanged hybrid nanoribbons in different ratios were incubated on roller mixer at 20 °C, and the CD spectra were measured after 20 h and 52 h (Figure 2-9). The CDs of all samples after 52 h clearly decreased, especially the sample with hybrid nanoribbons 50 µM that the CD signals at 300 - 400 nm completely disappeared.

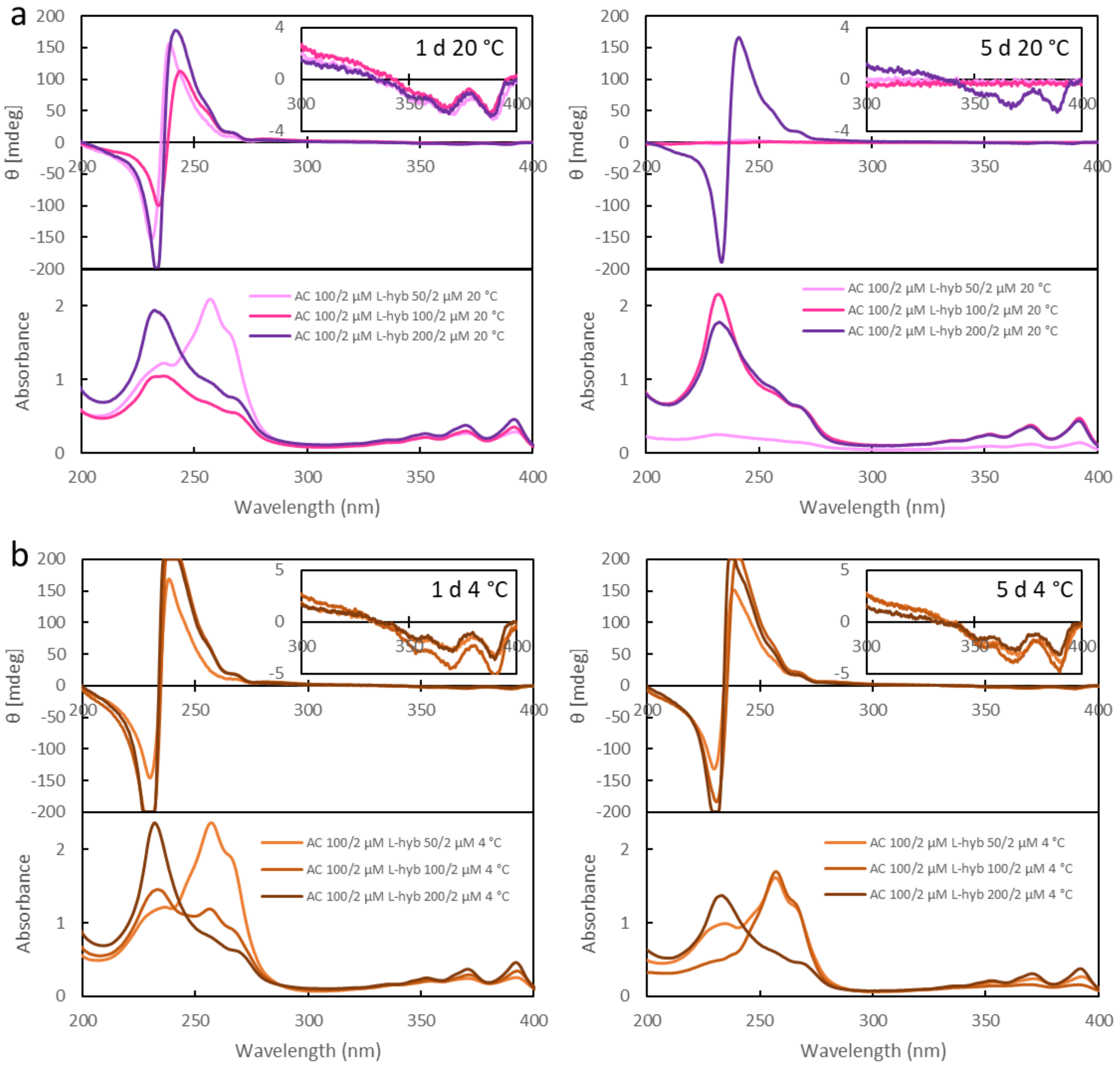

Figure 2-10. CD and UV-Vis absorption spectra of AC-exchanged L-hybrid nanoribbons ([AC] = 100 µM, [hybrid nanoribbons] = 50, 100 and 200 µM, diluted by half prior to the measurement) after incubation for 1 d and 5 d at (a) 20 °C and (b) 4 °C.

To understand why the CD signal decreases over time, the temperature dependency was investigated. The AC 100 µM and L-hybrid nanoribbons 50, 100 and 200 µM were mixed and incubated at 20 °C and 4 °C. The CD spectra were measured after 1 d and 5 d of incubation with half of the original concentration to reduce the saturation at the 220 - 280 nm range. As a result, the CD spectra of the samples incubated at 4 °C were more stable and have higher intensities than at 20 °C. (Figure 2-10)

The drawback of this measurement is the changes of absorption. Mixing the solution on a roller mixer for 5 d could cause a significant aggregation, resulting in reducing the absorption and increasing the scattering. Thus, the time-dependent CD measurements, shorter time of measurement and incubation, were performed.

The time-dependent CD measurements of AC-exchanged hybrid nanoribbons were performed to observe the time with maximum and stable CD intensity, which is necessary for reproducibility and consistency among each experiment. The parameters were the same as the other CD measurements except the accumulation is 1 instead of 4. The AC and hybrid nanoribbons were mixed (in the ice bath for 4 °C and at room temperature for 20 °C) in the quartz cell and immediately placed in the CD spectrometer. The temperature of the holder was preset at 4 and 20 °C. The solution was constantly stirred throughout the measurement.

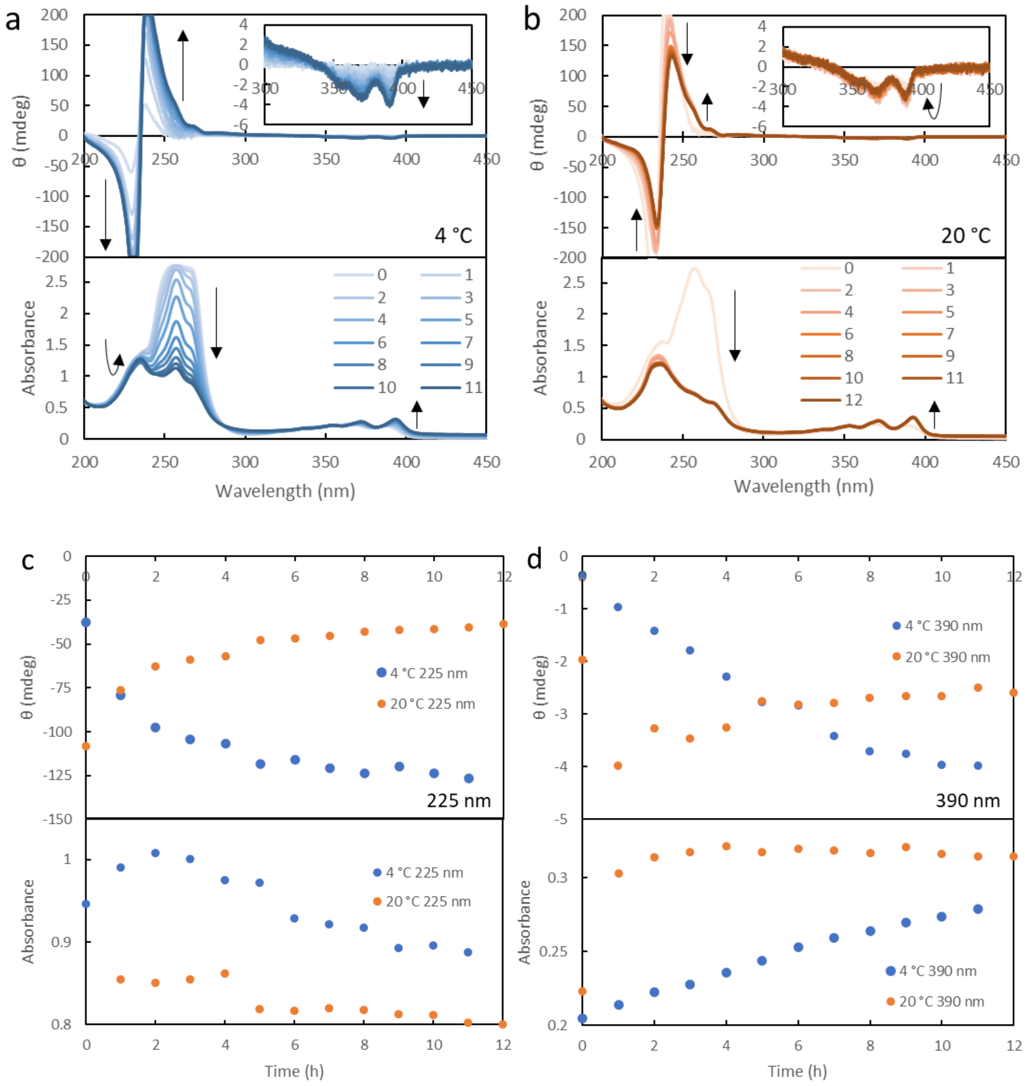

Figure 2-11. Time-dependent CD and UV-Vis absorption spectra of AC 50 µM and L-hybrid nanoribbons 50 µM mixture at (a) 4 °C and (b) 20 °C and the plots of CD intensity and UV absorption at (c) 225 nm and (d) 390 nm comparing 4 °C (blue) and 20 °C (orange).

The results of time-dependent CD measurements showed totally different CD evolution between 4 °C and 20 °C. (Figure 2-11 a and b) At 4 °C, the CD slowly increased over time with the similar shape of the overall spectra. The absorption peak at 257 nm, the original peak of AC in solution, also gradually decreased, coinciding with the decrease of free AC in the solution. The absorption at 234 nm decreased and then increased. This absorption peak corresponds to the AC bound to gemini. However, the free AC also has a high absorption here, causing the absorption to decrease at the beginning but then increase after the bound AC concentration overcome the free AC. On the other hand, 20 °C incubated sample showed more complicated results. The CD intensity reached the maximum immediate after mixing and decreased over time, suggesting the spontaneous exchange between AC and tartrate but with non-stable initial organization. In addition, the initial CD does not have a shoulder at 260 nm, and the initial absorption is too high considering high CD intensity, implying that there are different mechanisms of CD induction, so the induced CD spectra can be different. Even though the exchange mechanisms are still ambiguous, it is clear that more than one exchange mechanism are involved, and they are dependent to the temperature.

The plots at 225 nm (Figure 2-11 c) and 390 nm (Figure 2-11 d) showed that the CD signals of the AC-exchanged L-hybrid nanoribbons at 4 °C slowly increased to the constant with maximum CD intensity after 8 h. Contrarily, the AC-exchanged L-hybrid nanoribbons at 20 °C slowly decreased to the constant reached at around 8 h. Furthermore, both 4 °C and 20 °C have bathochromic shift at low energy transition (350 - 400 nm), a unique property of J-aggregation.[280,281]

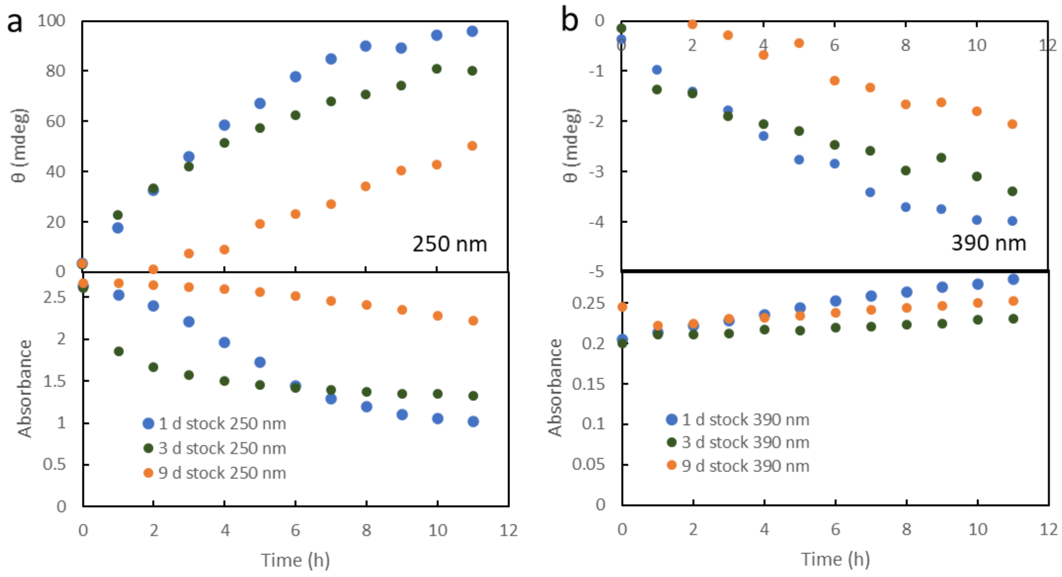

Figure 2-12. Plots of time-dependent CD and UV-Vis absorption of AC 50 µM and L-hybrid nanoribbons 50 µM mixture at (a) 250 nm and (b) 390 nm at 4 °C with 1-day-old (blue), 3-day-old (green) and 9-day-old (orange) L-hybrid nanoribbons.

Another important factor is the hybrid nanoribbons stock. Even though the hybrid nanostructures stocks kept at 4 °C showed the stable CD at least after a week, the AC-to-tartrate exchange decreased in the older stocks. Figure 2-12 shows the time-dependent CD measurements of the same L-hybrid nanoribbons stock at 4 °C. The time-dependent CD using 1-day-old L-hybrid nanoribbons had the highest CD intensity, the 3-day-old L-hybrid nanoribbons had slightly lower intensity, and 9-day-old L-hybrid nanoribbons had the lowest intensity less than half of 1-day-old one.

This is probably due to the structure of the silica walls. After the transcription, the silica walls were still porous due to incomplete dehydration, allowing molecules to pass through them easily. However, the dehydration continued over time, and the silica became less porous, so the exchange efficiency decreased. Nevertheless, the CD of the hybrid nanoribbons did not change because the gemini tartrate organizations were preserved, impossible to be detected. Therefore, the experiment in this research used hybrid nanoribbons within 3 days after preparation.

2.4.3 CD titration experiment between AC and hybrid nanoribbons

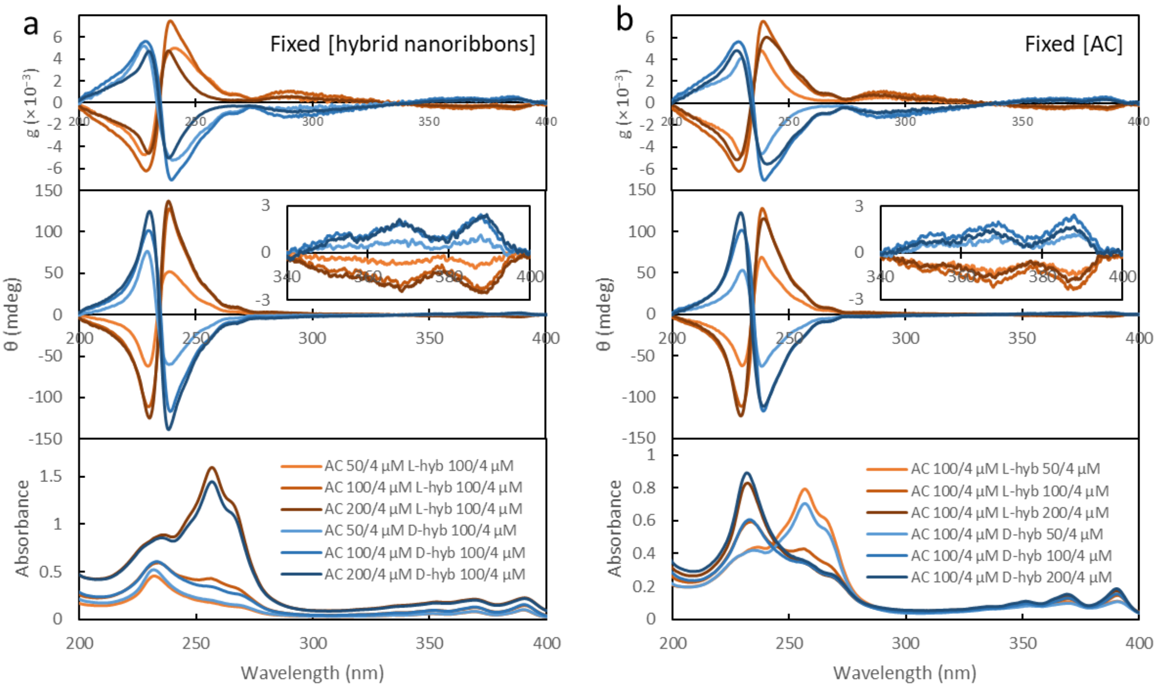

Figure 2-13. CD and UV-Vis absorption spectra of AC-exchanged L-hybrid ribbons in different ratios and the g-factors calculated from them. (a) AC (50, 100 and 200 µM) was varied with fixed L-hybrid nanoribbons (100 µM), and (b) vice versa. All suspensions were incubated at 4 °C for 16 h on a roller mixer and diluted to 25 % of the original concentration before the measurement.

The CD titration between AC and hybrid nanoribbons were conducted by fixing the concentration of either AC or hybrid nanoribbons. The titration with fixed AC concentration (Figure 2-13 a) shows the increase of CD intensity from the [AC] : [hybrid nanoribbons] 50 µM : 100 µM to 100 µM : 100 µM by twice. However, the intensities of 200 µM : 100 µM and 100 µM : 100 µM are almost no change. The UV-Vis absorption spectra shows that beyond [AC] : [hybrid nanoribbons] 1:1, the spectra mostly correspond to the free AC, indicating the saturation of AC exchange at this ratio despite the fact that the stoichiometry of the exchange is [AC] : [hybrid nanoribbons] 2 : 1. (Figure 2-8 c)

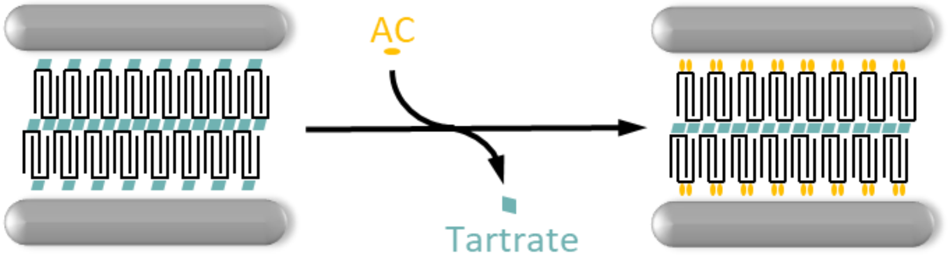

Figure 2-14. Schematic representation of AC exchange for hybrid nanostructures with gemini tartrate double-bilyer assemblies.

At the ratio 1 : 1, the CD of AC, induced by hybrid nanoribbons, shows the highest g-factor, particularly strong exciton-coupling CD signal (maximum g-factor of 7×10^{-3} at 240 nm and -6×10^{-3}

at 230 nm for L-hybrid nanoribbons and vice versa for D-hybrid nanoribbons). This exciton-coupling CD signal can be observed only when the AC molecules are located close to each other. Therefore, the organization of AC molecules are expected to be tightly packed inside the hybrid nanostructures.

The quantitative NMR of organic surfactant inside hybrid nanoribbons of 1 : 1 shows that the ratio of AC : tartrate : gemini was 1.2 : 0.45 : 1.0 (Appendix), meaning that all AC molecules can exchange with tartrate and incorporated inside hybrid nanoribbons at this ratio. The possible cause of half exchange of AC is the double-bilayer assemblies of gemini tartrate which separates tartrate to 2 types: outer-layer tartrate with more exchange efficiency and inner-layer with less exchange efficiency.

It is possible to exchange the inner-layer tartrate by other anions such as halides or methyl orange.[196,197] However, as the molecular size becomes larger, it becomes more difficult to reach the stoichiometric ratio. For example, the maximum exchange for methyl orange is 8 : 5, not 2 : 1. In addition, AC molecule is larger and has strong aromatic interactions with the other AC molecules,[281] making it more difficult to penetrate through gemini assemblies and can cause significant perturbation to the gemini organization. The perturbation was investigated with IR spectroscopy below.

The titration with fixed hybrid nanoribbons concentration shows consistent results. The CD intensity of [AC] : [hybrid nanoribbons] 100 µM : 50 µM is significantly lower than 100 uM : 100 uM, and the free AC absorption spectra are found at 100 µM : 5 µM ratio, revealing that there were not enough hybrid nanoribbons to induce chirality of AC at this ratio. In contrast, the 100 µM : 100 µM and 100 µM : 200 µM have similar CD intensities, meaning the excess gemini tartrate in the hybrid ribbons did not have any effect on chirality induction. The UV-Vis absorption spectra, however, are different possibly because the certain organization of AC inside the hybrid nanoribbons that did not affect chirality induction were different.

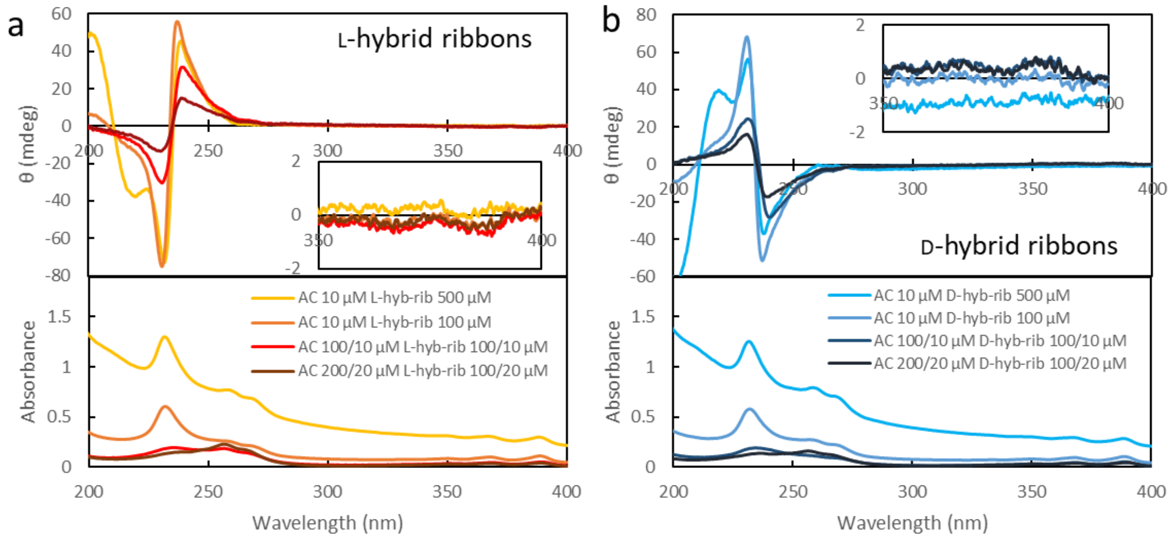

Figure 2-15. CD and UV-Vis absorption spectra of AC 10 µM with (a) L- and (b) D-hybrid nanoribbons in different concentrations after incubation for 19 h. To avoid using low concentration of hybrid nanoribbons, [AC] : [hybrid-nanoribbons] 1 : 1 and 2 : 1 were prepared using higher concentration and diluted prior the measurements.

Although the difference between [AC] : [hybrid nanoribbons] 1 : 1 and 1 : 2 was negligible, the 1 : 10, 5 times higher hybrid nanoribbons concentration than previous titration, showed an obvious increase in CD intensity. (Figure 2-15) Meaning, AC already perturbed the organization of the gemini even at the ratio 1 : 1. On the other hand, [AC] : [hybrid nanoribbons] 1 : 50, too high hybrid nanoribbons content, shows lower CD intensity because the chirality of AC was induced from only the organized gemini structure, but the AC molecules do not aggregate much to have high induced CD from their own organization. The scattering can also affect the CD measurement, but it was not a problem here because the HT was less than 450 V, which is in the normal range for CD measurement. Unfortunately, the concentration of AC (10 μM) was too low to discuss the low-energy band.

The different shapes at the wavelength lower than 220 nm of the CD at [AC] : [hybrid nanoribbons] 1 : 50 came from the CD and UV absorption of tartrate, which is up to 240 nm. The effect is estimated to be insignificant in the other ratios, but the titration of AC with chloride-exchanged hybrid nanoribbons, having no absorption peak longer than 200 nm, was performed.

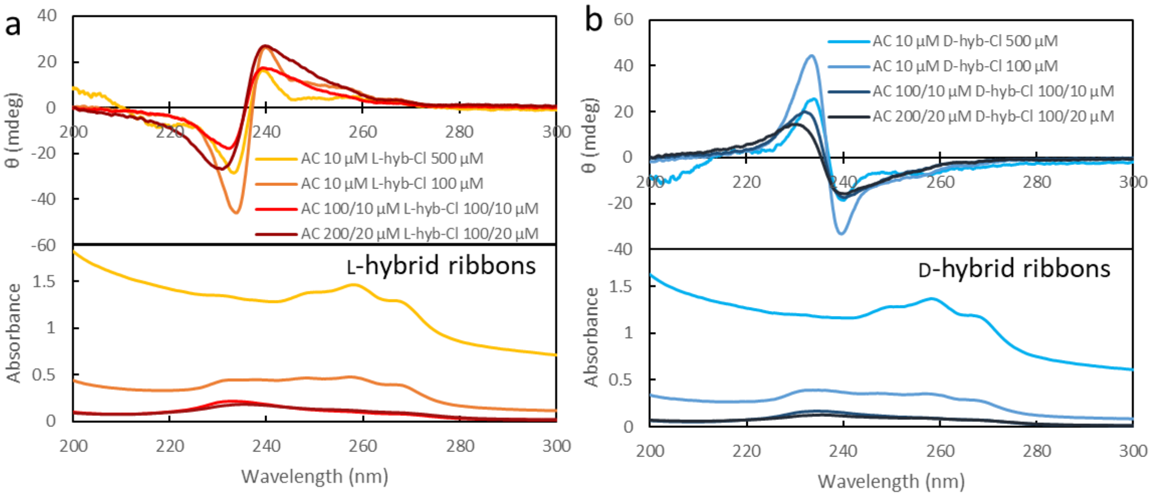

Figure 2-16. CD and UV-Vis absorption spectra of AC 10 μM with chloride-exchanged (a) L- and (b) D-hybrid nanoribbons in different concentrations after incubation for 22 h. To avoid using too low concentration of chloride-exchanged hybrid nanoribbons, 1 : 1 and 2 : 1 ratio were prepared using higher concentration and diluted prior the measurements.

The result of AC and chloride-exchanged hybrid nanoribbons titration shows induced CD with similar spectral shapes at all ratios. (Figure 2-16) The [AC] : [hybrid nanoribbons] 1 : 10 ratio gave the highest CD intensity, same as the previous hybrid nanoribbons titration. In this case, the increase of absorption came from the scattering of chloride-exchanged hybrid nanoribbons, not the absorption of AC. Also, AC could exchange with chloride faster than tartrate, causing the abrupt change of overall assemblies similar to the exchange at 20 °C.

2.4.4 **Fluorescence Spectra of AC-exchanged hybrid nanoribbons**

The AC-exchanged hybrid nanoribbons were expected to have high CPL because the exceptionally high CD intensities. Unfortunately, CPL could not be observed. Nevertheless, the changes of fluorescence spectra comparing to free AC in solution will be discussed.

Despite the fact that the AC concentration is the same (10 µM) for every samples, the fluorescence emission spectra showed different intensities and shapes for the different AC to hybrid nanoribbons ratios. Usually, the fluorescence intensity, even with the same excitation and emission wavelengths and bandwidths, cannot be compared because it depends on the detector, light source and factory setting of each fluorometer. Even the same fluorometer can show different intensities if the flux of the light source decreases, or the resistance of the detector increases due to the long-time usage. However, every measurement was conducted using the same CPL spectrometer with the same parameters within the same day (except the free AC 10 µM that was measured 1 day earlier), so the spectra can be compared with high reliability.

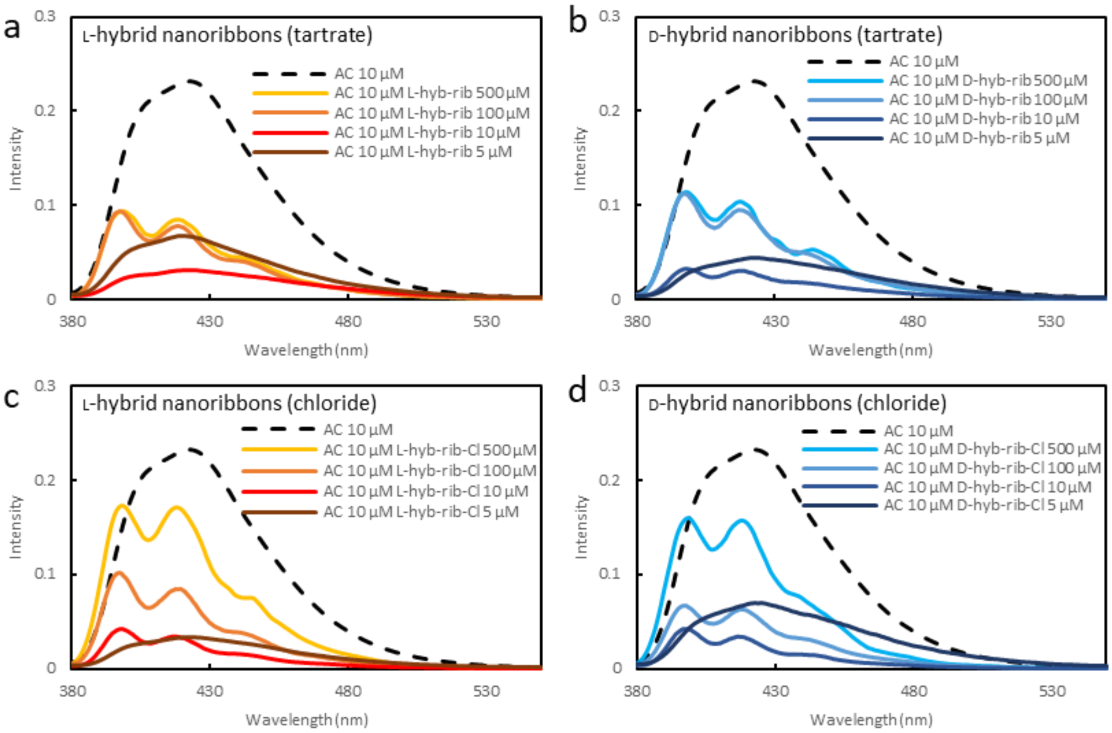

Figure 2-17. Fluorescence emission spectra of AC 10 µM in the presence of (a) L-hybrid nanoribbons, (b) D-hybrid nanoribbons, (c) chloride-exchanged L-hybrid nanoribbons and (d) chloride-exchanged D-hybrid nanoribbons with fixed AC and different hybird nanoribbons concentrations after overnight incubation at 4 °C on a roller mixer. The samples of hybrid nanoribbons 5 and 10 µM were prepared with 100 µM and then diluted prior the measurements. The spectra were measured with CPL-300 spectrometer. The excitation was 350 nm. Both excitation and emission bandwidths are 10 nm, and HT was 800 V.

From Figure 2-17, the [AC] : [hybrid ribbons] 1 : 50 to and 1 : 10 showed distinct vibrational states. It has been reported that the vibrational states of anthracenecarboxylic acid derivatives broaden because of the hydrogen bonding of carboxylic acid groups to the solution and/or other anthracenecarboxylic acid molecules.[282,283] Thus, the vibrational states are broader in protic solvent such as water and ethanol, but sharper and more distinct in non-protic solvent such as tetrahydrofuran. (Appendix). Therefore, the sharpening of vibronic bands in fluorescence spectra indicated the AC bound to gemini with electrostatic interactions, reducing the microenvironmental polarity of AC. (Figure 2-8 c) The spectra of 2 : 1 ratio are broad, similar to free AC, supporting this hypothesis.

Considering the fact that the absorption at 350 nm is the same for free AC and AC bound to hybrid nanoribbons (Figure 2-11 a), the fluorescence quantum yield of AC obviously decreases in the existence of hybrid nanoribbons. Because AC molecules are expected to tightly packed on the outer layer of double-bilayer assemblies, it is logical that the quenching was promoted by adjacent AC molecules (photocyclodimerization, re-absorption, excimer formation, energy transfer, etc.) or gemini and silica walls (non-radiative energy transfers). (Figure 2-17) The kinetics of photocyclodimerization will be discussed later in this chapter to support this assumption.

The difference between AC with gemini-tartrate hybrid nanoribbons and AC with chloride-exchanged hybrid nanoribbons is the fluorescence intensity of [AC] : [hybrid nanoribbons] 1 : 50 and 1 : 10. Chloride-to-AC exchange (Figure 2-17 c and d) showed stepwise decrease of fluorescence from 1 : 50 to 1 : 1, which correlates to the higher AC density on double-bilayer causing more efficient quenching. Instead, tartrate-to-AC exchange (Figure 2-17 a and b) showed the same fluorescence for 1 : 50 and 1 : 10, which is similar to chloride-to-AC exchange 1 : 10.

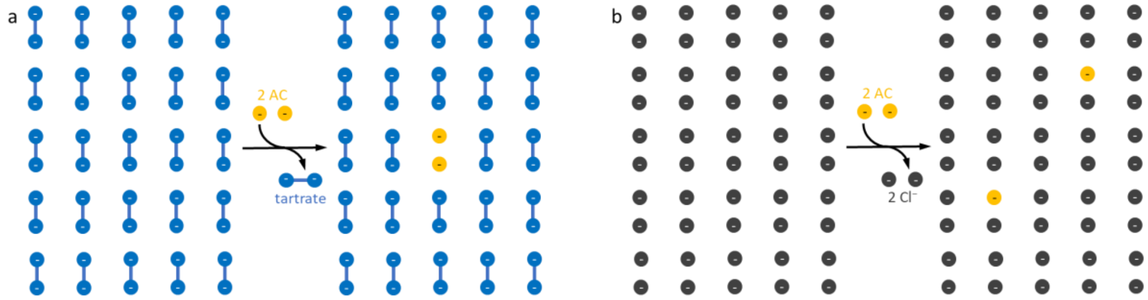

Figure 2-18. Schematic representation of the AC exchange at [AC] : [hybrid nanoribbons] 1 : 50. The position of tartrate (blue dumbbell) and chloride (grey circle) represent the top view of counteranions organized on the outer layer of double-bilayer assemblies of (a) gemini tartrate and (b) gemini chloride. 2 AC molecules (yellow circle) were exchanged with existed counteranions. Considering the fact that only the outer layer can be exchanged, 2 AC can be exchanged with 1 in 25 tartrate molecules and 2 in 50 chloride atoms.

The only difference is the starting anions. It is possible that a pair AC spontaneously exchanged with a single tartrate, while 2 AC exchanged with chloride randomly. (Figure 2-18) Therefore, the counterions-to-AC exchange occurred by mono-anions for chloride-to-AC exchange whereas it formed di-anions for tartrate-to-AC exchange; thus, the local density of AC on the double-bilayer of tartrate-to-AC exchange is higher than chloride-to-AC exchange at 1 : 50, causing the fluorescence quenching to be more efficient. The explanation of the same fluorescence of tartrate-to-AC exchange at 1 : 50 and 1 : 10 is too low AC density, so the quenching of the spontaneously exchanged pair is dominant.

2.4.5 **IR and VCD spectra of AC and hybrid nanoribbons**

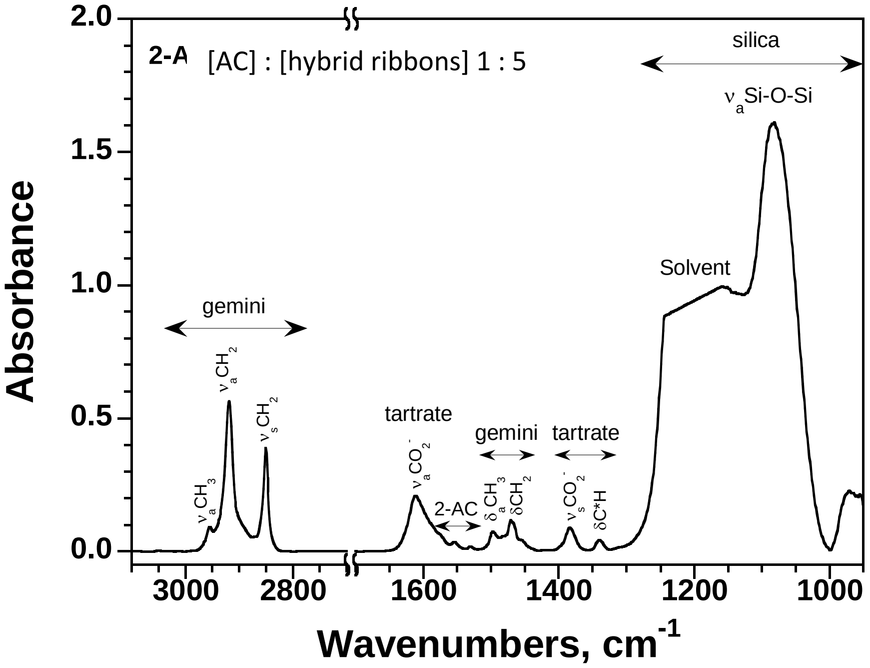

Figure 2-19. IR spectrum of hybrid nanoribbons of AC-exchanged gemini L-tartrate (1 : 5) in D_2O solution.

The IR spectrum of hybrid nanoribbons of AC-exchanged gemini L-tartrate (1 : 5) in D_2O is shown as a typical example (Figure 2-19) in the 3100-950 cm^{-1} spectral range. This IR spectrum exhibits bands related to the different constituents of the hybrid nanoribbons, which are gemini, L-tartrate, AC and silica. The gemini is characterized by the antisymmetric (ν_aCH_2) and symmetric (ν_sCH_2) stretching modes of the methylene groups at 2919 and 2850 cm^{-1}, respectively, by the antisymmetric (ν_aCH_3) stretching modes of the methyl groups at 2955 cm^{-1}, and by the bending modes of methyl (δ_aCH_3, $\delta_{s'}CH_3$ and δ_sCH_3) and methylene (δCH_2) groups in the 1510-1420 cm^{-1} region.[182] The frequencies obtained for the ν_aCH_2 (ca 2919 cm^{-1}) and ν_sCH_2 (ca 2850 cm^{-1}) modes along with the δCH_2 mode which shows a splitting (around 1470 and 1466 cm^{-1}) indicate that the alkyl chains are well organized in an orthogonal packing with mainly an all *trans* conformation. The L-tartrate is characterized by the antisymmetric ($\nu_aCO_2^-$) and symmetric ($\nu_sCO_2^-$) stretching modes of the carboxylate groups at 1611 and 1384 cm^{-1}, respectively, and by the bending mode of the C*H group at 1340 cm^{-1}.[182] The AC is characterized by several bands in the 1650-1510 cm^{-1} spectral range, related to carboxylate (1584 and 1414 cm^{-1}) and νC=C stretching modes of anthracene (1627, 1572, 1552, 1530 cm^{-1}).[284,285] Finally, the silica is characterized by the strong band at 1082 cm^{-1}, associated with the transverse optic (TO) mode of the asymmetric (ν_aSi-O-Si) stretching vibration of Si-O-Si groups.[187] The band at 970 cm^{-1} can be assigned to the Si-OH stretching vibration of free silanol groups.

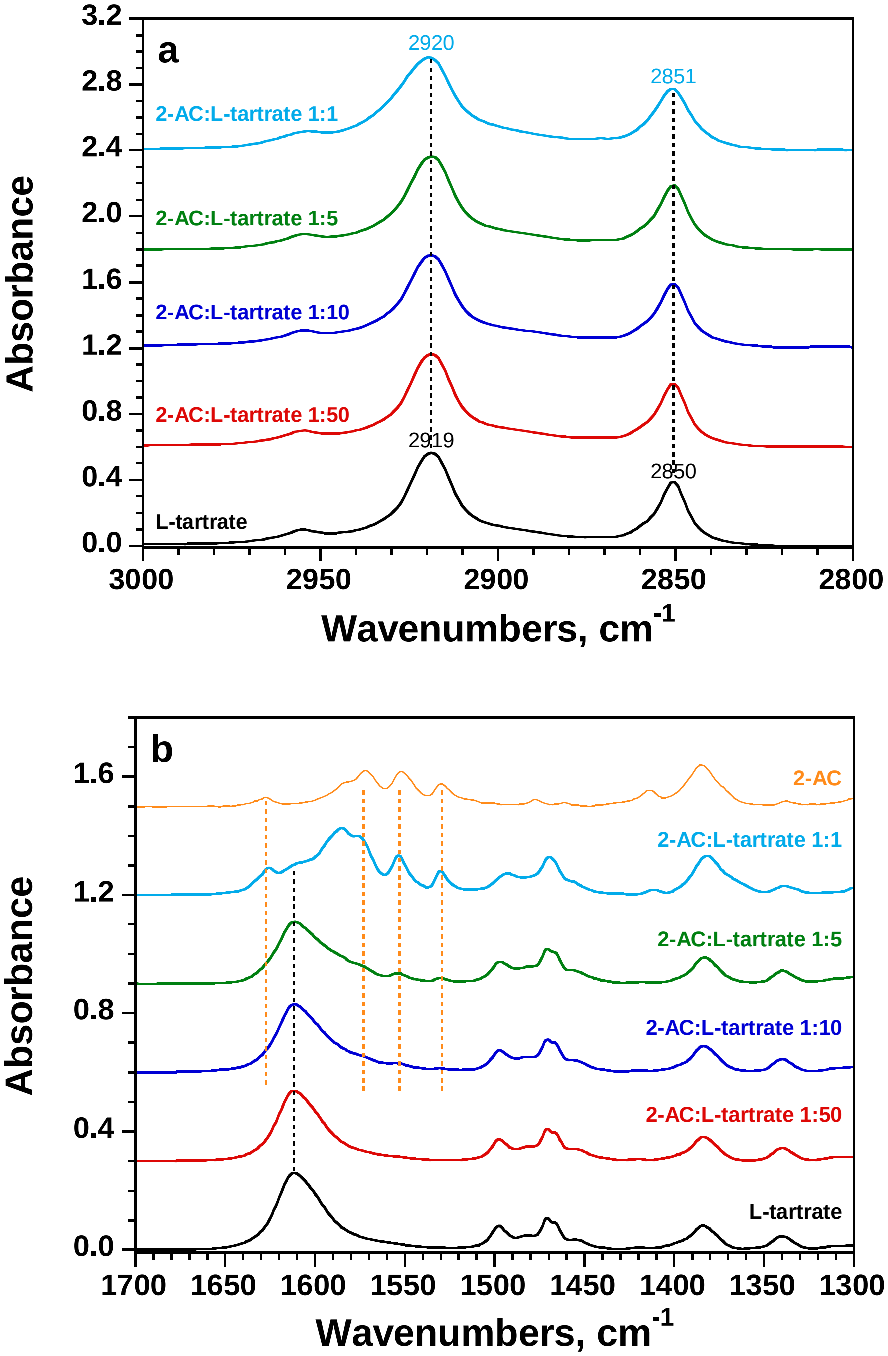

Figure 2-20. IR spectra of AC-exchanged L- hybrid nanoribbons in different ratios ([AC] : [hybrid nanoribbons] 1 : 1, 1 : 5, 1 : 10 and 1 : 50) in D_2O solution as well as IR spectra of L-hybrid nanoribbons and sodium salt of AC in (a) 3000-2800 cm^{-1} and (b) 1700-1300 cm^{-1} ranges.

The IR spectra of hybrid nanoribbons of AC-exchanged gemini L-tartrate in different ratios ([AC] : [hybrid] 1 : 1, 1 : 5, 1 : 10 and 1 : 50) in D_2O solution as well as IR spectra of L-hybrid nanoribbons and of sodium salt of AC were measured in the 3000-2800 cm^{-1} and 1700-1300 cm^{-1} ranges, respectively. (Figures 2-20) The spectra show that the organization of the alkyl chains of gemini, in an orthogonal packing with mainly an all *trans* conformation, is not modified by the exchange of tartrate with AC. Indeed, any modification of the frequencies for the ν_aCH_2 (ca 2919 cm^{-1}) and ν_sCH_2 (about 2850 cm^{-1}) modes is observed when the proportion of AC increases and the splitting of the δCH_2 mode is always present at 1470 and 1466 cm^{-1}. Only a very low broadening of the ν_aCH_2 and ν_sCH_2 bands associated with a shift by one wavenumber at higher frequencies are observed for the [AC] : [tartrate] = 1 : 1 sample.

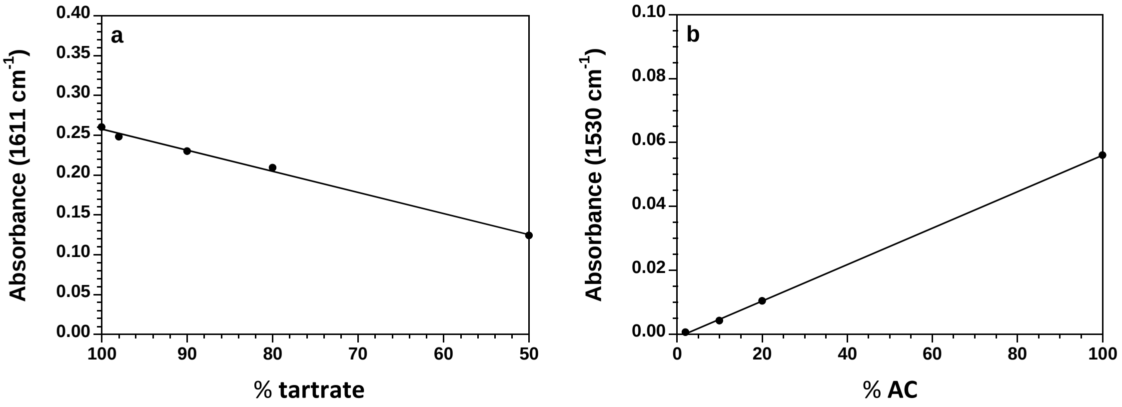

Figure 2-21. Variation of the intensities of (a) the 1611 cm^{-1} band with the % of tartrate (fitted line plot : $y = -0.0069 + 0.0026\,x$, r = 0.998) and (b) the 1530 cm^{-1} band with the % of AC (fitted line plot : $y = -0.001 + 0.00057\,x$, r = 0.9999).

Figure 2-20 b reveals the decrease of the antisymmetric ($\nu_aCO_2^-$) stretching modes of the carboxylate groups of L-tartrate at 1611 cm^{-1} (black dotted line) and the increase of the bands related to AC (orange dotted line) when the proportion of AC increases. This indicates that the exchange of tartrate with AC occurred, independent to the chiral induction property. The variation of the intensities of the 1611 and 1530 cm^{-1} bands with the % of tartrate and AC, respectively, are reported. (Figures 2-21 a and 2-21 b) These relations follow linear functions with y-intercepts close to zero, as expected for a perfect exchange, which agrees to the CD titration experiments.

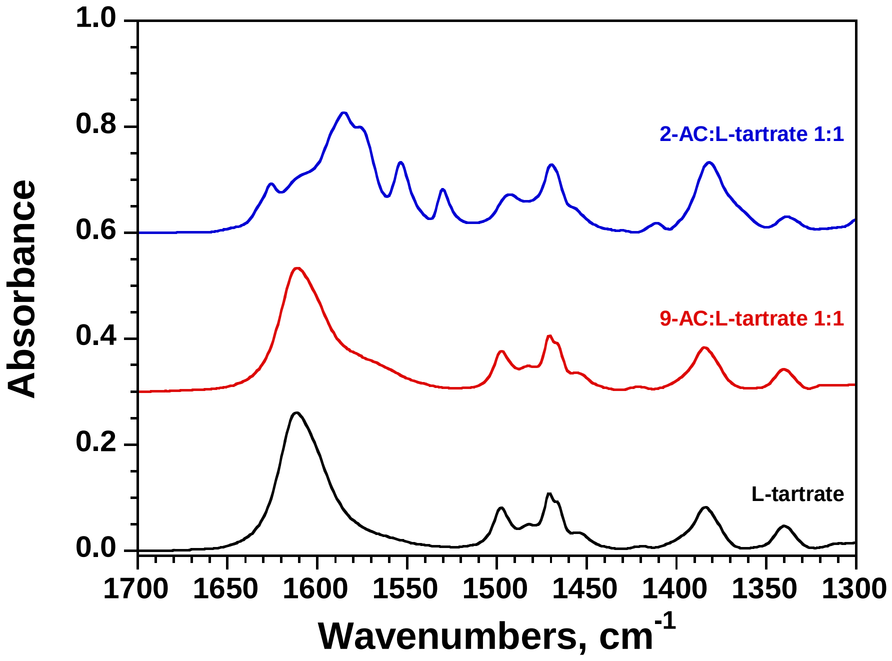

Figure 2-22. IR spectra of L-hybrid nanoribbons (black), 9-AC-exchanged L-hybrid nanoribbons (1 : 1) (red) and AC-exchanged L-hybrid nanoribbons (1 : 1) (blue) in D_2O in the 1700-1300 cm^{-1} range.

The comparison between the exchangeability of AC and 9-anthracenecarboxylate (9-AC) was studied. The IR spectra of L-hybrid nanoribbons, 9-AC-exchanged L-hybrid nanoribbons and AC-exchanged L-hybrid nanoribbons in D_2O in the 1700-1300 cm^{-1} range were recorded. (Figure 2-22) The black and red spectra are very similar, revealing that the exchange of tartrate with 9-AC did not occur, or occurred in relatively much low efficiency. The carboxylate group must be at one end of the anthracene to promote the efficient exchange with tartrate.

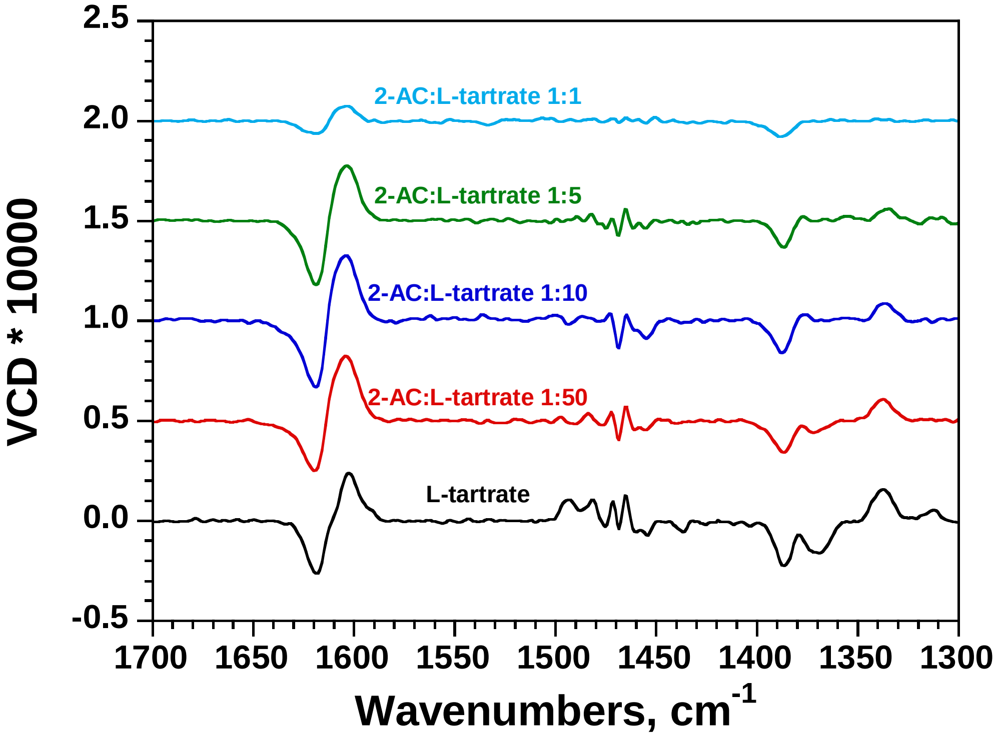

Figure 2-23. VCD spectra of AC-exchanged L- hybrid nanoribbons in different ratios ([AC] : [hybrid nanoribbons] 1 : 1, 1 : 5, 1 : 10 and 1 : 50) in D_2O as well as of L-hybrid nanoribbons in the 1700-1300 cm^{-1} spectral range.

The VCD spectra of AC-exchanged L-hybrid nanoribbons in different ratios in D_2O were measured in the 1700-1300 cm^{-1} range. (Figure 2-23) The VCD spectrum of organic gemini L-tartrate has already been reported.[182] This spectrum exhibits a bisignate band for the $\nu_a CO_2^-$ mode (positive couplet for gemini L-tartrate) and a negative band for the $\nu_s CO_2^-$ mode. The VCD spectrum reveals also the chirality induction from chiral tartrate to non-chiral gemini. Indeed, a (+, −, +) pattern is observed for the two split components of the bending (δCH_2) mode of methylene groups located at 1470 and 1466 cm^{-1}. The VCD spectrum of L-hybrid nanoribbons is similar to the one of gemini L-tartrate in the 1700-1300 cm^{-1} range. Moreover, this spectrum is slightly modified by the exchange of L-tartrate with AC, except of the 1 : 1 composition. Indeed, a marked diminution of the VCD intensities is observed for this composition, revealing a certain modification in the chiral structure of the supramolecular assemblies. In contrast, the AC at certain lower ratios enlarged the VCD intensities of tartrate, which might indicate more rigid chiral assemblies.

2.5 Supramolecular Regioselective [4+4] Photocyclodimerization of 2-Anthracenecarboxylate Using Chiral Silica-Organic Hybrid Nanoribbons

The AC-exchanged hybrid nanostructures were irradiated by UV light (352 nm), so that the AC aggregated inside the hybrid nanostructure underwent [4+4] photocyclodimerization. The effects of temperature, incubation time, concentration and ratios were studied.

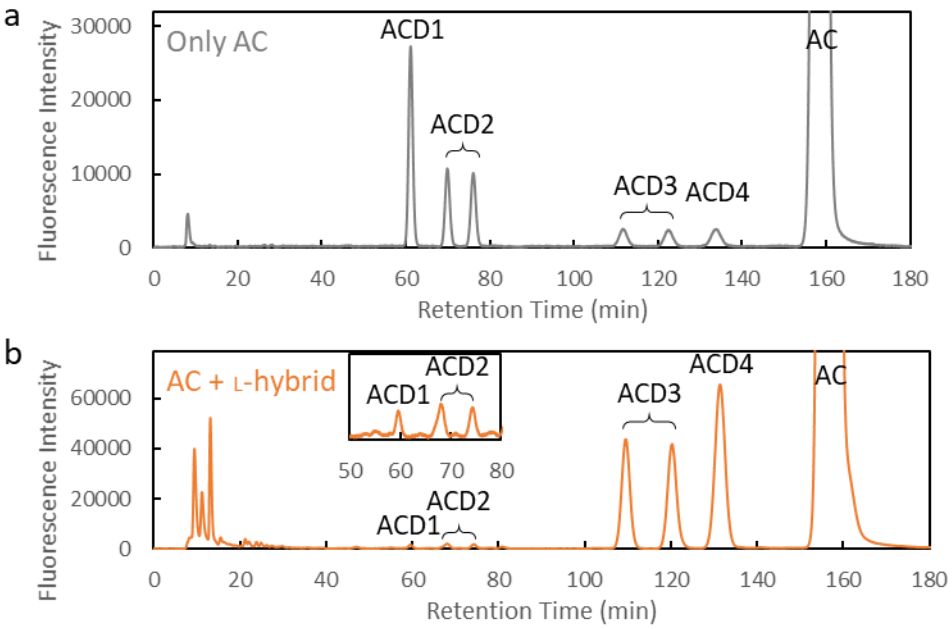

Figure 2-24. HPLC chromatograms of the products from (a) [4+4] photocyclodimerization of AC in alkaline solution and (b) supramolecular regioselective [4+4] photocyclodimerization of AC with L-hybrid nanoribbons.

The solvent in the suspension was removed and the nanostructures were dried by lyophilization. It is not only to remove the water but also to remove any dimerization products from free AC outside of hybrid nanostructures. The product of photocyclodimerization inside hybrid nanostructures was extracted from the lyophilized solid by hot methanol, and the methanol was dried to afford the solid organic components of hybrid nanostructures. Finally, the dried product was re-dissolved in acetonitrile and sodium hydroxide mixture, filtered, and injected to HPLC equipped with chiral column and fluorescence detector (excitation 254 nm, emission 420 nm). (Figure 2-24) The identity of each peak was reported[286] and the product distribution was calculated from integrating each peak area.

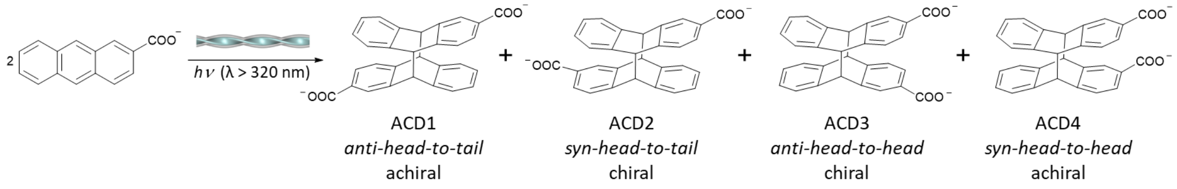

Figure 2-25 Supramoleculae regioselective [4+4] photocyclodimerization of AC using hybrid nanoribbons.

Table 2-1. Photoirradiation products of AC-exchanged hybrid nanoribbons at room temperature.

AC (µM)	Hybrid Nanoribbons		Volume	Product Distribution[a] (%)				% *head-to-head*
	Concentration (µM)	Isomer		ACD1	ACD2	ACD3	ACD4	
10	10	L	5 × 50 mL	n.d.	n.d.	64.3 ± 1.5	35.7 ± 1.5	-
10	10	D	5 × 50 mL	1.7 ± 1.0	1.8 ± 0.5	54.5 ± 0.5	42.0 ± 1.0	96.5 ± 0.5
100	100	L	2 × 25 mL	1.4 ± 0.4	1.8 ± 0.1	54.5 ± 0.2	42.4 ± 0.6	96.8 ± 0.5
100	100	D	2 × 25 mL	1.0 ± 0.3	1.6 ± 0.2	56.8 ± 0.3	40.7 ± 0.7	97.4 ± 0.5
10[b]	-	-	-	41	34	15	10	25

Photoreaction conditions: incubation 3 h at 20 °C on roller mixer, irradiation 3 h at rt, lamp F8T5BLB 8 W 352 nm. [a] Ratio of each dimer respect to all dimers, not absolute yield, ± s.d. [b] Reaction in buffer pH 7.5.

Starting from incubating [AC] : [hybrid nanoribbons] 1 : 1 at 20 °C for 3 h, the AC-exchanged hybrid nanoribbons were irradiated by 352 nm lamp at room temperature. (Figure 2-25) After 1 h, the fluorescence of the suspension disappeared, meaning that AC was significantly consumed. The products inside the hybrid nanoribbons were analyzed by HPLC. (Table 2-1) The average and s.d. showed in the table were calculated from 3 HPLC analyses of the same samples to show the error of the analysis.

Even though it was the first trial, the preference of the photocyclodimerization product is orthogonally *head-to-head*. As shown in Table 1, the product distribution of *head-to-head* dimers of ACDs are 97 %, which is the only system that can produce more than 95 % *head-to-head* in water at room temperature. Unfortunately, the ee of ACD3 (*anti* dimer) was too low and not consistent. Therefore, the ee will not be discussed further.

The ratio between ACD3 and ACD4 (*syn* dimer) are within 5 % difference. Still, AC-exchanged L-hybrid nanoribbons 10 µM yielded ACD3 slightly more than the other samples, which implies the stability problem. To improve this drawback, the other factors were studied.

2.5.1 Temperature, Time, Ratio Effects and Types of Hybrid Nanoribbons

To control the supramolecular regioselective [4+4] photocyclodimerization of AC, the different parameters that may affect the photochemical reactions were investigated. The effects of temperature, time, ratios and original hybrid nanoribbons are discussed.

Table 2-2. Photoirradiation of AC-exchanged hybrid nanoribbons at low temperature with different time.

AC (µM)	Hybrid Nanoribbons		Irradiation time (min)	Product Distribution[a] (%)				% *head-to-head*
	Concentration (µM)	Isomer		ACD1	ACD2	ACD3	ACD4	
100	100	L	30	10.3	15.3	37.8	36.6	74.4
100	100	L	60	4.8	10.2	46.0	39.0	85.0
100	100	L	180	4.3	11.5	49.8	34.5	84.3

Photoreaction conditions: no incubation, irradiation at 4 °C, volume 10 mL, lamp F8T5BL 8 W 352 nm. [a] Ratio of each dimer respect to all dimers, not absolute yield

From the results of time-dependent induced CD, the AC-exchanged hybrid nanoribbons are more stable at low temperature, so the temperature could be a potential factor to control the photocyclodimerization. The samples were prepared by mixing L-hybrid nanoribbons and AC stocks, and immediately irradiated by UV lamp without incubation. The irradiations were stopped after different time. The sample irradiated for 30 min showed less *head-to-head* product distribution, but after 60 min, the results are similar. (Table 2-2)

There are two possible reasons. First, the *head-to-tail* dimers are produced inside hybrid nanoribbons. The low concentration in hybrid nanoribbons surface allow bound AC to react with unbound free AC, which is at high concentration at the beginning. Second, the *head-to-tail* dimers are produced outside the hybrid nanoribbons and later exchange with tartrate, becoming dimers inside the ribbons. In both scenarios, the *head-to-head* dimers will be observed even the AC and ACDs in free solution were removed by centrifugation. Here, the conversion of the reaction was not determined, so the product distributions represent the ratios within the same sample but not the absolute yield. The challenge is to determine the absolute yield of the samples, but it is still impossible due to the gemini and tartrate contamination, and anthraquinone-2-carboxylate as a by-product.

Table 2-3. Photoirradiation of AC-exchanged hybrid nanoribbons incubated at 20 °C.

AC (μM)	Hybrid Nanoribbons		Incubation time (h)	Product Distribution[a] (%)				% *heat-to-head*
	Concentration (μM)	Isomer		ACD1	ACD2	ACD3	ACD4	
100	100	L	1	1.9	2.2	52.8	43.3	96.1
100	100	D	1	1.6	2.2	55.8	40.4	96.2
100	100	L	2	2.2	3.9	63.1	30.8	93.9
100	100	D	2	2.8	3.8	61.4	32.1	93.5

Photoreaction conditions: Incubation 20 °C on roller mixer, irradiation at 1 h 4 °C on roller mixer, glass tube, volume 10 mL, lamp F8T5BL 8 W 352 nm. [a] Ratio of each dimer respect to all dimers, not absolute yield

Next, the incubation at 20 °C was attempted. In the time-dependent CD measurement, the exchange rate of AC to tartrate in hybrid nanoribbons at 20 °C was much faster than at 4 °C, so the samples were mixed at room temperature, incubated at 20 °C for 1 or 2 h, and then irradiated at 4 °C for 1 h. The product distribution of *head-to-head* dimers are slightly lower for 2 h incubation. Unusually, samples with 2 h incubation show higher product distribution of ACD3 and lower product distribution of ACD4, leading to [ACD3] : [ACD4] 2 : 1, which is a unique result. (Table 2-3)

Table 2-4. Photoirradiation of AC-exchanged hybrid nanoribbons at low temperature after overnight incubation.

AC (μM)	Hybrid Nanoribbons		Product Distribution[a] (%)				% *head-to-head*
	Concentration (μM)	Isomer	ACD1	ACD2	ACD3	ACD4	
100	100	L	1.1 ± 0.5	1.8 ± 0.3	53.1 ± 1.5	44.3 ± 2.3	97.4 ± 0.8
100	100	D	0.8 ± 0.3	2.1 ± 0.4	53.8 ± 1.7	43.2 ± 1.4	97.0 ± 0.8
10[b]	-	-	41	34	15	10	25

Photoreaction conditions: incubation overnight at 4 °C on roller mixer, irradiation 1.5 or 3 h at 4 °C on roller mixer, glass tube, volume 10 mL, lamp F8T5BL 8 W 352 nm. [a] Ratio of each dimer respect to all dimers, not absolute yield, ± s.d. [b] Reaction in buffer pH 7.5.

From the results up to now, the simplest way to control the photoirradiation is to do the experiment at 4 °C. Three repetitions of [AC] : [hybrid nanoribbons] 100 μM : 100 μM samples were conducted in the different day from different hybrid nanoribbons stocks with different incubation time (but at least 12 h) and different irradiation time (1.5 h for 1 repetition and 3 h for 2 repetitions). After

1.5 h, the fluorescence was quenched similar to the case at room temperature. As a result, the product distributions are precise for all 3 repetitions, resulting in relatively low s.d. values. (Table 2-4) The results between L- and D-hybrid nanoribbons are also the same. In summary, the product distribution of ACD3 and ACD4 are 53 % and 44 %, resulting in 97 % *head-to-head* dimers.

Table 2-5. Photoirradiation of AC-exchanged hybrid nanoribbons at −20 °C.

AC (μM)	Hybrid Nanoribbons		Product Distribution[a] (%)				% *head-to-head*
	Concentration (μM)	Isomer	ACD1	ACD2	ACD3	ACD4	
100	100	L	0.6	1.8	34.9	62.7	97.7
100	100	D	1.6	3.9	36.2	58.3	94.5

Photoreaction conditions: incubation overnight at 4 °C on roller mixer, volume 10 mL, acetone −20 °C 10 mL was added before irradiation 1.5 h at −20 °C on while stirring, beaker, lamp F8T5BL 8 W 352 nm. [a] Ratio of each dimer respect to all dimers, not absolute yield.

The attempt with the lowest temperature was at −20 °C. The samples were prepared and incubated same as previous 4 °C experiment, but the reaction cannot be conducted directly at −20 °C because the water will be frozen. Therefore, the same volume of cold acetone was added to each sample, and the sample was irradiated while vigorous stirring in beaker. Acetone cannot dissolve gemini tartrate, so the double-bilayer self-assemblies of gemini tartrate and gemini AC will not be destroyed. However, acetone also absorbed the light at 352 nm, so the suspension still had fluorescence after 1.5 h. The major products are *head-to-head*, but the product distribution was shifted to ACD4. (Table 2-5) As a result, ACD4 became a major product at −20 °C.

This mean that the temperature can switch the major product of photocyclodimerization of AC, and it is likely that the ACD3 favors higher temperature than ACD4. By reducing the temperature, the rotation of AC molecules is more limited. In static state, *syn-head-to-head* AC orientation might be more favorable to resemble carboxylate group positions of tartrate. However, the *anti-head-to-head* AC orientation becomes more favorable at higher temperature probably because the electrostatic repulsion between carboxylate groups. Anyway, the effects of acetone cannot be neglected, so the pure effect of the low temperature is not easy to discuss with this information. The effect of the temperature higher than 20 °C is also difficult to be experimented because increasing the temperature can disturb the organization of gemini tartrate self-assemblies.

Table 2-6. Photoirradiation of AC-exchanged hybrid nanoribbons at different AC to hybrid nanoribbons ratio.

AC (μM)	Hybrid Nanoribbons		Product Distribution[a] (%)				% *head-to-head*
	Concentration (μM)	Isomer	ACD1	ACD2	ACD3	ACD4	
100	100	L	1.1 ± 0.5	1.8 ± 0.3	53.1 ± 1.5	44.3 ± 2.3	97.4 ± 0.8
10	500	L	1.4	3.9	55.5	39.2	94.7

Photoreaction conditions: incubation overnight at 4 °C on roller mixer, irradiation 1.5 h at 4 °C on roller mixer, glass tube, volume 10 mL, lamp F8T5BL 8 W 352 nm. [a] Ratio of each dimer respect to all dimers, not absolute yield, ± s.d.

The ratio between AC and hybrid nanoribbons are discussed. The result of 1 : 50 is slightly different from 1 : 1. (Table 2-6) This probably because the organization of 1 : 50, even though filled with tartrate, is less dense than 1 : 1, so the more freedom of AC molecules reduced the regioselectivity. Still, the substitution of a single tartrate molecule by 2 AC molecules allow the photodimerization to be occurred.

Table 2-7. Photoirradiation of AC-exchanged hybrid nanoribbons prepared from chloride-exchange hybrid nanoribbons.

AC (µM)	Chloride-Exchanged Hybrid Nanoribbons		Product Distribution[a] (%)				*% head-to-head*
	Concentration (µM)	Isomer	ACD1	ACD2	ACD3	ACD4	
10	100	L	1.7	3.3	44.4	50.7	95.1
100	100	L	1.1	0.9	48.6	49.5	98.0
100	100	D	1.8	2.8	53.9	41.4	95.4

Photoreaction conditions: incubation overnight at 4 °C on roller mixer, irradiation 3 h at 4 °C on roller mixer, glass tube, volume 10 mL, lamp F8T5BL 8 W 352 nm. [a] Ratio of each dimer respect to all dimers, not absolute yield

The photocyclodimerization products of the samples prepared from AC and chloride-exchanged hybrid nanoribbons does not have much different in the total product distribution of *head-to-head* dimers. (Table 2-7) The modest difference of orientation (the slightly different induced CD spectra) is probably not the one that differentiate *head-to-head* and *head-to-tail*.

2.5.2 CD and Absorption After Irradiation

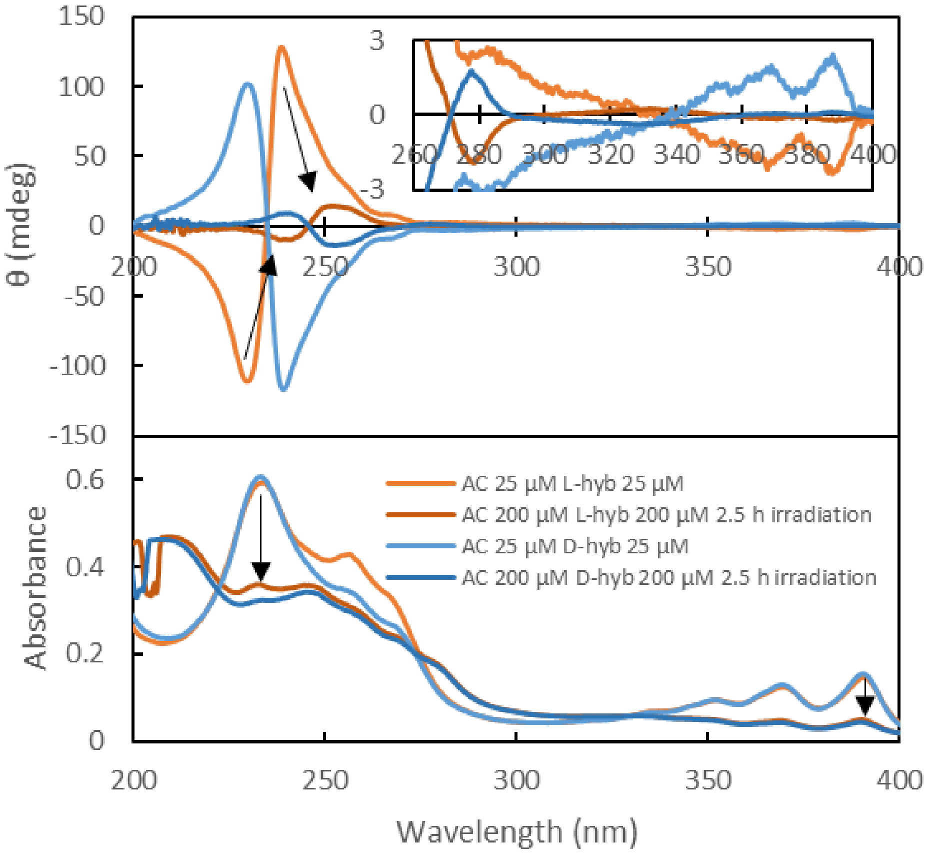

Figure 2-26. CD and UV-Vis absorption spectra of AC-exchanged hybrid nanoribbons before and after irradiation. Note that the spectra before and after the irradiation was from 25 µM and 200 µM, respectively.

After the irradiation, the intensity of absorption spectra decreased significantly, especially at 350 - 400 nm range, indicating the decrease of monomeric AC concentration. The shape of the spectrum also changed. The CD intensity immensely decreased throughout the spectrum. The shape of the CD also changed. The CD peaks have bathochromic shift, and instead of having 2 zero-crossing points (at 235 and 340 nm), there are 3 zero-crossing points (at 240, 270 and 290 nm) after irradiation. (Figure 2-26) This change clearly shows chemical reactions. The induced CD of ACD, which will be discussed in further session, is not the same as the CD after irradiation. Thus, it can be concluded that the ACDs produced from photocyclodimerized AC-exchanged hybrid nanoribbons are organized differently comparing to the ACDs that were mixed with hybrid nanoribbons.

2.5.3 Organization of AC in Hybrid Nanoribbons

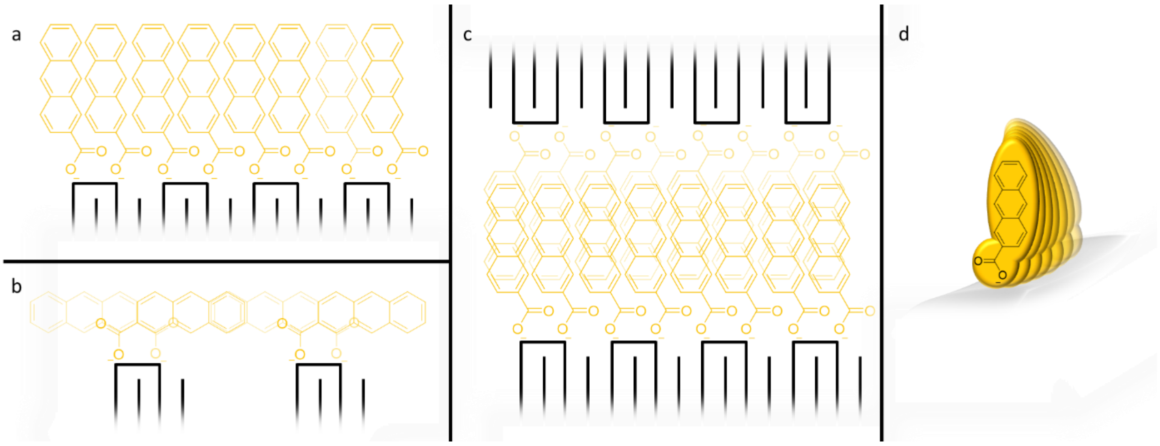

Figure 2-27. Orientation of AC in gemini double-bilayer self-assemblies. The orientation of AC molecules on the outer layer (a) pointing outward or (b) lie on the surface of double-bilayer, and (c) between double-bilyer (inner layer). Also, (d) the possible 3D orientation of AC on the twisted gemini double-bilayer self-assemblies.

The results of a strong preference on *head-to-head* dimers supports the earlier hypothesis that AC molecules organized closely to each other with the long side pointing outward the double-bilayer self-assemblies (Figure 2-27 a), not parallel to the bilayer surface. (Figure 2-27 b) That is the only case to obtain only *head-to-head* dimers. Also, AC does not exchange with the inner layer tartrate because there will not be any regioselectivity at the organization of inner layer. (Figure 2-27 c)

Nevertheless, this model representation is not complete. The AC molecules are not perfectly parallel to each other because they show strong exciton coupling on CD spectrum. Moreover, this exciton coupling is the highest CD signals over the spectrum, meaning the asymmetric orientation of AC, the origin of this exciton coupling, is uniformed throughout the structure. (Figure 2-27 d) The nonuniform orientation of AC will result in lower and non-reproducible exciton coupling. In addition, the surface of double-bilayer should be considered as 2-dimension, so that the orientation of AC should compose of 2 directions, both through aromatic stacking and side-to-side interactions. Therefore, the orientation of AC cannot be explained by simple helical organization as shown in Figure 2-27 d. The organization of exchanged counteranions in hybrid nanostructures is still a big mystery for the future of hybrid nanostructure research.

2.5.4 Kinetics of Photocyclodimerization of AC with or without Hybrid Nanoribbons

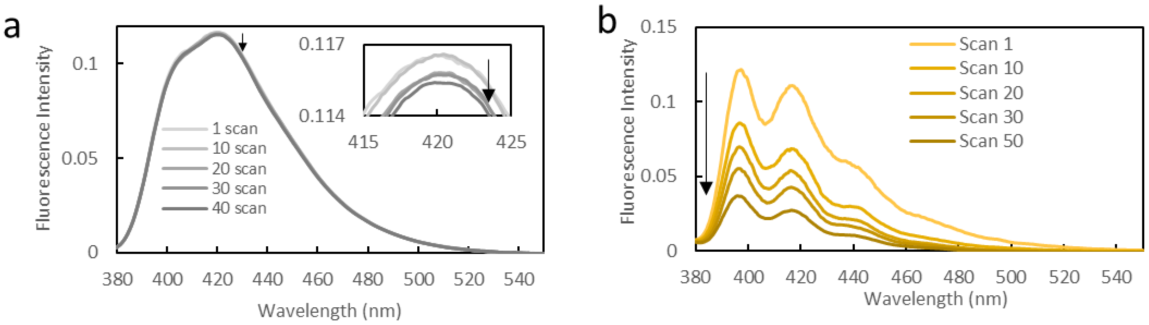

Figue 2-28. Fluorescence emission spectra of (a) AC 10 µM and (b) AC-exchanged L-hybrid nanoribbons ([AC] = [L-hybrid nanoribbons] = 10 µM, overnight incubation at 4 °C on roller mixer at 100 µM and diluted prior measurement) with repeated scans. The spectra were measured with CPL-300 spectrometer. The excitation was 350 nm, and excitation and emission bandwidths are 10 nm. The scan speed was 100 nm/min, and the detector HT was 700 and 850 V for AC and AC-exchanged L-hybrid nanoribbons, respectively.

As already mentioned, the AC-exchanged hybrid nanoribbons did not show clear CPL signals. However, the shape of fluorescence spectra changed drastically comparing to the free AC in solution, lower intensity and more distinct vibronic transitions. Moreover, the photostability also decreased rapidly. The fluorescence intensity of AC-exchanged hybrid nanoribbons 10 µM was reduced to half after 20 scans, while showing less than 2 % loss for AC 10 µM aqueous solution after 40 scans. (Figure 2-28) The main bleaching is considered to be [4+4] photocyclodimerization of AC because the AC molecules are aggregated on the surface of double-bilayer gemini assemblies in the hybrid nanohelices. The photooxidation of AC is considered to be the same with or without hybrid nanoribbons, so it is not considered as a major cause of bleaching.

Considering the photocyclodimerization of AC, it follows the second-order chemical reaction.

$$AC^* + AC \rightarrow ACD$$

Where AC* is electronically excited AC molecule, and ACD is a representative of AC dimers. Assuming reaction rate (*r*) and rate constant (*k*) are same for all dimers, the reaction rate can be expressed as:

$$r = k[AC^*][AC] = \frac{d[ACD]}{dt} \tag{2-1}$$

The formation of ACD is equal to the consumption of AC or AC*.

$$[ACD] = [AC^*]_0 - [AC^*] = [AC]_0 - [AC]$$

Hence, $$[AC^*] = [AC^*]_0 - [ACD] \text{ and } [AC] = [AC]_0 - [ACD] \tag{2-2}$$

By substituting equation (2-2) to equation (2-1) and solving the differential equation, the following equation can be derived.

$$\ln\left(\frac{[AC]}{[AC^*]} \cdot \frac{[AC^*]_0}{[AC]_0}\right) = ([AC]_0 - [AC^*]_0)kt \tag{2-3}$$

Normally, the [AC*] in the solution is approximated to be much lower than [AC] (Appendix), so the following assumption can be deduced.

$$[AC^*] \ll [AC]$$

Therefore,

$$\frac{[AC]}{[AC]_0} \approx 1 \text{ and } [AC]_0 - [AC^*]_0 \approx [AC]_0$$

The equation (2-3) can be approximated as:

$$\ln\left(\frac{[AC^*]_0}{[AC^*]}\right) = [AC]_0 kt$$

$$\ln[AC^*]_0 - \ln[AC^*] = [AC]_0 kt$$

$$\ln[AC^*] = -[AC]_0 kt + \ln[AC^*]_0 \tag{2-4}$$

This derivation is called pseudo first-order reaction, a useful approximation for the second-order reaction when one of the reactants has much higher concentration than the other.[287] Because the concentration of AC is low (10^{-5} M) and the fluorescence quantum yield is quenched by the reaction, the fluorescence emission intensity (I_{FL}) is approximately a direct variation of [AC*].

$$a \cdot I_{FL} = [AC^*]$$

when *a* is a constant. The equation (2-4) can be rewritten as:

$$\ln I_{FL} = -[AC]_0 kt + \ln\frac{[AC^*]_0}{a}$$

$$= -[AC]_0 kt + b \tag{2-5}$$

when *b* is a constant. As a result, by plotting ln I_{FL} versus time, *k* can be calculated from −slope/$[AC]_0$.

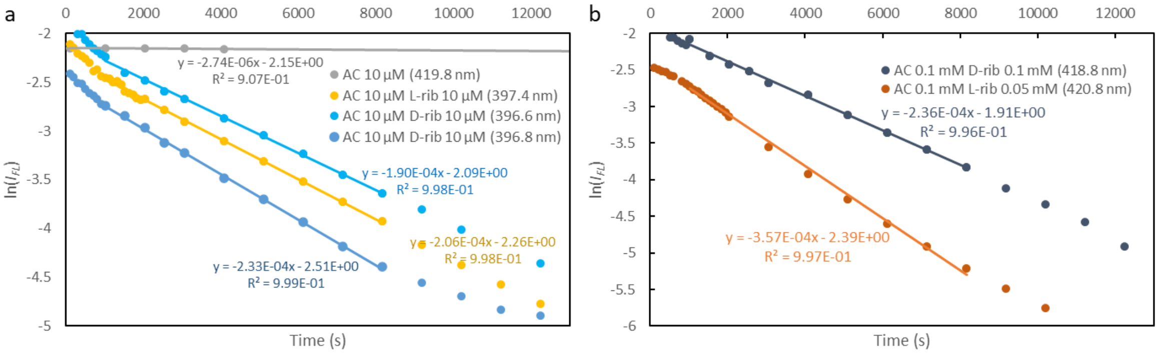

Figure 2-29 Plots of ln(I_{FL}) versus time of (a) AC 10 µM alone (grey) and with L- and D-hybrid nanoribbons 10 µM (yellow and blue, respectively), and (b) AC 100 µM and D-hybrid nanoribbons 100 µM (blue) and L-hybrid nanoribbons 50 µM (orange). The ln(I_{FL}) was calculated using the maximum I_{FL} of each sample.

The plot of natural logarithm of fluorescence emission intensity at 397 nm versus time (Figure 2-29 a) shows acceptable linear relationships over 2 h. Although the data taken from CPL is the intensity versus scanning rounds, the time of each scan (102 s) was calculated from the known scanning speed (100 nm/min) and scanning range (380 - 550 nm). For the AC solution, the linear regression functions were fitted to 1st, 10th, 20th, 30th and 40th scan. The obtained function is fitted with the R^2 of 0.91, not so high R^2 because the change of I_F is too minimal, so that the noise of the measurement also affects the calculation. The k was estimated to be 2.74×10^{-1} $M^{-1}s^{-1}$.

For the AC-exchanged hybrid nanoribbons, the data from 1000 to 9000 s range, which is the closest range to linear, was used to calculate k. The linear regression functions were fitted with the minimum R^2 of 0.98. The average of k was 2.10 (± 0.22) × 10^1 $M^{-1}s^{-1}$, 2 order of magnitude higher than of free AC in solution, indicating a significant acceleration of photocyclodimerization of AC. (Figure 2-29 a blue and yellow lines)

Unfortunately, the quantitative calculation is not simple. If this approximation can be applied to any concentration, photocyclodimerization of AC-exchanged hybrid nanoribbons at 100 µM, having the same k, must have 10 times steeper slope than 10 µM (Slope = $-k$[AC]). However, the graph showed only 1.1 times steeper, which contradicts to the approximation. (Figure 2-29 b, blue line) Moreover, the higher AC ratio ([AC] : [hybrid nanoribbons] 100 µM : 50 µM, Figure 2-29 b, orange line) showed higher k, which is not expected. More insight analysis of reaction mechanism is necessary for the accurate quantitative calculation of photocyclodimerization kinetics.

2.6 Chirality Induction of Naphthalene Derivatives, Anthracene Derivatives and 2-Anthracenecarboxylate Dimers Using Chiral Silica-Organic Hybrid Nanoribbons

Carboxylate group is no doubt the important component in the exchange and aggregation of AC in hybrid nanoribbons. To demonstrate this, the incubation of AC and hybrid nanoribbons in acetone was performed. Under this condition, AC takes carboxylic acid form. Similarly, the exchange of anthracene, without any acidic functional groups, and hybrid nanoribbons in acetone was investigated. The naphthalene derivatives with 1 and 2 carboxylate groups were used to investigate the importance of the number of carboxylate groups. The anthracene derivatives were used to attest the effects of acid groups and positions. Finally, the selective exchange between tartrate and the mixture of ACDs are discussed.

2.6.1 Induced CD of Anthracene and AC in Acetone by Hybrid Nanoribbons

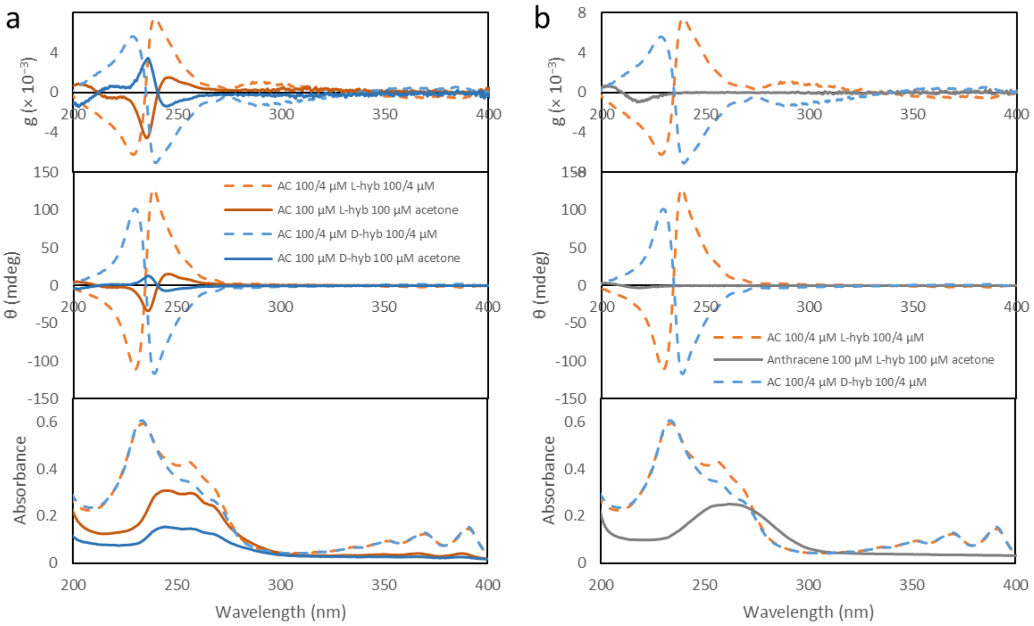

Figure 2-30 CD spectra, UV-Vis absoprtion spectra and g-factor of (a) AC and hybrid nanoribbons mixture (both 100 μM, solid line), and (b) anthracene and L-hybrid nanoribbons (both 100 μM, solid line) compared with AC-exchanged L-hybrid nanoribbons ([AC] : [hybrid nanoribbons] 25 μM : 25 μM, dash line).

Acetone (4 °C) was used as a solvent during incubation because gemini tartrate double-bilayer self-assemblies are stable in acetone, AC dissolves well in acetone, and AC is in carboxylic acid form. The incubation procedure are same as the incubation in water (2 mL). However, acetone has a high cut-off wavelength causing impossible CD and UV-Vis absoprtion measurement in solvated state. Consequently, the suspension was centrifuged at 3893 × g and 4 °C for 12 min in order to remove acetone. The gel was washed by water 4 °C twice, and re-suspended in water at 4 °C 2 mL. The g-factor obtained from AC incubated with gemini-tartrate hybrid nanoribbons in acetone is significantly lower than in water, demonstrating lower chirality induction. Also, the absolute CD intensities and UV-Vis absorptions, even though slightly suffered from the lost during washing, is much lower (Figure 2-30 a. Note that the concentration of the sample incubated in acetone is 4 times higher than in water.), meaning the less exchange between AC and tartrate. Anyway, the original CD pattern of hybrid nanoribbons with lower intensity (200-230 nm) was found, implying that the organization of gemini tartrate is preserved in acetone.

The binding between anthracene and L-hybrid nanoribbons was investigated with similar procedure in acetone. As expected, only original CD of L-hybrid nanoribbons was found. (Figure 2-30 b) This is an evidence that the AC aggregation in the hybrid nanoribbons occur solely through anion exchange driven by carboxylate group. These two experiments clearly demonstrated that carboxylate group (anions) is nessesary for molecules to bind and aggregate in hybrid nanostructures.

2.6.2 Induced CD of Naphthalene Derivatives by Hybrid Nanoribbons

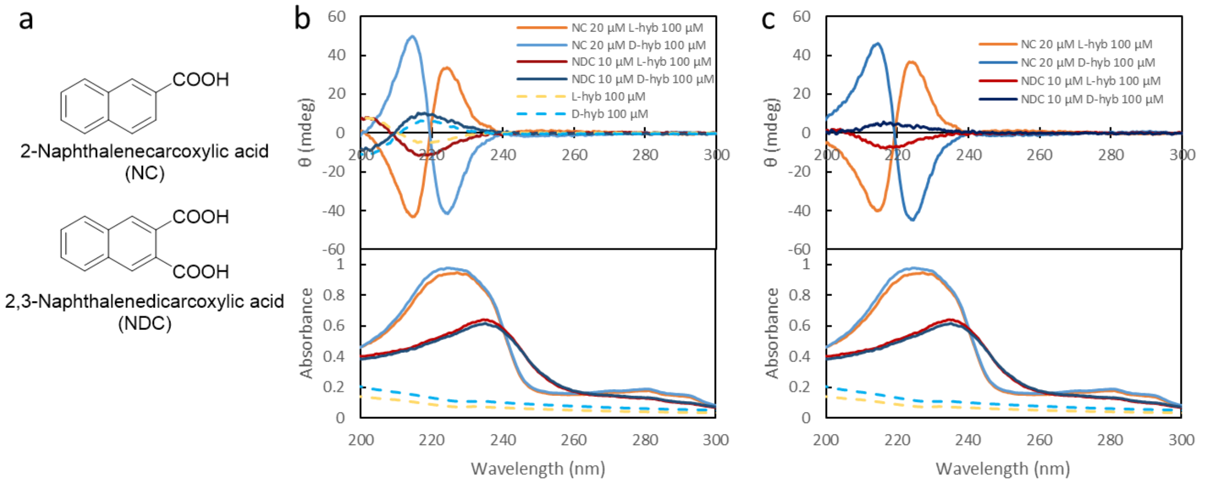

Figure 2-31 (a) Structure of NC and NDC, (b) CD and UV-Vis absorption spectra of NC and NDC with hybrid nanoribbons, and (c) CD spectra after subtracted by CD spectra of gemini tartrate.

The effect of the number of carboxylate groups on the chirality induction are evaluated. To compare with AC, 2,3-anthracenedicarboxylic must be synthesized. Fortunately, 2-naphthalene-carboxylic acid (NC) and 2,3-naphthalenedicarboxylic acid (NDC) are commercially available. (Figure 2-31 a) Although naphthelene has weaker aromatic interactions than anthracene,[288] it can be easily dissolved in alkaline solution, a good model to study the effect of the number of carboxylate groups.

The experiment was conducted similar to AC-exchanged hybrid nanoribbons. To make the same stoichiometry between naphthalene and tartrate, NC 20 µM and NDC 10 µM dissolved in alkaline solution were incubated with hybrid nanoribbons 100 µM in water. As a result, the NC showed strong induced exciton-coupling CD similar to the AC cases. However, the CD of NDC is rather complicated.

The induced CD of NDC in hybrid nanoribbons is too low, overwhelmed by the CD signals from tartrate in the original hybrid nanoribbons structure. (Figure 2-31 b) Assuming that NDC was completely exchanged with tartrate, the ratio of anions in hybrid nanoribbons will be [NDC] : [tartrate] : [gemini] 20 : 80 : 100 µM. By subtracting the CD with the original CD of hybrid nanoribbons 80 µM, the estimated induced CD of NDC was obtained. (Figure 2-31 c) As a result, relatively low induced CD without exciton-coupling was found. With higher NDC ratio, the exciton-coupling can also be observed. (Appendix)

This result shows that the number of carboxylic groups strongly affects the chirality induction at the low exchanging anions : hybrid nanoribbons ratio. While the monoanionic aromatic molecules with single carboxylic acid group will exchange with tartrate in pairs, showing exciton-coupling CD even at low concentration, dianionic aromatic molecules with two carboxylic acid groups will exchange randomly, so the concentration threshold to obtain exciton coupling is higher.

2.6.3 Induced CD of Anthracene Derivatives

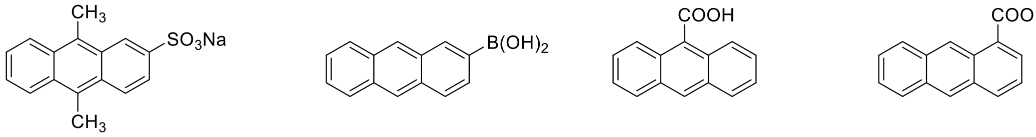

Sodium 9,10-dimethylanthracene-2-sulfonate ASONa

2-Anthraceneboronic Acid (AB)

9-Anthracenecarboxylic Acid (9-AC)

1-Anthracenecarboxylic Acid (1-AC)

Figure 2-32. Some of commercially available acidic anthracene derivatives

The other commercially available acidic anthracene derivatives (Figure 2-32) were also exchanged to tartrate in hybrid nanoribbons and compared with AC. However, it was difficult to determine the concentration of each derivative because they do not dissolve completely in NaOH 1 mM solution, except sulfonate derivative. Therefore, the stock solution of each derivative was prepared with the same method as AC, and the concentration is considered to be no more than 1 mM. In the case of AC, more than 1 : 1 ratio to hybrid nanoribbons will saturate the CD signals. Comparatively, the other derivatives were prepared with no more than 1 : 1 ratio, and the g factors were compared instead of absolute CD signals.

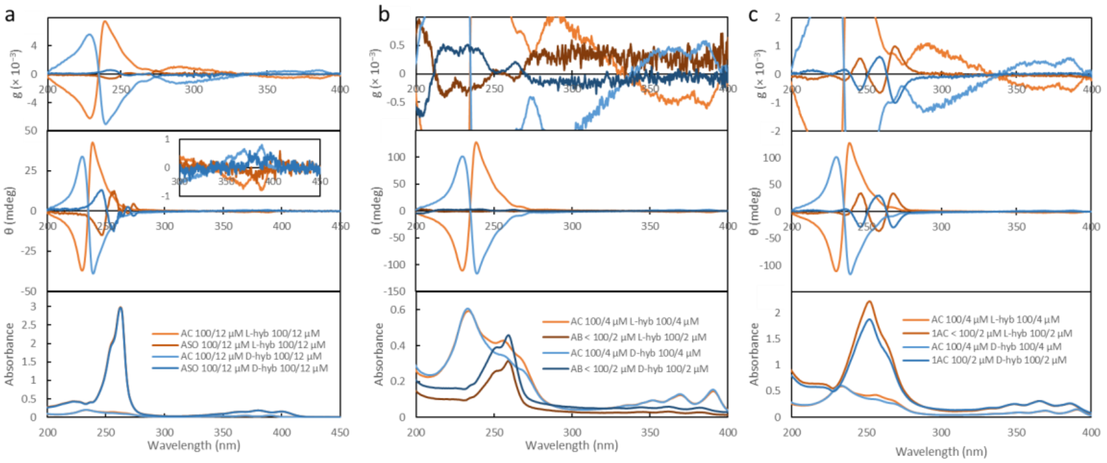

Figure 2-33. CD spectra, UV-Vis absorption spectra and g factor of (a) AC 8.3 µM (light blue and ligh orange) and 9,10-dimethylanthracene-2-sulfonate (ASO) 8.3 µM (dark blue and drak orange) with hybrid nanoribbons (1 : 1), (b) AC 25 µM with hybrid nanoribbons 25 µM (light blue and ligh orange) and 2-anthraceneboronate (AB) less than 50 µM with hybrid nanoribbons 50 µM (dark blue and drak orange), and (c) AC 25 µM with hybrid nanoribbons 25 µM (light blue and ligh orange) and 1-anthracenecarboxylate (1-AC) less than 50 µM with hybrid nanoribbons 50 µM (dark blue and drak orange).

Previously, methyl orange was reported to be a good anion to exchange with tartrate.[195] Therefore, sodium 9,10-dimethylanthracene-2-sulfonate (ASONa), the closest sulfonate derivative of AC, was used. Surprisingly, the induced CD, both absolute signal and g factor, is much lower than AC, probably due to 2 factors. (Figure 2-33 a) First, the substitution at 9 and 10 positions of anthracene and/or the size of overall anions are crucial. Second, it is also possible that at nearly neutral pH, sulfonate (strong acid) or carboxylate (pK_a 4.2)[289] functional groups on anthracene do not show significant different. As a result, tartrate can exchange with AC relatively easy comparing to ASONa.

2-Anthraceneboronate (AB) was also exchanged to tartrate in hybrid nanoribbons. Boronic acid usually has pK_a more than 8, weaker acid than carboxylate. Therefore, interactions of AB are much lower than AC. Nevertheless, it was proved in the case of AC that if the AC to hybrid nanoribbons ratio is less than 1 : 1, g factor does not change (or even slightly increase when decrease AC proportion). Thus, if AB has less exchange efficiency but same induced chirality as AC, the g factors of AB and AC should be similar. However, the g factor of AB is much lower than AC and does not have exciton coupling signal. (Figure 2-33 b) (The cross point at 210 nm is originated from tartrate.) This is possibly because 2 protons of boronic acid can be deprotonated, becoming dianion. Exchanging one tartrate then requires only one AB, reducing the aromatic stacking interactions that usually happened with AC.

Next, 1-anthracenecarboxylate (1-AC) was used to investigate the importance of the positions of the functional group. 1-AC also showed less exchanging efficiency with much lower g-factor even though the exciton coupling was observed. (Figure 2-32 c). As already discussed in IR and VCD section, 9-AC has less exchange efficiency than AC. These two results reach to the same conclusion that the carboxylate group at the end of anthracene molecular structure allows better stacking of anthracene molecules in hybrid nanoribbons confined space, which corresponds to the proposed organization (Figure 2-27). The stackings of 1-AC and 9-AC molecules are limited comparing to AC because the substitution requires more space on the surface of double-bilayer plane.

2.6.4 **Induced CD and Selective Binding of ACDs**

The mixture of ACDs synthesized from AC photodimerization in tetrahydrofuran was mixed with L-hybrid nanoribbons and incubated at 4 °C overnight. The ACDs inside the nanoribbons were analyzed by HPLC. Considering that ACDs have 2 carboxylate groups, and only half of the tartrate (outer-layer tartrate) can be exchanged, the maximum stoichiometry to exchange ACD to tartrate will be [ACD] : [gemini tartrate] 1 : 2. If every ACD is equally presented in the mixture (HPLC of pure ACDs was analyzed after this experiment.), the minimum ratio of 1 : 1 and 2 : 1 ratio should be more than enough for the tartrate to completely exchange with *head-to-head* ACDs and single ACD, respectively.

Table 2-7. Distribution of ACDs obtained inside the hybrid nanoribbons from mixing the mixture of different ACDs to L-hybrid nanoribbons.

ACDs (μM)	L-Hybrid Nanoribbons (μM)	Temperature (°C)	ACD Distribution Inside Nanoribbons (%)				% *head-to-head*
			ACD1	ACD2	ACD3	ACD4	
pure[a]	-	-	35.4	27.8	19.0	17.8	36.8
200	100	4	17.0	18.6	23.6	40.8	64.4
200	100	20	3.7	10.8	24.7	60.8	85.5
200	50	4	26.6	22.0	17.8	33.6	51.4
50	50	4	18.3	20.0	19.6	42.0	61.6

Incubation overnight on roller mixer, [a]ACDs mixture was synthesized by photoirradiation of AC 1 mM in tetrahydrofuran while bubbled with N_2.

Interestingly, all the samples with different AC to hybrid ratio show the increase product distribution of *head-to-head* dimers. The efficiency strongly depends on the ratio and temperature. (Table 2-7). With the ACDs to hybrid nanoribbons ratio of 1 : 1 and 2 : 1, the selectivity of the *head-to-head* dimers increased to 62 and 64 % respectively comparing to 36.8 % in free solution, while the 4 : 1 ratio can selectively bind only 51.4 % *head-to-head* product distribution. It was clear that the main dimers responsible for the variation of the % *head-to-head* for all three ratios was the increase of ACD4 and the decrease of ACD1. The binding constant of each dimer can be ranked as ACD4 > ACD3 > ACD2 > ACD1. Moreover, this trend becomes clear when incubating at 20 °C, which *head-to-head* dimers 86 % can be obtained. This time, the distribution of *head-to-tail* dimers are relatively low and the ACD4 increases, but the ACD3 remains the same. Therefore, the hybrid nanoribbons can be used to selectively capture and enrich the product distribution of ACD4.

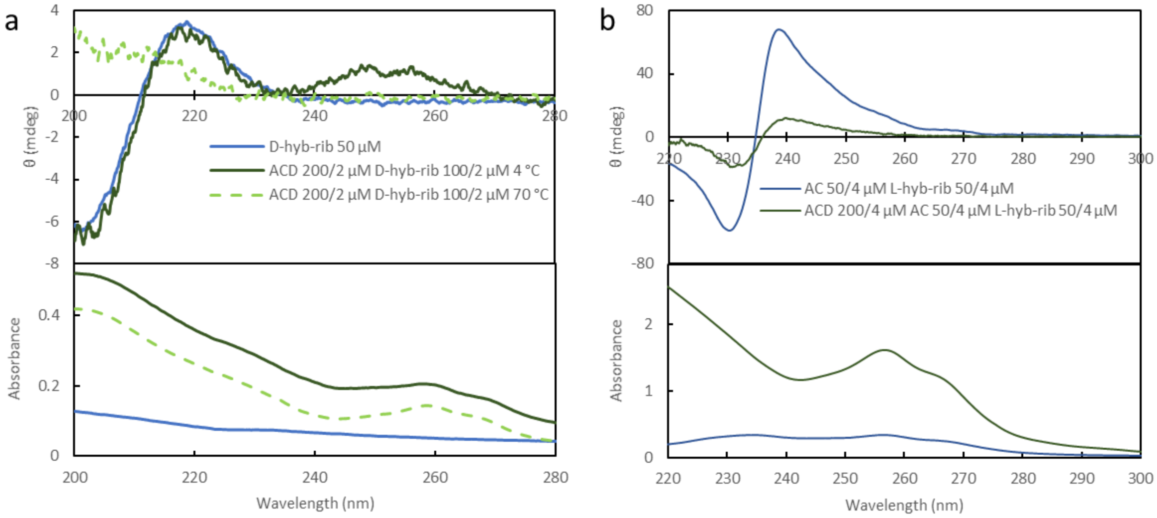

Figure 2-34. CD and UV-Vis absorption spectra of (a) ACDs-exchanged L-hybrid nanoribbons and (b) ACDs (all dimers 50 μM) and AC (13 μM) mixture with D-hybrid nanoribbons (13 μM).

Unfortunately, the enantiomeric excess (ee) cannot be observed. The ACDs exchange was repeated with D-hybrid nanoribbons with [ACDs] : [hybrid nanoribbons] 2 :1. The water was removed by centrifugation at 3893 × g and 4 °C for 20 min, and the nanoribbons were re-dispersed in water 4 °C. Comparing to pure D-hybrid nanoribbons, the UV absorption increased, indicating the presence of ACDs. (Figure 2-34 a) The CD signal belonging to ACDs (240 - 270 nm) was also found. However, after heating the ACDs-exchanged hybrid nanoribbons at 70 °C, the CD peak of ACDs disappeared, indicating that the CD was not originated from the ee of ACDs, but it was an induced CD originated from the chiral organization of ACDs entrapped in the chirally arranged gemini.

Finally, the difference in the affinity between AC and ACDs with the hybrid nanoribbons was examined. (Figure 2-33 b) The mixture of ACDs and AC with excess amount of ACDs (4 times higher concentration than AC, 8 times more carboxylate groups) were mixed with D-hybrid nanoribbons. The resulting CD spectrum shows induced CD profile similar to AC-exchanged D-hybrid nanoribbons (Figure 2-33 b, green line), but the intensity is much lower, while the absorption was higher, indicating that major exchanging anion is ACDs. The induced CD of ACDs in hybrid nanoribbons is much lower than of AC, causing the opposite results between CD and absorption. Still, the fact that induced CD of AC can still be observed even with excess ACDs concentration means that AC can bind hybrid nanoribbons even in the existence of ACDs, showing a possibility to recycle hybrid nanoribbons after photocyclodimerization of AC inside.

2.7 Conclusion

The chiral hybrid nanoribbons were synthesized and used as a chiral template to induce chirality of AC. Because of the anion exchange between tartrate and AC, the AC exhibits the induced CD throughout the spectrum with particularly strong exciton-coupling CD signal with the g-factor difference (positive absolute maxima − negative absolute maxima at the exciton-coupling) of 1.3×10^{-2}. The chirality of AC was induced from the chiral double-bilayer self-assemblies of gemini molecules, not the chiral tartrate. Lowering the temperature slows down the exchange between tartrate and AC but gives a more stable and higher induced CD spectrum. The exchange efficiency also depends on the age of hybrid nanoribbons stocks. The AC can exchange with only half of the tartrate on the outer layer of double-bilayer assemblies. At higher AC content, the AC molecules will begin to penetrate through gemini layer, revealed by VCD and IR spectra, causing the perturbation to the assemblies. The exchange efficiency depends not only on the acidity but also on the structure of anions. For example, the position of carboxylate group can greatly affect the exchange, and the number of carboxylate groups is an essential factor to obtain the exciton-coupling CD at low concentration ratio. These studies on dynamics of AC and tartrate exchange are useful to not only this system but also the other systems utilizing hybrid nanostructures or any other hybrid surfactant self-assemblies.

Even though the enantioselectivity was too low to be discussed, hybrid nanoribbons showed high regioselectivity toward *head-to-head* dimers (ACD3 and ACD4). The maximum selectivity was 97 %, which is a near perfect absolute regioselectivity. This is so far the only complete supramolecular *head-to-head* regioselective photocyclodimerization of AC using only water as a solvent and at the temperature higher than 0 °C (even at room temperature).[233,246,259,263] (the combination of chiral ionic liquid and cucurbit[*8*]uril in aqueous solution show the closest result of 91 % at 25 °C,[258] and complete *head-to-head* selectivity of anthracene is also possible on dried surface of helical nanometal.[259]) Also, this is the first regioselective reaction utilizing hybrid nanoribbons.[189,190,290] Moreover, the photocyclodimerization of AC using hybrid nanoribbons is exceptionally versatile. From temperature −20 °C to 20 °C, the product distribution of *head-to-head* dimers are more than 90 % in almost any conditions. The temperature (and maybe additional solvent) is important to control the ratio between *syn-* and *anti-head-to-head* dimers. The enantioselectivity and the selectivity between *syn-* and *anti-*isomers can be interesting topics for the future research. Together with the titration experiment, the orientation of AC on the self-assembled double-bilayer of gemini surfactants was proposed.

The kinetics determination also showed a significant increase of photocyclodimerization rates by using hybrid nanoribbons as chiral media even at 10 µM. The hybrid nanoribbons can be used for capturing and enriching ACD4. In addition, AC can exchange with tartrate in hybrid nanoribbons even with relatively higher ACDs concentration, illustrating the possibility to recycle the hybrid nanoribbons after reactions. Using hybrid nanoribbons demonstrates not only a significant improvement of regioselectivity but also a potential reduction of time, energy and cost in photoreactions.

2.8 Experimental Procedure

2.8.1 Synthesis of Gemini Bromide (*N,N'*-dihexadecyl-*N,N,N',N'*-tetramethylethylene diammonium bromide)

Tetramethylethylenediamine 1.00 mL (6.63 mmol) and 1-bromohexadecane 6.08 mL (19.88 mmol, 3 eq) were dissolved in acetonitrile 50 mL. The solution was stirred at 85 °C for 2 d, and the white precipitate was formed. The solution was cooled to room temperature. The precipitate was centrifuged at 3893 × g and 20 °C for 20 min. The supernatant was removed, and the precipitate was washed by acetone 40 mL 4 times. The precipitate was dried under vacuum to give gemini bromide 2.76 g (3.83 mmol, 57.8 % yield) as a white solid: ^{1}H NMR (CD_3OD, 400 MHz): δ (ppm) = 0.87 (t, *J* = 6.6 Hz, 6H, CH_3), 1.18 - 1.45 (m, 52H, CH_2), 1.82 (br, 4H, CH_2), 3.23 (s, 12H, N-CH_3), 3.45 (t, *J* = 8.5 Hz, 4H, N-CH_2), 3.98 (s, 4H, N-CH_2).

2.8.2 Synthesis of Gemini Acetate (*N,N'*-dihexadecyl-*N,N,N',N'*-tetramethylethylene diammonium acetate)

Gemini bromide 2.78 g (3.83 mmol) was dissolved in methanol 60 mL while heated at 50 °C. Silver acetate 2.44 g (14.6 mmol, 4 eq) was added to the solution and stirred at 50 °C in the dark for 1 d. The solution was filtered by celite. The precipitate was washed by methanol. The combined filtrate was dried by evaporator resulting in the yellow viscous oil. The oil was re-dissolved in methanol 2 mL, heated at 40 °C and sonicated until completely dissolved. Acetone 10 mL was added, and the white precipitate was observed. The suspension was kept at 4 °C overnight. The supernatant was removed by centrifugation at 3893 × g and 4 °C for 10 min. The precipitate was washed by acetone 40 mL 3 times and dried under vacuum to give gemini acetate 2.29 g (3.34 mmol, 87.2 % yield) as a white solid: ^{1}H NMR (CD_3OD, 300 MHz): δ (ppm) = 0.87 (t, *J* = 6.6 Hz, 6H, CH_3), 1.25 - 1.45 (m, 52H, CH_2), 1.84 (br, 4H, CH_2), 1.89 (s, 6H, CH_3), 3.23 (s, 12H, N-CH_3), 3.41 (t, *J* = 8.7 Hz, 4H, N-CH_2), 3.90 (s, 4H, N-CH_2).

2.8.3 Synthesis of Gemini L- and D-Tartrate (*N,N'*-dihexadecyl-*N,N,N',N'*-tetramethylethylene diammonium L- and D-tartrate)

D-Tartaric acid 302 mg (2.01 mmol, 2 eq) was dissolved in methanol and acetone mixture 35 mL (1:9). Gemini acetate 687 mg (1.00 mmol) in the same solvent mixture with the same volume was added dropwise to the tartaric acid solution. The white precipitation was formed during addition. The solution was stirred for 3 h at room temperature. The suspension was centrifuged at 3893 × g and 4 °C for 10 min, and the supernatant was removed. The precipitate was washed by methanol and acetone mixture 45 mL (1:9) 2 times and cold water 9 times until the pH became more than 6. The solid was washed by acetone 45 mL 2 times and dried under vacuum to give gemini D-tartrate 562 mg (786 µmol, 78.4 % yield) as a white solid. The similar procedure was carried out with L-tartaric acid 320 mg (2.13 mmol, 2 eq) and gemini acetate 685 mg (1.00 mmol) to give gemini L-tartrate 589 mg (824 µmol, 82.4 % yield) as a white solid: ^{1}H NMR (CD_3OD, 300 MHz): δ (ppm) = 0.90 (t, *J* = 6.8 Hz, 6H, CH_3), 1.25 - 1.45 (m, 52H, CH_2), 1.82 (br, 4H, CH_2), 3.21 (s, 12H, N-CH_3), 3.41 (t, *J* = 7.5 Hz, 4H, N-CH_2), 3.91 (s, 4H, N-CH_2), 4.30 (s, 2H, CH).

2.8.4 Synthesis of Organic Nanoribbons, Nanohelices and Nanotubes

The gemini L- or D-tartrate was dissolved in water to the final concentration of 1 mM. The solution was heated at 60 - 70 °C in water bath for 5 min, sonicated in the sonication bath for 2 min, and heated again for 5 min. If the volume of the solution was more than 5 mL, it would be divided to 5 mL each into 15 mL centrifuge tube while heating in water bath. The solution was cooled and aged in the temperature-controlled chamber at 20 °C. The organic nanoribbons, nanohelices and nanotubes were formed after 1 h, 2 d and 15 d, respectively.

2.8.5 Synthesis of Hybrid Nanoribbons, Nanohelices and nanotubes

First, the tetraethyl orthosilicate 5 % v was pre-hydrolyzed in tartaric acid solution (aq) 0.1 mM (final concentration) with the same enantiomer as the gemini tartrate. The solution was vortexed and sonicated for 1 min before mixed by roller mixer at 20 °C for 5 h. The solution was sonicated again and transferred to the gemini-tartrate-aging tube (1 h for nanoribbons, 3 d for nanohelices and 3 weeks for nanotubes) with the exact same volume. The solution was mixed by gentle inversed-shaking to avoid breaking the formed nanofibers. The solution was aged for 14 h on roller mixer at 20 °C. The nanofiber aggregates could be observed after the aging. The solution was centrifuged at 3893 × g and 4 °C for 12 min, and the supernatant was disposed to remove the excess hydrolyzed tetraethyl orthosilicate and quench the transcription. To completely remove excess tetraethyl orthosilicate, the obtained precipitate (hydrogel) was washed 4 times with the following procedure. The hydrogel was re-dispersed in water 14 mL at 4 °C by vortexing and sonicating 1 min in ice bath, the suspension was centrifuged at 3893 × g and 4 °C for 12 min, and the supernatant was disposed. After washing, the hydrogel was re-dissolved in water 5 mL at 4 °C (or less). The suspension was sonicated by the probe sonicator for 5 s 2 times to make homogeneous suspension. The concentration was determined by lyophilization of 200 µL sample in a small aluminium cup. The morphology was checked by TEM, and the organization of gemini tartrate was confirmed by CD.

2.8.6 Synthesis of Silica Nanoribbons and Nanohelices

To remove the gemini tartrate assemblies, the hybrid nanofibers were washed by methanol 5 times with the following procedure. First, the suspension was centrifuged at 3893 × g and room temperature for 12 min. The supernatant was disposed, and the gel was re-dispersed in methanol by vortexing and sonicating. The suspension was heated at 60 °C for 5 min and sonicated for 10 min, it was centrifuged at 3893 × g and room temperature for 12 min, and the methanol supernatant was removed. The gel was re-dispersed in designated solvent, and the suspension was sonicated by the probe sonicator for 5 s 2 times to make homogeneous suspension. The concentration was determined by drying 200 µL sample in a small aluminium cup using oven or by lyophilization. The morphology was checked by TEM. The CD spectrum from 200 to 240 nm must be 0, showing the complete removal of the gemini tartrate from the silica structure.

2.8.7 Transmitted Electron Microscope Measurement

The TEM sample was prepared using blotting technique. The 400-mesh carbon-coated copper grids (DELTA Microscopies, France) were used. First, the carbon side of the grid was hydrophilized by

UV/Ozone ProCleaner 220 for 20 - 30 min. After that, the suspension containing nanostructures 8 µL was dropped on the carbon surface. After 1 min, the excess liquid was blotted using filter paper. In case of organic nanostructures, uranyl acetate 2 % w 8 µL was dropped and blotted after 1 min. The surface was dried at the room temperature. The TEM images were taken from either Philips CM-120 20-120 kV (FEI Company, USA) or LVEM5 5 kV (Delong Instruments, Czech Republic). The ImageJ software (NIH and University of Wisconsin) was used to edit or scale the final images.

2.8.8 Synthesis of Chloride-Exchanged Hybrid Nanoribbons

The hybrid nanoribbons were washed by KCl 100 mM solution (aq) at 4 °C until CD signal of tartrate was minimized or disappeared. First, the hybrid nanoribbons suspension was centrifuged at 3893 × g and 4 °C for 12 min, and supernatant was removed. Few mL of KCl solution was added, and the suspension was mixed by pipetting. After that, the tube was filled by KCl and vortexed. The suspension was centrifuged at 3893 × g and 4 °C for 12 min, the supernatant was removed, and the procedure was repeated for 5 to 10 rounds until CD signal of tartrate was minimized. To remove excess KCl, the same procedure was repeated with water at 4 °C for 3 to 5 rounds. The suspension was stored in the desired volume at 4 °C. The concentration was determined by lyophilization similar to the case of hybrid nanostructures. The molar concentration was calculated with the same method as hybrid nanoribbons with gemini tartrate but converted to gemini chloride molecular weight.

2.8.9 Preparation of AC Stock in Alkaline Solution

The excess amount of AC powder was dissolved in NaOH 1 mM aqueous solution. The solution was sonicated using probe sonicator for 5 min (1 s on and 1 s off, total 10 min) in the ice bath. The solution was filtered by 0.25 µM syringe filter unit. The concentration of AC was determined by absorption spectra at 387 nm.

2.8.10 Titration between 2-Anthracenecarboxylate and Hybrid Nanoribbons

The AC stock was added to the hybrid nanoribbons and diluted to the desired concentration at the designated temperature. For the CD measurement, 3 mL of each sample was prepared and incubated on a roller mixer. The lowest concentration of hybrid nanoribbons was prepared at 100 µM to avoid the CMC problems, and the samples were diluted to the desired concentration just before the CD measurements. All samples in the same spectra were prepared from the same AC and hybrid nanoribbons stock with the 20 min interval, which is the time required for each CD measurement, ensuring as precise as possible incubation time for the same set. The samples for the other CD measurements were prepared in the similar manner.

2.8.11 Circular Dichroism Spectroscopy Measurement

The JASCO J-815 CD machine (JASCO, Japan) was equipped with Single Position Peltier Cell Holder. The suspension sample was diluted to the designated concentration for at least 2 mL volume in 1 × 1 cm quartz cuvette with a stirrer bar. All the preparation procedure was done in an ice bath unless otherwise mentioned. The measurement was conducted with scan speed 100 nm / min, bandwidth 2.00 nm, data integration time 0.5 s, standard sensitivity, accumulation 4 times at 4 °C while stirring, unless otherwise mentioned. All the data discussed in this chapter has linear dichroism (LD) less than 0.001 and high tension (HT) less than 600 V to ensure the identity of the CD signal.

2.8.12 **Fluorescence Spectroscopy Measurement**

The fluorescence emission spectra were measured from the CPL-300 spectrometer (JASCO, Japan). The sample 2 mL was in 1 × 1 cm quartz cuvette with stirrer bar. The sample chamber was cooled to 4 °C, and the sample was always stirred. The excitation wavelength is 350 nm and detection wavelength is 380 - 540 nm range with 100 nm / min scan speed. For the comparison of fluorescence intensity, the detector HT was set at 800 V for both AC and AC-exchanged hybrid nanoribbons samples with single scan. For the photochemical reaction kinetics study, the samples were scan repeatedly. The detector HT was set to 700 for AC and 850 V for AC-exchanged hybrid nanoribbons to give the best quality of the fluorescence intensity.

2.8.13 **Infrared and Vibrational Circular Dichroism Measurements.**

The infrared (IR) and Vibrational Circular Dichroism (VCD) spectra were recorded with a ThermoNicolet Nexus 670 FTIR spectrometer equipped with a VCD optical bench.[291] In this optical bench, the light beam was focused on the sample by a BaF_2 lens (191 mm focal length), passing an optical filter (1850-800 cm^{-1}), a BaF_2 wire grid polarizer (Specac) and a ZnSe photoelastic modulator (Hinds Instruments, Type II/ZS50). The light was then focused by a ZnSe lens (38.1 mm focal length) onto a 1 × 1 mm HgCdTe (ThermoNicolet, MCTA* E6032) detector. IR absorption and VCD spectra were recorded at a resolution of 4 cm^{-1} by coadding 50 scans and 24000 scans (8h acquisition time), respectively.

The samples of hybrid nanoribbons were prepared by exchanging of D- or L-tartrate with AC in different proportions for 5 mL in water at 4 °C overnight. The suspensions were centrifuged at 3893 × g and 4 °C for 10 min. The supernatant of each sample was removed, and the gel was washed by D_2O 4 °C 5 mL twice. The samples were held in a demountable CaF_2 cell (Biotools) with fixed path length of 55 μm. In order to compare the IR spectra and to ensure the consistency of the gel in the cell, the IR spectra were normalized with respect to the 2919 cm^{-1} band related to the antisymmetric (ν_aCH_2) stretching vibration of the methylene groups of gemini.

Additional IR and VCD spectra were performed for L-hybrid nanoribbons and 9-AC-exchanged L-hybrid nanoribbons (1 : 1) as well as IR spectrum of sodium salt of AC. Baseline corrections of the VCD spectra were performed by subtracting the raw VCD spectra of the D_2O solvent. The photoelastic modulator was adjusted for a maximum efficiency in the mid-IR region at 1400 cm^{-1}. Calculations were performed via the standard ThermoNicolet software, using Happ and Genzel apodization, de-Haseth phase-correction and a zero-filling-factor of one. Calibration spectra were recorded using a birefringent plate (CdSe) and a second BaF_2 wire grid polarizer, following the experimental procedure previously published.[292] IR spectra were shown with solvent absorption subtracted.

2.8.14 **Photocyclodimerization of AC Mediated with Hybrid Nanoribbons or Nanohelices**

The water used for AC stock preparation and dilution in photocyclodimerization was bubbled by N_2 gas for at least 1 h. The hybrid nanoribbons were diluted and the AC stock was added to the suspension to the desired concentration and volume. If the temperature is 4 °C, all the components were cooled in ice bath or refrigerator before mixing. The suspension was incubated before irradiated by lamp F8T5BL 8 W 352 nm (Ushio) under the designated conditions.

After irradiation, the suspension was centrifuged at 3893 × g and 4 °C for 20 min. The supernatant was removed, and the gel was washed twice by water 4 °C with the same volume as the removed supernatant. The hydrogel obtained from the last centrifugation was lyophilized to completely remove water.

The methanol 4 mL was added to the dried hybrid nanostructures. The suspension was heated at 50 °C for 10 min and sonicated for 10 min. The suspension was centrifuged at 3893 × g and 25 °C for 20 min. The supernatant 3 mL was separated, filtered by cotton and dried in the oven to obtain the powder for further HPLC analysis.

2.8.15 **HPLC Analysis of 2-Anthracenecarboxylate Dimers**

Table 2-8. Parameters for analysis HPLC of ACDs with chiral column

Parameters	Analysis Conditions
HPLC Equipment	JASCO
Column	5C$_{18}$-MS-II 4.6ID × 150 mm CHIRALCEL OJ-RH 2.1ID × 120 mm
Temperature	Room temperature
Injection Volume	20 µL (or otherwise noted)
Solvent	Acetonitrile 36 % (TFA 0.1 %)
Flow Rate	0.5 mL / min
Detector	UV 280 nm Fluorescence excitation 254 nm / detection 420 nm

The powder containing ACDs were dissolved in NaOH 10 mM. The same volume of acetonitrile was added, and the sample was filtered through 0.45 µM pore size syringe filter unit. Regarding the previous report, the sample was injected to the fluorescence-detector-equipped HPLC. (Table 2-8)

2.8.16 **Preparation of Anthracene and Naphthalene Derivatives Stock in Alkaline Solution**

The acidic anthracene derivatives were prepared similar to AC stock. The powder was dissolved in NaOH 1 mM solution (aq). The solution was sonicated using probe sonicator for 5 min (1 s on and 1 s off, total 10 min) in the ice bath. The solution was filtered by 0.25 µM syringe filter unit. The concentration was assumed to be no more than 1 mM. For NC, NDC and ASO, the powders were dissolved by mixing and shaking, and the concentration was calculated by weight.

2.8.17 **The Selective Binding of ACDs to L-Hybrid Nanoribbons**

The ACDs stock solution was prepared by dissolving ACDs powder in NaOH solution (aq) same as AC stock. The estimate concentration was calculated using the absorption at 201 nm ($\varepsilon_{201} \approx 85000$ $M^{-1}cm^{-1}$) The ACDs stock, L-hybrid nanoribbons and water were cooled and mixed in the ice bath. The suspension was incubated overnight at 4 °C on roller mixer. The suspension was centrifuged at 3893 × g and 4 °C for 20 min. The supernatant was removed. The hydrogel obtained from the last centrifugation was lyophilized to completely remove water. The same methanol extraction procedure and the HPLC analysis are the same as for the photocyclodimerization products.

CHAPTER 3: SUPRAMOLECULAR REGIO- AND ENANTIOSELECTIVE [4+4] PHOTOCYCLODIMERIZATION OF 2-ANTHRACENECARBOXYLATE USING SYNTHETIC ANTIBODY OBTAINED FROM PHAGE DISPLAY TECHNIQUE

3.1 Objective

The objective of this chapter is to utilize synthetic antibody as a supramolecular host for photocyclodimerization of AC in water. The antibody synthesis, starting from the ligand synthesis for phage display panning to antibody expression, and the optimized supramolecular photocyclodimerization conditions of AC are reported.

3.2 Introduction

From cyclodextrin and serum albumin cases, the possibility of supramolecular asymmetric syntheses mediated by biomolecules had been indicated with high efficiency and wide variety of media. Especially, the photocycloaddition is one of the most compatible reactions because the starting material can be specifically excited at the wavelength that products and host molecules do not absorb, avoiding reversible reaction and damage to the host molecules. However, a major drawback is the variety of the product distribution and ee causing the difficult selection of the products. In addition, the product distribution and ee can be in the opposite directions depends on which protein was utilized. For example, the native γ-cyclodextrin can induce product distribution of ACD2 to 46 % with 41 % ee,[223] and HSA induces the ee of ACD3 to 88 % but suppresses product distribution to only 11 %.[245] Also, they have multiple reaction sites which can produce different products.[254] The natural biomolecules were not designed for photochemical reaction, so it is difficult to predict the products when utilizing any biomolecules even with thorough knowledge of their structures. Synthetic antibody can be used as the simple and customizable biomolecular reaction template.

Besides the generality in thermal reaction, only few cases of catalytic antibodies for supramolecular photochirogenesis have been reported,[138,139,142–144] even though the concepts of catalytic enzyme are more appropriate in the design of synthetic antibody.[293] The antibodies are usually obtained by conjugating target molecules[294] with proteins to elicit monoclonal antibodies by standard hybridoma technique.[149,150,295] On the other hand, the phage display technique, despite the fact that it is very efficient method to obtain therapeutic antibody with high binding affinity to specific targets,[296–299] has not been used for obtaining synthetic antibodies for photochirogenesis. Even though using antibody phage display technique reduced a diversity of antibodies because the limitation of antibody structure, the structure can be approximated using the identified sequence and the known antibody structure from protein database as a model, which is simpler than hybridoma technique. Furthermore, it is also possible to conduct mutagenesis with the known information of amino acid residues by directly manipulate the vector.

Based on these backgrounds, we reported the utilization of synthetic antibody obtained by *in vitro* selection from a conventional phage display technique, an animal-free and inexpensive technique providing antibody in a relatively short time,[299] to the [4+4] photocyclodimerization of AC from the phage display panning and protein engineering to the optimization of photoirradiation conditions. Due to the customizability, high efficiency, low cost, short time and animal-free experiment, it is proved that the synthetic antibody obtained from phage display technique can be a good chiral reaction templates in a wide variety of photochemical reactions.

3.3 Synthesis of ACD3-PEG5-Lys-Biotin Ligand

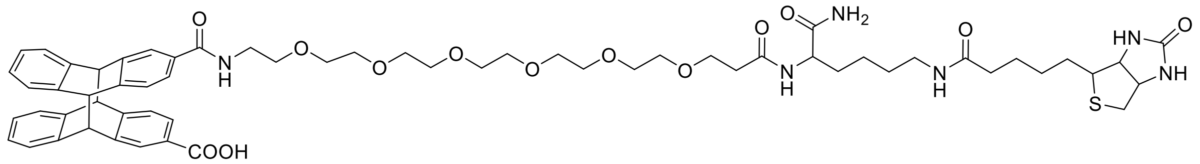

Chemical Formula: $C_{61}H_{76}N_6O_{13}S$
Exact Mass: 1132.52
Molecular Weight: 1133.37

Figure 3-1. ACD3-PEG5-Lys(Biotin) ligand.

For phage display screening, the ligand consisting of the target for antibody, linker and binding part for the paramagnetic beads. Based on the assumption that ACD molecules resembled the transition state orientation of the AC photocyclodimerization, ACD3 was used as a target for antibody. The ligand was designed composing of ACD3 as a target site, a flexible polyethylene glycol (3-[(17-Amino-3,6,9,12,15-pentaoxaheptadec-1-yl)oxy]propanoic acid: NH_2-PEG5-COOH) linker, and a biotin moiety for binding to streptavidin magnetic beads. (Figure 3-1)

The designed ACD3-PEG5-Lys(Biotin) ligand was synthesized by the stepwise peptide solid-phase synthesis of Fmoc-amino acids on Novasyn TGR resin according to a reported procedure[300] with Fmoc-AA-OH (Fmoc-Lys(Biotin)-OH and Fmoc-NH-PEG5-OH) using 2-(7-aza-1H-benzotriazole-1-yl)-1,1,3,3-tetramethyluronium hexafluorophosphate (HATU) and 1-Hydroxy-7-azabenzotriazole (HOAt) in diisopropylethylamine (DIEA) as coupling reagents. (Figure 3-2) Each coupling step was checked by Fmoc test and Kaiser test.

The enantiopure *(P)*-ACD3 was synthesized following the method of Fukuhara, *et al.*[264,22] (provided by M. Nishijima and G. Fukuhara). For the conjugation of ACD3 to the N-terminal amino group, Fmoc deprotected peptide resin, was incubated with the mixture of ACD3, HATU, HOAt, and DIEA in *N*-methyl-2-pyrrolidone / dimethyl sulfoxide for 2 h. The resin was washed by chloroform and ethanol, and dried under vacuum overnight.

A crude product was purified with Reverse-Phase (RP-) HPLC to afford ACD3-PEG5-Lys(Biotin) ligand stock solution (370 µM, 200 µL, 74 nmol). Although, the overall yield of the synthesis was only 1.5%, it was enough for phage display screening. The purity was calculated to be 80 % based on the HPLC analysis of purified ligand. The purified ACD3-PEG5-Lys(Biotin) ligand was identified by mass spectroscopy.

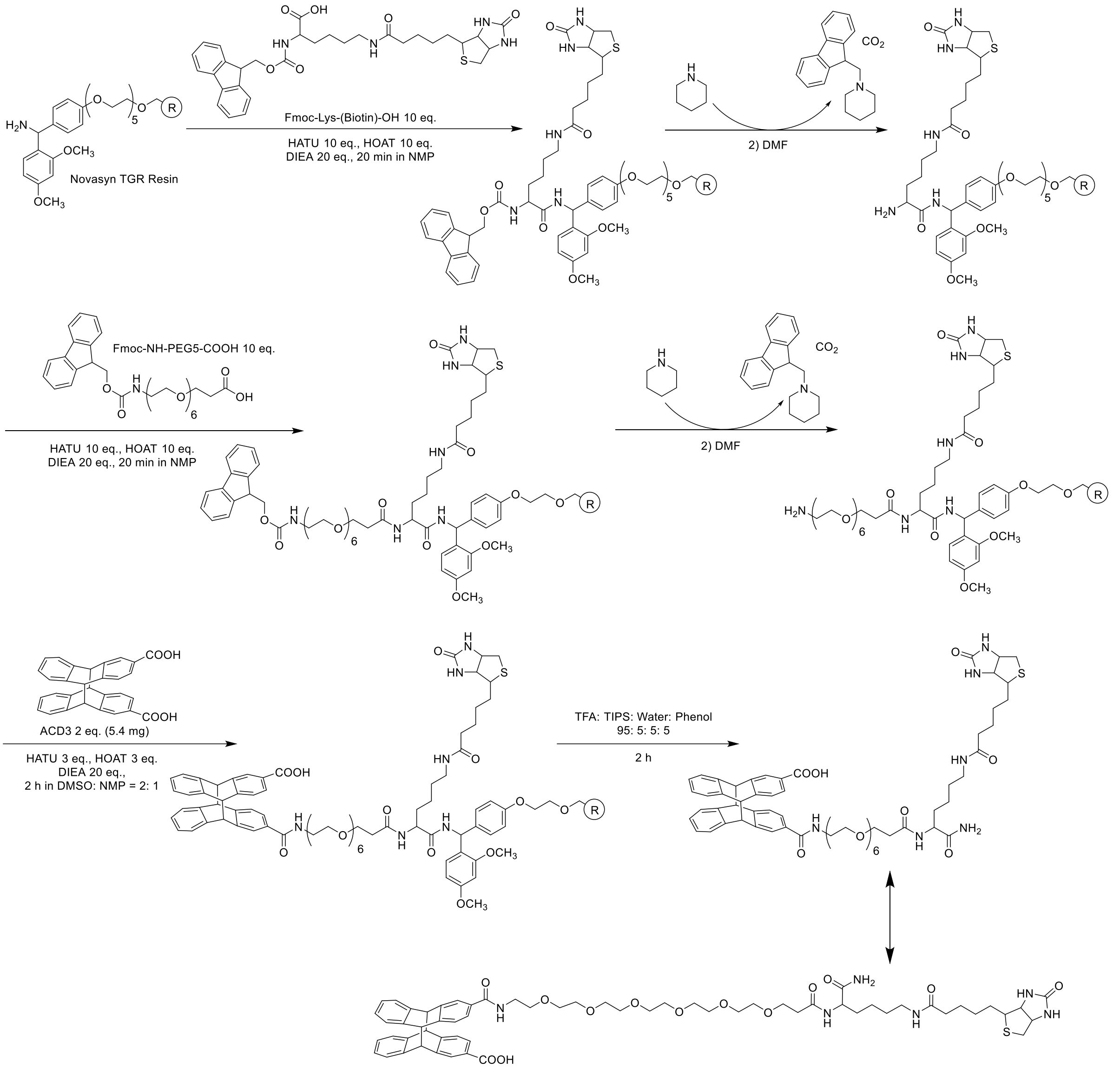

Figure 3-2. Solid phase synthetic scheme for ACD3-PEG5-Lys(Biotin)

3.4 Antibody Phage Display Screening and Protein Expression

The antibody phage display technique was performed using ACD3-PEG5-Lys(Biotin) ligand. With solution phase panning method, phages bound to ACD3 moiety can be isolated by the strong interactions between the biotin and streptavidin immobilized on paramagnetic beads.[301,302,303] After three rounds of panning procedure, monoclonal phage candidates from the last phage pool were isolated and screened by Enzyme-Linked Immunosorbent Assay (ELISA).[304,305] The phage with the high selectivity to ACD3 was chosen. The DNA sequence for protein expression was determined and stop codon was eliminated. The amino acid residues were mapped on the known antibody structure. The vector was subcloned and the protein was expressed in periplasm of *E. coli*.

3.4.1 Antibody Phage Display Panning Procedure

Figure 3-3. Structure of scFv antibody (PDB: 3AUV).[306] The CDRs region, containing random sequences, is expected to be the binding site to ACD3, which is shown in blue and pink colors.

Tomlinson I and J phagemid synthetic libraries were used in this experiment.[307] Tomlinson I and J libraries are commercially available scFv libraries widely used, composed of a single human framework for υ_h and υ_κ with the diversity of 18 random amino acids incorporated in complementary-determining region (CDR) 2 and 3, often contributed to the antigen binding (Figure 3-3).

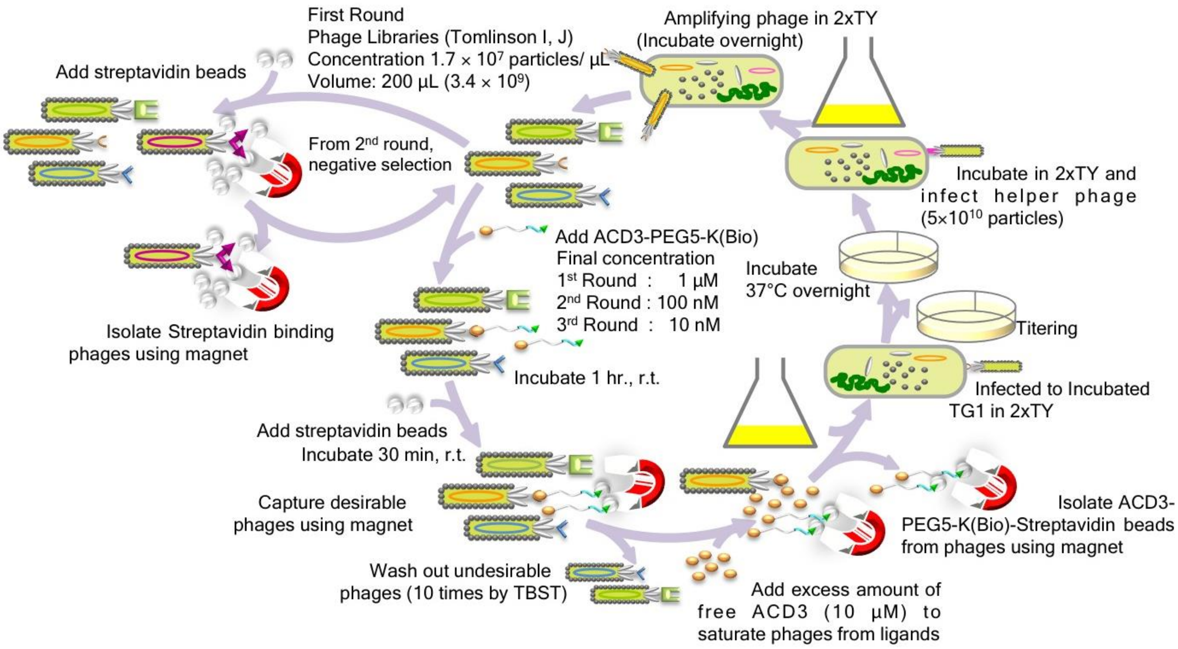

Figure 3-4. Schematic representation of antibody phage display panning. The panning was conducted 3 rounds with reducing concentration of the ACD3-PEG5Lys(Biotin) ligand. The negative selection was also conducted before 2nd and 3rd rounds using bare streptavidin paramagnetic beads.

The solution phase panning procedure was performed using streptavidin-conjugated paramagnetic beads. (Figure 3-4) The beads were pre-incubated with blocking buffer to prevent unspecific bindings. Also, the 2-Amino-2-hydroxymethyl-propane-1,3-diol hydrochloride (Tris HCl) buffer solution containing Tween-20 (0.1 %) was used as a washing reagent for the same reason. The phages were first incubated with ACD3-PEG5-Lys(Biotin) ligand, and then the solution mixture was added to the beads and incubated at room temperature. The beads, which is bound to the ACD3-PEG5-Lys(Biotin) ligand bound to phages in this state, were isolated by washing multiple times on magnetic stand. Next, the phages must be infected to the *E. coli* TG1 cells for the amplification. However, the phages bound to the magnetic beads cannot infect the bacterial cells, so the free ACD3 molecules were added to saturate and remove phages from the beads. The solution was separated completely from the beads and the phages were infected to TG1 cells.

Before the panning procedure of the 2nd and 3rd rounds, the negative selection, incubation of phages in with streptavidin-conjugated paramagnetic beads, was conducted to eliminate the phages that bind to streptavidin instead of the ligand. To prepare *E. coli* TG1 cells for the infection, the cells were grown in 2xTY medium until they reach an OD of 0.4 at 600 nm. The infection was conducted by mixing the recovered phages solution with the TG1 cells in the medium and incubating without shaking. The titering procedure was performed to estimate the number of recovered phages. The cells were plated on the LB agar plate and grown overnight. The grown *E. coli* cells were collected and stored in the LB medium containing 15% glycerol at −20 °C. A part of the stock was amplified and infected by helper phages, allowing bacterial cells to reproduce phages. The phages were purified and prepared as a new library for the next round of panning procedure.

After the 3 rounds of panning process, the monoclonal phages were isolated from single colonies on a titering plate. The cells were grown in LB medium and infected by helper phages. The purified phages were used for ELISA[304,305] on the streptavidin immobilized plate in three different protocols: with ACD3-PEG5-Lys(Biotin) ligand, without ACD3-PEG5-Lys(Biotin) ligand, and with both ACD3-PEG5-Lys(Biotin) ligand and excess amount of free ACD3. The phage having desired affinity must show binding affinity in the presence of ACD3-PEG5-Lys(Biotin) ligand. However, if the phage also shows binding affinity in the absence of the ligand, the phage is binding to the streptavidin instead of to the ACD3-PEG5-Lys(Biotin) ligand. Likewise, if the phage shows high affinity in the excess amount of free ACD3, it binds to another part of the ligand instead of ACD3. Thus, the phage must have low binding affinity in the case of without ACD3-PEG5-Lys(Biotin) ligand, and with ACD3-PEG5-Lys(Biotin) ligand and excess amount of free ACD3.

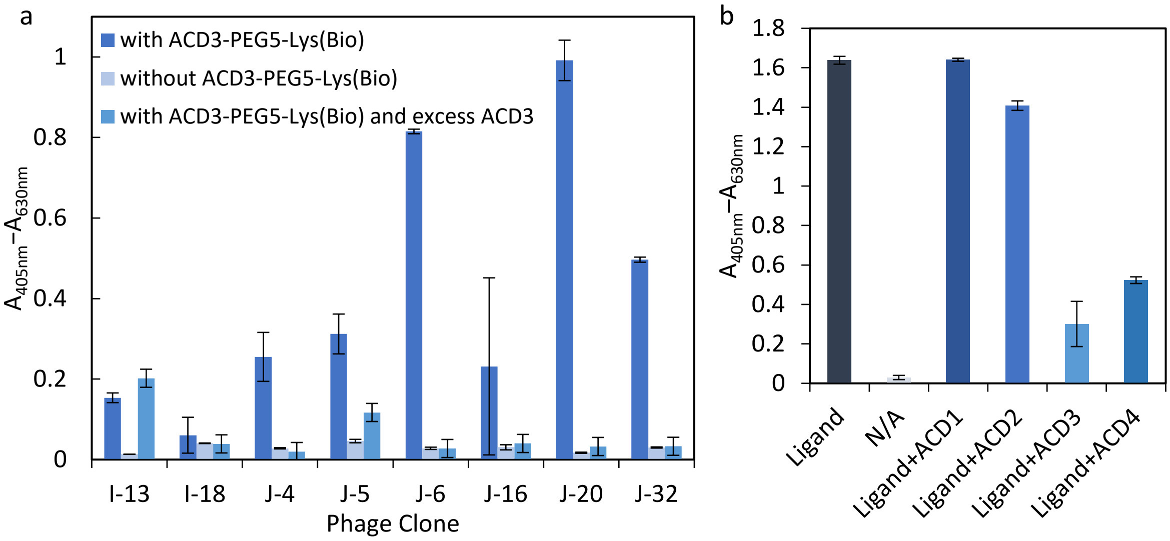

Figure 3-5. Absorption from ELISA screening of (a) first-selected candidates and (b) scFv J-20 clone.

From Tomlinson library I and J, 2 and 6 candidates were obtained from the screening of 48 clones each (Figure 3-5 a). Although Tomlinson I and J libraries are based on the same human scFv antibody, only 2 candidates with moderate results were obtained using Tomlinson I library while 6 candidates with much better results were given by Tomlinson J library. The difference between these libraries is the availability of the random sequence pattern. Thus, the amino acid sequences of the human scFv antibody are crucial to define the binding properties to ACD3.

For assessing the target selectivity of obtained phages, the competitive ELISA assay using the other ACD isomers was performed. Mostly, The ELISA signals were selectively decreased by the addition of ACD3. However, the addition of ACD4 also reduced the signals in most cases because of the similarity of *head-to-head* conformation. On the other hand, the addition of ACD1 and ACD2 must not affect the signals. Otherwise, the selectivity of the antibody will not fit the criteria. As a result, scFv J-20 clone showed the most suitable properties among the candidates. (Figure 3-5 b) Therefore, scFv J-20 clone was selected for subclone and protein expression.

3.4.2 Sequencing and Protein Expression of scFv J-20 Antibody

It is known that antibody phage display technique has less diversity of antibody library than hybridoma because the antibody structures are identical, human scFv. Nevertheless, one significant advantage over hybridoma technique is the possibility to determine amino acid sequences from the specific engineered vector of the library. The location of amino residues can be estimated using the known scFv structure, and they can be easily manipulated directly on the DNA plasmid vector. Besides, another advantage is no experiment in animals, causing faster, cheaper, less facilities needed and more environmental friendly.[308]

```
                 1/1                                     31/11

                 Nde I
5’-G GAA TTC cat atg AAA TAC CTA TTG CCT ACG G -3’ 32nt Tm=62°C SS-pelB-Fw-01
                 ATG AAA TAC CTA TTG CCT ACG GCA GCC GCT GGA TTG TTA TTA CTC GCg gcc cag ccg gcC
                 MET Lys Tyr Leu Leu Pro Thr Ala Ala Ala Gly Leu Leu Leu Leu Ala Ala Gln Pro Ala
                 -> pelB Leader

                 61/21                                   91/31
                 ATG GCC GAG GTG CAG CTG TTG GAG TCT GGG GGA GGC TTG GTA CAG CCT GGG GGG TCC CTG
                 Met Ala Glu Val Gln Leu Leu Glu Ser Gly Gly Gly Leu Val Gln Pro Gly Gly Ser Leu
                   Heavy ->
                 121/41                                  151/51
                 AGA CTC TCC TGT GCA GCC TCT GGA TTC ACC TTT AGC AGC TAT GCC ATG AGC TGG GTC CGC
                 Arg Leu Ser Cys Ala Ala Ser Gly Phe Thr Phe Ser Ser Tyr Ala Met Ser Trp Val Arg

                 181/61                                  211/71
                 CAG GCT CCA GGG AAG GGG CTG GAG TGG GTC TCA ACG ATT GGT GGT TAG GGT ACT CGG ACA
                 Gln Ala Pro Gly Lys Gly Leu Glu Trp Val Ser Thr Ile Gly Gly Gln Gly Thr Arg Thr

                 241/81                                  271/91
                 TTT TAC GCA GAC TCC GTG AAG GGC CGG TTC ACC ATC TCC AGA GAC AAT TCC AAG AAC ACG
                 Phe Tyr Ala Asp Ser Val Lys Gly Arg Phe Thr Ile Ser Arg Asp Asn Ser Lys Asn Thr

                 301/101                                 331/111
                 CTG TAT CTG CAG ATG AAC AGC CTG AGA GCC GAG GAC ACG GCC GTA TAT TAC TGT GCG AAA
                 Leu Tyr Leu Gln Met Asn Ser Leu Arg Ala Glu Asp Thr Ala Val Tyr Tyr Cys Ala Lys

                 361/121                                 391/131
                 ACG AGT CGG CCT TTT GAC TAC TGG GGC CAG GGA ACC CTG GTC ACC GTC TCG AGC GGT GGA
                 Thr Ser Arg Pro Phe Asp Tyr Trp Gly Gln Gly Thr Leu Val Thr Val Ser Ser Gly Gly
                                                                          G3S Linker ->
                 421/141                                 451/151
                 GGC GGT TCA GGC GGA GGT GGC AGC GGC GGT GGC GGG TCG ACG GAC ATC CAG ATG ACC CAG
                 Gly Gly Ser Gly Gly Gly Gly Ser Gly Gly Gly Gly Ser Thr Asp Ile Gln Met Thr Gln
                                                               Light ->
                 481/161                                 511/171
                 TCT CCA TCC TCC CTG TCT GCA TCT GTA GGA GAC AGA GTC ACC ATC ACT TGC CGG GCA AGT
                 Ser Pro Ser Ser Leu Ser Ala Ser Val Gly Asp Arg Val Thr Ile Thr Cys Arg Ala Ser

                 541/181                                 571/191
                 CAG AGC ATT AGC AGC TAT TTA AAT TGG TAT CAG CAG AAA CCA GGG AAA GCC CCT AAG CTC
                 Gln Ser Ile Ser Ser Tyr Leu Asn Trp Tyr Gln Gln Lys Pro Gly Lys Ala Pro Lys Leu

                 601/201                                 631/211
                 CTG ATC TAT CAT GCA TCC TCG TTG CAA AGT GGG GTC CCA TCA AGG TTC AGT GGC AGT GGA
                 Leu Ile Tyr His Ala Ser Ser Leu Gln Ser Gly Val Pro Ser Arg Phe Ser Gly Ser Gly

                 661/221                                 691/231
                 TCT GGG ACA GAT TTC ACT CTC ACC ATC AGC AGT CTG CAA CCT GAA GAT TTT GCA ACT TAC
                 Ser Gly Thr Asp Phe Thr Leu Thr Ile Ser Ser Leu Gln Pro Glu Asp Phe Ala Thr Tyr

                 721/241                                 751/251
                 TAC TGT CAA CAG GCT GCT GCG AAT CCT CCT ACG TTC GGC CAA GGG ACC AAG GTG GAA ATC
                 Tyr Cys Gln Gln Ala Ala Ala Asn Pro Pro Thr Phe Gly Gln Gly Thr Lys Val Glu Ile

                 781/261    Not I                        811/271
                 AAA CGG gcg gcc gcA CAT CAT CAT CAC CAT CAC GGG GCC GCA GAA CAA AAA CTC ATC TCA
                 Lys Arg Ala Ala Ala His His His His His His Gly Ala Ala Glu Gln Lys Leu Ile Ser
                                     -> 6 x His Tag                        Myc Tag

                 841/281                        Amber    871/291
                 GAA GAG GAT CTG AAT GGG GCC GCA TAG ACT GTT GAA AGT TGT TTA GCA AAA CCT CAT ACA
                   <- 3’- TA GAC TTA CCC CGG CGT ATC -5’ 20nt Tm = 62°C  pHEN-Term-01
                 Glu Glu Asp Leu Asn Gly Ala Ala *** Thr Val Glu Ser Cys Leu Ala Lys Pro His Thr
                                                     ->Phage gIII Coat Protein
```

Figure 3-6 DNA and amino acid sequences of scFv J-20 in pIT2 vector. The bold and underlined characters indicate the random sequences and CDRs. The primers (SS-pelB-Fw-01 and pHEN-Term-01) used for PCR are also shown.

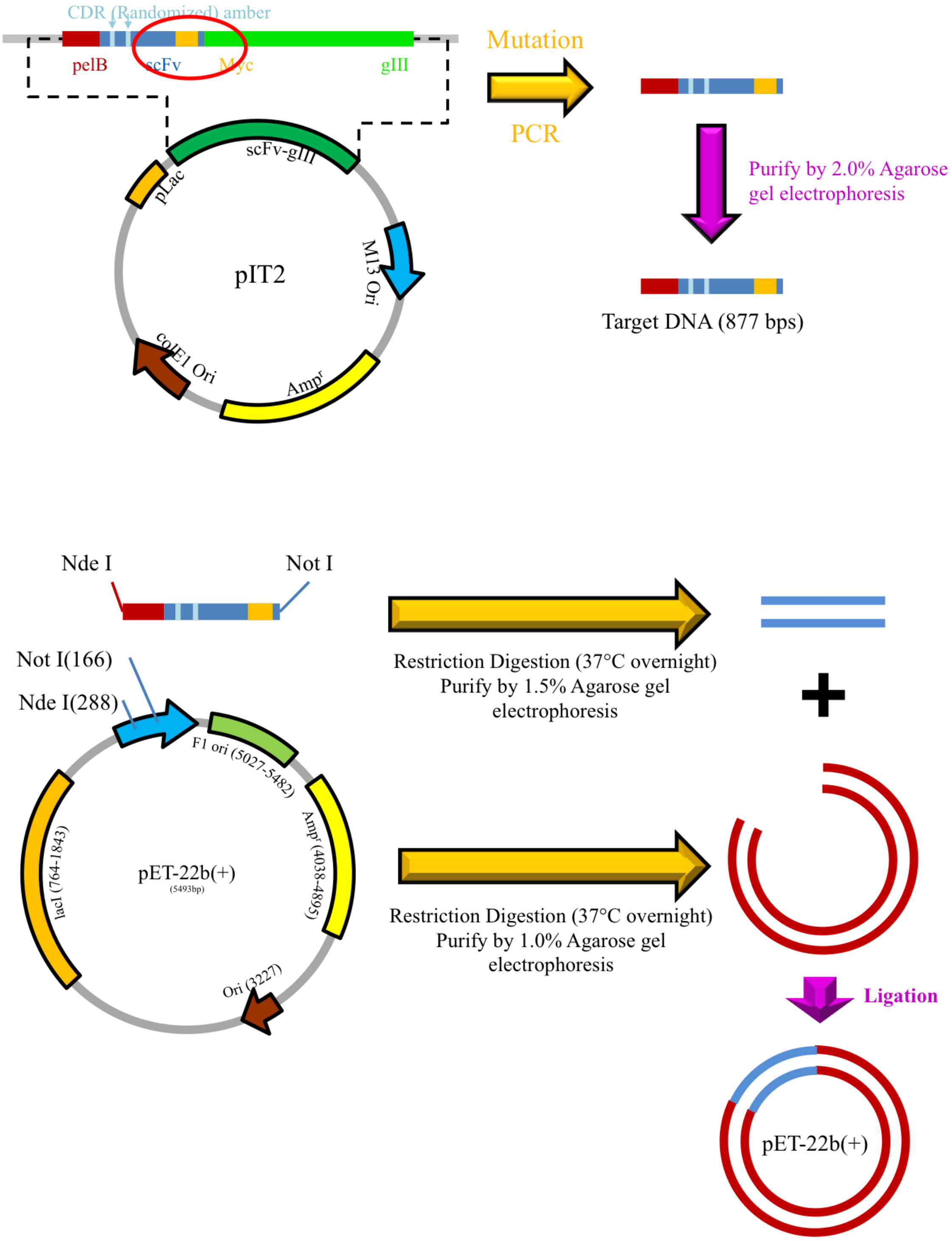

Figure 3-7. Subcloning of scFv J-20 into pET-22b(+) vector.

```
                                                          T7-Pro-01 Primer, 20b, Tm = 56 °C
                                  BgIII                 5′-T AAT ACG ACT CAC TAT AGG G-3′ ->
                 GCG TAG AGG ATC aga tct CGA TCC CGC GAA ATT AAT ACG ACT CAC TAT AGG GGA ATT GTG

                                         Xba I                   rbs           Nde I
                 AGC GGA TAA CAA TTC CCC tct aga AAT AAT TTT GTT TAA CTT TAA GAA GGA GAT ATA cat

                 1/1                                    31/11
                 Nde I
5′-G GAA TTC cat atg AAA TAC CTA TTG CCT ACG G -3′  32nt Tm=62°C SS-pelB-Fw-01
                 ATG AAA TAC CTA TTG CCT ACG GCA GCC GCT GGA TTG TTA TTA CTC GCg gcc cag ccg gcC
                 MET Lys Tyr Leu Leu Pro Thr Ala Ala Ala Gly Leu Leu Leu Leu Ala Ala Gln Pro Ala
                 -> pelB Leader

                 61/21                                  91/31
                 ATG GCC GAG GTG CAG CTG TTG GAG TCT GGG GGA GGC TTG GTA CAG CCT GGG GGG TCC CTG
                 Met Ala Glu Val Gln Leu Leu Glu Ser Gly Gly Gly Leu Val Gln Pro Gly Gly Ser Leu
                   Heavy ->
                 121/41                                 151/51
                 AGA CTC TCC TGT GCA GCC TCT GGA TTC ACC TTT AGC AGC TAT GCC ATG AGC TGG GTC CGC
                 Arg Leu Ser Cys Ala Ala Ser Gly Phe Thr Phe Ser Ser Tyr Ala Met Ser Trp Val Arg

                 181/61                                 211/71
                 CAG GCT CCA GGG AAG GGG CTG GAG TGG GTC TCA ACG ATT GGT GGT cAG GGT ACT CGG ACA
                 Gln Ala Pro Gly Lys Gly Leu Glu Trp Val Ser Thr Ile Gly Gly Gln Gly Thr Arg Thr

                 241/81                                 271/91
                 TTT TAC GCA GAC TCC GTG AAG GGC CGG TTC ACC ATC TCC AGA GAC AAT TCC AAG AAC ACG
                 Phe Tyr Ala Asp Ser Val Lys Gly Arg Phe Thr Ile Ser Arg Asp Asn Ser Lys Asn Thr

                 301/101                                331/111
                 CTG TAT CTG CAG ATG AAC AGC CTG AGA GCC GAG GAC ACG GCC GTA TAT TAC TGT GCG AAA
                 Leu Tyr Leu Gln Met Asn Ser Leu Arg Ala Glu Asp Thr Ala Val Tyr Tyr Cys Ala Lys

                 361/121                                391/131
                 ACG AGT CGG CCT TTT GAC TAC TGG GGC CAG GGA ACC CTG GTC ACC GTC TCG AGC GGT GGA
                 Thr Ser Arg Pro Phe Asp Tyr Trp Gly Gln Gly Thr Leu Val Thr Val Ser Ser Gly Gly
                                                                          G3S Linker ->
                 421/141                                451/151
                 GGC GGT TCA GGC GGA GGT GGC AGC GGC GGT GGC GGG TCG ACG GAC ATC CAG ATG ACC CAG
                 Gly Gly Ser Gly Gly Gly Gly Ser Gly Gly Gly Gly Ser Thr Asp Ile Gln Met Thr Gln
                                                               Light ->
                 481/161                                511/171
                 TCT CCA TCC TCC CTG TCT GCA TCT GTA GGA GAC AGA GTC ACC ATC ACT TGC CGG GCA AGT
                 Ser Pro Ser Ser Leu Ser Ala Ser Val Gly Asp Arg Val Thr Ile Thr Cys Arg Ala Ser

                 541/181                                571/191
                 CAG AGC ATT AGC AGC TAT TTA AAT TGG TAT CAG CAG AAA CCA GGG AAA GCC CCT AAG CTC
                 Gln Ser Ile Ser Ser Tyr Leu Asn Trp Tyr Gln Gln Lys Pro Gly Lys Ala Pro Lys Leu

                 601/201                                631/211
                 CTG ATC TAT CAT GCA TCC TCG TTG CAA AGT GGG GTC CCA TCA AGG TTC AGT GGC AGT GGA
                 Leu Ile Tyr His Ala Ser Ser Leu Gln Ser Gly Val Pro Ser Arg Phe Ser Gly Ser Gly

                 661/221                                691/231
                 TCT GGG ACA GAT TTC ACT CTC ACC ATC AGC AGT CTG CAA CCT GAA GAT TTT GCA ACT TAC
                 Ser Gly Thr Asp Phe Thr Leu Thr Ile Ser Ser Leu Gln Pro Glu Asp Phe Ala Thr Tyr

                 721/241                                751/251
                 TAC TGT CAA CAG GCT GCT GCG AAT CCT CCT ACG TTC GGC CAA GGG ACC AAG GTG GAA ATC
                 Tyr Cys Gln Gln Ala Ala Ala Asn Pro Pro Thr Phe Gly Gln Gly Thr Lys Val Glu Ile

                 781/261    Not I     XhoI              811/271
                 AAA CGG gcg gcc gcA ctc gag CAC CAC CAC CAC CAC CAC TAA TAA TGA CTA GTC AGC TGA
                 Lys Arg Ala Ala Ala Leu Glu His His His His His His *** *** ***
                                             -> 6 x His Tag
```

Figure 3-8. DNA and amino acid sequences of scFv J-20 in pET-22b(+) vector. The bold and underlined characters indicate the random sequences and CDRs. The primer T7-Pro-1 used for PCR are also shown. The TAG codon on the random sequence was mutated to CAG.

The target plasmid can be easily produced and extracted from the infectious *E. coli* TG1 cells. The cells infected with scFv J-20 phages were inoculated into 2xTY medium 1 mL containing ampicillin 100 µg / mL and glucose 1 %. This culture was incubated at 30 °C overnight while shaking. pIT2 vector containing scFv J-20 coding was purified using QIAGEN Plasmid Purification Kits and the plasmid stock was kept at −20 °C. The sequences of all constructs were verified by dye-terminator sequencing.[309–311] (Figure 3-6) Here, one stop codon TAG was found on a randomly generated sequence, which is translated to glutamine in *E. coli* TG1.[312] The codon was mutated to CAG using overlap-extension[313] mutation method and subcloned to pET-22b(+) vector. (Figure 3-7 and Figure 3-8) The vector was transformed into BL21(DE3) competent *E. Coli* cells.

The protein was expressed in periplasmic space of BL21(DE3) at 25 °C overnight in the LB medium containing ampicillin 100 µg / mL and glucose 0.2 % under the control of T7 promoter with Isopropyl β-D-1-thiogalactopyranoside (IPTG) 0.2 mg / mL (0.84 mM). After centrifugation at 2330 × g and 4 °C for 10 min to remove the *E. coli* cells, the protein was purified from the medium with Ni-NTA and Sephadex G-25 (GE Healthcare) columns. The purity and MW were characterized by sodium dodecyl sulfate–polyacrylamide gel electrophoresis (SDS-PAGE)[314] and gel permeation chromatography. The typical protein expression with LB 250 mL produces scFv J-20 antibody 2.5 mL with approximately 8 µM. The concentration of the antibody was calculated by the absorption at 280 nm (ε_0 = 38640 $M^{-1}cm^{-1}$ for secreted protein based on ExPASy[315]). The CD spectrum was measured and used to analyze the formation of protein secondary structure using BeStSel specially developed for β-structure selection.[316,317] The result showed that scFv J-20 antibody composes of antiparallel β-structure 39.7 %, others (loop in this case) 44.4 %, turn 14.3 % and α-helix 1.7 %, which is consistent to the structure of scFv antibody. (Figure 3-3) (Appendix)

Table 3-1. Summary of amino acid residues of scFv J-20 in total, only in CDRs and only randomly generated sequences.

Amino Acid	Total		CDRs		Random Sequences	
	Number	%	Number	%	Number	%
Gly	34	13.4	5	9.1	2	11.1
Ala	20	7.9	7	12.7	3	16.7
Val	12	4.7	1	1.8	0	0.0
Leu	18	7.1	2	3.6	0	0.0
Ile	8	3.2	2	3.6	0	0.0
Pro	10	4.0	3	5.5	2	11.1
Phe	9	3.6	2	3.6	1	5.6
Tyr	11	4.3	3	5.5	0	0.0
Trp	4	1.6	0	0.0	0	0.0
Ser	36	14.2	10	18.2	2	11.1
Thr	20	7.9	5	9.1	3	16.7
Cys	4	1.6	0	0.0	0	0.0
Met	4	1.6	1	1.8	0	0.0
Asn	5	2.0	2	3.6	1	5.6
Gln	16	6.3	5	9.1	1	5.6
Lys	9	3.6	1	1.8	0	0.0
Arg	11	4.3	3	5.5	2	11.1
His	7	2.8	1	1.8	1	5.6
Asp	8	3.2	2	3.6	0	0.0
Glu	7	2.8	0	0.0	0	0.0
Total	253		55		18	

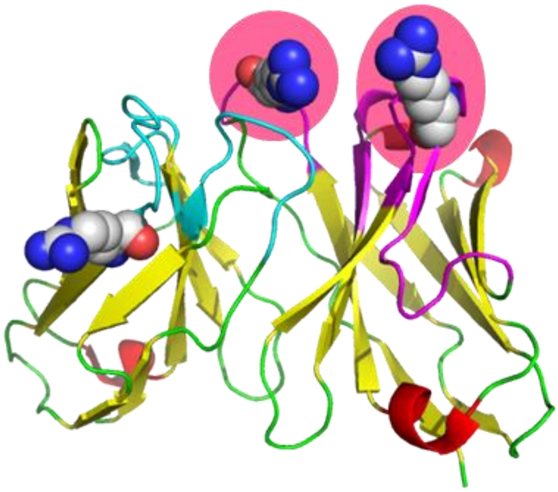

Figure 3-9 Location of 3 arginine residues in CDRs of scFv J-20. The randomly generated arginine residues, expected to interact with carboxylate groups of ACD3, are highlighted in pink.

It is possible that the main driving force of ACD3 binding scFv J-20 antibody is hydrophobic interactions. However, the discrimination among different ACDs is the position of 2 carboxylate groups. Therefore, the electrostatic interactions must exist on the binding site, which will determine the location of carboxylate groups. As it is in aqueous solution with pH 7.5, the carboxylate groups will have strong electrostatic interactions toward basic amino acids. There are 1 lysine and 3 arginine residues in CDRs of scFv J-20 (Table 3-1), and 2 arginine residues generated from random codons are located nearby each other. (Figure 3-9) This region is expected to be the binding site of ACD3 during phage display panning.

3.5 Interactions of scFv J-20 Antibody to 2-Anthracenecarboxylate and Dimers

Although the selective binding of the phage clone J-20 to ACD3 is high, the properties of free antibody (not on the membrane of the phages) should be confirmed. From ACDs to AC, the interactions of antibody are discussed.

3.5.1 Ground-State Interaction between Antibody and ACD Isomers

There is a chance that antibodies in the solution will have the different binding properties as the ones on the phage particles. Therefore, the binding properties of scFv J-20 were tested with ACDs mixture. Unlike the hybrid nanoribbons, the antibodies are stable in the maximum concentration of 10^{-6} M, and they have strong UV absorptions and CD spectra up to 300 nm due to amino acid side chains.[318,319] Therefore, the qualitative binding property was observed by simply adding ACD mixture stock to scFv J-20 in Tris HCl 20 mM buffer pH 7.5 containing NaCl 150 mM (TBS), filtering scFv J-20 using protein filter (Millipore), and analyzing the free ACD mixture left in the filtrate. The filtrate was diluted by acetonitrile before injecting to HPLC analysis equipped with chiral column and fluorescence detector (excitation 254 nm, emission 420 nm).[286] The control chromatogram was prepared in the same way but using only TBS instead of scFv J-20 in TBS.

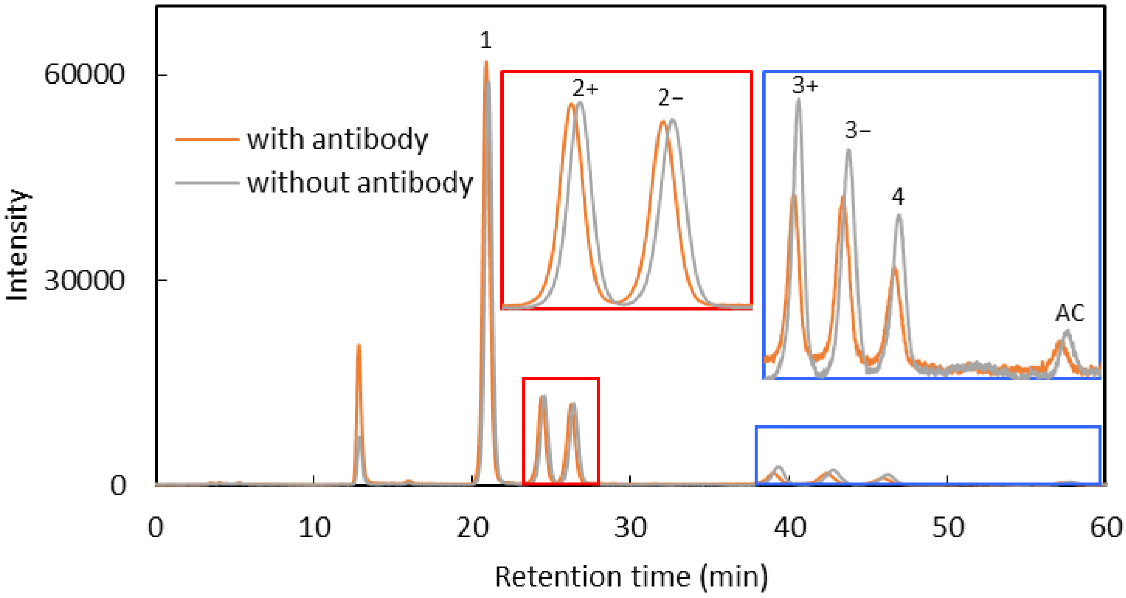

Figure 3-10. Analystical HPLC (fluoresence) of free ACDs in the solution with scFv J-20 (orange) and control (grey). The number 1 to 4 indicates ACD1 to ACD4, while + and − indicate the different enatiomer.

The chromatograms were normalized by the peaks of ACD2. Clearly, the proportions of ACD3 and ACD4 in free solution after mixed with scFv J-20 are reduced. (Figure 3-10) Although the absolute binding affinity cannot be calculated, it is clear that the scFv J-20 antibody has a higher binding affinity to *head-to-head* dimers than *head-to-tail* dimers.

3.5.2 Ground- and Excited-State Interactions Between Antibody and AC

Using ACD3 as a target molecule in phage display technique, it is not certain that scFv J-20 can also bind AC monomer. If it cannot, scFv J-20 can only be used for ACD3 and ACD4 purification, which is not the main objective of this research. Therefore, the interactions between scFv J-20 and AC must be inspected. In the case of serum albumins having high stability at 10^{-5} M, the CD titration is used to determine the binding affinity to AC.[244,245] In the case of scFv J-20, the CD titration was also attempted, but only the decrease of the original CD of antibody was observed similar to ACD case, which means the binding constant could not be quantitatively analyzed by this technique. However, the qualitative study was conducted similarly to the case of scFv J-20 and ACDs, but analyzed by simple fluorimeter. The AC stock was added to scFv J-20 in TBS in the ratio 2 to 1, the solution was filtered by protein filter, and the filtrate was analyzed by fluorescent emission spectroscopy. The control sample was prepared with the same manner using only TBS instead of scFv J-20 in TBS.

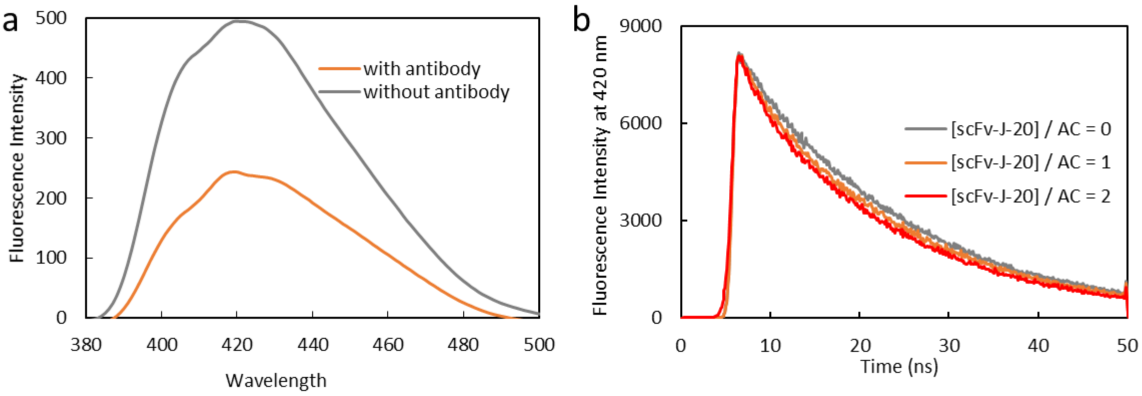

Figure 3-11. (a) Fluorescence spectra of free AC in the solution with scFv J-20 (orange) and control (grey). The excitation wavelength was 365 nm with 5 nm bandwidth, the emission bandwidth was 3 nm, the pathlength for excitation was 0.2 cm and for emission was 1.0 cm, and the sensitivity was set to high with 1 s respense. (b) The fluorescence decay spectrum of AC in the presence of scFv J-20 antibody. The excitation laser was 390 nm, the detection was at 420 nm, and the AC and scFv J-20 ratios were 1 µM : 0 µM, 2 µM : 2 µM and 1 µM : 2 µM.

The filtrate from AC and scFv J-20 mixture showed fluorescence intensity of 243 a.u., while the control experiment has fluorescence intensity of 495 a.u. at 420 nm. (Figure 3-11 a) The concentration of AC used was 17 µM, which was low enough to estimate the linear relationship between concentration and fluorescence intensity.[283] Meaning, half of AC was efficiently bound to scFv J-20, which is high considering the fact that AC was not used as a target for phage display panning.

The fluorescence lifetime measurement was used to study the excited-state interactions. The fluorescence lifetime of AC was measured in the presence of the scFv J-20 antibody in different ratios. From the decay graph (Figure 3-11 b), the decay curve can be fitted to the following equation.

$$I(t) = A_1\, e^{-t/\tau_1} + A_2\, e^{-t/\tau_2} \tag{3-1}$$

I(t) is fluorescence intensity with function of time, *t* is time, and A_1 and A_2 are the contribution of τ_1 and τ_2. In this case, 2 lifetime decays are considered.

Table 3-2. Fluorescence lifetime components of AC in the presence of scFv J-20.

[scFv-J-20] / [AC]	τ_1 (ns)	A_1	τ_2 (ns)	A_2	χ^2
0	18.1	1.00	-	-	1.18
1	17.9	0.90	1.60	0.10	1.20
2	17.7	0.86	1.66	0.14	1.05

From equation (3-1), the lifetimes of AC in the presence of scFv J-20 can be calculated. The fitting shows second component with a short lifetime decay in the presence of scFv-J-20 antibody (Table 3-2), suggesting the microenvironmental changes of AC. This can be due to the hydrophobic environment in scFv J-20 antibody cavity, fluorescence quenching by tryptophan composed in scFv

J-20 antibody or the promotion of AC photocyclodimerization.[245,250] Either way, this result shows that AC molecules are incorporated in the confined cavity of scFv J-20 antibody.

3.6 Supramolecular Regio- and Enantioselective [4+4] Photocyclodimerization of 2-Anthracenecarboxylate Using Synthetic scFv Antibody

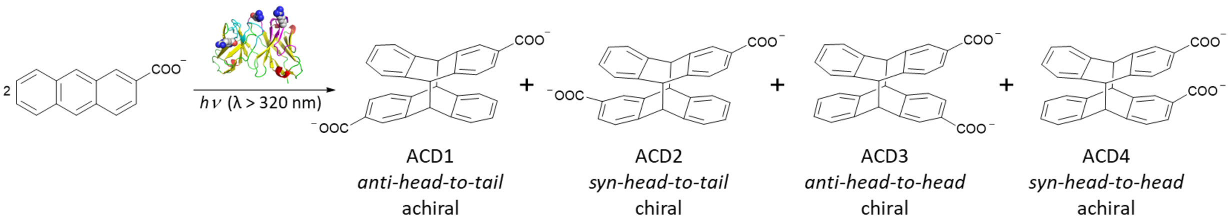

Figure 3-12 Supramolecular regio- and enantioselective [4+4] photocyclodimerization of AC using scFv J-20 antibody as a chiral host.

After confirming the ground- and excited-state interactions to AC and ACDs, the scFv J-20 antibody was used as a chiral host for supramolecular [4+4] photocyclodimerization of AC. (Figure 3-12) The reactions were carried out using different ratios of scFv J-20 and AC. The optimized external factors, photochemical reaction conditions, are also described.

3.6.1 Photocyclodimerization of AC Using scFv J-20 and Analysis of ACD Products

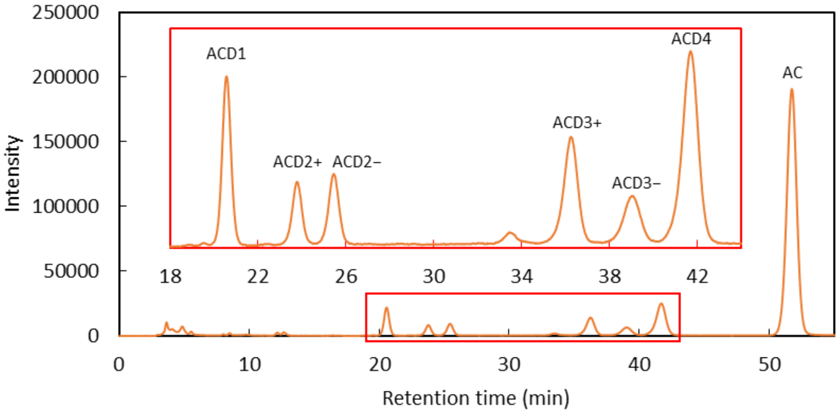

Figure 3-13. Analytical HPLC (fluoresence) of supramolecular [4+4] photocyclodimerization of AC mediated by scFv J-20 antibody. AC concentration was 5.0 µM and scFv J-20 antibody concentration was 2.5 µM.

The photocyclodimerization was conducted by irradiating the mixture of AC and scFv J-20 antibody in TBS. The scFv J-20 antibody stocks were freshly prepared. TBS was bubbled by Ar to reduce the oxygen in the solution. The AC 5.0 µM was mixed with scFv J-20 antibody 0 to 5.0 µM. The mixture was incubated at room temperature for 30 min before irradiation. The sample was irradiated for 1 h at 20 °C. The light source for irradiation was xenon lamp 500 W with the glass filter to give only light with the wavelength longer than 320 nm (340 nm longpass filter). At this wavelength, only AC absorb the light. Therefore, ACDs photodissociation or protein photo-denaturation are negligible. The scFv J-20 antibody was denatured by adding acetonitrile with the same volume as the original solution. The solution was incubated overnight and filtered. The filtrate was analyzed by HPLC. (Figure 3-13) The product distribution and ee of each ACD were calculated based on the integration of HPLC peaks. Here, + and − sign of % ee refer to the first and second elution of the ACD2 and ACD3, which correspond to *(M)*- and *(P)*-isomer of both dimers.[22]

Table 3-3. Photocyclodimerization of AC mediated by scFv J-20 antibody.

[AC] / [scFv-J-20]	% Product Distribution				% ee		% *head-to-head*
	ACD1	ACD2	ACD3	ACD4	ACD2	ACD3	
∞	41.4	34.0	14.5	10.1	0	0	24.6
4	20.2	15.5	27.1	37.2	+6	+32	64.3
3	18.4	13.8	27.5	40.3	+9	+36	67.8
2	13.8	12.5	30.0	43.7	+8	+38	73.7
1	8.4	7.8	32.4	51.4	−40	+41	83.8

AC concentration is 5.0 μM. scFv J-20 antibody concentration is 0 to 5.0 μM. The mixture was incubated at room temperature for 30 min. The irradiation was conducted at 20 °C for 1 h using xenon lamp 500 W equipped with 320 nm longpass glass filter.

As mentioned in chapter 2, the *head-to-tail* products (ACD1 and ACD2) are relative favorable comparing to the *head-to-head* products (ACD3 and ACD3), especially in aqueous solution. However, the existence of scFv J-20 antibody significantly increased the product distribution of ACD3 and ACD4 from 14.5 % and 10.1 % to 32.4 % and 51.4 %, increasing the *head-to-head* product distribution for 3.4 times. Not only product distribution, but also the ee of ACD2 and ACD3 were observed at 40 % and 41 %. It is important to disclaim that the product distribution of ACD2 was low, so the 40 % ee analysis was not as accurate as of ACD3.

The assumption that ground-state interactions between scFv J-20 antibody and AC was crucial to achieve the contribution of scFv J-20 antibody as a chiral reaction media in photocyclodimerization was undoubtedly demonstrated with these results. From previous section, the ground-state interactions between scFv J-20 antibody and AC showed not perfect binding affinity. Half of AC was found in the filtrate even though the ratio of AC to scFv J-20 antibody was 2 to 1, suggesting not complete binding. Also, the contribution of short decay component in excited-state interactions was only 10 %. Consequently, even in the case of 1 to 1 ratio, there are also ACD1 and ACD2, likely to be produced from the dimerization of AC in the solution rather than inside the cavity of scFv J-20 antibody. In addition, the ELISA test and ground-state interactions study showed that the scFv J-20 antibody has high binding affinity to not only ACD3, but also ACD4, which is the cause of the increase of ACD4 product distribution, too.

Another unexpected result is that *(P)*-ACD3 was produced by this antibody, but the *(M)*-ACD3 was used as a target for antibody phage display. So, the result does not exactly follow the plan. It might be the nature of proteins that the cavity is more favorable for *(P)*-ACD3. For example, mammalian serum albumins usually produce *(P)*-ACD3, which can be a serious limitation.[246] On the other hand, the anisotropy of ACD3 production solely comes from the nature of phage library. Therefore, by utilizing racemic ligand for phage display, there is a great chance to observe the ee from the supramolecular asymmetric reactions mediated by obtained synthetic antibodies.

3.6.2 **Effects of External Factors to Photocyclodimerization**

Even though the significant improvement in regio- and enantioselectivity is clear, the product distribution and ee are still far from practical uses. There are 3 components which can improve the results of this strategy, antibody phage libraries, ligand and external factors. The antibody libraries can be improved by optimizing the antibody structures and random sequences. However, the antibody phage library is usually custom made, so it is difficult to access any new libraries. In addition, it is also difficult to predict the performance of the new libraries with present computational techniques. For the ligand, the new design will be discussed in chapter 4. Here, the optimization of external factors, photochemical reaction conditions, is explained.

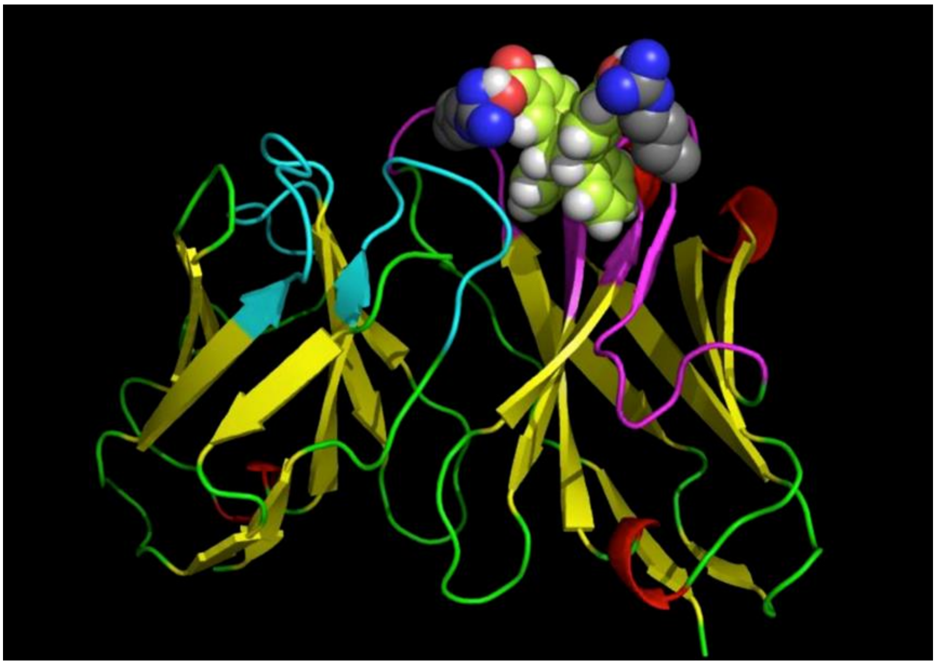

Figure 3-14. Docking model of ACD3 and scFv J-20 antibody. (Software: PyMOL)

According to the docking model (Figure 3-14), the positions of the randomly generated arginine residues on CDR are similar to the distance between carboxylate groups of ACD3. Therefore, these two arginine residues may provide electrostatic interactions to ACs, resulting in the discrimination of the production among ACDs. Unfortunately, they are located at the outer space of the antibody, a high microenvironmental polarity region. The interactions between carboxylate group of AC and guanidino group of arginine are disturbed by the solvation of water and ions in the solution, giving different possibilities of AC orientation in the cavity. Hence, not only *(P)*-ACD3, but also antipodal *(M)*-ACD3 and another *head-to-head* product, ACD4, were produced competitively.

Assuming that the origin of this limitation is the location of the arginine residues, there are two solutions: obtaining new antibody having the arginine residues located inside the cavity, and increasing the interactions between arginine residues and AC. The strategy in obtaining new antibodies is related to the new ligand design in the next chapter. The external factors, however, can be applied to increase the specific orientation of AC molecules in the cavity, especially when the reaction site is located at the outside of the antibody. 4 factors were studied: temperature, time, pH and salt. The knowledge of the effects from these factors are useful not only to this system but also bio-molecular reaction hosts in general.

Table 3-4. Temperature-dependent photocyclodimerization of AC mediated by scFv J-20 antibody.

[AC] / [scFv-J-20]	Temperature	% Product Distribution				% ee		% *head-to-head*
		ACD1	ACD2	ACD3	ACD4	ACD2	ACD3	
∞	rt	41.4	34.0	14.5	10.1	0	0	24.6
4	20 °C	20.2	15.5	27.1	37.2	+6	+32	64.3
	4 °C	13.7	12.3	28.8	45.3	−11	+38	74.1
3	20 °C	18.4	13.8	27.5	40.3	9	+36	67.8
	4 °C	10.2	9.7	30.5	49.5	−15	+41	80.0
2	20 °C	13.8	12.5	30.0	43.7	8	+38	73.7
	4 °C	5.3	4.4	32.7	57.6	−27	+43	90.3
1	20 °C	8.4	7.8	32.4	51.4	−40	+41	83.8
	4 °C	3.3	3.6	34.9	58.1	−45	+43	93.0

AC concentration is 5.0 μM. scFv J-20 antibody concentration is 0 to 5.0 μM. The mixture was incubated for 0.5 to 1 h. The solution was irradiated for 1 h using xenon lamp 500 W equipped with 320 nm longpass glass filter.

The [4+4] Photocyclodimerization of AC mediated by scFv J-20 antibody was conducted in the same protocol, but the incubation and irradiation temperature at 4 °C was carried out. The reduction of temperature shows small increase of ACD3 product distribution, moderate increase of ee, but significant increase of ACD 4, causing the *head-to-head* product distribution to be more than 90 %. (Table 3-4) The possible reasons are the stability of antibody and at low temperature and/or the motions of antibody. Moreover, this result also corresponded to the previous study about the entropy-controlled asymmetric photochemistry.[320] Hence, the temperature is an important factor for protein as a regio- and enantioselective template.

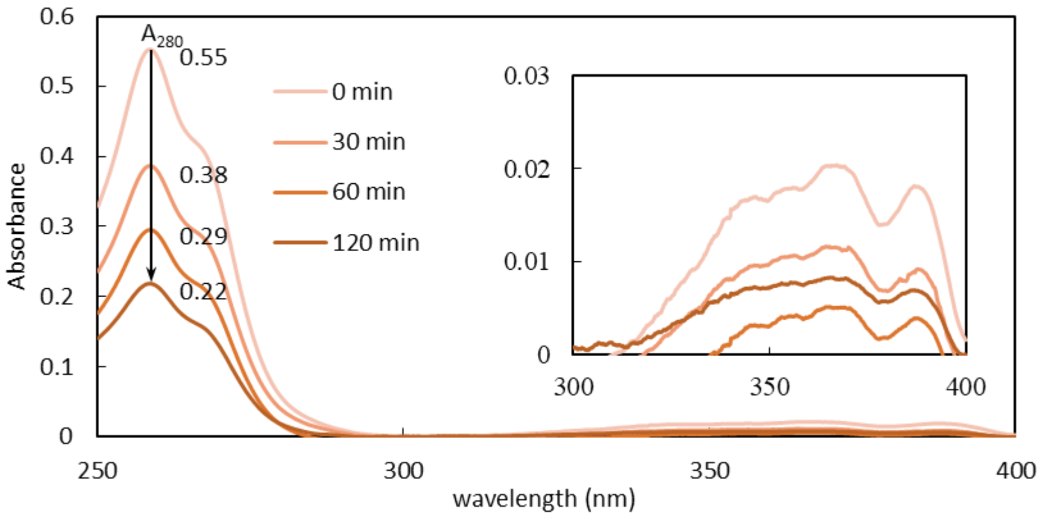

Figure 3-15. UV-Vis absorption spectra of photocyclodimerization solution of AC 5.0 μM mediated by scFv J-20 antibody 2.5 μM after different irradiation time (0 - 120 min). The conditions are described in table 3-5.

Table 3-5. Irradiation-time-dependent photocyclodimerization of AC mediated by scFv J-20 antibody.

Time (min)	% Product Distribution				% ee		% *head-to-head*
	ACD1	ACD2	ACD3	ACD4	ACD2	ACD3	
30	8.4	6.5	31.0	54.2	−5	+46	85.2
60	5.3	4.4	32.7	57.6	−27	+43	90.3
120	6.2	5.1	32.4	56.2	−10	+45	88.6

AC concentration is 5.0 µM. scFv J-20 antibody concentration is 2.5 µM. The mixture was incubated for 1 h at 4 °C. The solution was irradiated at 4 °C using xenon lamp 500 W equipped with 320 nm longpass glass filter.

Next, the effects of irradiation time were investigated. The absorbance at 387 nm is too low to be accurately determined, so the absorbance at 280 nm was used instead. (Figure 3-15) Both AC and ACDs can absorb at this wavelength, but AC has significantly higher molar extinction coefficient. Therefore, the absorption decreases with the increase of irradiation time. There is not much difference in product distribution and ee. The 60 min irradiation time has slightly higher regioselectivity than the others. Therefore, the irradiation time is set at 60 min in the other experiments.

Table 3-6. pH-dependent photocyclodimerization of AC mediated by scFv J-20 antibody.

pH	% Product Distribution				% ee		% *head-to-head*
	ACD1	ACD2	ACD3	ACD4	ACD2	ACD3	
7.5	5.3	4.4	32.7	57.6	−27	+43	90.3
8.0	4.1	4.5	33.6	57.8	−20	+48	91.4
8.5	6.4	6.4	31.5	55.8	−26	+46	87.3

AC concentration is 5.0 µM. scFv J-20 antibody concentration is 2.5 µM. The mixture was incubated for 1 h at 4 °C. The solution was irradiated for 1 h at 4 °C using xenon lamp 500 W equipped with 320 nm longpass glass filter.

The pH dependency was studied by changing the pH of TBS. Normally, the pH of TBS is 7.5, but the higher pH buffer solutions were prepared. Here, the scFv J-20 stocks were prepared separately with different TBS. In this range of pH 7.5 to 9.0, the electrostatic interactions should remain unchanged because the pK_a of AC and arginine are 4.2 and 12.5, respectively.[289] However, at pH 8.0, the ee of ACD3 increased to 48 %. (Table 3-6) The cause of this moderate improvement might be the conformational change of scFv J-20 antibody, which pI was estimated to be 9.03 (ExPASy[315,321,322]). Thus, the net charge of protein is closer to neutral, and the hydrophobicity of the antibody was increased, inducing more compact conformation, reducing the microenvironmental polarity of the reaction site because the arginine residues are more enclosed inside the antibody. As a result, there was a slight improvement of ee.

On the other hand, at pH 8.5, the hydrophobicity of the scFv J-20 antibody causes the aggregation, and the result turned to be slightly worse, especially the decrease of % *head-to-head*. The aggregation can suppress the binding affinity of proteins, so the *head-to-tail* dimers, assumed to be formed in the solution, increase. This postulation was supported by the failure of the scFv J-20 antibody harvesting in TBS at pH 9.0 probably due to the aggregation. So, the effects of pH are complicated yet important for improving the supramolecular asymmetric synthesis mediated by any proteins or biomolecules.

Table 3-7. Salt-dependent photocyclodimerization of AC mediated by scFv J-20 antibody.

Salt		Ionic Strength (mM)	% Product Distribution				% ee		*% head-to-head*
Type	Concentration (mM)		ACD1	ACD2	ACD3	ACD4	ACD2	ACD3	
NaCl	75	95	6.5	7.2	32.9	53.4	−18	+33	86.3
	150	170	5.3	4.4	32.7	57.6	−27	+43	90.3
	500	520	9.9	9.5	32.2	48.6	−9	+46	80.8
KCl	75	95	7.2	6.1	31.2	55.5	−30	+36	86.7
	500	520	6.9	6.8	33.1	53.6	−5	+42	86.7

AC concentration is 5.0 µM. scFv J-20 antibody concentration is 2.5 µM. The mixture was incubated for 1 h at 4 °C. The solution was irradiated for 1 h at 4 °C using xenon lamp 500 W equipped with 320 nm longpass glass filter.

Another factor is the salt in buffer. Usually for scFv antibody, TBS contains NaCl 150 mM. In this experiment, TBS (pH 7.5) with different salt concentration and types were prepared and used for antibody harvesting. The ionic strength can be calculated from the following equation.

$$Ionic\ Strength = \frac{1}{2}\sum_{i=1}^{n} c_i z_i^2 \tag{3-2}$$

c_i is the molar concentration of each ion, and z_i is the charge of each ion. Considering the relative low concentration of HCl used for adjusting the pH of the buffer and the low concentration of AC, the ionic strength can be estimated from the Tris HCl concentration (20 mM) and salt concentration (75-500 mM). (Table 3-7)

The result of 500 mM NaCl (ionic strength 520 mM) showed the slight increased ee of ACD3. This improvement was assumed to be the result of the ionic strength of NaCl in the solution, limiting the motion of the antibody. However, the high concentration of NaCl also interrupts the interactions between AC and arginine, so the product distributions of ACD1 and ACD2 increase. Changing the types of salt to KCl do not show any significant effects to the photocyclodimerization products at 75 mM. However, they are quite different at 500 mM concentration. In KCl 500 mM, the head-to-head product distribution is higher than NaCl 500 mM, but the ee is slightly lower. Therefore, not only the ionic strength but also the type of ions also affects the photochemical reaction.

3.6.3 Organic Solvent Toleration of scFv J-20 Antibody During Photocyclodimerization

A mixture of water and organic solvents can increase the solubility of most of starting material of chemical reactions, so the toleration of scFv J-20 antibody to ethanol and dimethyl sulfoxide were studied because both of the solvents have UV cut-off lower than 280 nm, and they are miscible in water. Apart from the product distribution and ee, the conversion rate should also be compared, but because the concentration is too low, the absorbance at 387 nm cannot be quantified. Even though the reduction of the absorbance at 280 nm does not represent the real conversion, it is still a good indication to compare the relative conversion (similar to time-dependent study). In addition, the preparation for HPLC analysis was changed. The solvent incompatibility from ethanol and dimethyl sulfoxide caused the duplication of HPLC peaks. Thus, after denaturation by acetonitrile, the solvent exchange using monolithic silica extraction tips was used instead of simple filtration.

Table 3-8. Photocyclodimerization of AC mediated by scFv J-20 antibody in the solution of TBS mixed with ethanol and dimethyl sulfoxide.

Mixed Solvent		% Product Distribution				% ee		% *head-to-head*	A_{280} reduction
Type	%	ACD1	ACD2	ACD3	ACD4	ACD2	ACD3		
None*	-	13.8	12.5	30.0	43.7	+8	+38	73.7	48.6 %
Ethanol	10	18.2	18.3	30.4	33.0	0	+37	63.4	38.3 %
	20	32.7	29.3	20.9	17.0	+2	+27	37.9	29.1 %
	30	34.9	31.4	22.4	11.3	+6	+5	33.7	24.0 %
	40	30.7	32.1	22.9	14.4	+4	+4	37.3	19.3 %
DMSO	5	19.8	15.4	27.2	37.7	+6	+36	64.9	39.6 %
	10	29.2	23.1	22.7	24.9	+5	+25	47.6	30.8 %
None* no antibody	-	41.4	34.0	14.5	10.1	0	0	24.6	n.d.

AC concentration is 5.0 µM. scFv J-20 antibody concentration is 2.5 µM. The base solvent is TBS pH 8.0. The mixture was incubated for 1 h at 10 °C. The solution was irradiated for 1 h at 10 °C using xenon lamp 500 W equipped with 320 nm longpass glass filter. *Pure TBS pH 7.5 and at 20 °C

As expected, % ee and % *head-to-head* decreased with the increase of organic solvent concentration. (Table 3-8) At ethanol 10 % and dimethyl sulfoxide 5 %, the ee of ACD3 slightly decreases. In contrast, the regioselectivity is greatly affected. The % *head-to-head* reduced to less than 65, and it becomes less than half at double concentration for both solvents. The existence of organic solvents affects the regioselectivity more than enantioselectivity. Still, with ethanol 30 %, the ee drastically reduced to almost 0. Interestingly, A_{280} reduction also decreased when adding ethanol and dimethyl sulfoxide. Both of organic solvents do not absorb at the irradiated wavelength, so the decrease of A_{280} reduction is from the protein denaturation. At the same time, this means scFv J-20 antibody increases the AC photocyclodimerization efficiency. Also, the tertiary structure of scFv J-20 is crucial to provide the appropriate cavity for reaction.

3.7 Conclusion

To obtain synthetic antibody from phage display screening, ACD3-PEG5-Lys(Biotin) ligand containing ACD3 as a target product was synthesized from solid-phase synthesis. After 3 rounds of panning and ELISA screening of 96 phage clones, 2 and 6 candidates having binding affinity to ACD3 were isolated from Tomlinson I and J libraries, respectively. From the competitive ELISA screening, J-20 candidate showed high selectivity to *head-to-head* over *head-to-tail* ACDs. The randomly generated STOP codon was mutated, the target DNA was subcloned into pET-22b(+) vector, and the synthesis and purification of scFv J-20 antibody was achieved by protein expression in *E. coli* BL21(DE3) cells using Ni-NTA and Sephadex G-25. The amino acid sequence of the scFv J-20 was determined. Together with the human scFv structure from the protein database, the binding site of ACD3 was located based on the position of arginine residues.

The ground-sate interaction between scFv J-20 antibody and ACD3, and the ground- and excited-state interaction between scFv J-20 antibody and AC were observed. Although, the quantitative analysis was not successfully conducted, the existence of AC-antibody complex was explicit. In the existence of scFv J-20 antibody, supramolecular regio- and enantioselective [4+4] photocyclodimerization of AC clearly occurred. The product distributions of ACD3 and ACD4, which are less favorable in an aqueous solution, increased to 32.4 % and 51.4 %. Also, 41 % ee of ACD3 was found. This efficient increase of product distributions and ee proved the possibility on our proposed strategy, supramolecular regio- and enantioselective photoreactions mediated by synthetic antibody obtained from phage display technique. Moreover, the photochemical reaction conditions, including AC to scFv J-20 antibody ratio, pH, temperature, time and salt, were optimized.

Even though each of these factors did not show strong improvement on the photocyclodimerization, the synergistic effects of pH and temperature significantly improved the result. The ee and product distribution of ACD3 can be increased to 48 % and 33 %, respectively. In addition, % *head-to-head* ratio was maximized to 91 %. From these results, the cause of moderate product distribution and ee of ACD3 is likely to be the high microenvironmental polarity of arginine residues at the reaction sites, leading to the different strategies for enhancing the interactions between arginine and AC by optimizing effects of external factors, photochemical reaction conditions, which is important to not only synthetic antibody but also any supramolecular reactions mediated by biomolecules.

3.8 Experimental Procedure

3.8.1 Synthesis of ACD3-PEG-5-Lys(Biotin) Ligand

The ACD3-PEG-5-Lys(Biotin) ligand was synthesized by the solid-phase stepwise elongation of Fmoc-amino acids. Novasyn TGR resin (Novabiochem) 22 mg (5 µmol) was placed into the empty column PD-10 with the filter (GE Healthcare) and washed by dimethylformamide 2 mL 5 times and piperidine 20 % in *N*-methyl-2-pyrrolidone 2 mL. The resin was incubated in piperidine 20 % in *N*-methyl-2-pyrrolidone 2 mL for 20 min, and washed again by dimethylformamide 2 mL × 5 times. The mixture of Fmoc-Lys(Biotin)-OH 31 mg (52 µmol, 10 eq), HATU 23 mg (60 µmol, 10 eq), and HOAt 7.7 mg (57 µmol, 10 eq) dissolved in DIEA 18 µL and *N*-methyl-2-pyrrolidone 500 µL was added to the resin and incubated for 20 min.

The solution was removed by filtration, and the resin was washed by dimethylformamide 2 mL 5 times. The Kaiser test was conducted, and the resin was washed by piperidine 20 % in *N*-methyl-2-pyrrolidone 2 mL. The resin was incubated in piperidine 20 % in *N*-methyl-2-pyrrolidone 2 mL for 20 min, and washed again by dimethylformamide 2 mL 5 times. The absorption at 301 nm of the combined filtrate from the piperidine 20 % in *N*-methyl-2-pyrrolidone washing step was measured and the amount of the removed Fmoc was calculated (4.6 µmol). The resin was washed again by dimethylformamide 2 mL 5 times. The mixture of Fmoc-NH-PEG5-COOH 1 M 50 µL (50 µmol, 10 eq), HATU 19.9 mg (52 µmol, 10 eq) and HOAt 7.5 mg (55 µmol, 10 eq) dissolved in DIEA 18 µL and *N*-methyl-2-pyrrolidone 500 µL was added to the resin and incubated for 25 min.

The solution was removed and the resin was washed by dimethylformamide 2 mL 5 times. The Kaiser test was conducted, and the resin was washed by piperidine 20 % in *N*-methyl-2-pyrrolidone 2 mL. The resin was incubated in piperidine 20 % in *N*-methyl-2-pyrrolidone 2 mL for 20 min, and washed again by dimethylformamide 2 mL 5 times. The absorption at 301 nm of the combined filtrate from the piperidine 20 % in *N*-methyl-2-pyrrolidone washing step was measured and the amount of the removed Fmoc was calculated (4.04 µmol). The resin was washed again by dimethylformamide 2 mL 5 times. The solution of enantiopure (*P)*-ACD3 provided by M. Nishijima and G. Fukuhara 5.4 mg (12 µmol, 2 eq) in dimethyl sulfoxide 250 µL was added to the solution of HATU 6.0 mg (15 µmol, 3 eq) and HOAt 2.3 mg (17 µmol, 3 eq) in DIEA 11 µL and NMP 500 µL. The mixed solution was added to the resin and incubated for 2 h.

The solution was removed by filtration, and the resin was washed by dimethylformamide 2 mL. The filtrate was kept, and the resin was washed by dimethylformamide 2 mL 5 times, chloroform 2 mL 5 times, and ethanol 2 mL 5 times, respectively. The column was blown by Ar gas for 1 min and dried under vacuum overnight. The synthesized ligand was cleaved from the dried resin (25.5 mg) by stirring with phenol 0.25 g, trifluoroacetic acid 5 mL, water 250 µL and triisopropylsilane 250 µL at room temperature for 2 h. The reaction solution was transferred back to the column and filtered. The filtrate was evaporated to obtain small amount of colorless liquid. The ether was added to the residue and the solution was centrifuged at 2330 × g and 4 °C for 10 min. The supernatant was removed and the same procedure was repeated. The pellet was dried under vacuum for 1 h and dissolved in acetonitrile 300 µL and acetic acid 700 µL.

Table 3-9. Parameters for RP-HPLC for ACD3-PEG5-Lys(Biotin) ligand purification and analysis.

Parameters	Purification Condition	Analysis Condition
HPLC Equipment	SHIMADZU	JASCO
Column	5C$_{18}$-AR-II 10.0ID × 250 mm	5C$_{18}$-AR-II 4.6ID × 150 mm
Temperature	Room Temperature	40 °C
Injection Volume	50 - 300 µL	6 µL
Solvent	Acetonitrile (0.08 % TFA) Water (0.10 % TFA)	Acetonitrile (0.08 % TFA) Water (0.10 % TFA)
Gradient	30 - 60 % Acetonitrile 0 - 30 min	30 - 60 % Acetonitrile 0 - 30 min
Flow Rate	3 mL / min	1 mL / min
Detector	UV 260 nm	UV 260 nm

A crude ACD3-PEG5-Lys(Biotin) ligand was purified and analyzed with RP-HPLC. (Table 3-9) The purity was calculated to be 80 % base on the analysis of purified ligand (Appendix). The purified ACD3-PEG5-Lys(Biotin) was dried by evaporator and lyophilized to obtain a white solid. It was dissolved in acetonitrile 50 % (aq) 200 µL to afford 370 µM ACD3-PEG5-Lys(Biotin) ligand solution stock, which was stored at −20 °C. MS (ESI-TOF) m/z: $[M + H]^+$ Calcd for $C_{61}H_{76}N_6O_{13}S$ 1133.37; Found 1133.64.

3.8.2 **Kaiser Test**

The Kaiser test was performed by mixing phenol 4 g / mL in ethanol 20 µL, potassium cyanide 13 mg / mL in ethanol 20 µL, ninhydrin 50 mg / mL in ethanol 20 µL and small amount of the resin. The solution was mixed by tapping and heating in hot water (near 100 °C). If the color turns to blue or purple (positive result), it indicates the uncoupled amino group on the resin. In that case, the coupling will be repeated. However, all the tests showed negative results in this chapter.

3.8.3 **Solution Phase Panning Procedure**

The solution phase panning procedure was performed using streptavidin-conjugated paramagnetic beads (Promega). The beads (0.6 mL suspension) were incubated in Protein-Free (TBS) blocking buffer 1 mL (Piercs) at 4 °C for 1 h and washed with Tris HCl 50 mM buffer containing NaCl 150 mM and Tween-20 (TBST) 0.1 % with pH 7.5 (TBST 0.5 % for the following rounds) 1 mL 4 times. The phages (3.4×10^9, 4.2×10^{11}, 3.2×10^3 pfu for 1st, 2nd, 3rd round, respectively for Tomlinson I library; 4×10^9, 5.2×10^9, 5.4×10^9 pfu for 1st, 2nd, 3rd round, respectively for Tomlinson J library) were incubated with ACD3-PEG5-Lys(Biotin) ligand (1, 0.1, 0.01 µM for 1st, 2nd, 3rd round, respectively) in TBST (0.1 % for 1st round and 0.5 % for the following rounds) at 25 °C for 30 min.

The phages and ACD3-PEG5-Lys(Biotin) mixture was added to the beads and incubated at room temperature for 20 min. The beads were pelleted by centrifugation in a low-speed benchtop centrifuge and captured by a magnetic stand. The unbound phages in the supernatant were removed and the target-bound beads were washed 10 times with TBST (0.1 % for 1st round and 0.5 % for the following rounds). Free ACD3 10 µM in Tris HCl buffer containing NaCl 150 mM (TBS) 500 µL was added to the beads and incubated at room temperature for 1 h to elute the phages. The beads were pelleted by centrifugation in a low-speed benchtop centrifuge and the solution contained recovered phages was isolated from the beads on magnetic stand, and this procedure was repeated again to ensure the complete removal of the beads. The recovered phages were submitted to a titering procedure for quantification and amplified for the next round.

Before the panning procedure of the 2nd and 3rd rounds, the negative selection was conducted. The streptavidin magnetic beads (0.6 mL suspension) were incubated in Protein-Free (TBS) blocking buffer 1 mL at 4 °C for 1 h and washed with TBST 0.5 % 1 mL 4 times. The phages in TBS 200 µL, and TBST 2.5 % 50 µL were added to the beads. The solution was incubated at room temperature for 30 min. The supernatant containing phages, which did not bind to streptavidin beads, was separated from the beads by transferring to the new tube on magnetic holder. The separation was repeated to ensure the complete removal of the beads. The phages were then subjected to the solution phase panning procedure mentioned above.

3.8.4 **Phage Titering**

E. coli TG1 cells were grown in 2xTY medium at 37 °C until reaching 0.4 of OD at 600 nm. Recovered phages after each panning (250 µL) were added to the TG1 culture 1.75 mL and incubated at 37 °C for 30 min without shaking, allowing phages to infect to TG1 cells. The incubated media 5 µL was diluted by 2xTY medium 495 µL, making a serial dilution of factors of 100. Each dilution (10 µL) was plated on a LB agar plate containing ampicillin 100 µg / mL and glucose 1 %, and incubated at 37 °C overnight. The number of colonies was counted to determine the quantity of infectious phages.

3.8.5 **Amplification of Recovered Phage**

The infected TG1 culture (Recovered phage 250 µL) was added to the TG1 culture with an OD of 0.4 at 600 nm (1.75 mL) and incubated at 37 °C without shaking for 30 min allowing the infection. The culture was centrifuged at 3000 × g for 10 min and the supernatant was removed. The pelleted cells were resuspended in 2xTY medium 100 µL and plated on an LB agar plate containing ampicillin 100 µg / mL and glucose 1 %. After incubation at 37 °C overnight, the cells were suspended in LB medium 2 mL containing 15 % glycerol using a glass spreader. The glycerol stock was stored at −20 °C.

Before storing in the freezer, the recovered TG1 cells (50 µL from 2 mL glycerol stock) were added to 2xTY medium 50 mL containing ampicillin 100 µg / mL and glucose 1 % and incubated at 37 °C with shaking until they reach an OD of 0.4 at 600 nm. The grown cells (10 mL) were transferred into a new tube and added KM13 helper phage (2 x 10^{11} pfu). The cells were incubated at 37 °C without shaking for 30 min allowing the infection. The cells were harvested by centrifugation at 3000 × g for 10 min and resuspended in 2xTY medium 50 mL containing ampicillin 100 µg / mL, kanamycin 50 µg / mL and glucose 0.1 %. The infected cells were incubated at 30 °C with shaking overnight and then centrifuged at 3300 × g for 15 min. The supernatant was transferred into a new tube and centrifuged again at 3300 × g for another 15 min. The supernatant 40 mL was transferred into a new tube and polyethylene glycol 8000 20 % solution containing NaCl 2.5 M (PEG/NaCl) 10 mL was added. The mixture was incubated at 0 °C on an ice bath for 1 h and centrifuged at 3300 × g for 30 min at 4 °C. The precipitate was dissolved in TBS 1 mL and centrifuged at 11600 × g for 5 min and 4 °C to remove insoluble substances. The supernatant was transferred into a new tube and stored at 4 °C for the use in the next round panning procedure.

3.8.6 **Preparation of Monoclonal Phage Clone for ELISA**

The single colonies from the titration plate from the 3rd round of panning procedure LB agar plate were steaked out on an LB agar plate containing ampicillin 100 µg / mL and glucose 1 %. After incubation at 30 °C overnight, a single colony from each clone was inoculated in 2xTY medium 2 mL containing ampicillin 100 µg / mL and glucose 1 %. The cells were grown at 30 °C with shaking overnight. Each starting cell culture 20 µL was added to the new 2xTY medium 2 mL containing ampicillin 100 µg / mL and glucose 1 %. (The rest was stored in the form of glycerol stock as mentioned above.) The medium was incubated at 37 °C with shaking for 2 h. The KM13 helper phage (1 x 10^{10} pfu) dissolved in 2xTY medium 250 µL containing ampicillin 100 µg / mL and glucose 1 % was added to the cell culture and incubated at 30 °C without shaking for 30 min allowing the infection. The cells were centrifuged at 3000 × g for 10 min and the supernatant was removed. The cells were resuspended in 2xTY medium 2 mL containing ampicillin 100 µg / mL and kanamycin 50 µg / mL, and incubated at 30 °C overnight. The overnight culture 1.25 mL was transferred into a new tube and centrifuged at 130000 rpm for 5 min. The supernatant 1 mL containing monoclonal phages was transferred into a fresh tube and used for ELISA.

3.8.7 Monoclonal Phage Enzyme-Linked Immunosorbent Assay (ELISA)

The phage ELISA was performed using 96-wells immobilizer amino plate (NUNC). The streptavidin 10 µg / mL in $NaHCO_3$ buffer (0.1 M, pH 8.3) 100 µL was added into each well and incubated at 4 °C overnight. After removing the excess streptavidin in solution, Protein-Free (TBS) blocking buffer 200 µL was added into each well and the plate was incubated at 4 °C for 1 h. Each monoclonal phage clone was incubated with ACD3-PEG5-Lys(Biotin) ligand 0.1 µM, without ACD3-PEG5-Lys(Biotin) ligand, and with ACD3-PEG5-Lys(Biotin) ligand 0.1 µM and excess amount of ACD3 0.1 mM in TBST 0.1 % for 1 h at room temperature, and transferred into a streptavidin-coated 96-well plate. After incubation at 25 °C for 1 h, the plate was washed 6 times with phosphate buffer saline solution containing NaH_2PO_4 3 mM, Na_2HPO_4 9 mM, NaCl 150 mM and Tween-20 0.1 % with pH 7.2 (PBST). The horseradish peroxidasbe (HRP) conjugated anti-M13 monoclonal antibody (GE Healthcare) dissolved in Protein-Free (TBS) blocking buffer (1 : 5000 dilution) 100 µL was added into each well and incubated at room temperature for 1 h. After washing the plate 10 times with PBST, the HRP substrate solution (2,2'-azino-bis(3-ethylbenzothiazoline-6-sulphonic acid) (ABTS) 11 mg and H_2O_2 30 % in 50 mM sodium citrate buffer (pH 4.0) 137 mL) 200 µL / well was added and the plate was measured the absorption at 405 nm subtracted by absorption at 630 nm to remove the background scattering.

From the ELISA test, the candidates having high absorption (high binding affinity) in the presence of ACD3-PEG5-Lys(Biotin) ligand, but low absorption without ACD3-PEG5-Lys(Biotin) ligand or excess amount of free ACD3 (competitive binding) were isolated. From Tomlinson I and J libraries, 2 and 6 candidates were obtained from the screening of 48 clones each. The candidates were screened by the ELISA test again with a similar procedure, but each monoclonal phage clone was incubated also with ACD3-PEG5-Lys(Biotin) ligand (0.1 µM) and excess amount of free ACD1, ACD2 and ACD4 (0.1 mM). The candidate having low ELISA signal with the excess amount of ACD3, but high signal in the others was selected as the best candidate, which was J-20.

3.8.8 Purification and Sequence Determination of pIT2-scFv-J-20 Vector

The *E. Coli* TG1 cells having the desired pIT2-scFv-J-20 vector were amplified by streaking out on LB agar plate from the glycerol stock and grown at 37 °C overnight. A single colony was inoculated into 2xTY medium 5 mL containing ampicillin 100 µg / mL. The cells were grown overnight by incubating at 37 °C with shaking and collected by centrifuging at 3000 × g for 10 min.

After removing supernatant, the purification and sequencing protocols were conducted using QIAGEN Plasmid Purification Kits. The buffer P1 250 µL was added, and the TG1 cells were resuspended by pipetting. The solution was transferred to a new tube. The buffer P2 250 µL was added and mixed by inverse shaking following by buffer N3 350 µL with similar method. The solution was centrifuged at 9500 × g for 10 min and the supernatant was transferred and filtered by QIAprep 2.0 Spin Column on the benchtop centrifuge. The precipitate was washed by buffer PB 500 µL and buffer PE 750 µL. Then, the filter was dried by centrifuging at 16000 × g for 1 min. The column containing precipitate on the filter was transferred to a new tube. The filter was incubated in buffer EB 50 µL for 1 min to elute the plasmids from the filter, and the eluted solution was collected by centrifuging at 16000 × g for 1 min. The solution was transferred to a new tube and stored at −20 °C as a pIT2-scFv-J-20 plasmid stock.

DNA sequence was verified by dye-terminator sequencing (Sanger sequencing) method using sequencer kit (ThermoFisher). The two PCRs (forward and backward) were conducted with two primers: 5’- G GAA TTC CAT ATG AAA TAC CTA TTG CCT ACG G -3’ (ss-pelB-FW-01) and 5’- CTA TGC GGC CCC ATT CAG AT -3’ (pHEN-Term-01). The PCRs were conducted using the following protocols

PCR Mixture

Plasmid 300 ng	1 µL
Primer 1.6 pmol/ µL	1 µL
sH$_2$O	3 µL
1 / 3 BIGDYE / 5 × Sequence buffer	3 µL
Total	8 µL

Thermal Cycle

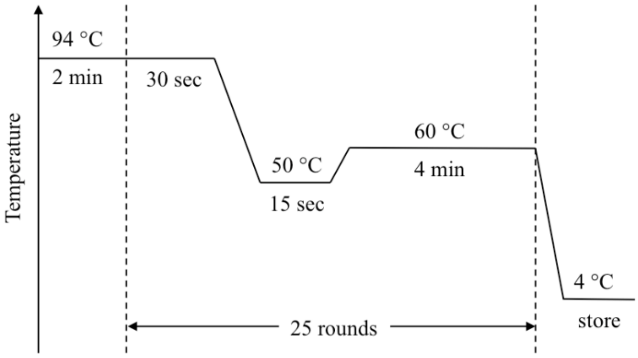

The PCR products were purified by mixing with ethanol 95 % 25 µL, sodium acetate 3 M 1.2 µL, and sterilized water (sH$_2$O) 5.8 µL. The mixture was incubated for 20 min at room temperature, and centrifuged at 21500 × g and 4 °C for 30 min. The supernatant was removed and the ethanol 70 % 125 µL was added and mixed by vortexing. The solution was centrifuged at 21500 × g and 4 °C for 15 min, and the supernatant was removed. The pellet was dried on the 95 °C water bath for 1 min and in the clean bench at room temperature for 20 min. The dried pallet was resuspended in Hi-Di formamide (ThermoFisher) 20 µL. The solution was heated at 95 °C on water bath for 2 min and subjected to the DNA sequencer.

3.8.9 Subcloning of scFv-J-20 Fragment to pET-22b(+) Vector

The TAG stop codon on υ_h of pIT2-scFv-J-20 vector was mutated to CAG by overlap extension PCR using Blend TAQ enzyme with two pairs of primers: ss-pelB-FW-01 and 5’- ACC ACC AAT CGT TGA GAC CCA CTC CAG C -3’, and pHEN-Term-01 and 5’- CTA TGC GGC CCC ATT CAG AT -3’. The PCRs were conducted using the following protocols.

PCR Mixture

1 / 30 diluted pIT2 plasmid stock	5 µL
Primer 1 10 pmol / µL	5 µL
Primer 2 10 pmol / µL	5 µL
dNTP 2 mM	5 µL
10 × Blend TAQ buffer	5 µL
Blend TAQ	1 µL
sH$_2$O	24 µL
Total	50 µL

Thermal Cycle

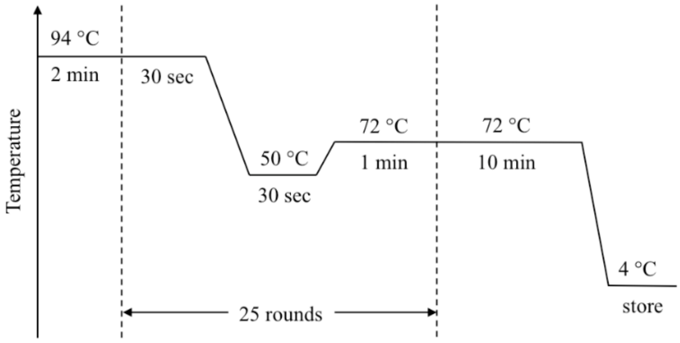

The PCR mixtures were then mixed together and the thermal cycling was conducted again with the same thermal cycle, and the desired DNA fragments (877 bp) were purified by agarose gel electrophoresis. The 100-bp marker 5 µL and the mixture of PCR product 100 µL with 5 × loading dye 25 µL were loaded to agarose gel 1.5 %. Electrophoresis was conducted with 100 V in 5 × TBE. The gel was soaked in ethidium bromide for 20 min and 5 × tris-borate-EDTA buffer (TBE) for 30 min before observed under UV-light illuminator. A part containing desired fragments was separated by cutting.

The gel containing desired DNA fragment was weighted (150 mg) in the new tube, and QG buffer 450 µL (3 eq) was added. The gel was dissolved by heating at 55 °C on water bath for 10 min and vortexing. Isopropanol 150 µL (1 eq) was added, and the solution was vortexed again. The solution was filtered by QIAquick Spin Column (100 bp ~ 10 kbp) and DNA fragments on the filter were washed with QG buffer 500 µL and buffer PE 750 µL using the benchtop centrifuge. The filter was dried by centrifuge at 16000 × g for 1 min. The filter was transferred to a new tube, and the DNA fragments were eluted by buffer EB 50 µL. The filter was centrifuged at 16000 × g for 1 min, and the filtrate was kept as a scFv-J-20 PCR product stock at −20 °C.

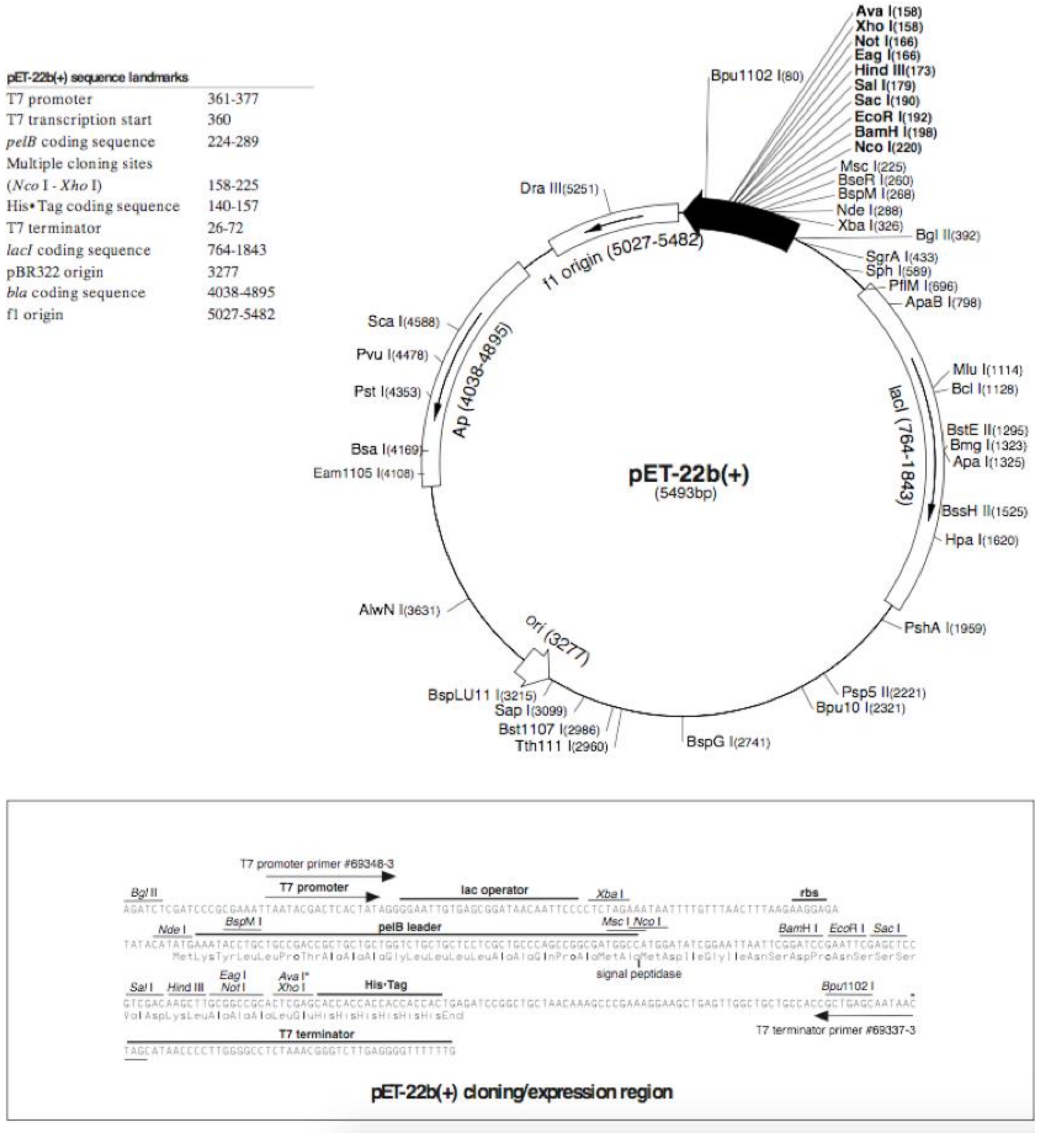

pET-22b(+) sequence landmarks	
T7 promoter	361-377
T7 transcription start	360
pelB coding sequence	224-289
Multiple cloning sites	
(*Nco* I - *Xho* I)	158-225
His•Tag coding sequence	140-157
T7 terminator	26-72
lacI coding sequence	764-1843
pBR322 origin	3277
bla coding sequence	4038-4895
f1 origin	5027-5482

Figure 3-16. pET-22b(+) vector map (Novagen)

The PCR products were ligated into pET-22b(+) vector (Figure 3-16) via the NdeI/NotI restriction sites. First, the restriction digestions of scFv-J-20 PCR product and the pET-22b(+) were conducted by incubated the following mixtures at room temperature overnight.

Restriction Digestion of scFv-J-20 PCR Product

scFv-J-20 PCR product	48	µL
NE buffer 4	6.5	µL
NdeI (20 u / µL)	6.5	µL
NotI (20 u / µL)	2	µL
10 × BSA	2	µL
Total	65	µL

Restriction Digestion of pET-22b(+) vector

pET-22b(+) pATCH	10	µL
NE buffer 4	10	µL
NdeI (20 u / µL)	2	µL
NotI (20 u / µL)	2	µL
10 × BSA	10	µL
sH_2O	66	µL
Total	100	µL

The digested scFv-J-20 PCR product (790 bp) and pET-22b(+) vector (5.4 kbp) were purified by agarose gel electrophoresis. For digested scFv-J-20 PCR product, the 100-bp marker 5 µL and the mixture of digested PCR scFv-J-20 product 65 µL with 5 × loading dye 16 µL were loaded to agarose gel 1.5 %. For digested pET-22b(+) vector, the 1-kbp marker 5 µL and the mixture of digested PCR pET-22b(+) vector 100 µL with 5 × loading dye 25 µL were loaded to agarose gel 1.0 %. Both electrophoreses were conducted with 100 V in 5 × TBE. The separation and extraction were conducted in the same way as previously described. The purified digested products were stored at −20 °C.

The ligation was conducted by incubating the ligation mixture composed of purified digested scFv-J-20 PCR product 1 µL (PCR insert), purified Digested pET-22b(+) vector 3 µL, T4 DNA ligase 1 µL and sH_2O 5 µL at room temperature for 1 h. After 40 min of incubation, *E. coli* XL1-Blue competent cells 200 µL were prepared by dissolving on ice bath. After 1 h of incubation, the transformation was performed by transferring XL1-Blue competent cells to the ligation mixture. The solution was mixed by pipetting and incubated on ice for 30 min. Cells were heated at 43 - 45 °C on water bath for exactly 45 seconds and immediately cooled on ice for 2 min. LB medium 800 µL was added and, the medium was incubated at 37 °C for 20 min.

The LB medium containing XL1-Blue cells 25 µL was plated on the LB agar plate containing ampicillin 100 µg / mL. The rest was centrifuged at 3400 × g for 1 min, and 900 µL of supernatant was removed. XL1-Blue cells were resuspended in the leftover LB medium and plated on the LB agar plate containing ampicillin 100 µg / mL. The cells were grown at 37 °C overnight.

8 single colonies were streaked out on LB agar plate containing ampicillin 100 µg / mL and glucose 1 % and grown at 37 °C overnight. The colonial PCR was performed by inoculating single colony from each streak out to the following PCR mixture before thermal cycling using ss-pelB-FW-01 and pHEN-Term-01 as primers.

PCR Mixture

Primer 1 10 pmol / µL	5 µL
Primer 2 10 pmol / µL	5 µL
dNTP mix 2 mM	5 µL
10 × Blend TAQ buffer	5 µL
Blend TAQ	0.5 µL
sH_2O	29.5 µL
Total	50 µL

Thermal Cycle

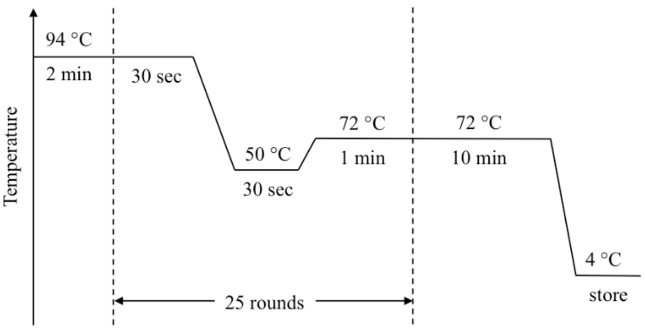

The PCR products were analyzed by agarose gel electrophoresis. The 100-bp marker 5 µL and the mixture of each colonial PCR product 5 µL with 5 × loading dye 1.25 µL were loaded to agarose gel 2.0 %. Electrophoresis was conducted with 100 V in 5 × TBE. The gel was dyed and observed using the previously described procedure. As a results, all colonies giving the electrophoresis band around 900 bp (target DNA size is 877 bp), meaning all cells are consisted of the pET22b(+)-scFv-J-20 vector. The vector was purified, the sequence was determined, and the vector was transformed to the BL21(DE3) cells using the same procedures as already described in the case of XL1-Blue. The new sequence showing the success of STOP codon mutation from TAG to CAG. The glycerol stock of *E. coli* BL21(DE3) having pET22b(+)-scFv-J-20 vector was prepared and stored previously described.

3.8.10 **Antibody Expression and Purification**

The antibody was expressed using T7 promoter in BL21(DE3) cells activated by IPTG. The glycerol stock of BL21(DE3) having pET22b(+)-scFv-J-20 vector was streaked out on the LB agar plate containing ampicillin 100 µg / mL and incubated at 37 °C overnight. The single colony obtained from the streak out plate was inoculated into LB medium 5 mL containing ampicillin 100 µg / mL and incubated at 30 °C overnight with shaking to make a starting culture. The main culture was prepared by diluting starting culture 100 times (or more) to the LB medium 50 to 250 mL containing ampicillin 100 µg / mL and glucose 0.2 %. The main culture was incubated at 37 °C with shaking for 2 h before reducing temperature to 25 °C. When an OD at 600 nm reached 0.6, the IPTG 100 mg / mL was added to give a final concentration of 0.2 mg / mL. The cells were continuously incubated overnight.

The main culture containing scFv J-20 antibody was centrifuged at 2330 × g and 4 °C for 10 (50 mL) to 30 min (250 mL) depending on the volume of the medium. The supernatant (medium) was filtered by Sartolab RF 180C2 vacuum filter 0.22 µm (Sartorius AG), kept in ice, and subjected to Ni-NTA agarose gel. The cells left in the centrifuge tube were stored at −20 °C for at least 30 min. The 5 × BugBuster Master Mix (2.5 mL in the case of medium 100 mL) was added. After resuspended, the cells were shaken for 30 min at room temperature. The cells were centrifuged at 9500 × g for 10 min. The supernatant was separated, subjected to Ni-NTA agarose gel and incubated for 15 min.

The Ni-NTA agarose gel was prepared by adding Ni-NTA agarose gel solution 1 mL (Ni-NTA agarose gel 500 mg) to the GE-PD10 empty column with a filter. The agarose gel was recharged according to the manual when it was reused. The gel was then washed by binding buffer (Tris HCl 20 mM buffer pH 7.9 containing imidazole 5.0 mM and NaCl 500 mM) 5 mL. The solution (extracted from cells or filtered medium) was subjected to the gel, and the gel was washed by binding buffer 5 mL and washing buffer (Tris HCl 20 mM buffer pH 7.9 containing imidazole 30 mM and NaCl 500 mM) 3 mL. The antibody was eluted by adding elution buffer (Tris HCl 20 mM buffer pH 7.9 containing imidazole 1.0 M and NaCl 500 mM) 3 mL. The gel was washed by water and kept at 4 °C for next usage.

The eluted solution containing desired antibody was exchanged and the product was purified by GE-PD10 column. The column was pre-eluted by TBS 25 mL. Then, the solution containing desired antibody 2.5 mL was added to column and the solution coming out of the column in this step was discarded. The solution was collected when TBS 3 mL was added to the column. The column was washed by water 25 mL and kept at 4 °C for the next usage. The collected antibody solution was stored at 4 °C.

Table 3-10. Parameters for gel permeation chromatography of scFv J-20 antibody.

Parameters	Analysis Conditions
HPLC Equipment	JASCO
Column	GPC Superdex 75 10/300 GL
Temperature	Room temperature
Injection Volume	50 µL
Solvent	10 mM Phosphate buffer pH 7.0 containing NaCl 150 mM
Flow Rate	0.4 mL / min
Detector	UV 280 nm

The leftover antibody in elution buffer (0.5 mL) was used for SDS-PAGE to determine the purity. The 100-kDa marker and the mixture of sample 100 µL and SDS loading buffer 100 µL were loaded to polyacrylamide gel 15 % SDS. The electrophoresis was conducted at 200 V in SDS-PAGE running buffer (Tris 3 g / L, glycine 14 g / L and SDS 5 g / L). The result showed a clear single band near 29.0 kDa marker from antibody purified from medium, while 2 unclear bands (the same band near 29.0 kDa and the other smaller-size band) were found from antibody purified from cells. (Appendix) The gel permeation chromatography was used to analyze the antibody purified from medium, confirming the purity of the antibody. (Table 3-10) Thus, the antibody that would be mediated in the photocyclodimerization of AC was collected and purified from medium. The concentration of the antibody was determined by absorption at 280 nm (ε_0 = 38640 $M^{-1}cm^{-1}$).

3.8.11 **Circular Dichroism Spectroscopy Measurement**

The JASCO J-820 CD machine (JASCO, Japan) was equipped with Single Position Peltier Cell Holder. The antibody sample was diluted to 2 µM with TBS buffer solution (pH 7.5) in 1 × 1 cm quartz cuvette. The measurement was conducted with scan speed 100 nm/min, bandwidth 1.00 nm, data integration time 2 s, standard sensitivity, accumulation 4 times at 4 °C. The TBS buffer has high absorption at 200 nm, inducing high HT at this wavelength and below. At scFv J-20 2 µM concentration, HT at 200 nm is 850 V, but it was rapidly reduced to less than 600 V at 203 nm and longer wavelength, indicating the acceptable accuracy of the spectrum for calculating the protein secondary structure.

3.8.12 **HPLC Analysis of 2-Anthracenecarboxylate Dimers**

Table 3-11. Parameters for analytical HPLC of ACDs with chiral column.

Parameters	Analysis Conditions
HPLC Equipment	JASCO
Column	$5C_{18}$-MS-II 4.6ID × 150 mm CHIRALCEL OJ-RH 2.1ID × 120mm
Temperature	Room temperature
Injection Volume	20 µL (or otherwise noted)
Solvent	Acetonitrile 40 % (TFA 0.1 %)
Flow Rate	1 mL / min
Detector	UV 280 nm Fluorescence excitation 254 nm / detection 420 nm

The sample was prepared by adding acetonitrile to give the final 50 % acetonitrile solution (aq), and injecting to HPLC. (Table 3-11) In the case of photocyclodimerization products containing antibody, the solution was diluted by the same volume of acetonitrile and incubated overnight for antibody denaturation. The solution was filtered using syringe filter unit 0.45 µM (Starlab), removing the denatured antibody. The sample was injected to HPLC with the same conditions.

If the solution is a mixture of TBS and the other organic solvents, such as in the organic solvent toleration experiment, the HPLC sometimes showed double or broad peaks due to the solvent incompatibility. In that case, the MonoTip^{TM} C18 (GLScience) was used for the solvent exchange instead of filtering with syringe filter. The sample was eluted by acetonitrile 50 µM containing TFA 0.1 %, and directly injected 30 µL to HPLC.

3.8.13 **Ground-State Interactions Between scFv J-20 Antibody and ACD Isomers**

The mixture of scFv-J-20 antibody 2.4 µM and ACD1, 2, 3 and 4 mixture (synthesized by photodimerization in tetrahydrofuran) 12 µM (in total) was incubated for 1 h at room temperature in TBS. The scFv J-20 antibody was filtered using the centrifugal protein filter (AmiconUltra-0.5 mL, Millipore). The filtrate was separated and diluted by the same amount of acetonitrile before injected 100 µL to the analytical HPLC. The control experiment was conducted with the similar protocols, but TBS was used instead of scFv-J-20 antibody solution.

3.8.14 **Ground-State Interactions Between scFv J-20 Antibody and AC**

The mixture of scFv J-20 antibody 8.3 µM and AC 16.7 µM was incubated for 1 h at room temperature in TBS. The scFv J-20 antibody was filtered using the centrifugal protein filter (AmiconUltra-0.5 mL). the filtrate 500 µL was placed into the 0.2 cm × 1.0 cm quartz cell and the fluorescence emission spectrum was measured (excitation 365 nm with 5 nm bandwidth and 0.2 cm pathlength, emission bandwidth 3 nm with 1.0 cm pathlength, response 1 s, high sensitivity, scan speed 100 nm / min). The control experiment was conducted with the similar protocols, but TBS was used instead of scFv J-20 antibody solution.

3.8.15 **Excited-State Interactions Between scFv J-20 Antibody and AC**

The mixture of scFv J-20 antibody 2 µM and AC 1 or 2 µM 1 mL was prepared in the 0.2 × 1.0 cm quartz cell. The temperature of the solution was adjusted to 10 °C before the measurement. AC was excited at 390 nm using a pulse laser from a Ti:sapphire laser system (Spectra-Physics, Tsunami; 3950-L2S, fwhm 150 fs, 82 MHz) converted from 780 nm to 390 nm using SHG crystals. The emission at 420 nm was captured by a streak camera (Hamamatsu C4334) in photon counting mode. The fluorescence decay curve was analyzed using the U8167-01 program (Hamamatsu).

3.8.16 **Photocyclodimerization of AC Mediated by scFv J-20 antibody**

TBS was bubbled by Ar for minimum of 30 min before use. The scFv J-20 antibody stocks were freshly prepared by protein expression of *E. Coli* BL21(DE3) having pET22b(+)-scFv-J-20 plasmid in LB medium 250 or 500 mL. The scFv J-20 stock was stored at 4 °C and used within 24 h after preparation. The AC solution was prepared by dissolving AC in TBS, sonicating, and filtering by syringe filter 0.45 µm (Starlab). The concentrations of scFv J-20 antibody (ε_0 at 280 nm = 38640 $M^{-1}cm^{-1}$) and AC (ε_0 at 387 nm = 3400 $M^{-1}cm^{-1}$) solution were determined by UV-Vis absorption spectra.

The reaction solution was prepared by mixing the scFv J-20 antibody solution, AC solution, and the same TBS to the required concentration for a final volume of 3 mL in 1.0 cm × 1.0 cm quarts cell. The solution was incubated in the dark before irradiated by Xe lamp 500 W equipped 340 nm longpass glass filter. The initial and final absorption spectra were measured to confirm the conversion. For the control experiment, the AC was mixed with TBS instead of scFv J-20 antibody solution. For the external factor experiments, the TBS conditions and temperature are changed as mentioned in each session.

CHAPTER 4: SYNTHESIS OF HETERODIMER OF 2-ANTHRACENECARBOXYLIC ACID AND 6-HYDROXY-2-ANTHRACENECARBOXYLIC ACID TO IMPROVE PHAGE DISPLAY TECHNIQUE

4.1 Objective

The objective of this chapter is to synthesize a new type of anthracene heterodimer based on the new designed target structure for antibody phage display panning. The concept of the design, the optimized synthesis of 6-methoxy-2-anthracenecarboxylic acid, and the synthesis of 6-hydroxy-2-anthracenecarboxylic acid and 2-anthracenecarboxylic acid using covalent linker are reported.

4.2 Introduction

In previous chapter, the synthetic antibody obtained from phage display technique showed a promising potential as a chiral supramolecular host for [4+4] photocyclodimerization of AC, especially after the optimization of external factors. However, the limitation is at 48 % ee and 34 % product distribution of ACD3. To improve this limitation, a better antibody must be obtained. As Tomlinson I and J libraries were the only commercially available libraries, optimizing the ligand for phage display technique is simpler than obtaining a new phage library.

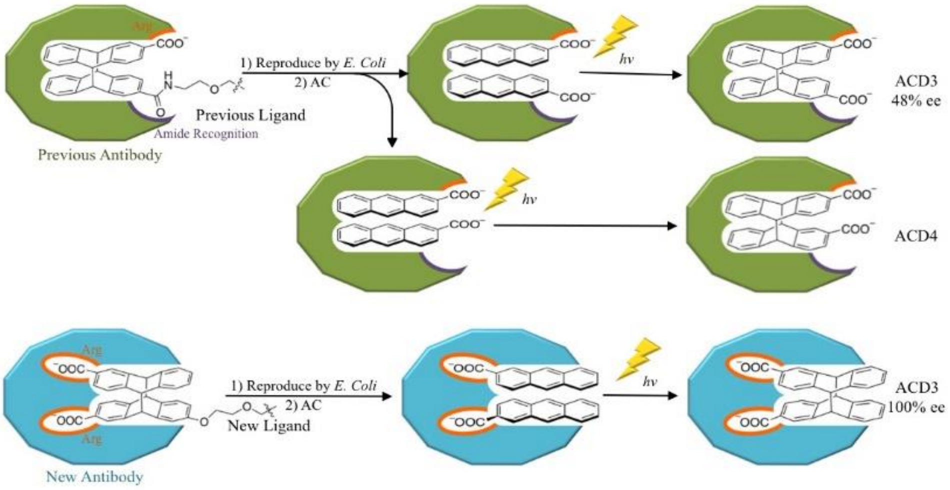

Figure 4-1. Schematic representative explaining the flaws of the antibody obtained using previous ligand (green) and the expected imrpovement from the new antibody obtained using the new designed ligand (blue).

The new ligand was designed to improve 3 issues: the number of carboxylate groups, the position of carboxylate groups and the existence of amide bond. (Figure 4-1) Previously, ACD3 was used as a starting material for the ligand synthesis, one of the carboxylate group was modified to amide bond. Therefore, only 1 carboxylate was available for the recognition of antibody, while the selectivity of AC dimerization solely depends on the position of 2 carboxylate groups. Moreover, this modification introduced amide bond, which does not exist in the product. The recognition of antibody to amide group can reduce the selectivity of synthetic antibody to ACD3. In addition, the position of carboxylate points outward the antibody, so the recognition site (containing arginine residues) are located in outer layer of antibody. Therefore, the recognition site has relatively high microenvironmental polarity, a reasonable cause of undesired ACD4 and the other ACD3 enantiomer.

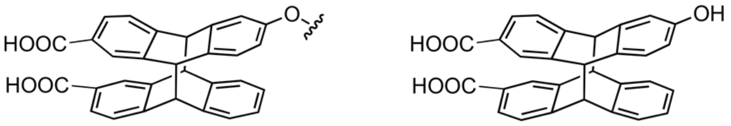

Figure 4-2. Structure of (left) the head of the new ligand and (right) the *anti-head-to-head* anthracene heterodimer needed for new ligand synthesis.

The most challenging part of this design is to synthesize the heterodimer between AC and 6-hydroxy-2-anthracenecarboxylic acid (HAC) (Figure 4-2). In this chapter, the synthesis of 6-methoxy-2-anthracenecarboxylic acid (MAC), the selective dimerization between AC and HAC, and the synthesis of the new ligand were discussed.

4.3 Synthesis of 6-Methoxy-2-anthracenecarcoxylic Acid

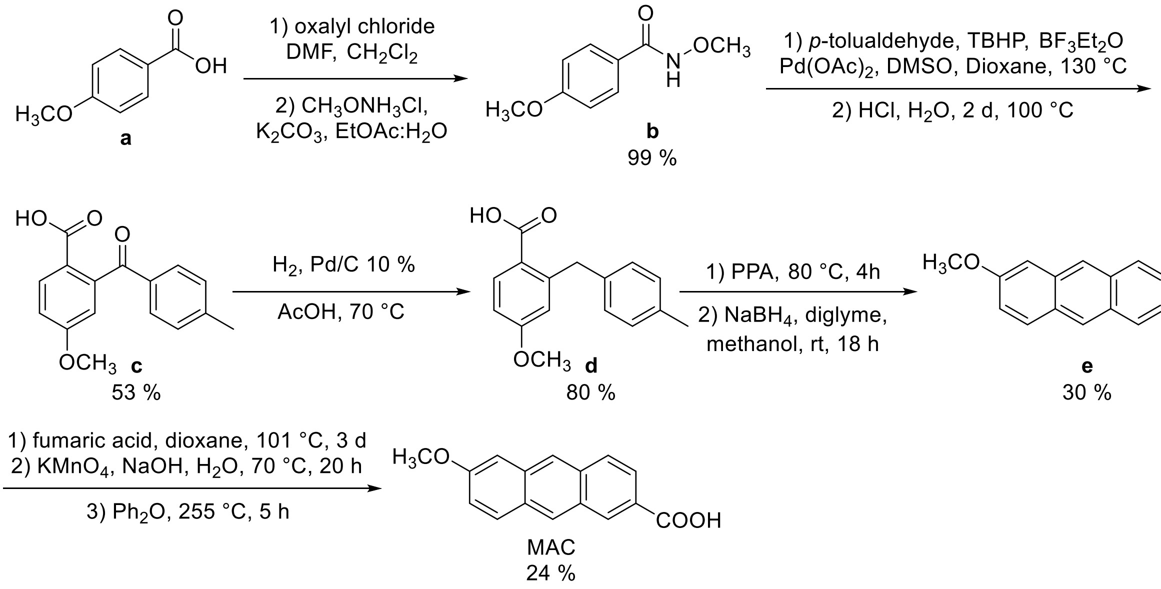

Figure 4-3. Synthesis scheme of MAC.

The synthesis of MAC was divided into 5 main steps containing one to few reactions (Figure 4-3). Even though this synthesis was based on reported protocols, some reactions did not proceed as described possibly because the scales were different. Here, the reactions for preparative-scale synthesis were optimized and discussed.

The first step was to synthesize Weinreb amide.[323] This reaction had a very high yield even with 9 g scale synthesis without any further purification. The synthesis of compound **c** started from the formation of diaryl ketone. By using palladium catalyst and *tert*-butyl hydroperoxide, *ortho*-directed aryl imino carboxylic acid was synthesized.[324] Hydrochloric was used to hydrolyze oxime to form diaryl ketone **c**.[325,326] The purification, however, was complicated. By only column chromatography, the purified ketone was brown and the NMR result showed significant amount of impurities. The only way to get a high-purity product is recrystallization, but the yield lost is also too high. Therefore, activated charcoal and basic extraction were used to purify the crude product before column chromatography. The limitation of this synthesis is the amount that can be purified by column chromatography each time. It was difficult to sperate ketone and imine. To purify crude product 3 - 5 g, the amount of silica gel and eluent used were 400 g and 5 L, respectively. Still, the purified ketone is pale-yellow, not white solid as it should.

Compound **c** was first reduced by triethylsilane for 5 d, selective reduction at carbonyl group and avoiding the reduction of carboxylic acid group.[327,328] However, the reaction did not proceed. Thus, the Pd / C and H_2 were used instead,[329] and compound **d** was synthesized. Nevertheless, increasing the synthesis scale was difficult. At gram-scale synthesis, the reduction sometimes needed to be repeated even with Pd / C 30 w% probably because the impurities from the previous step quenched the Pd / C. Moreover, H_2 bubbling in acetic acid for long time dried the solution at the end of H_2 tube. This accumulated the dried starting material and Pd / C at the end of the tube, clogging the H_2 flow.

The synthesis of compound **e** was divided into 2 steps: the anthrone cyclization and the reduction.[330] Polyphosphoric acid was used in the first step,[331,332] and the viscosity was the main problem. The cyclized anthrone was reduced to anthracene by $NaBH_4$.[333] The NMR of the crude products from both steps showed that the majority of the product were anthrone and anthracene, but the color of the crude produce was grey, while anthracene color should be yellow. After column chromatography, compound **e** was obtained with yellow color as expected but in low yield.

The final step of the synthesis was the oxidation of methyl group, but position 9 and 10 of anthracene are sensitive to oxidation, forming anthraquinone. Therefore, they were protected by fumaric acid, which took 3 d, before oxidation using potassium permanganate.[330] After purification, the deprotection was conducted at a high temperature, causing partial dissociation of anthracene itself. The crude product was brown, clearly indicating the impurity. The crude product was purified by sublimation and less than half of the product was recovered, causing the overall yield of this step to be the lowest. On the other hand, the purified product was in bright yellow color, and the NMR showed a high purity.

4.4 Synthesis of Chd(AC-HAC dimer3)

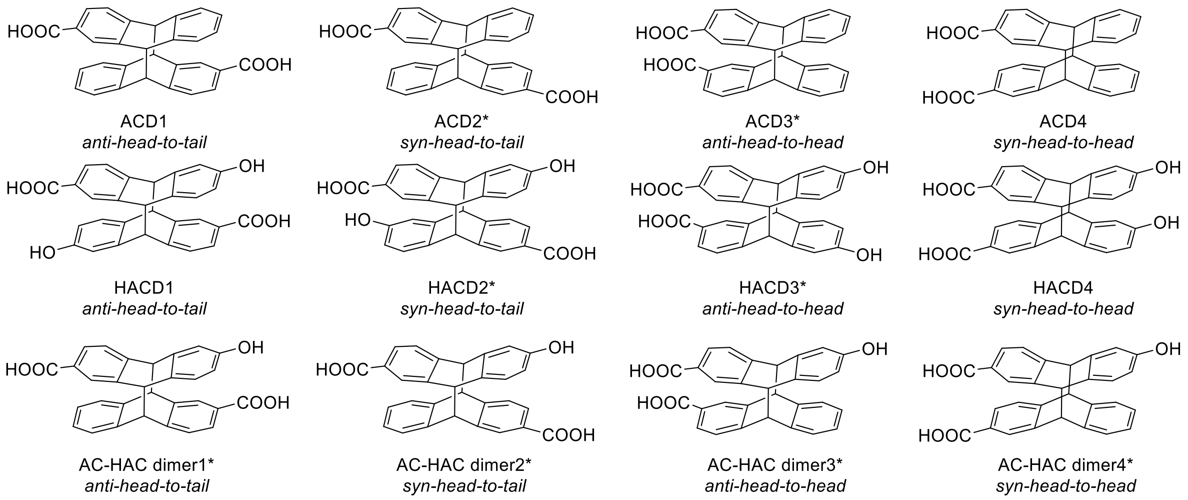

Figure 4-4. Possible products from [4+4] photocyclodimerization of AC and HAC. There are (top) AC dimers, (middle) HAC dimers and (bottom) AC-HAC heterodimers. The “*” indicate the chiral dimers.

Normally, the cross-dimerization of 2 different anthracene derivatives will give a variety of different products. For example, the photodimerization of AC and HAC will give a total of 12 different dimers, and 8 of them are chiral. (Figure 4-4) Therefore, simple dimerization and purification are not suitable for having the desired *anti-head-to-head* AC-HAC heterodimer (hereinafter referred to as AC-HAC dimer3).

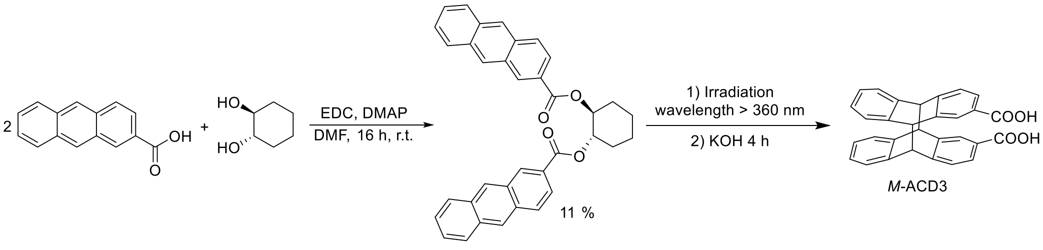

Figure 4-5. The synthesis of ACD3 using *trans*-1,2-cyclohexanediol as a chiral linker.

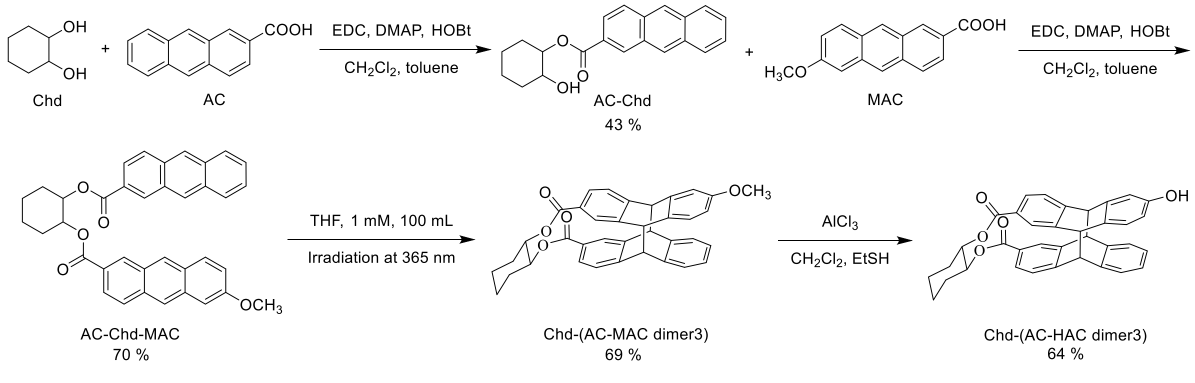

Figure 4-6. Selective synthesis of Chd-(AC-HAC dimer3).

The synthesis of AC-HAC dimer3 was inspired by the selective synthesis of enantiopure ACD3 (*anti-head-to-head* anthracenecarboxylic acid dimer) using *trans*-1,2-cyclohexanediol (Chd) as a covalent linker.[267] (Figure 4-5) However, the reaction conditions were optimized to suite the preparative-scale synthesis. The coupling was performed in two step using EDC, DMAP and HOBt as coupling reagents. Also, the additional demethylation was necessary. (Figure 4-6)

First, Chd was coupled with AC to form AC-Chd monoester. Although the AC was added dropwise to the Chd solution, the diester was also formed. Therefore, the product was purified by column chromatography. Less than 50 % yield was recovered because the condition of the esterification was mild. Next, excess amount of AC-Chd was coupled with MAC to form AC-Chd-MAC diester. The product was purified again to remove non-reacted starting material. 70 % yield of product was obtained because of the excess amount of AC-Chd and coupling reagents.

The product was irradiated by 365 nm light under Ar atmosphere, avoiding oxidation of anthracene. According to the reference, the photoirradiation was performed at the maximum of 10^{-5} M scale. However, it was not applicable for the synthesis purpose. Hence, the photocyclodimerization was tested at the concentration of 10^{-3} M with 3, 20 and 100 mL. The NMR showed that the dimer was formed as a major product. The product was purified by column chromatography to remove intermolecular dimerization products. As a result, the pure product was obtained with 69 % yield.

The *trans*-1,2-cyclohexanediol was kept in this step as a protection group in further step. Finally, the methoxy group was hydrolyzed under mild conditions ($AlCl_3$ in the mixture of ethanethiol and dichloromethane) to preserve the ester groups linking the dimer with Chd. After purification, the Chd(AC-HAC dimer3) was obtained.

4.5 Synthesis of (AC-HAC dimer3)-PEG4-Biotin Ligand

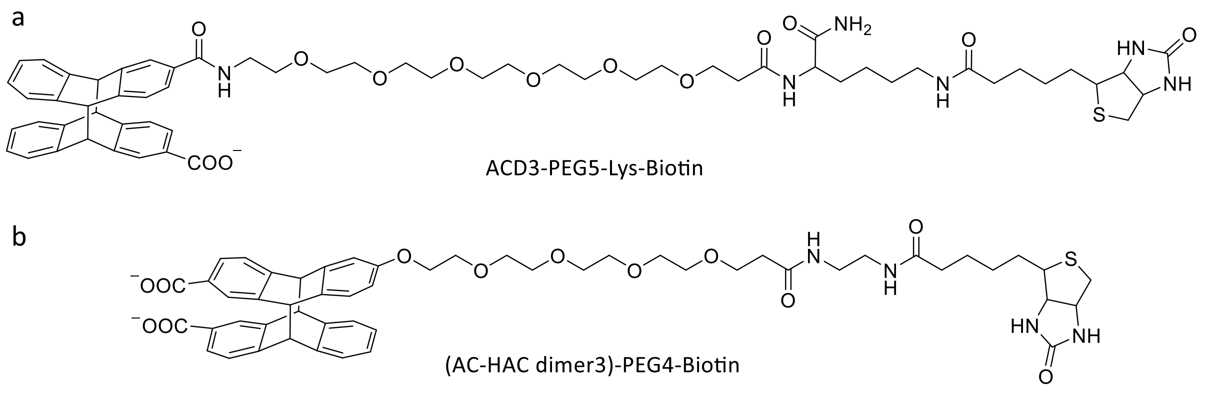

Figure 4-7. Structure of (a) the previously used ligand and (b) the design of new ligand with AC-HAC dimer3.

The new ligand structure was modified from the previous ligand not only the dimer part but also the linker (Figure 4-7). Although the structure is simpler than the previous one, the synthesis was more complicated. Each component of the previous ligand was linked by peptide bond, so that only consecutive solid-phase peptide synthesis was enough. On the other hand, AC-HAC dimer3 in the new ligand was linked by ether bond, so the Williamson ether synthesis was required.

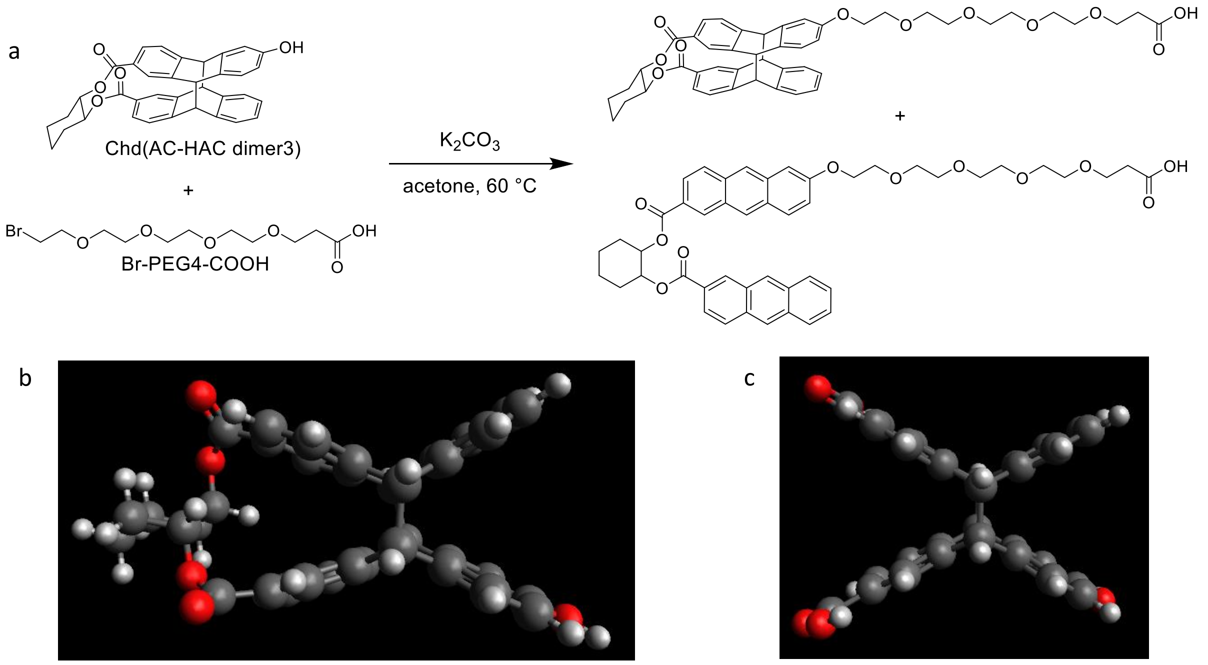

Figure 4-8. (a) Synthesis of (AC-HAC dimer3)-PEG4-COOH resulting in dissociation of dimer to monomer, and (b) the optimized structure of Chd-(AC-HAC dimer3) and (c) AC-HAC dimer 3 based on UFF minimum energy calculation from Avogadro software.

The first attempt was to link dimer and polyethylene glycol, creating (AC-HAC dimer3)-PEG4-COOH molecule. After that, the carboxylic acid group at the end of polyethylene glycol, which is not protected, will be used to form peptide bond to biotin using solid-phase synthesis. However, the result was not as expected. From the NMR spectrum, the dimer was dissociated (Figure 4-8 a), even though the AC dimers and MAC dimers are known to be stable at 70 °C.[334,335] The photo-induced dissociation is unlikely because the reaction was performed in the dark, and acetone, the reaction solvent, has a high absorption at the wavelength lower than 300 nm. One of the possible explanations is that the *trans*-1,2-cyclohexanediol linker distorts the structure of AC-HAC dimer3, decreasing the thermal stability of Chd-(AC-HAC). (Figure 4-8 b and c) Moreover, the isolation of (AC-HAC dimer3)-PEG4-COOH was failed, same as the re-intramolecular photocyclodimerization of the dissociated product.

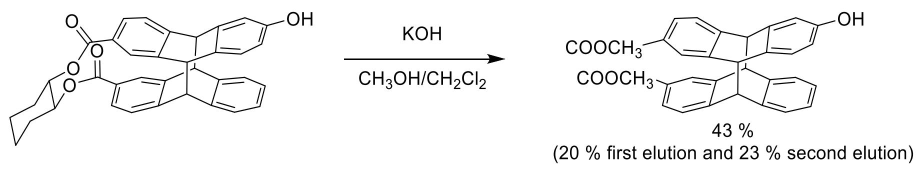

Figure 4-9. Deprotection by *trans*-1,2-cyclohexandiol cleavage in basic solution.

Therefore, the best solution was to remove *trans*-1,2-cyclohexanediol in ambient temperature. The hydrolysis was conducted in the mixture of methanol and dichloromethane using KOH as a catalyst.[336] (Figure 4-9) According to NMR spectrum, the AC-HAC dimer3 was expected to be a major product with small amount of AC and HAC monomer. For the purification, HPLC equipped with

CHIRALPAK® IA column was used instead of normal column chromatography to perform both purification and enantioseparation simultaneously. As a result, the *(P)*- and *(M)*-dimers were isolated. Only 43 % yield in total was recovered after purification because of two reasons: the monomers (from the dissociation of dimers) were found, and the *syn-head-to-head* dimers were also formed during the photocyclodimerization step.

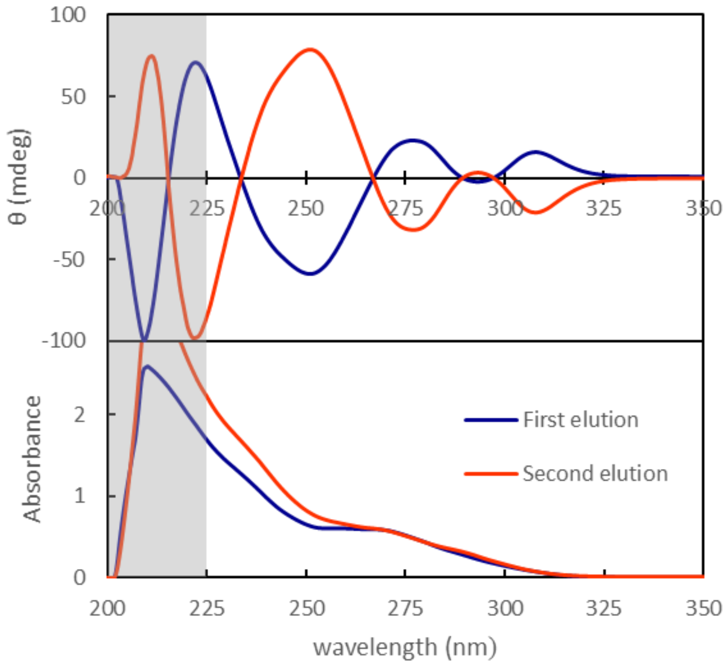

Figure 4-10. CD and UV-Vis absorption spectra of dimethyl(AC-HAC dimer3) first (blue) and second (orange) elution purified by HPLC with chiral column. The spectra were normalized to have the same absorption at 270 nm. The grey area signify the region with HT more than 600 V.

The CD spectra indicate that the purified samples were enantiomers as expected. (Figure 4-10) However, the NMR and MS revealed that the products were dimethyl(AC-HAC dimer3), which was not obtained in the previous report.[336] Even with the addition of water, the product was still dimethyl ester instead of dicarboxylic acid.

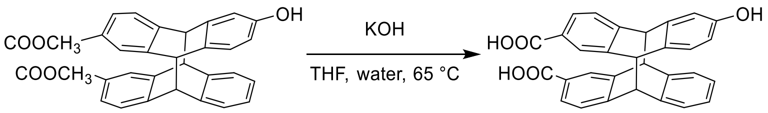

Figure 4-11. Hydrolysis of methyl ester groups in basic solution.

Therefore, further hydrolysis was attempted using KOH (aq) and the mixture of water and tetrahydrofuran as a solvent at 65 °C. (Figure 4-11) The crude product dissolved in only polar solvent, such as methanol and tetrahydrofuran, so the purification was complicated. However, the mass spectroscopy confirmed that methoxy groups were completely hydrolyzed. In addition, the monomers were not observed, which supports the idea that the *trans*-1,2-cyclohexanediol is the cause of the reduced stability of AC-HAC heterodimer.

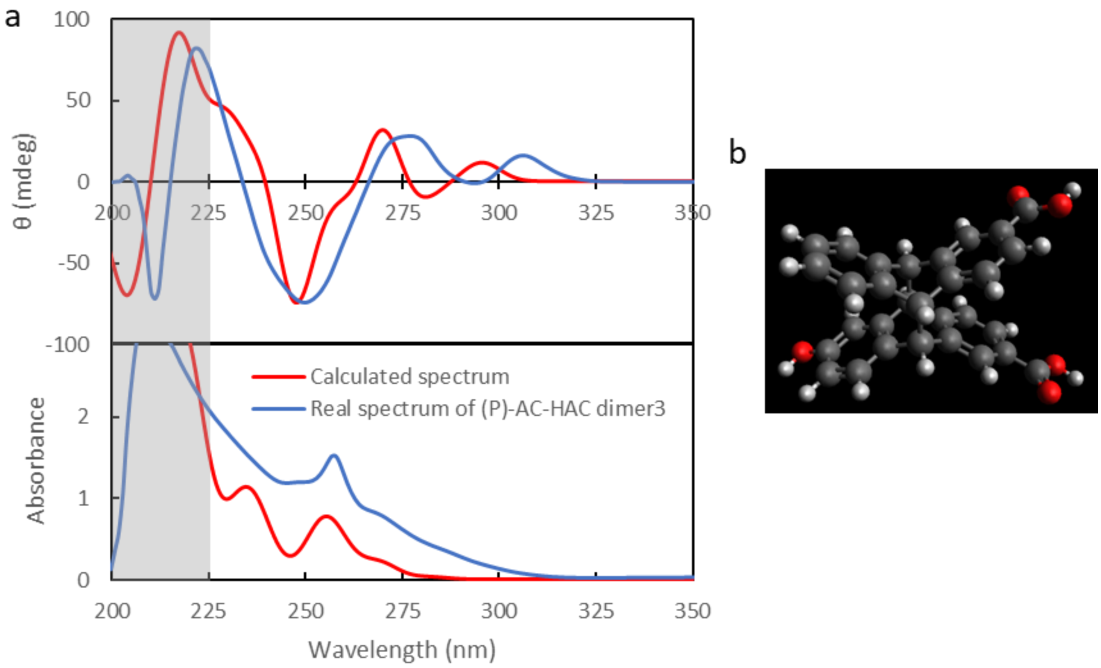

Figure 4-12. (a) CD and UV-Vis absorption spectrum of AC-HAC dimer3 hydrolyzed from dimethyl(AC-HAC dimer3) first elution (blue) and the calculated CD and UV-Vis absorption spectrum of *(P)*-AC-HAC dimer3 (red). The intensity of calculated spectra are not absolute. The grey area signify the region with HT more than 600 V. (b) The optimized structure of AC-HAC dimer3

The CD spectrum of AC-HAC dimer3 was, as expected, similar to dimethyl(AC-HAC dimer3). (Figure 4-12 a) The enantiomers were assigned based on the CD calculation of *(P)*-AC-HAC dimer3 similar to previously reported anthracene derivative dimers.[22] In brief, the excited-state properties were calculated using RICC2/DFT-D4-TPSS level with def2-TZVPP basis-set. The CD spectrum identified the first elution to be *(P)*-dimethyl(AC-HAC dimer3). (Figure 4-12)

4.6 Conclusion

The 6-methoxy-2-anthracenecarboxylic acid was synthesized from 4-anisic acid. The synthesis including 5 main steps was optimized. The *anti-head-to-head* heterodimer between 6-methoxy-2-anthracenecarboxylic acid and 2-anthracenecarboxylic acid was synthesized from intramolecular photocyclodimerization using *trans*-1,2-cyclohexanediol as a covalent linker. The methoxy group of the heterodimer was converted to hydroxy group, and the linker was cleaved to methyl ester. The heterodimer was purified and the enantiomers were separated using HPLC equipped with chiral column. The methyl ester was hydrolyzed to give a final *anti-head-to-head* heterodimer of 6-hydroxy-2-anthracenecarboxylic acid and 2-anthracenecarboxylic acid. Even though (AC-HAC dimer3)-PEG4-Biotin ligand was not synthesized at the moment, the synthetic pathway and identifications of AC-HAC dimer3, the key building block to the ligand, were established.

4.7 Experimental Procedure

4.7.1 **Synthesis of compound b (*N*,4-Dimethoxybenzamide: $C_9H_{11}NO_3$)**

Compound **a** (4-anisic acid: $C_8H_8O_3$) 9.11 g (59.9 mmol) was dissolved as much as possible in 85 mL dichloromethane under Ar in the ice bath. Oxalyl chloride 6.2 mL (72 mmol, 1 eq), followed by DMF 8 drops, were added dropwise at 0 °C. During the addition of dimethylformamide, the gas was formed. After the addition, the solution was stirred at room temperature while monitored with TLC. After 1 h, the solution became clear and colorless. The solution was dried by rotatory evaporator to yield acid chloride derivative (white crystal in yellow oil). Small amount of ethyl acetate was added. K_2CO_3 16.6 g (120 mmol, 2 eq) and *O*-Methylhydroxylammonium chloride were dissolved in ethyl acetate 240 mL and water 120 mL in ice bath. The acid chloride solution was added dropwise at 0 °C with vigorous stirring. The solution was stirred at room temperature for 1.5 h while monitored with TLC. The biphasic solution was separated, and the aqueous layer was extracted by ethyl acetate 3 times. The combined ethyl acetate solution was dried by Na_2SO_4 and rotatory evaporator. The compound b 10.8 g (59.6 mmol, 99.5 % yield) was obtained as white solid with high purity: ^{1}H NMR ($CDCl_3$, 400 mHz): δ (ppm) = 3.85 (s, 3H), 3.88 (s, 3H), 6.92 (d, *J* = 8.8 Hz, 2H), 7.71 (d, *J* = 9.2 Hz, 2H), 8.60 (s, 1H); MS (ESI-QTOF) m/z: $[M + H]^+$ Calcd for $C_9H_{12}NO_3$ 182.08; Found 182.09.

4.7.2 **Synthesis of compound c (4-methoxy-2-(4-methylbenzoyl)benzoic acid: $C_{16}H_{14}O_4$)**

Compound **b** 2.91 g (16.1 mmol), *tert*-butyl hydroperoxide 70 % (aq) 10.8 mL (80 mmol, 5 eq), palladium(II) acetate 36.0 mg (0.16 mmol, 0.01 eq), *p*-tolualdehyde 8 mL (64 mmol, 4eq), dimethyl sulfoxide 40 mL and dioxane 10 mL were mixed. Borontrifluoride diethyl ether complex 0.8 mL (6.4 mmol, 0.25 eq) was added to the mixture while stirring. The solution was refluxed at 130 °C for 12 h. The solution was cooled down and monitored by TLC. HCl 12 M 30 mL (360 mmol, 23 eq) was added, and the solution was heated at 100 °C for 2 d. The solution was cooled down to room temperature. Water 80 mL and ethyl acetate 40 mL were added to the solution. The solution was separated and the aqueous layer was extracted by ethyl acetate 4 times. The combined organic layer was washed by water 1 time, and dried by brine and Na_2SO_4. The product was purified in 3 steps: activated charcoal, basic extraction and column chromatography, respectively.

The activated charcoal 5 g was added to the product solution in ethyl acetate and stirred for 1.5 h. After filtering charcoal, the solution was dried by rotatory evaporator. The crude product was re-dissolved by diethyl ether 100 mL and NaOH 5 % (aq) 50 mL. The biphasic solution was separated, and the organic layer was extracted by NaOH 5 % (aq) 2 times. The combined aqueous solution was washed by diethyl ether 3 times. The diethyl ether was removed completely by rotatory evaporator. Then, the solution was cooled in ice bath and acidified by HCl until pH less than 3. The light-brown precipitate was formed. The suspension was filtered and dried under vacuum. The product was purified by column chromatography using diethyl ether and hexane at 1:1 to 3:1 with 1 % acetic acid and 50 times silica gel weight. The compound **c** 2.29 g (8.51 mmol, 52.9 % yield) was obtained as pale-brown solid: ^{1}H NMR (500 mHz, $CDCl_3$): δ (ppm) = 2.40 (s, 3H), 3.86 (s, 3H), 6.81 (d, *J* = 7.5 Hz, 1H), 7.00 (dd, *J* = 2.6 Hz, *J* = 11.5 Hz, 2H), 7.21 (d, *J* = 7.9 Hz, 2H), 7.62 (d, *J* = 8.2 Hz, 2H), 8.03 (d, *J* = 8.8 Hz, 1H);

^{13}C NMR ($CDCl_3$, 125 MHz): δ (ppm) = 21.66, 42.65, 55.68, 61.68, 112.78, 114.66, 119.70, 129.14, 133.13, 134.47, 163.43, 169.70; MS (ESI-TOF) m/z: $[M - H]^-$ Calcd for $C_{16}H_{13}O_4$ 269.08; Found 269.08.

4.7.3 Synthesis of compound d (4-methoxy-2-[(4-methylphenyl)methyl]benzoic acid: $C_{16}H_{16}O_3$)

Compound **c** 510 mg (1.89 mmol) was dissolved in acetic acid 3 mL and dimethylformamide 3 mL at 70 °C until completely dissolved. The solution was bubbled by Ar for 50 min to minimize oxygen content. Pd / C 10 % 46 mg (10 w %) was added to the solution under Ar flow. The solution was bubbled by H_2 and the reaction was monitored by TLC. After 24 h, the Pd / C suspension was filtered and washed by dimethylformamide. Water 150 mL was added to the filtrate, and the product was precipitated in the form of white solid. The solution was cooled at 4 °C overnight to maximize the recovery. The white precipitate was recovered by filtering and dried under vacuum. The compound **d** 388 mg (1.51 mmol, 79.9 % yield) was obtained as white solid: ^{1}H NMR ($CDCl_3$, 400 MHz): δ (ppm) = 2.33 (s, 3H, Ar-CH_3), 3.82 (s, 3H, OCH_3), 4.43 (s, 2H, CH_2), 6.72 (d, *J* = 2.4 Hz, 1H, Ar-H), 6.82 (dd, *J* = 2.8 Hz, *J* = 8.8 Hz, 1H, Ar-H), 7.09 (m, 4H, Ar-H), 8.10 (d, *J* = 8.8 Hz, 1H, Ar-H), 11.10 (br, 1H, COOH). MS (ESI-TOF) m/z: $[M - H]^-$ Calcd for $C_{16}H_{15}O_3$: 255.10; Found 255.19.

4.7.4 Synthesis of compound e (2-methoxy-6-methylanthracene: $C_8H_8O_3$)

Compound **d** 1.44 g (5.60 mmol) and polyphosphoric acid 18 g was stirred and heated at 80 °C for 4 h. Water 100 mL and dichloromethane 100 mL were added to the solution and separated. The aqueous solution was extracted by dichloromethane 3 times. The combined organic layer was washed by NaOH 10 % (aq) 50 mL and brine, and dried by Na_2SO_4, rotatory evaporator and under vacuum overnight. The dried compound was dissolved in diglyme 20 mL under Ar. The solution was bubbled by Ar for 1.5 h before addition of $NaBH_4$ 869 mg (23 mmol, 4 eq). The solution was bubbled for 30 min and stopped. The solution was cooled in the ice bath. Additional $NaBH_4$ 436 mg (12 mmol, 2 eq) in methanol 10 mL was added, and the solution was stirred at room temperature for 18 h. Acetic acid 50 mL was added, and the solution was stirred for additional 3 h. Water 100 mL was slowly added while the solution was vigorously stirred. The precipitate was filtered, washed by water 100 mL and dried under vacuum overnight. The precipitate was purified by column chromatography (hexane : ethyl acetate 1 : 0 to 100 : 1). The pure compound **e** 371 mg (1.67 mmol, 29.8 % yield) was obtained as yellow solid: ^{1}H NMR ($CDCl_3$, 400 MHz): δ (ppm) = 2.53 (s, 3H, Ar-CH_3), 3.96 (s, 3H, OCH_3), 7.14 (dd, *J* = 2.4 Hz, *J* = 8.0 Hz, 1H, Ar-H), 7.18 (d, *J* = 2.4 Hz, 1H, Ar-H), 7.30 (m, 1H, Ar-H), 7.72 (s, 1H, Ar-H), 7.86 (m, 2H, Ar-H), 8.23 (d, *J* = 4.0 Hz, 1H, Ar-H).

4.7.5 Synthesis of MAC (6-methoxy-2-anthracenecarboxylic acid: $C_8H_8O_3$)

The synthesis of MAC composed of 3 steps: protection, oxidation and deprotection. The protection step was ethanoanthracene synthesis. Compound **e** 301 mg (1.36 mmol) and fumaric acid 351 mg (3.02 mmol, 2 eq) were dissolved in 8.5 mL dioxane under Ar atmosphere. The solution was refluxed for 3 d and dried by rotatory evaporator. The dried product was dissolved in chloroform 15 mL. The precipitate (fumaric acid) was washed by chloroform 5 mL 2 times. The combined organic solution was extracted by NaOH 10 % (aq) 30 mL 2 times and water 20 mL. The combined aqueous layer was acidified by HCl until pH less than 4 and extracted by chloroform 50 mL 2 times. The combined organic layer was dried by Na_2SO_4 and rotatory evaporator. 2-methoxy-6-methyl-9,10-dihydro-9,10-Ethanoanthracene-11,12-dicarboxylic acid (ethanoanthracene derivative) 314 mg (0.929 mmol, 68.5 % yield) was obtained as pale-yellow solid. This step was repeated several times with the same scale.

The ethanoanthracene derivative was oxidized by $KMnO_4$. The ethanoanthracene derivative 919 mg (2.72 mmol) was dissolved in NaOH 0.5 M (aq) 30 mL at 70 °C until completely dissolved. $KMnO_4$ 1.07 g (6.79 mmol, 2.5 eq) was added, and the solution was stirred for 20 h. The solution was filter. The precipitate was washed by hot water 8 mL 2 times. The filtrate was acidified by HCl until pH less than 4 and extracted by diethyl ether 30 mL 3 times. The combined organic layer was dried by Na_2SO_4 and rotatory evaporator. The crude oxidized ethanoanthracene derivative 800 mg (2.17 mmol, 80.0 % yield) was obtained.

The fumaric acid was deprotected from anthracene under high temperature. The oxidized ethanoanthracene derivative 503 mg (1.37 mmol) was dissolved in diphenylether 10 mL. The solution was freeze-pump-thaw degassed 7 times. Then, it was heated at 255 °C for 5 h. The sublimed white solid (fumaric acid) was observed. The solution was separated from the sublimed solid. Hexane was added and filtered. The precipitate was washed by hexane, carbon tetrachloride and small amount of ethyl acetate. The precipitate was purified by sublimation (210 °C, 18 mmHg). The pure MAC 150 mg (0.595 mmol, 43 % yield, overall yield for 3 steps is 24 %) was obtained as bright-yellow solid: : 1H NMR ($(CD_3)_2SO$, 600 MHz): δ (ppm) = 3.95 (s, 3H, OCH_3), 7.44 (d, *J* = 2.4 Hz, 1H, Ar-H), 7.91 (dd, *J* = 1.8 Hz, *J* = 9.0 Hz, 1H, Ar-H), 8.05 (d, *J* = 9.0 Hz, 1H, Ar-H), 8.08 (d, *J* = 9.0 Hz, 1H, Ar-H), 8.47 (s, 1H, Ar-H), 8.72 (s, 1H, Ar-H), 8.74 (s, 1H, Ar-H). 13.02 (br, 1H, COOH); ^{13}C NMR ($(CD_3)_2SO$, 150 MHz): δ (ppm) = 55.22, 103.78, 120.86, 123.81, 124.23, 127.72, 128.44, 128.45, 130.01, 131.64, 132.55, 133.91, 157.59, 157.59, 167.39; MS (ESI-TOF) m/z: $[M - H]^-$ Calcd for $C_{16}H_{11}O_3$: 251.07; Found 251.06.

4.7.6 Synthesis of AC-Chd ((2-*trans*-hydroxycyclohexyl)-2-anthroate: $C_{21}H_{20}O_3$)

AC 229 mg (1.0 mmol), *trans*-1,2-cyclohexanediol 118 mg (1.0 mmol, 1 eq), DMAP 62 mg (0.51 mmol, 0.5 eq), EDC·HCl 384 mg (2.0 mmol, 2 eq) and HOBt 337 mg (2.5 mmol, 2.5 eq) were dissolved in the solvent mixture of toluene 16 mL and dichloromethane 8 mL in the ice bath under Ar atmosphere. The solution was heated to room temperature and stirred overnight. The additional dichloromethane 10 mL was added and the reaction solution was kept stirring until 24 h. The crude product was obtained from solvent evaporation and purified by column chromatography (dichloromethane : hexane 1 : 1 to 2 : 1). The pure AC-Chd 143 mg (0.446 mmol, 43 % yield) was obtained as pale yellow solid: ^1H NMR ($(CD_3)_2SO$, 400 MHz): δ (ppm) = 1.25-1.53 (m, 4H, C-H_2), 1.63-1.74 (m, 2H, C-H_2), 1.90-1.98 (m, 1H, C-H_2), 1.99-2.07 (m, 1H, C-H_2), 3.65 (m, 1H, O-C-H), 4.81 (m, 1H, H-C-O), 5.05 (d, *J* = 7.4 Hz, 1H, OH), 7.60 (m, 2H, Ar-H), 7.97 (dd, *J* = 13.3 Hz, *J* = 2.4 Hz, 1H, Ar-H), 8.15 (dd, *J* = 10.8 Hz, *J* = 3.7 Hz, 2H, Ar-H), 8.19 (d, *J* = 13.7 Hz, 1H, Ar-H), 8.67 (s, 1H, Ar-H), 8.85 (m, 2H, Ar-H); ^{13}C NMR ($(CD_3)_2SO$, 150 MHz): δ (ppm) = 23.02, 23.24, 29.34, 32.92, 70.08, 77.53, 123.82, 126.04, 126.72, 127.07, 128.02, 128.28, 128.45, 128.57, 129.77, 131.49, 131.61, 131.99, 132.51, 165.42; MS (ESI-TOF) m/z: $[M + Na]^+$ Calcd for $C_{21}H_{20}O_3Na$ 343.13; Found 343.14.

4.7.7 Synthesis of AC-Chd-MAC (*trans*-1,2-cyclohexanediyl 1-(6-methoxy-2-anthroate)-2-(2-anthroate): $C_{37}H_{30}O_5$)

MAC 50 mg (0.20 mmol), AC-Chd 157 mg (0.49 mmol, 2.5 eq), DMAP 26 mg (0.21 mmol, 1 eq), EDC·HCl 76 mg (0.40 mmol, 2 eq) and HOBt 64 mg (0.48 mmol, 2.4 eq) were dissolved in the solvent mixture of toluene 12 mL and dichloromethane 8 mL in the ice bath under Ar atmosphere. The solution was heated to room temperature and stirred for 49 h. The crude product was obtained from solvent evaporation and purified by column chromatography (dichloromethane : hexane 1 : 1 to 2 : 1, chloroform). The pure AC-Chd-MAC 77 mg (0.14 mmol, 70 % yield) was obtained as a pale yellow solid: ^{1}H NMR (($(CD_3)_2SO$, 400 MHz): δ (ppm) = 1.50-1.61 (m, 2H, CH_2), 1.72-1.81 (m, 2H, CH_2), 1.81-1.88 (m, 2H, CH_2), 2.23 (m, 1H, CH_2), 2.26 (m, 1H, CH_2), 3.90 (s, 3H, OCH_3), 5.29-5.36 (m, 2H, OCH), 7.21 (dd, *J* = 9.2 Hz, *J* = 2.4 Hz, 2H, Ar-H), 7.36 (d, *J* = 2.4 Hz, 1H, Ar-H), 7.52-7.58 (m, 2H, Ar-H), 7.83 (dd, *J* = 8.9 Hz, *J* = 1.6 Hz, 1H, Ar-H), 7.85 (dd, *J* = 8.9 Hz, *J* = 1.7 Hz, 1H, Ar-H), 7.99 (d, *J* = 5.9 Hz, 1H, Ar-H), 8.00 (d, *J* = 5.9 Hz, 1H, Ar-H), 8.05-8.10 (m, 3H, Ar-H), 8.36 (s, 1H, Ar-H), 8.64 (s, 1H, Ar-H), 8.70 (d, *J* = 0.6 Hz, 1H, Ar-H), 8.73 (s, 1H, Ar-H), 8.76 (d, *J* = 0.7 Hz, 1H, Ar-H); MS (ESI-TOF) m/z: $[M]^+$ Calcd for $C_{37}H_{30}O_5Na$ 554.21; Found 553.99, $[M + Na]^+$ Calcd for $C_{37}H_{30}O_5Na$ 577.20; Found 576.93.

4.7.8 Synthesis of Chd(AC-MAC dimer3) (*trans*-1,2-cyclohexanediyl 6-methoxy-2-anthroate 2-anthroate *anti-head-to-head* heterodimer: $C_{37}H_{30}O_5$)

AC-Chd-MAC 77 mg (0.14 mmol) was dissolved in tetrahydrofuran 140 mL under Ar atmosphere. To completely remove the oxygen, the solution was freeze-pump-thaw degassed for 7 times and warmed to room temperature. The solution was then irradiated by 365 nm light using monochrome LED 365L2 (max 360 mW, max 700 mA, mounted LED by Thorlabs, Inc.) with 300 mA (100 mW) for 11 h. The time of irradiation is varied depending on the volume. The reaction was followed by absorption spectra at 380 nm, which is typical anthracene absorption but will be disappeared when becoming dimers. The crude product was recovered by solvent evaporation as brown clear viscous oil. The dimer was purified by column chromatography (dichloromethane : hexane 4 : 1 to 8 : 1, chloroform). The pure Chd(AC-MAC dimer3) 53 mg (0.096 mmol, 69 % yield) was obtained as a light cream color solid: ^{1}H NMR ($CDCl_3$, 600 MHz): δ (ppm) = 1.48 (m, 2H, CH_2), 1.63 (m, 2H, CH_2), 1.88 (m, 2H, CH_2), 2.18 (d, *J* = 13.6 Hz, 2H, CH_2), 3.65 (s, 3H, OCH_3), 4.36 (d, *J* = 10.5 Hz, 1H, Ar-CH), 4.39 (d, *J* = 10.4 Hz, 1H, Ar-CH), 4.47 (d, *J* = 10.6 Hz, 1H, Ar-CH), 4.50 (d, *J* = 10.6 Hz, 1H, Ar-CH), 5.01 (m, 2H, OCH), 6.43 (dd, *J* = 2.5 Hz, *J* = 8.1 Hz, 1H, Ar-H), 6.48 (d, *J* = 2.5 Hz, 1H, Ar-H), 6.86-7.02 (m, 9H, Ar-H), 7.50 (m, 2H, Ar-H); MS (MALDI-TOF) m/z: $[M]^+$ Calcd for $C_{37}H_{30}O_5$ 554.21; Found 554.21, $[M + Na]^+$ Calcd for $C_{37}H_{30}O_5Na$ 577.20; Found 576.83

4.7.9 Synthesis of Chd(AC-HAC dimer3) (*trans*-1,2-cyclohexanediyl 6-hydroxy-2-anthroate 2-anthroate *anti-head-to-head* heterodimer: $C_{36}H_{28}O_5$)

Chd(AC-MAC dimer3) 53 mg (0.096 mmol) was dissolved in dichloromethane 1 mL in the ice bath under Ar atmosphere. $AlCl_3$ 387 mg (2.9 mmol, 30 eq) was dissolved in ethanethiol 1 mL and dichloromethane 1 mL in the ice bath under Ar atmosphere. The $AlCl_3$ solution was added to the Chd(AC-MAC dimer3) solution under Ar atmosphere. The solution was heated to room temperature and stirred overnight. The cold HCl (aq) pH 3 20 mL was added to the cold reaction solution followed by dichloromethane 20 mL. The solution was separated and the aqueous layer was extracted by dichloromethane 4 times. The combined organic layer was dried by Na_2SO_4 and rotatory evaporator, and purified by column chromatography (dichloromethane, chloroform). The fairy pure (85 % purity estimated by ^{1}H NMR) Chd(AC-HAC dimer3) 33 mg (0.061 mmol, 64 % yield) was obtained as light cream solid: ^{1}H NMR ($CDCl_3$, 600 MHz): δ (ppm) = 1.48 (m, 2H, CH_2), 1.63 (m, 2H, CH_2), 1.89 (m, 2H, CH_2), 4.34-4.54 (m, 4H, Ar-CH), 5.01 (m, 2H, OCH), 6.36 (dd, J = 3.8 Hz, J = 11.9 Hz, 1H, Ar-H), 6.43 (d, J = 3.8 Hz, 1H, Ar-H), 6.83 (d, J = 11.9 Hz, 1H, Ar-H), 6.89-7.03 (m, 8H, Ar-H), 7.51 (m, 2H, Ar-H); MS (ESI-QTOF) m/z: $[M - H]^-$ Calcd for $C_{36}H_{27}O_5$ 539.19; Found 539.16.

4.7.10 **Synthesis of dimethyl(AC-HAC dimer3) (methyl 6-hydroxy-2-anthroate methyl 2-anthroate *anti-head-to-head* heterodimer: $C_{32}H_{24}O_5$)**

Chd(AC-HAC dimer3) 33 mg (0.061 mmol assuming 100 % purity) was dissolved in dichloromethane 4 mL and methanol 3 mL. KOH 1 M in methanol 618 uL (10 eq) was added to the solution and stirred for 2 h. Water 10 mL and dichloromethane 5 mL was added to the solution and separated. The aqueous layer was extract by DCM 5 mL. The combined organic layer was dried by Na_2SO_4 and rotatory evaporator to yield basic extraction product 30 mg. The aqueous layer was acidified by HCl until pH less than 2. Then, it was extracted by dichloromethane 5 mL 3 times and diethyl ether 5 mL 1 time. The combined organic layer was dried by Na_2SO_4 and rotatory evaporator to afford the acidic extraction product 8 mg.

Table 4-1. Parameters for HPLC purification of dimethyl(AC-HAC dimer3)

Parameters	Purification Condition
HPLC Equipment	JASCO
Column	CHIRALPAK® IA 20ID × 250 mm
Temperature	Room Temperature
Injection Volume	50 - 300 µL
Solvent	Chloroform and Hexane
Gradient	60 % Chloroform 0 - 15 min 60 - 75 % Chloroform 15 - 45 min 75 % Chloroform 45 - 75 min 75 - 60 % Chloroform 75 - 90 min
Flow Rate	8 mL / min
Detector	UV 250 nm Array 250 nm and 370 nm

Both acidic and basic products were purified by HPLC equipped with chiral column. (Table 4-1) Two enantiomers of dimethyl(AC-HAC dimer3) were obtained as pale-yellow powder 6.6 mg (0.014 mmol, 23 %) and 6.0 mg (0.012 mmol, 20 % yield). The CDs were mirror images, and the NMRs were identical: ^{1}H NMR ($CDCl_3$, 500 MHz): δ (ppm) = 3.83 (s, 6H, OCH_3), 4.51 (d, J = 11.0 Hz, 1H, Ar-CH), 4.65-4.78 (br, 1H, OH), 6.29 (dd, J = 2.5 Hz, J = 8.0 Hz, 1H, Ar-H), 6.47 (d, J = 2.5 Hz, 1H, Ar-H), 6.77 (d, J = 8.0 Hz, 1H, Ar-H), 6.87 (m, 2H, Ar-H), 6.92-7.01 (m, 4H, Ar-H), 7.50 (d, J = 1.5 Hz, 1H, Ar-H) , 7.49 (d, J = 2.0 Hz, 1H, Ar-H) 7.58 (br, 2H, Ar-H); ^{13}C NMR ($CDCl_3$, 125 MHz): δ (ppm) = 51.98, 52.50, 53.19, 53.43, 53.55, 112.18, 114.68, 126.00, 126.06, 127.15, 127.17, 127.38, 127.47, 127.68, 127.74, 127.88, 128.14, 134.98, 142.34, 143.26, 143.77, 144.10, 149.07, 153.57, 167.02; MS (ESI-QTOF) m/z: $[M + H]^+$ Calcd for $C_{32}H_{25}O_5$ 489.2; Found 489.2.

4.7.11 Synthesis of *(P)*-AC-HAC dimer3 (*(P)*-6-hydroxy-2-anthracenecarboxylic acid 2-anthracenecarboxylic acid *anti-head-to-head* heterodimer: $C_{30}H_{20}O_5$)

(P)-Dimethyl(AC-HAC dimer3) 6.3 mg (12 µmol) was dissolved in THF 300 µL and water 420 µL. After completely dissolved, KOH 5 M (aq) 480 µL was added, and the solution was stirred at 65 °C for 3 h. Water 10 mL and chloroform 10 mL were added and separated. The organic layer was dried by Na_2SO_4 and rotatory evaporator, and kept as basic extracted solution. The aqueous solution was then acidified by HCl 6 M and extracted by chloroform 20 mL 2 times and dichloromethane 20 mL 2 times. The solid formed during the acidification that did not dissolve in organic layer was also kept. The combined organic layer was dried by Na_2SO_4 and rotatory evaporator, and kept as acidic extract. The acidic extract was purified by TLC, but the product was not pure and used as a crude *(P)*-AC-HAC: MS (ESI-QTOF) m/z: $[M - H]^-$ Calcd for $C_{30}H_{19}O_5$ 459.12; Found 459.12.

4.7.12 Circular Dichroism Measurement of Dimethyl(AC-HAC dimer3) and *(P)*-(AC-HAC dimer3)

The JASCO J-820 CD machine (JASCO, Japan) was equipped with Single Position Peltier Cell Holder. The sample was diluted by tetrahydrofuran in 1 × 1 cm quartz cuvette. The measurement was conducted with scan speed 100 nm / min, bandwidth 1.00 nm, data integration time 4 s, standard sensitivity, accumulation 4 times. Tetrahydrofuran has UV cut off at 220 nm; therefore, HT exceeds 600 nm at 225 nm and the shorter wavelength. In this region, the CD and absorption intensities are not reliable, so only the rough spectral patterns are considered.

4.7.13 Circular Dichroism Calculation of *(P)*-(AC-HAC dimer3)

The calculation mostly based on previously reported method with some slight modification.[22] The calculation was performed using TURBOMOLE Version 7.4.1 software.[337] The basis set used for all atoms is def2-TZVPP.[338] For the ground state, the DFT calculation was carried out with TPSS meta-GAA (generalized gradient approximation) functional and DFT-D4 dispersion.[339] The excited-state calculation was performed in RICC2 (coupled cluster with the resolution of identity approximation) level.[340,341] The information, including energy, oscillator strength and rotator strength, of 30 excited states was generated.

With large basis set of def2-TZVPP, the length and velocity rotational strengths are less than 10 % difference, showing comparable calculated rotatory strength to the experimental CD spectrum. The CD and UV-Vis absorption spectra were simulated by overlapping Gaussian functions of all 30 transitions with the length-gauge representations as relative intensity. The 0.2 eV red shift was performed similar to previous report.[22] The distribution coefficient (variance) is the same for both CD and absorption spectra; however, the intensities were fitted differently corresponding to the experimental data.

GENERAL CONCLUSION

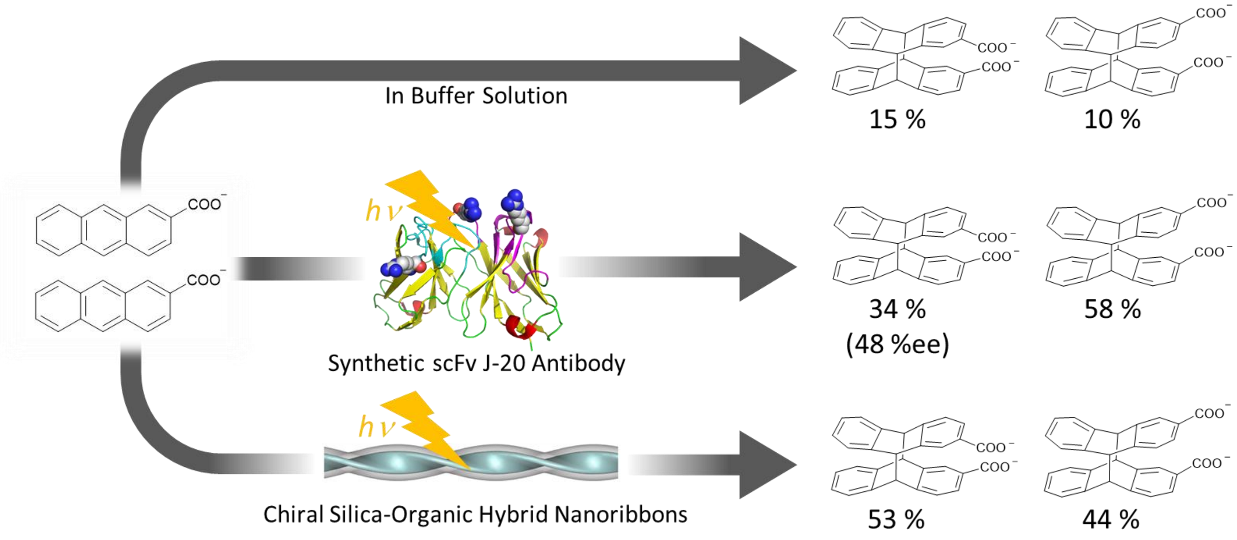

Supramolecular photocyclodimerization of 2-anthracenecarboxylate mediated by two different media in water were demonstrated with high regioselectivity of *head-to-head* 2-anthracenecarboxylate dimers, which are not favourable in water due to the steric hinderance and electrostatic repulsion, and enantioselectivity of *anti-head-to-head* 2-anthracenecarboxylate dimer.

The chiral silica-organic hybrid nanoribbons, containing self-assembled twisted double-bilayer of gemini L- or D-tartrate surfactants inside silica walls, were used as a template for the chirality induction of 2-anthracenecarboxylate. Strong exciton-coupling induced CD signal at 240 nm was found (g-factor −6 and 7 × 10^{-3} at the maxima for L-isomer and vice versa). The anion exchange between tartrate and 2-anthracenecarboxylate depends on the temperature and the condition of hybrid nanoribbons stock. The intensity and stability of induced CD depend on concentration, time and temperature. For 2-anthracenecarboxylate, the maximum of half of gemini surfactant was utilized for AC binding. The exchange efficiency depends on not only the acidity but also the structure of anions. Together, the orientation of 2-anthracenecarboxylate was proposed. This insight information is useful to expand the use of chiral silica-organic hybrid nanostructures and other surfactant self-assemblies.

The supramolecular [4+4] photocyclodimerization of 2-anthracenecarboxylate was conducted inside the silica-organic hybrid nanoribbons, which is the first time utilizing this silica-organic hybrid nanostructure as a reaction template. At the ratio of 2-anthracenecarboxylate to hybrid nanoribbons 1 to 1, the *head-to-head* dimers can be produced up to 97 % product distribution, which can be considered as a near-perfect regioselectivity. This result is by far the only absolute *head-to-head* photocyclodimerization of 2-anthracenecarboxylate using only water as a solvent at room temperature. Any lower temperature and / or 2-anthracenecarboxylate to hybrid nanoribbons ratio can afford more than 90 % *head-to-head* product distribution. The reaction rate increased significantly, so typical 8 W UV-A lamp can be used as a light source for the photocyclodimerization. Using hybrid nanoribbons demonstrates not only a significant improvement of regioselectivity but also a potential reduction of time, energy and cost used in photochemical reactions. There are many interesting prospects in this system such as enantioselectivity, *syn*- and *anti*-isomer selectivity, or recycling silica-organic hybrid nanoribbons.

The synthetic antibody, obtained from phage display screening, was used as a chiral supramolecular host for [4+4] photocyclodimerization of 2-anthracenecarboxylate. The phage display technique does not involve animal experiment, reducing time and cost of operations. The confined cavity of synthetic antibody was designed to resemble target product, *anti-head-to-head* 2-anthracenecarboxylate dimer. The amino acid sequence of obtained antibody is accessible, so the binding site can be located, and the manipulation of antibody is possible. Although this technique has been used in protein therapeutics, it has not been widely used for catalytic antibodies.

The antibody was synthesized by protein expression in *E. coli* BL21(DE3) cells containing the engineered plasmid. The protein was collected and purified from periplasm. The interactions between the synthetic antibody and both 2-anthracenecarboxylate and dimer were investigated. By using this antibody as a chiral supramolecular host, [4+4] photocyclodimerization of 2-anthracenecarboxylate favors *head-to-head* dimers and affords enantioselectivity for *anti*-isomer. With optimized external factors, the product distributions of *syn*- and *anti-head-to-head* dimers became 58 % and 33 %, giving a total of 91 % *head-to-head* selectivity. In addition, 48 % enantiomeric excess of *anti-head-to-head* was found. Effect of external factors is important information for not only synthetic antibody but also any supramolecular biomolecule templates. This result can lead to different possible future research such as different photochemical reactions or products, stabilization of antibody, different antibody libraries, and the improvement of the other phage display protocols.

The initiation on improving phage display protocols is also reported in this work. The new target molecule, *anti-head-to-head* heterodimer of 6-hydroxy-2-anthracenecarboxylic acid and 2-anthracenecarboxylic acid, was designed based on the combination of external factor effects and reaction site structures. The synthesis and purification of heterodimer was finished, and hopefully can be applied to phage display screening in the near future.

Moreover, this work proposed sustainable supramolecular photochemical reaction systems. The silica-organic hybrid nanostructures are good candidates for stable and recyclable templates. Synthetic antibodies obtained from animal-free experiment are biodegradable. In addition, both systems can be performed in water without any rare metal catalysts, and both templates can increase the reaction rates, reducing time and energy consumption. Finally, they possess potential to be generalized and widely used in different photochemical reactions and products.

REFERENCE

(1) McMurry, J. Chapter 5 Stereochemistry and Tetrahedral Centers. In *Organic Chemistry*; Cengage Learning: Boston, 2016; pp 115–148.

(2) Barron, L. D. Chirality and Magnetism Shake Hands. *Nat. Mater.* **2008**, *7*, 691–692.

(3) Pasteur, L. Mémoires Sur La Relation Qui Peut Exister Entre La Forme Crystalline et Al Composition Chimique, et Sur La Cause de La Polarization Rotatoire. *Compt. rend.* **1848**, *26*, 535–538.

(4) Pasteur, L. Mémoire Sur La Fermentation de l'acide Tartrique. *Compt. rend.* **1858**, *45*, 615–618.

(5) Barnett, J. A. A History of Research on Yeasts 2: Louis Pasteur and His Contemporaries, 1850-1880. *Yeast* **2000**, *16*, 755–771.

(6) Gal, J. The Discovery of Biological Enantioselectivity: Louis Pasteur and the Fermentation of Tartaric Acid, 1857—A Review and Analysis 150 Yr Later. *Chirality* **2008**, *20*, 5–19.

(7) Van't Hoff, J. H. Sur Le Formules de Structure Dans l'espace. *Arch Neerl* **1874**, *9*, 1–10.

(8) Le Bel, J. A. Sur Les Relations Qui Existent Entre Les Formules Atomiques Des Corps Organiques et Le Pouvoir Rotatoire de Leurs Dissolutions. *Bul Soc Chim Paris* **1874**, *22*, 337–347.

(9) Gal, J.; Cintas, P. Early History of the Recognition of Molecular Biochirality. *Top Curr Chem* **2013**, *333*, 1–40.

(10) Gal, J. The Discovery of Stereoselectivity at Biological Receptors: Arnaldo Piutti and the Taste of the Asparagine Enantiomers—History and Analysis on the 125th Anniversary. *Chirality* **2012**, *24*, 959–976.

(11) Kawai, M.; Sekine-Hayakawa, Y.; Okiyama, A.; Ninomiya, Y. Gustatory Sensation of L-And D-Amino Acids in Humans. *Amino Acids* **2012**, *43*, 2349–2358.

(12) Bassoli, A.; Borgonovo, G.; Caremoli, F.; Mancuso, G. The Taste of D- and L-Amino Acids: In Vitro Binding Assays with Cloned Human Bitter (TAS2Rs) and Sweet (TAS1R2/TAS1R3) Receptors. *Food Chem.* **2014**, *150*, 27–33.

(13) Cretin, B. N.; Sallembien, Q.; Sindt, L.; Daugey, N.; Buffeteau, T.; Waffo-Teguo, P.; Dubourdieu, D.; Marchal, A. *How Stereochemistry Influences the Taste of Wine: Isolation, Characterization and Sensory Evaluation of Lyoniresinol Stereoisomers*; Elsevier Ltd, 2015; Vol. 888.

(14) Bachmanov, A. A.; Bosak, N. P.; Glendinning, J. I.; Inoue, M.; Li, X.; Manita, S.; McCaughey, S. A.; Murata, Y.; Reed, D. R.; Tordoff, M. G.; Beauchamp, G. K. Genetics of Amino Acid Taste and Appetite. *Adv. Nutr. An Int. Rev. J.* **2016**, *7*, 806S-822S.

(15) Fischer, E. Ueber Die Configuration Des Traubenzuckers Und Seiner Isomeren. *Berichte der Dtsch. Chem. Gesellschaft* **1891**, *24*, 1836–1845.

(16) Fischer, E. Ueber Die Configuration Des Traubenzuckers Und Seiner Isomeren. II. *Berichte der Dtsch. Chem. Gesellschaft* **1891**, *24*, 2683–2687.

(17) Smyth, D. R. Helical Growth in Plant Organs: Mechanisms and Significance. *Dev.* **2016**, *143*, 3272–3282.

(18) Schilthuizen, M.; Davison, A. The Convoluted Evolution of Snail Chirality. *Naturwissenschaften*

2005, *92*, 504–515.

(19) Grande, C.; Patel, N. H. Nodal Signalling Is Involved in Left-Right Asymmetry in Snails. *Nature* **2009**, *457*, 1007–1011.

(20) Bailey, J. Astronomical Sources of Circularly Polarized Light and the Origin of Homochirality. *Orig. Life Evol. Biosph.* **2001**, *31*, 167–183.

(21) Sun, P.; Krishnan, A.; Yadav, A.; MacDonnell, F. M.; Armstrong, D. W. Enantioseparations of Chiral Ruthenium(II) Polypyridyl Complexes Using HPLC with Macrocyclic Glycopeptide Chiral Stationary Phases (CSPs). *J. Mol. Struct.* **2008**, *890*, 75–80.

(22) Wakai, A.; Fukasawa, H.; Yang, C.; Mori, T.; Inoue, Y. Theoretical and Experimental Investigations of Circular Dichroism and Absolute Configuration Determination of Chiral Anthracene Photodimers. *J. Am. Chem. Soc.* **2012**, *134*, 4990–4997.

(23) Harada, N. Chiral Molecular Science: How Were the Absolute Configurations of Chiral Molecules Determined? "Experimental Results and Theories." *Chirality* **2017**, *29*, 774–797.

(24) Xu, H.; Zou, X. Absolute Structure, at the Nanoscale. *Science (80-.).* **2019**, *364*, 632–633.

(25) Tanaka, H.; Inoue, Y.; Mori, T. Circularly Polarized Luminescence and Circular Dichroisms in Small Organic Molecules: Correlation between Excitation and Emission Dissymmetry Factors. *ChemPhotoChem* **2018**, *2*, 386–402.

(26) Gad, S. C.; Zsila, F. Electronic Circular Dichroism Spectroscopy. *Pharm. Sci. Encycl.* **2010**, 1–61.

(27) Shindo, Y.; Ohmi, Y. Problems of CD Spectrometers. 3. Critical Comments on Liquid Crystal Induced Circular Dichroism. *J. Am. Chem. Soc.* **1985**, *107*, 91–97.

(28) Riehl, J. P.; Richardson, F. S. Circularly Polarized Luminescence Spectroscopy. *Chem. Rev.* **1986**, *86*, 1–16.

(29) Kumar, J.; Nakashima, T.; Kawai, T. Circularly Polarized Luminescence in Chiral Molecules and Supramolecular Assemblies. *J. Phys. Chem. Lett.* **2015**, *6*, 3445–3452.

(30) Rikken, G. L. J. A.; Raupach, E. Observation of Magneto-Chiral Dichroism. *Nature* **1997**, 2–3.

(31) Train, C.; Gheorghe, R.; Krstic, V.; Chamoreau, L. M.; Ovanesyan, N. S.; Rikken, G. L. J. A.; Gruselle, M.; Verdaguer, M. Strong Magneto-Chiral Dichroism in Enantiopure Chiral Ferromagnets. *Nat. Mater.* **2008**, *7*, 729–734.

(32) Van Der Wel, H.; Van Der Heijden, A.; Peer, H. G. Sweeteners. *Food Rev. Int.* **1987**, *3*, 193–268.

(33) Mosandl, A. Chirality in Flavor Chemistry – Recent Developments in Synthesis and Analysis. *Food Rev. Int.* **1988**, *4*, 1–43.

(34) Fanali, C.; D'Orazio, G.; Gentili, A.; Fanali, S. Analysis of Enantiomers in Products of Food Interest. *Molecules* **2019**, *24*.

(35) Ye, J.; Zhao, M.; Niu, L.; Liu, W. Enantioselective Environmental Toxicology of Chiral Pesticides. *Chem. Res. Toxicol.* **2015**, *28*, 325–338.

(36) Franks, M. E.; Macpherson, G. R.; Figg, W. D. Thalidomide. *Lancet* **2004**, *363*, 1802–1811.

(37) Kim, J. H.; Scialli, A. R. Thalidomide: The Tragedy of Birth Defects and the Effective Treatment of Disease. *Toxicol. Sci.* **2011**, *122*, 1–6.

(38) Yu, T.; Ding, Z.; Nie, W.; Jiao, J.; Zhang, H.; Zhang, Q.; Xue, C.; Duan, X.; Yamada, Y. M. A.; Li, P.

Recent Advances in Continuous-Flow Enantioselective Catalysis. *Chem. - A Eur. J.* **2020**.

(39) Ma, X.; Pu, M.; Li, X.; Guo, Y.; Gao, P.; Luo, X. Meta-Chirality: Fundamentals, Construction and Applications. *Nanomaterials* **2017**, *7*.

(40) Zhang, D. W.; Li, M.; Chen, C. F. Recent Advances in Circularly Polarized Electroluminescence Based on Organic Light-Emitting Diodes. *Chem. Soc. Rev.* **2020**, *49*, 1331–1343.

(41) Ding, Y.; Pau, S. Circularly and Elliptically Polarized Light under Water and the Umov Effect. *Light Sci. Appl.* **2019**, *8*, 4–9.

(42) Schadt, M. LIQUID CRYSTAL MATERIALS AND LIQUID CRYSTAL DISPLAYS. *Annu. Rev. Mater. Sci.* **1997**, *27*, 305–379.

(43) Chen, Y.; Yang, X.; Gao, J. 3D Janus Plasmonic Helical Nanoapertures for Polarization-Encrypted Data Storage. *Light Sci. Appl.* **2019**, *8*, 45.

(44) Lodahl, P.; Mahmoodian, S.; Stobbe, S.; Rauschenbeutel, A.; Schneeweiss, P.; Volz, J.; Pichler, H.; Zoller, P. Chiral Quantum Optics. *Nature* **2017**, *541*, 473–480.

(45) Yang, Y.; da Costa, R. C.; Smilgies, D.-M.; Campbell, A. J.; Fuchter, M. J. Induction of Circularly Polarized Electroluminescence from an Achiral Light-Emitting Polymer via a Chiral Small-Molecule Dopant. *Adv. Mater.* **2013**, *25*, 2624–2628.

(46) He, D.-Q.; Lu, H.-Y.; Li, M.; Chen, C.-F. Intense Blue Circularly Polarized Luminescence from Helical Aromatic Esters. *Chem. Commun.* **2017**, *53*, 6093–6096.

(47) Zinna, F.; Di Bari, L. Lanthanide Circularly Polarized Luminescence: Bases and Applications. *Chirality* **2015**, *27*, 1–13.

(48) Thorpe, S. L.; Snyder, G. N.; Mammana, A. Spectroscopic Study of Porphyrin Self-Assembly: Role of PH, Time, and Chiral Template. *Chirality* **2020**, *32*, 5–16.

(49) Wolf, C.; Bentley, K. W. Chirality Sensing Using Stereodynamic Probes with Distinct Electronic Circular Dichroism Output. *Chem. Soc. Rev.* **2013**, *42*, 5408–5424.

(50) Fukuhara, G. Polymer-Based Supramolecular Sensing and Application to Chiral Photochemistry. *Polym. J.* **2015**, *47*, 649–655.

(51) Lee, Y. Y.; Kim, R. M.; Im, S. W.; Balamurugan, M.; Nam, K. T. Plasmonic Metamaterials for Chiral Sensing Applications. *Nanoscale* **2020**, *12*, 58–66.

(52) Brandt, J. R.; Salerno, F.; Fuchter, M. J. The Added Value of Small-Molecule Chirality in Technological Applications. *Nat. Rev. Chem.* **2017**, *1*, 45.

(53) Archibald, S. C.; Barden, D. J.; Bazin, J. F. Y.; Fleming, I.; Foster, C. F.; Mandal, A. K.; Mandal, A. K.; Parker, D.; Takaki, K.; Ware, A. C.; Williams, A. R. B.; Zwicky, A. B. Stereocontrol in Organic Synthesis Using Silicon-Containing Compounds. Studies Directed towards the Synthesis of Ebelactone A. *Org. Biomol. Chem.* **2004**, *2*, 1051–1064.

(54) Sudina, P. R.; Motati, D. R.; Seema, A. Stereocontrolled Total Synthesis of Nonenolide. *J. Nat. Prod.* **2018**, *81*, 1399–1404.

(55) Lam, N. Y. S.; Paterson, I. Stereocontrolled Synthesis as an Enabling Tool for the Configurational Assignment of Marine Polyketide Natural Products. *European J. Org. Chem.* **2019**, 1–12.

(56) Ohrui, H. Development of Highly Potent Chiral Discrimination Methods That Solve the Problems of Diastereomer Method. *Anal. Sci.* **2007**, *83*, 127–135.

(57) Harada, N. HPLC Separation of Diastereomers: ChiralMolecular Tools Useful for the Preparation of Enantiopure Compounds and Simultaneous Determination of Their Absolute Configurations. *Molecules* **2016**, *21*, 1328.

(58) Colomban, C.; Châtelet, B.; Martinez, A. Different Strategies for Obtaining Enantiopure Hemicryptophanes. *Synth.* **2019**, *51*, 2081–2099.

(59) Toyo'oka, T. Resolution of Chiral Drugs by Liquid Chromatography Based upon Diastereomer Formation with Chiral Derivatization Reagents. *J. Biochem. Biophys. Methods* **2002**, *54*, 25–56.

(60) Ward, T. J.; Ward, K. D. Chiral Separations: A Review of Current Topics and Trends. *Anal. Chem.* **2012**, *84*, 626–635.

(61) Chankvetadze, B. Recent Trends in Preparation, Investigation and Application of Polysaccharide-Based Chiral Stationary Phases for Separation of Enantiomers in High-Performance Liquid Chromatography. *TrAC - Trends Anal. Chem.* **2020**, *122*, 115709.

(62) Pinto, M. M. M.; Fernandes, C.; Tiritan, M. E. Chiral Separations in Preparative Scale: A Medicinal Chemistry Point of View. *Molecules* **2020**, *25*, 1931.

(63) Vespalec, R.; Boček, P. Chiral Separations in Capillary Electrophoresis. *Chem. Rev.* **2000**, *100*, 3715–3753.

(64) Sarkany, A.; Hancu, G.; Cârje, A.; Drăguț, C.; Papp, L. A. Chiral Separation of Tramadol Enantiomers by Capillary Electrophoresis Using Cyclodextrins as Chiral Selectors and Experimental Design Method Optimization. *Chem. Pap.* **2019**, *73*, 2363–2370.

(65) Papp, L. A.; Hancu, G.; Gyéresi, Á.; Kelemen, H.; Szabó, Z. I.; Noszál, B.; Dubský, P.; Tóth, G. Chiral Separation of Lansoprazole and Rabeprazole by Capillary Electrophoresis Using Dual Cyclodextrin Systems. *Electrophoresis* **2019**, *40*, 2799–2805.

(66) Peng, Y.; Gong, T.; Zhang, K.; Lin, X.; Liu, Y.; Jiang, J.; Cui, Y. Engineering Chiral Porous Metal-Organic Frameworks for Enantioselective Adsorption and Separation. *Nat. Commun.* **2014**, *5*, 4406.

(67) Tassinari, F.; Steidel, J.; Paltiel, S.; Fontanesi, C.; Lahav, M.; Paltiel, Y.; Naaman, R. Enantioseparation by Crystallization Using Magnetic Substrates. *Chem. Sci.* **2019**, *10*, 5246–5250.

(68) Tulashie, S. K.; Lorenz, H.; Hilfert, L.; Edelmann, F. T.; Seidel-Morgenstern, A. Potential of Chiral Solvents for Enantioselective Crystallization. 1. Evaluation of Thermodynamic Effects. *Cryst. Growth Des.* **2008**, *8*, 3408–3414.

(69) Tulashie, S. K.; Lorenz, H.; Seidel-Morgenstern, A. Potential of Chiral Solvents for Enantioselective Crystallization. 2. Evaluation of Kinetic Effects. *Cryst. Growth Des.* **2009**, *9*, 2387–2392.

(70) Escorihuela, J.; Burguete, M. I.; Luis, S. V. New Advances in Dual Stereocontrol for Asymmetric Reactions. *Chem. Soc. Rev.* **2013**, *42*, 5595–5617.

(71) Griesbeck, A. G.; Meierhenrich, U. J. Asymmetric Photochemistry and Photochirogenesis. *Angew. Chemie - Int. Ed.* **2002**, *41*, 3147–3154.

(72) *Handbook of Synthetic Photochemistry*; Albini, A., Fagnoni, M., Eds.; Wiley-VCH Verlag GmbH & Co. KGaA: Weinheim, Germany, 2010.

(73) Jabłońſtski, A. Efficiency of Anti-Stokes Fluorescence in Dyes. *Nature* **1933**, *131*, 839–840.

(74) Coyle, J. D. *Introduction to Organic Photochemistry*; John Wiley & Sons Ltd: Great Britain, 1986.

(75) Griesbeck, A. G. The Future of Photochemistry: Just Bright. *ChemPhotoChem* **2018**, 8–9.

(76) *CRC Hand Book of Organic Photochemistry and Photobiology*, 2nd ed.; Horspool, W., Lenci, F., Eds.; CRC Press LLC: Boca Raton, FL, 1962; Vol. 194.

(77) Diels, O.; Alder, K. Synthesen in Der Hydroaromatischen Reihe. *Justus Liebigs Ann. Chem.* **1928**, *460*, 98–122.

(78) McMurry, J. Chapter 30 Orbitals and Organic Chemistry: Pericycle Reactions. In *Organic Chemistry*; Cengage Learning: Boston, 2016; pp 1013–1036.

(79) Sarkar, D.; Bera, N.; Ghosh, S. [2+2] Photochemical Cycloaddition in Organic Synthesis. *European J. Org. Chem.* **2020**, *2020*, 1310–1326.

(80) Sieburth, S. M. N.; Cunard, N. T. The [4 + 4] Cycloaddition and Its Strategic Application in Natural Product Synthesis. *Tetrahedron* **1996**, *52*, 6251–6282.

(81) Fritzsche, J. Ueber Die Festen Kohlenwasserstoffe Des Steinkohlentheers. *J. Prakt. Chemie* **1867**, *101*, 333–343.

(82) Becker, H. D. Unimolecular Photochemistry of Anthracenes. *Chem. Rev.* **1993**, *93*, 145–172.

(83) Noyes, W. A. Jr.; Kassel, L. S. A Review of Photochemistry. *Chem. Rev.* **1926**, *3*, 199–225.

(84) Suzuki, S.; Fujii, T.; Yoshiike, N.; Komatsu, S.; Iida, T. Absorption and Fluorescence Spectra of Anthracenecarboxylic Acids. I. 9-Anthroic Acid and Formation of Excimer. *Bull. Chem. Soc. Jpn.* **1978**, *51*, 2460–2466.

(85) Bouas-Laurent, H.; Castellan, A.; Desvergne, J. P.; Lapouyade, R. Photodimerization of Anthracenes in Fluid Solution: Structural Aspects. *Chem. Soc. Rev.* **2000**, *29*, 43–55.

(86) Bouas-Laurent, H.; Castellan, A.; Desvergne, J. P.; Lapouyade, R. Photodimerization of Anthracenes in Fluid Solutions: (Part 2) Mechanistic Aspects of the Photocycloaddition and of the Photochemical and Thermal Cleavage. *Chem. Soc. Rev.* **2001**, *30*, 248–263.

(87) Schuster, D. I.; Lem, G.; Kaprinidis, N. A. New Insights into an Old Mechanism: [2 + 2] Photocycloaddition of Enones to Alkenes. **1993**, *93*, 3–22.

(88) Taylor, H. A.; Lewis, W. C. M. STUDIES IN CHEMICAL REACTIVITY II. THE ANTHRACENE ⇆ DIANTHRACENE REACTIONS, PHOTOCHEMICAL AND THERMAL. *J. Am. Chem. Soc.* **1924**, *46*, 1606–1614.

(89) Capper, N. S.; Marsh, J. K. Light Absorption and Emission Phenomena in Anthracene. *J. Am. Chem. Soc.* **1925**, *47*, 2847–2850.

(90) Chandross, E. A.; Ferguson, J.; McRae, E. G. Absorption and Emission Spectra of Anthracene Dimers. *J. Chem. Phys.* **1966**, *45*, 3546–3553.

(91) Bearpark, M. J.; Deumal, M.; Robb, M. A.; Vreven, T.; Yamamoto, N.; Olivucci, M.; Bernardi, F. Modeling Photochemical [4 + 4] Cycloadditions: Conical Intersections Located with CASSCF for Butadiene + Butadiene. *J. Am. Chem. Soc.* **1997**, *119*, 709–718.

(92) Tapilin, V. M.; Bulgakov, N. N.; Chupakhin, A. P.; Politov, A. A.; Druganov, A. G. On Mechanochemical Dimerization of Anthracene. Different Possible Reaction Pathways. *J. Struct. Chem.* **2010**, *51*, 635–641.

(93) Politov, A. A.; Chupakhin, A. P.; Tapilin, V. M.; Bulgakov, N. N.; Druganov, A. G. To

Mechanochemical Dimerization of Anthracene. Crystalline Phenanthrene under High Pressure and Shear Conditions. *J. Struct. Chem.* **2010**, *51*, 1064–1069.

(94) Zade, S. S.; Zamoshchik, N.; Reddy, A. R.; Fridman-Marueli, G.; Sheberla, D.; Bendikov, M. Products and Mechanism of Acene Dimerization. A Computational Study. *J. Am. Chem. Soc.* **2011**, *133*, 10803–10816.

(95) Jones, G.; Reinhardt, T. E.; Bergmark, W. R. Photon Energy Storage in Organic Materials- The Case of Linked Anthracenes. *Sol. Energy* **1978**, *20*, 241–248.

(96) Ganguly, G.; Sultana, M.; Paul, A. Designing Efficient Solar-Thermal Fuels with [n.n](9,10)Anthracene Cyclophanes: A Theoretical Perspective. *J. Phys. Chem. Lett.* **2018**, *9*, 328–334.

(97) Frank, P. G.; Tuten, B. T.; Prasher, A.; Chao, D.; Berda, E. B. Intra-Chain Photodimerization of Pendant Anthracene Units as an Efficient Route to Single-Chain Nanoparticle Fabrication. *Macromol. Rapid Commun.* **2014**, *35*, 249–253.

(98) Chidanguro, T.; Blank, D. R.; Garrett, A.; Reese, C. M.; Schekman, J. M.; Yu, X.; Patton, D. L.; Ayres, N.; Simon, Y. C. Fabrication of Single-Chain Nanoparticles through the Dimerization of Pendant Anthracene Groups: Via Photochemical Upconversion. *Dalt. Trans.* **2018**, *47*, 8663–8669.

(99) Li, Z.; Su, S.; Yu, L.; Zheng, Z.; Wang, X. Preparation of a Photo- and Thermo-Responsive Topological Gel from Anthracene-Modified Polyrotaxanes. *Soft Matter* **2018**, *14*, 2767–2771.

(100) Fabre, B.; Bassani, D. M.; Liang, C. K.; Lhenry, S.; Hapiot, P. Photodimerization and Micropatterning of Anthracene-Appended Receptors Covalently Bound to Silicon Surfaces: En Route to Write-Read-Erase Molecular Print Board. *J. Phys. Chem. C* **2013**, *117*, 12725–12734.

(101) Tu, M.; Reinsch, H.; Rodríguez-Hermida, S.; Verbeke, R.; Stassin, T.; Egger, W.; Dickmann, M.; Dieu, B.; Hofkens, J.; Vankelecom, I. F. J.; Stock, N.; Ameloot, R. Reversible Optical Writing and Data Storage in an Anthracene-Loaded Metal–Organic Framework. *Angew. Chemie - Int. Ed.* **2019**, *58*, 2423–2427.

(102) Huang, Z. A.; Chen, C.; Yang, X. Di; Fan, X. B.; Zhou, W.; Tung, C. H.; Wu, L. Z.; Cong, H. Synthesis of Oligoparaphenylene-Derived Nanohoops Employing an Anthracene Photodimerization-Cycloreversion Strategy. *J. Am. Chem. Soc.* **2016**, *138*, 11144–11147.

(103) Guo, L.; Yang, X.; Cong, H. Synthesis of Macrocyclic Oligoparaphenylenes Derived from Anthracene Photodimer. *Chinese J. Chem.* **2018**, *36*, 1135–1138.

(104) Xu, W.; Yang, X.-D.; Fan, X.-B.; Wang, X.; Tung, C.-H.; Wu, L.-Z.; Cong, H. Synthesis and Characterization of a Pentiptycene-Derived Dual Oligoparaphenylene Nanohoop. *Angew. Chemie Int. Ed.* **2019**, *58*, 3943–3947.

(105) Wang, X.; Liu, W.-G.; Tung, C.-H.; Wu, L.-Z.; Cong, H. A Monophosphine Ligand Derived from Anthracene Photodimer: Synthetic Applications for Palladium-Catalyzed Coupling Reactions. *Org. Lett.* **2019**, *21*, 8158–8163.

(106) Bowen, E. J. The Photochemistry of Aromatic Hydrocarbon Solutions. In *Advances in Photochemistry Volume 1*; Noyes, W. A. Jr., Hammond, G. S., Pitts, J. N. Jr., Eds.; Advances in Photochemistry; John Wiley & Sons, Inc.: Easton, Pennsylvania, 1963; pp 23–42.

(107) Stevens, B. Photoassociation in Aromatic Systems. In *Advances in Photochemistry Volume 8*; Pitts, J. N. Jr., Hammond, G. S., Noyes, W. A. Jr., Eds.; Advances in Photochemistry; John Wiley & Sons, Inc.: Easton, Pennsylvania, 1971; pp 161–226.

(108) Bunker, C. E.; Rollins, H. W.; Gord, J. R.; Sun, Y. P. Efficient Photodimerization Reaction of Anthracene in Supercritical Carbon Dioxide. *J. Org. Chem.* **1997**, *62*, 7324–7329.

(109) Barthelemy, A. L.; Dagousset, G.; Magnier, E. Metal-Free Visible-Light-Mediated Hydrotrifluoromethylation of Unactivated Alkenes and Alkynes in Continuous Flow. *European J. Org. Chem.* **2020**, *2020*, 1429–1432.

(110) Okumura, M.; Sarlah, D. Visible-Light-Induced Dearomatizations. *European J. Org. Chem.* **2020**, *2020*, 1259–1273.

(111) Jiang, Y.; Wang, C.; Rogers, C. R.; Kodaimati, M. S.; Weiss, E. A. Regio- and Diastereoselective Intermolecular [2+2] Cycloadditions Photocatalysed by Quantum Dots. *Nat. Chem.* **2019**, *11*, 1034–1040.

(112) Yoon, T. P.; Ischay, M. A.; Du, J. Visible Light Photocatalysis as a Greener Approach to Photochemical Synthesis. *Nat. Chem.* **2010**, *2*, 527–532.

(113) Sheldon, R. A.; Brady, D. Broadening the Scope of Biocatalysis in Sustainable Organic Synthesis. *ChemSusChem* **2019**, *12*, 2859–2881.

(114) J.-M. Lehn. Supramolecular Chemistry-Scope and Perspectives Molecules, Supermolecules, and Molecular Devices (Nobel Lecture). *Angew. Chemie Int. Ed. English* **1988**, *27*, 89–112.

(115) Amabilino, D. B.; Smith, D. K.; Steed, J. W. Supramolecular Materials. *Chem. Soc. Rev.* **2017**, *46*, 2404–2420.

(116) Webber, M. J.; Appel, E. A.; Meijer, E. W.; Langer, R. Supramolecular Biomaterials. *Nat. Mater.* **2015**, *15*, 13–26.

(117) Ganjali, M. R.; Norouzi, P.; Rezapour, M.; Faridbod, F.; Pourjavid, M. R. Supramolecular Based Membrane Sensors. *Sensors* **2006**, *6*, 1018–1086.

(118) Caminade, A. M.; Padié, C.; Laurent, R.; Maraval, A.; Majoral, J. P. Uses of Dendrimers for DNA Microarrays. *Sensors* **2006**, *6*, 901–914.

(119) Mako, T. L.; Racicot, J. M.; Levine, M. Supramolecular Luminescent Sensors. *Chem. Rev.* **2019**, *119*, 322–477.

(120) Raynal, M.; Ballester, P.; Vidal-Ferran, A.; Van Leeuwen, P. W. N. M. Supramolecular Catalysis. Part 1: Non-Covalent Interactions as a Tool for Building and Modifying Homogeneous Catalysts. *Chem. Soc. Rev.* **2014**, *43*, 1660–1733.

(121) Raynal, M.; Ballester, P.; Vidal-Ferran, A.; Van Leeuwen, P. W. N. M. Supramolecular Catalysis. Part 2: Artificial Enzyme Mimics. *Chem. Soc. Rev.* **2014**, *43*, 1734–1787.

(122) Meeuwissen, J.; Reek, J. N. H. Supramolecular Catalysis beyond Enzyme Mimics. *Nat. Chem.* **2010**, *2*, 615–621.

(123) Mason, S. F. Induced Circular Dichroism. *Chem. Phys. Lett.* **1975**, *32*, 201–203.

(124) Gawroński, J.; Grajewski, J. The Significance of Induced Circular Dichroism. *Org. Lett.* **2003**, *5*, 3301–3303.

(125) Tejedor, R. M.; Oriol, L.; Serrano, J. L.; Sierra, T. Chiral Photochemical Induction in Liquid Crystals. *J. Mater. Chem.* **2008**, *18*, 2899–2908.

(126) Brimioulle, R.; Lenhart, D.; Maturi, M. M.; Bach, T. Enantioselective Catalysis of Photochemical Reactions. *Angew. Chemie - Int. Ed.* **2015**, *54*, 3872–3890.

(127) Ma, W.; Xu, L.; De Moura, A. F.; Wu, X.; Kuang, H.; Xu, C.; Kotov, N. A. Chiral Inorganic Nanostructures. *Chem. Rev.* **2017**, *117*, 8041–8093.

(128) Pieraccini, S.; Masiero, S.; Ferrarini, A.; Piero Spada, G. Chirality Transfer across Length-Scales in Nematic Liquid Crystals: Fundamentals and Applications. *Chem. Soc. Rev.* **2011**, *40*, 258–271.

(129) Morales-Vidal, J.; López, N.; Ortuño, M. A. Chirality Transfer in Gold Nanoparticles by l -Cysteine Amino Acid: A First-Principles Study. *J. Phys. Chem. C* **2019**, *123*, 13758–13764.

(130) Bibal, B.; Mongin, C.; Bassani, D. M. Template Effects and Supramolecular Control of Photoreactions in Solution. *Chem. Soc. Rev.* **2014**, *43*, 4179–4198.

(131) Noyori, R. Asymmetric Catalysis: Science and Opportunities (Nobel Lecture). *Angew. Chemie - Int. Ed.* **2002**, *41*, 2008–2022.

(132) Melchiorre, P.; Marigo, M.; Carlone, A.; Bartoli, G. Asymmetric Aminocatalysis - Gold Rush in Organic Chemistry. *Angew. Chemie - Int. Ed.* **2008**, *47*, 6138–6171.

(133) Geiger, Y.; Achard, T.; Maisse-François, A.; Bellemin-Laponnaz, S. Hyperpositive Nonlinear Effects in Asymmetric Catalysis. *Nat. Catal.* **2020**.

(134) Hasserodt, J. Organic Synthesis Supported by Antibody Catalysis. *Synlett* **1999**, No. 12, 2007–2022.

(135) Hanson, C. V.; Nishiyama, Y.; Paul, S. Catalytic Antibodies and Their Applications. *Curr. Opin. Biotechnol.* **2005**, *16*, 631–636.

(136) Ward, T. R. Artificial Enzymes Made to Order: Combination of Computational Design and Directed Evolution. *Angew. Chemie - Int. Ed.* **2008**, *47*, 7802–7803.

(137) Wentworth, P.; Witter, D. P. Antibody-Catalyzed Water-Oxidation Pathway. *Pure Appl. Chem.* **2008**, *80*, 1849–1858.

(138) Cochran, A. G.; Sugasawara, R.; Schultz, P. G. Photosensitized Cleavage of a Thymine Dimer by an Antibody. *J. Am. Chem. Soc.* **1988**, *110*, 7888–7890.

(139) Jacobsen, J. R.; Schultz, P. G.; Cochran, A. G.; Stephans, J. C.; King, D. S. Mechanistic Studies of Antibody-Catalyzed Pyrimidine Dimer Photocleavage. *J. Am. Chem. Soc.* **1995**, *117*, 5453–5461.

(140) Simeonov, A.; Matsushita, M.; Juban, E. A.; Thompson, E. H. Z.; Hoffman, T. Z.; Beuscher IV, A. E.; Taylor, M. J.; Wirsching, P.; Rettig, W.; McCusker, J. K.; Stevens, R. C.; Millar, D. P.; Schultz, P. G.; Lerner, R. A.; Janda, K. D. Blue-Fluorescent Antibodies. *Science (80-.).* **2000**, *290*, 307–313.

(141) Dickerson, T. J.; Tremblay, M. R.; Hoffman, T. Z.; Ruiz, D. I.; Janda, K. D. Catalysis of the Photo-Fries Reaction: Antibody-Mediated Stabilization of High Energy States. *J. Am. Chem. Soc.* **2003**, *125*, 15395–15401.

(142) Balan, A.; Doctor, B. P.; Green, B. S.; Torten, M.; Ziffer, H. Antibody Combining Sites as Templates for Selective Organic Chemical Reactions. *J. Chem. Soc. Chem. Commun.* **1988**, 106–108.

(143) Taylor, M. J.; Hoffman, T. Z.; Yli-Kauhaluoma, J. T.; Lerner, R. A.; Janda, K. D. A Light-Activated Antibody Catalyst. *J. Am. Chem. Soc.* **1998**, *120*, 12783–12790.

(144) Saphier, S.; Sinha, S. C.; Keinan, E. Antibody-Catalyzed Enantioselective Norrish Type II Cyclization. *Angew. Chemie - Int. Ed.* **2003**, *42*, 1378–1381.

(145) Saphier, S.; Hu, Y.; Sinha, S. C.; Houk, K. N.; Keinan, E. Origin of Selectivity in the Antibody 20F10-Catalyzed Yang Cyclization. *J. Am. Chem. Soc.* **2005**, *127*, 132–145.

(146) Pollack, S. J.; Jacobs, J. W.; Schultz, P. G. Selective Chemical Catalysis by an Antibody. *Science (80-.).* **1986**, *234*, 1570–1573.

(147) Tramontano, A.; Janda, K. D.; Lerner, R. A. Catalytic Antibodies. *Science (80-.).* **1986**, *234*, 1566–1570.

(148) Winter, G.; Milstein, C. Man-Made Antibodies. **1991**, *349*.

(149) Little, M.; Kipriyanov, S. M.; Le Gall, F.; Moldenhauer, G. Of Mice and Men: Hybridoma and Recombinant Antibodies. *Immunol. Today* **2000**, *21*, 364–370.

(150) Zaroff, S.; Tan, G. Hybridoma Technology: The Preferred Method for Monoclonal Antibody Generation for in Vivo Applications. *Biotechniques* **2019**, *67*, 90–92.

(151) Baldwin, E.; Schultz, P. G. Generation of a Catalytic Antibody by Site-Directed Mutagenesis. *Science (80-.).* **1989**, *245*, 1104–1107.

(152) Jackson, D. Y.; Prudent, J. R.; Baldwin, E. P.; Schultz, P. G. A Mutagenesis Study of a Catalytic Antibody. *Proc. Natl. Acad. Sci. U. S. A.* **1991**, *88*, 58–62.

(153) Stewart, J. D.; Roberts, V. A.; Thomas, N. R.; Getzoff, E. D.; Benkovic, S. J. Site-Directed Mutagenesis of a Catalytic Antibody: An Arginine and a Histidine Residue Play Key Roles. *Biochemistry* **1994**, *33*, 1994–2003.

(154) Yang, H.; Swartz, A. M.; Park, H. J.; Srivastava, P.; Ellis-Guardiola, K.; Upp, D. M.; Lee, G.; Belsare, K.; Gu, Y.; Zhang, C.; Moellering, R. E.; Lewis, J. C. Evolving Artificial Metalloenzymes via Random Mutagenesis. *Nat. Chem.* **2018**, *10*, 318–324.

(155) Wang, C.; Wang, Z.; Zhang, X. Amphiphilic Building Blocks for Self-Assembly: From Amphiphiles to Supra-Amphiphiles. *Acc. Chem. Res.* **2012**, *45*, 608–618.

(156) Ramanathan, M.; Shrestha, L. K.; Mori, T.; Ji, Q.; Hill, J. P.; Ariga, K. Amphiphile Nanoarchitectonics: From Basic Physical Chemistry to Advanced Applications. *Phys. Chem. Chem. Phys.* **2013**, *15*, 10580–10611.

(157) Lombardo, D.; Kiselev, M. A.; Magazù, S.; Calandra, P. Amphiphiles Self-Assembly: Basic Concepts and Future Perspectives of Supramolecular Approaches. *Adv. Condens. Matter Phys.* **2015**, *2015*, 151683.

(158) Myers, D. *Surfactant Science and Technology*, 3rd ed.; John Wiley & Sons, Inc.: Hoboken, 2006; Vol. 3.

(159) Manet, S.; Karpichev, Y.; Dedovets, D.; Oda, R. Effect of Hofmeister and Alkylcarboxylate Anionic Counterions on the Krafft Temperature and Melting Temperature of Cationic Gemini Surfactants. *Langmuir* **2013**, *29*, 3518–3526.

(160) Parikh, K.; Singh, S.; Desai, A.; Kumar, S. An Interplay between Spacer Nature and Alkyl Chain Length on Aqueous Micellar Properties of Cationic Gemini Surfactants: A Multi-Technique Approach. *J. Mol. Liq.* **2019**, *278*, 290–298.

(161) Chu, Z.; Feng, Y. Empirical Correlations between Krafft Temperature and Tail Length for Amidosulfobetaine Surfactants in the Presence of Inorganic Salt. *Langmuir* **2012**, *28*, 1175–1181.

(162) Lee, H. E.; Kim, R. M.; Ahn, H. Y.; Lee, Y. Y.; Byun, G. H.; Im, S. W.; Mun, J.; Rho, J.; Nam, K. T.

Cysteine-Encoded Chirality Evolution in Plasmonic Rhombic Dodecahedral Gold Nanoparticles. *Nat. Commun.* **2020**, *11*, 1–10.

(163) Selinger, R. L. B.; Selinger, J. V; Malanoski, A. P.; Schnur, J. M. Shape Selection in Chiral Self-Assembly. *Phys. Rev. Lett.* **2004**, *93*, 158103.

(164) Ziserman, L.; Lee, H.-Y.; Raghavan, S. R.; Mor, A.; Danino, D. Unraveling the Mechanism of Nanotube Formation by Chiral. *J. Am. Chem. Soc.* **2011**, *133*, 2511–2517.

(165) Menger, F. M.; Littau, C. A. Gemini Surfactants: Synthesis and Properties. *J. Am. Chem. Soc.* **1991**, *113*, 1451–1452.

(166) Menger, F. M.; Littau, C. A. Gemini Surfactants: A New Class of Self-Assembling Molecules. *J. Am. Chem. Soc.* **1993**, *115*, 10083–10090.

(167) Liu, M.; Zhang, L.; Wang, T. Supramolecular Chirality in Self-Assembled Systems. *Chem. Rev.* **2015**, *115*, 7304–7397.

(168) Sommerdijk, N. A. J. M.; Lambermon, M. H. L.; Feiters, M. C.; Nolte, R. J. M.; Zwanenburg, B. Supramolecular Expression of Chirality in Assemblies of Gemini Surfactants. *Chem. Commun.* **1997**, No. 15, 1423–1424.

(169) Oda, R.; Huc, I.; Schmutz, M.; Candau, S. J.; MacKintosh, F. C. Tuning Bilayer Twist Using Chiral Counterions. *Nature* **1999**, *399*, 566–569.

(170) Oliveira, I. S.; Lo, M.; Araújo, M. J.; Marques, E. F. Temperature-Responsive Self-Assembled Nanostructures from Lysine-Based Surfactants with High Chain Length Asymmetry: From Tubules and Helical Ribbons to Micelles and Vesicles. *Soft Matter* **2019**, *15*, 3700–3711.

(171) Shimizu, T.; Masuda, M.; Minamikawa, H. Supramolecular Nanotube Architectures Based on Amphiphilic Molecules. *Chem. Rev.* **2005**, *105*, 1401–1443.

(172) Jin, W.; Fukushima, T.; Niki, M.; Kosaka, A.; Ishii, N.; Aida, T. Self-Assembled Graphitic Nanotubes with One-Handed Helical Arrays of a Chiral Amphiphilic Molecular Graphene. *Proc. Natl. Acad. Sci. U. S. A.* **2005**, *102*, 10801–10806.

(173) Oda, R.; Huc, I.; Candau, S. J. Gemini Surfactants as New, Low Molecular Weight Gelators of Organic Solvents and Water. *Angew. Chemie Int. Ed.* **1998**, *37*, 2689–2691.

(174) Oda, R.; Huc, I.; Homo, J. C.; Heinrich, B.; Schmutz, M.; Candau, S. Elongated Aggregates Formed by Cationic Gemini Surfactants. *Langmuir* **1999**, *15*, 2384–2390.

(175) Berthier, D.; Buffeteau, T.; Léger, J. M.; Oda, R.; Huc, I. From Chiral Counterions to Twisted Membranes. *J. Am. Chem. Soc.* **2002**, *124*, 13486–13494.

(176) Oda, R.; Artzner, F.; Laguerre, M.; Huc, I. Molecular Structure of Self-Assembled Chiral Nanoribbons and Nanotubules Revealed in the Hydrated State. *J. Am. Chem. Soc.* **2008**, *130*, 14705–14712.

(177) Kiagus-Armad, R.; Brizard, A.; Tang, C.; Blatchly, R.; Desbat, B.; Oda, R. Cooperative and Reciprocal Chiral Structure Formation of an Alanine-Based Peptide Confined at the Surface of Cationic Surfactant Membranes. *Chem. - A Eur. J.* **2011**, *17*, 9999–10009.

(178) Dedovets, D.; Martin, B.; Okazaki, Y.; Buffeteau, T.; Pouget, E.; Oda, R. Hierarchical Chirality Expression of Gemini Surfactant Aggregates via Equilibrium between Chiral Nucleotide and Nonchiral Mono-Anions. *Chirality* **2020**, 1–12.

(179) Oda, R.; Huc, I.; Candau, S. J. Gemini Surfactants, the Effect of Hydrophobic Chain Length and

Dissymmetry. *Chem. Commun.* **1997**, No. 21, 2105–2106.

(180) Oda, R.; Laguerre, M.; Huc, I.; Desbat, B. Molecular Organization of Gemini Surfactants in Cylindrical Micelles: An Infrared Dichroism Spectroscopy and Molecular Dynamics Study. *Langmuir* **2002**, *18*, 9659–9667.

(181) Brizard, A.; Aimé, C.; Labrot, T.; Huc, I.; Berthier, D.; Artzner, F.; Desbat, B.; Oda, R. Counterion, Temperature, and Time Modulation of Nanometric Chiral Ribbons from Gemini-Tartrate Amphiphiles. *J. Am. Chem. Soc.* **2007**, *129*, 3754–3762.

(182) Brizard, A.; Berthier, D.; Aimé, C.; Buffeteau, T.; Cavagnat, D.; Ducasse, L.; Huc, I.; Oda, R. Molecular and Supramolecular Chirality in Gemini-Tartrate Amphiphiles Studied by Electronic and Vibrational Circular Dichroisms. *Chirality* **2009**, *21*, E153–E162.

(183) Tamoto, R.; Daugey, N.; Buffeteau, T.; Kauffmann, B.; Takafuji, M.; Ihara, H.; Oda, R. In Situ Helicity Inversion of Self-Assembled Nano-Helices. *Chem. Commun.* **2015**, *51*, 3518–3521.

(184) Sugiyasu, K.; Tamaru, S. I.; Takeuchi, M.; Berthier, D.; Huc, I.; Oda, R.; Shinkai, S. Double Helical Silica Fibrils by Sol-Gel Transcription of Chiral Aggregates of Gemini Surfactants. *Chem. Commun.* **2002**, *2*, 1212–1213.

(185) Delclos, T.; Aimé, C.; Pouget, E.; Brizard, A.; Huc, I.; Delville, M. H.; Oda, R. Individualized Silica Nanohelices and Nanotubes: Tuning Inorganic Nanostructures Using Lipidic Self-Assemblies. *Nano Lett.* **2008**, *8*, 1929–1935.

(186) Okazaki, Y.; Cheng, J.; Dedovets, D.; Kemper, G.; Delville, M. H.; Durrieu, M. C.; Ihara, H.; Takafuji, M.; Pouget, E.; Oda, R. Chiral Colloids: Homogeneous Suspension of Individualized SiO2 Helical and Twisted Nanoribbons. *ACS Nano* **2014**, *8*, 6863–6872.

(187) Okazaki, Y.; Buffeteau, T.; Siurdyban, E.; Talaga, D.; Ryu, N.; Yagi, R.; Pouget, E.; Takafuji, M.; Ihara, H.; Oda, R. Direct Observation of Siloxane Chirality on Twisted and Helical Nanometric Amorphous Silica. *Nano Lett.* **2016**, *16*, 6411–6415.

(188) Faridi, A.; Sun, Y.; Okazaki, Y.; Peng, G.; Gao, J.; Kakinen, A.; Faridi, P.; Zhao, M.; Javed, I.; Purcell, A. W.; Davis, T. P.; Lin, S.; Oda, R.; Ding, F.; Ke, P. C. Mitigating Human IAPP Amyloidogenesis In Vivo with Chiral Silica Nanoribbons. *Small* **2018**, *14*, 1–13.

(189) Attoui, M.; Pouget, E.; Oda, R.; Talaga, D.; Bourdon, G. L. Le; Buffeteau, T.; Nlate, S. Optically Active Polyoxometalate-Based Silica Nanohelices: Induced Chirality from Inorganic Nanohelices to Achiral POM Clusters. *Chem. - A Eur. J.* **2018**, *24*, 11344–11353.

(190) Attoui, M.; Pouget, E.; Oda, R.; Talaga, D.; Buffeteau, T.; Nlate, S. Silica Twisted and Helical Nanoribbons as Chiral Inducers for Peroxophosphotungstate Anions. *Inorganica Chim. Acta* **2019**, *498*.

(191) Tamoto, R.; Lecomte, S.; Si, S.; Moldovan, S.; Ersen, O.; Delville, M. H.; Oda, R. Gold Nanoparticle Deposition on Silica Nanohelices: A New Controllable 3D Substrate in Aqueous Suspension for Optical Sensing. *J. Phys. Chem. C* **2012**, *116*, 23143–23152.

(192) Cheng, J.; Le Saux, G.; Gao, J.; Buffeteau, T.; Battie, Y.; Barois, P.; Ponsinet, V.; Delville, M. H.; Ersen, O.; Pouget, E.; Oda, R. GoldHelix: Gold Nanoparticles Forming 3D Helical Superstructures with Controlled Morphology and Strong Chiroptical Property. *ACS Nano* **2017**, *11*, 3806–3818.

(193) Gao, J.; Wu, W.; Lemaire, V.; Carvalho, A.; Nlate, S.; Buffeteau, T.; Oda, R.; Battie, Y.; Pauly, M.; Pouget, E. Tuning the Chiroptical Properties of Elongated Nano-Objects via Hierarchical Organization. *ACS Nano* **2020**, *14*, 4111–4121.

(194) Gao, J.; Semlali, S.; Hunel, J.; Montero, D.; Battie, Y.; Gonzalez-Rodriguez, D.; Oda, R.; Drisko, G. L.; Pouget, E. Creating Regular Matrices of Aligned Silica Nanohelices: Theory and Realization. *Chem. Mater.* **2020**, *32*, 821–829.

(195) Ryu, N.; Okazaki, Y.; Hirai, K.; Takafuji, M.; Nagaoka, S.; Pouget, E.; Ihara, H.; Oda, R. Memorized Chiral Arrangement of Gemini Surfactant Assemblies in Nanometric Hybrid Organic-Silica Helices. *Chem. Commun.* **2016**, *52*, 5800–5803.

(196) Ryu, N.; Okazaki, Y.; Pouget, E.; Takafuji, M.; Nagaoka, S.; Ihara, H.; Oda, R. Fluorescence Emission Originated from the H-Aggregated Cyanine Dye with Chiral Gemini Surfactant Assemblies Having a Narrow Absorption Band and a Remarkably Large Stokes Shift. *Chem. Commun.* **2017**, *53*, 8870–8873.

(197) Okazaki, Y.; Ryu, N.; Buffeteau, T.; Pathan, S.; Nagaoka, S.; Pouget, E.; Nlate, S.; Ihara, H.; Oda, R. Induced Circular Dichroism of Monoatomic Anions: Silica-Assisted the Transfer of Chiral Environment from Molecular Assembled Nanohelices to Halide Ions. *Chem. Commun.* **2018**, *54*, 10244–10247.

(198) Jiang, J.; Ouyang, G.; Zhang, L.; Liu, M. Self-Assembled Chiral Nanostructures as Scaffolds for Asymmetric Reactions. *Chem. - A Eur. J.* **2017**, *23*, 9439–9450.

(199) Cohen, M. D.; Schmidt, G. M. J.; Sonntag, F. I. 384. Topochemistry. Part II. The Photochemistry of Trans-Cinnamic Acids. *J. Chem. Soc.* **1964**, No. 0, 2000–2013.

(200) Ramamurthy, V.; Venkatesan, K. Photochemical Reactions of Organic Crystals. *Chem. Rev.* **1987**, *87*, 433–481.

(201) Cohen, M. D. Solid-State Photochemical Reactions. *Tetrahedron* **1987**, *43*, 1211–1224.

(202) Salzillo, T.; Brillante, A. Commenting on the Photoreactions of Anthracene Derivatives in the Solid State. *CrystEngComm* **2019**, *21*, 3127–3136.

(203) Salzillo, T.; Venuti, E.; Della Valle, R. G.; Brillante, A. Solid-State Photodimerization of 9-Methyl-Anthracene. *J. Raman Spectrosc.* **2017**, *48*, 271–277.

(204) Spinelli, F.; D'Agostino, S.; Taddei, P.; Jones, C. D.; Steed, J. W.; Grepioni, F. Activating [4 + 4] Photoreactivity in the Solid-State: Via Complexation: From 9-(Methylaminomethyl)Anthracene to Its Silver(i) Complexes. *Dalt. Trans.* **2018**, *47*, 5725–5733.

(205) Yamada, S.; Kawamura, C. Photodimerization of Azaanthracenes in Both Solution and Solid Phase Controlled by Cation-π Interactions. *Org. Lett.* **2012**, *14*, 1572–1575.

(206) Kohmoto, S.; Ono, Y.; Masu, H.; Yamaguchi, K.; Kishikawa, K.; Yamamoto, M. Enantioselective Intramolecular Aromatic [4 + 4] Photocycloaddition in Crystalline State: Parameters for Reactivity. *Org. Lett.* **2001**, *3*, 4153–4155.

(207) Moré, R.; Busse, G.; Hallmann, J.; Paulmann, C.; Scholz, M.; Techert, S. Photodimerization of Crystalline 9-Anthracenecarboxylic Acid: A Nontopotactic Autocatalytic Transformation. *J. Phys. Chem. C* **2010**, *114*, 4142–4148.

(208) Craig, D. P.; Sarti-Fantoni, P. Photochemical Dimerisation in Crystalline Anthracenes. *Chem. Commun.* **1966**, No. 20, 742–743.

(209) Cohen, M. D.; Ludmer, Z.; Thomas, J. M.; Williams, J. O. The Role of Structural Imperfections in the Photodimerization of 9-Cyanoanthracene. *Proc. R. Soc. London. A. Math. Phys. Sci.* **1971**, *324*, 459–468.

(210) Wolff, T.; Müller, N. Regioselective Photodimerization of Polar 9-Substituted Anthracenes in Micellar Solutions. *J. Photochem.* **1983**, *23*, 131–140.

(211) Salzillo, T.; Venuti, E.; Femoni, C.; Della Valle, R. G.; Tarroni, R.; Brillante, A. Crystal Structure of the 9-Anthracene-Carboxylic Acid Photochemical Dimer and Its Solvates by X-Ray Diffraction and Raman Microscopy. *Cryst. Growth Des.* **2017**, *17*, 3361–3370.

(212) Nguyen, D. P.; Lusic, H.; Neumann, H.; Kapadnis, P. B.; Deiters, A.; Chin, J. W. Genetic Encoding and Labeling of Aliphatic Azides and Alkynes in Recombinant Proteins via a Pyrrolysyl-TRNA Synthetase/TRNACUA Pair and Click Chemistry. *J. Am. Chem. Soc.* **2009**, *131*, 8720–8721.

(213) Kim, T.; Zhu, L.; Mueller, L. J.; Bardeen, C. J. Mechanism of Photoinduced Bending and Twisting in Crystalline Microneedles and Microribbons Composed of 9-Methylanthracene. *J. Am. Chem. Soc.* **2014**, *136*, 6617–6625.

(214) Medishetty, R.; Sahoo, S. C.; Mulijanto, C. E.; Naumov, P.; Vittal, J. J. Photosalient Behavior of Photoreactive Crystals. *Chem. Mater.* **2015**, *27*, 1821–1829.

(215) Tapilin, V. M.; Bulgakov, N. N.; Chupakhin, A. P.; Politov, A. A. On the Mechanism of Mechanochemical Dimerization of Anthracene. Quantum-Chemical Calculation of the Electronic Structure of Anthracene and Its Dimer. *J. Struct. Chem.* **2008**, *49*, 581–586.

(216) Jezowski, S. R.; Zhu, L.; Wang, Y.; Rice, A. P.; Scott, G. W.; Bardeen, C. J.; Chronister, E. L. Pressure Catalyzed Bond Dissociation in an Anthracene Cyclophane Photodimer. *J. Am. Chem. Soc.* **2012**, *134*, 7459–7466.

(217) Koshima, H.; Uchimoto, H.; Taniguchi, T.; Nakamura, J.; Asahi, T.; Asahi, T. Mechanical Motion of Molecular Crystals Induced by [4 + 4] Photodimerisation. *CrystEngComm* **2016**, *18*, 7305–7310.

(218) Rideout, D. C.; Breslow, R. Hydrophobic Acceleration of Diels-Alder Reactions. *J. Am. Chem. Soc.* **1980**, *102*, 7816–7817.

(219) Tamaki, T. REVERSIBLE PHOTODIMERIZATION OF WATER-SOLUBLE ANTHRACENES INCLUDED IN γ-CYCLODEXTRIN. *Chem. Lett.* **1984**, *13*, 53–56.

(220) Ueno, A.; Moriwaki, F.; Osa, T.; Hamada, F.; Murai, K. Association, Photodimerization, and Induced-Fit Types of Host-Guest Complexation of Anthracene-Appended γ-Cyclodextrin Derivatives. *J. Am. Chem. Soc.* **1988**, *110*, 4323–4328.

(221) Tamaki, T.; Kawanishi, Y.; Seki, T.; Sakuragi, M. Triplet Sensitization of Anthracene Photodimerization in γ-Cyclodextrin. *J. Photochem. Photobiol. A Chem.* **1992**, *65*, 313–320.

(222) Tamaki, T.; Kokubu, T.; Ichimura, K. Regio- and Stereoselective Photodimerization of Anthracene Derivatives Included by Cyclodextrins. *Tetrahedron* **1987**, *43*, 1485–1494.

(223) Nakamura, A.; Inoue, Y. Supramolecular Catalysis of the Enantiodifferentiating [4 + 4] Photocyclodimerization of 2-Anthracenecarboxylate by γ-Cyclodextrin. *J. Am. Chem. Soc.* **2003**, *125*, 966–972.

(224) Yang, C.; Fukuhara, G.; Nakamura, A.; Origane, Y.; Fujita, K.; Yuan, D. Q.; Mori, T.; Wada, T.; Inoue, Y. Enantiodifferentiating [4+4] Photocyclodimerization of 2-Anthracenecarboxylate Catalyzed by 6A,6X -Diamino-6A,6X-Dideoxy-γ-Cyclodextrins: Manipulation of Product Chirality by Electrostatic Interaction, Temperature and Solvent in Supramolecular Photochirog. *J. Photochem. Photobiol. A Chem.* **2005**, *173*, 375–383.

(225) Yang, C.; Nakamura, A.; Fukuhara, G.; Origane, Y.; Mori, T.; Wada, T.; Inoue, Y. Pressure and

Temperature-Controlled Enantiodifferentiating [4+4] Photocyclodimerization of 2-Anthracenecarboxylate Mediated by Secondary Face- and Skeleton-Modified γ-Cyclodextrins. *J. Org. Chem.* **2006**, *71*, 3126–3136.

(226) Yang, C.; Nakamura, A.; Wada, T.; Inoue, Y. Enantiodifferentiating Photocyclodimerization of 2-Anthracenecarboxylic Acid Mediated by γ-Cyclodextrins with a Flexible or Rigid Cap. *Org. Lett.* **2006**, *8*, 3005–3008.

(227) Yang, C.; Mori, T.; Inoue, Y. Supramolecular Enantiodifferentiating Photocyclodimerization of 2-Anthracenecarboxylate Mediated by Capped γ-Cyclodextrins: Critical Control of Enantioselectivity by Cap Rigidity. *J. Org. Chem.* **2008**, *73*, 5786–5794.

(228) Yang, C.; Wang, Q.; Yamauchi, M.; Yao, J.; Zhou, D.; Nishijima, M.; Fukuhara, G.; Mori, T.; Liu, Y.; Inoue, Y. Manipulating γ-Cyclodextrin-Mediated Photocyclodimerization of Anthracenecarboxylate by Wavelength, Temperature, Solvent and Host. *Photochem. Photobiol. Sci.* **2014**, *13*, 190–198.

(229) Wang, Q.; Yang, C.; Fukuhara, G.; Mori, T.; Liu, Y.; Inoue, Y. Supramolecular FRET Photocyclodimerization of Anthracenecarboxylate with Naphthalene-Capped Y-Cyclodextrin. *Beilstein J. Org. Chem.* **2011**, *7*, 290–297.

(230) Rao, M.; Kanagaraj, K.; Fan, C.; Ji, J.; Xiao, C.; Wei, X.; Wu, W.; Yang, C. Photocatalytic Supramolecular Enantiodifferentiating Dimerization of 2-Anthracenecarboxylic Acid through Triplet-Triplet Annihilation. *Org. Lett.* **2018**, *20*, 1680–1683.

(231) Ke, C.; Yang, C.; Mori, T.; Wada, T.; Liu, Y.; Inoue, Y. Catalytic Enantiodifferentiating Photocyclodimerization of 2anthracenecarboxylic Acid Mediated by a Non-Sensitizing Chiral Metallosupramolecular Host. *Angew. Chemie - Int. Ed.* **2009**, *48*, 6675–6677.

(232) Qiu, H.; Yang, C.; Inoue, Y.; Che, S. Supramolecular Photochirogenesis with Cyclodextrin- Silica Composite. Enantiodifferentiating Photocyclodimerization of 2-Anthrancenecarboxylate with Mesoporous Silica Wall-Capped γ-Cyclodextrin. *Org. Lett.* **2009**, *11*, 1793–1796.

(233) Yao, J.; Yan, Z.; Ji, J.; Wu, W.; Yang, C.; Nishijima, M.; Fukuhara, G.; Mori, T.; Inoue, Y. Ammonia-Driven Chirality Inversion and Enhancement in Enantiodifferentiating Photocyclodimerization of 2-Anthracenecarboxylate Mediated by Diguanidino-γ-Cyclodextrin. *J. Am. Chem. Soc.* **2014**, *136*, 6916–6919.

(234) Wei, X.; Wu, W.; Matsushita, R.; Yan, Z.; Zhou, D.; Chruma, J. J.; Nishijima, M.; Fukuhara, G.; Mori, T.; Inoue, Y.; Yang, C. Supramolecular Photochirogenesis Driven by Higher-Order Complexation: Enantiodifferentiating Photocyclodimerization of 2-Anthracenecarboxylate to Slipped Cyclodimers via a 2:2 Complex with β-Cyclodextrin. *J. Am. Chem. Soc.* **2018**, *140*, 3959–3974.

(235) Ji, J.; Wu, W.; Liang, W.; Cheng, G.; Matsushita, R.; Yan, Z.; Wei, X.; Rao, M.; Yuan, D. Q.; Fukuhara, G.; Mori, T.; Inoue, Y.; Yang, C. An Ultimate Stereocontrol in Supramolecular Photochirogenesis: Photocyclodimerization of 2-Anthracenecarboxylate Mediated by Sulfur-Linked β-Cyclodextrin Dimers. *J. Am. Chem. Soc.* **2019**, *141*, 9225–9238.

(236) Yang, C.; Ke, C.; Liang, W.; Fukuhara, G.; Mori, T.; Liu, Y.; Inoue, Y. Dual Supramolecular Photochirogenesis: Ultimate Stereocontrol of Photocyclodimerization by a Chiral Scaffold and Confining Host. *J. Am. Chem. Soc.* **2011**, *133*, 13786–13789.

(237) Hu, X.; Liu, F.; Zhang, X.; Zhao, Z.; Liu, S. Expected and Unexpected Photoreactions of 9-(10-)Substituted Anthracene Derivatives in Cucurbit[n]Uril Hosts . *Chem. Sci.* **2020**, *11*, 4779–4785.

(238) Yang, C.; Mori, T.; Origane, Y.; Young, H. K.; Selvapalam, N.; Kim, O.; Inoue, Y. Highly Stereoselective Photocyclodimerization of α-Cyclodextrin- Appended Anthracene Mediated by γ-Cyclodextrin and Cucurbit[8]Uril: A Dramatic Steric Effect Operating Outside the Binding Site. *J. Am. Chem. Soc.* **2008**, *130*, 8574–8575.

(239) Fukuhara, G.; Umehara, H.; Higashino, S.; Nishijima, M.; Yang, C.; Mori, T.; Wada, T.; Inoue, Y. Supramolecular Photocyclodimerization of 2-Hydroxyanthracene with a Chiral Hydrogen-Bonding Template, Cyclodextrin and Serum Albumin. *Photochem. Photobiol. Sci.* **2014**, *13*, 162–171.

(240) Krämer, R. Supramolecular Bioinorganic Hybrid Catalysts for Enantioselective Transformations. *Angew. Chemie - Int. Ed.* **2006**, *45*, 858–860.

(241) Mogharabi, M.; Rezaei, S.; Faramarzi, M. A. Trends in Peptide and Protein Sciences. *Trends Pept. Protein Sci.* **2017**, *1*, 88–98.

(242) Winkler, M.; Geier, M.; Hanlon, S. P.; Nidetzky, B.; Glieder, A. Human Enzymes for Organic Synthesis. *Angew. Chemie - Int. Ed.* **2018**, *57*, 13406–13423.

(243) Xue, Y. P.; Cao, C. H.; Zheng, Y. G. Enzymatic Asymmetric Synthesis of Chiral Amino Acids. *Chem. Soc. Rev.* **2018**, *47*, 1516–1561.

(244) Wada, T.; Nishijima, M.; Fujisawa, T.; Sugahara, N.; Mori, T.; Nakamura, A.; Inoue, Y. Bovine Serum Albumin-Mediated Enantiodifferentiating Photocyclodimerization of 2-Anthracenecarboxylate. *J. Am. Chem. Soc.* **2003**, *125*, 7492–7493.

(245) Nishijima, M.; Wada, T.; Mori, T.; Pace, T. C. S.; Bohne, C.; Inoue, Y. Highly Enantiomeric Supramolecular [4 + 4] Photocyclodimerization of 2-Anthracenecarboxylate Mediated by Human Serum Albumin. *J. Am. Chem. Soc.* **2007**, *129*, 3478–3479.

(246) Nishijima, M.; Goto, M.; Fujikawa, M.; Yang, C.; Mori, T.; Wada, T.; Inoue, Y. Mammalian Serum Albumins as a Chiral Mediator Library for Bio-Supramolecular Photochirogenesis: Optimizing Enantiodifferentiating Photocyclodimerization of 2-Anthracenecarboxylate. *Chem. Commun.* **2014**, *50*, 14082–14085.

(247) Bujacz, A. Structures of Bovine, Equine and Leporine Serum Albumin. *Acta Crystallogr. Sect. D Biol. Crystallogr.* **2012**, *68*, 1278–1289.

(248) He, X. M.; Carter, D. C. Atomic Structure and Chemistry of Human Serum Albumin. *Nature* **1992**, *358*, 209–215.

(249) Sugio, S.; Kashima, A.; Mochizuki, S.; Noda, M.; Kobayashi, K. Crystal Structure of Human Serum Albumin at 2.5 Å Resolution. *Protein Eng.* **1999**, *12*, 439–446.

(250) Pace, T. C. S.; Nishijima, M.; Wada, T.; Inoue, Y.; Bohne, C. Photophysical Studies on the Supramolecular Photochirogenesis for the Photocyclodimerization of 2-Anthracenecarboxylate within Human Serum Albumin. *J. Phys. Chem. B* **2009**, *113*, 10445–10453.

(251) Fuentealba, D.; Kato, H.; Nishijima, M.; Fukuhara, G.; Mori, T.; Inoue, Y.; Bohne, C. Explaining the Highly Enantiomeric Photocyclodimerization of 2-Anthracenecarboxylate Bound to Human Serum Albumin Using Time-Resolved Anisotropy Studies. *J. Am. Chem. Soc.* **2013**, *135*, 203–209.

(252) Chang, J.; Nishijima, M.; Sekiguchi, H.; Ichiyanagi, K.; Kuramochi, M.; Inoue, Y.; Sasaki, Y. C. X-Ray Observations of Single Bio-Supramolecular Photochirogenesis. *Biophys. Chem.* **2018**, *242*, 1–5.

(253) Nishijima, M.; Kato, H.; Yang, C.; Fukuhara, G.; Mori, T.; Araki, Y.; Wada, T.; Inoue, Y. Catalytic Bio-Supramolecular Photochirogenesis: Batch-Operated Enantiodifferentiating Photocyclodimerization of 2-Anthracenecarboxylate with Human Serum Albumin. *ChemCatChem* **2013**, *5*, 3237–3240.

(254) Nishijima, M.; Pace, T. C. S.; Bohne, C.; Mori, T.; Inoue, Y.; Wada, T. Highly Enantiodifferentiating Site of Human Serum Albumin for Mediating Photocyclodimerization of 2-Anthracenecarboxylate Elucidated by Site-Specific Inhibition/Quenching with Xenon. *J. Photochem. Photobiol. A Chem.* **2016**, *331*, 89–94.

(255) Nishijima, M.; Kato, H.; Fukuhara, G.; Yang, C.; Mori, T.; Maruyama, T.; Otagiri, M.; Inoue, Y. Photochirogenesis with Mutant Human Serum Albumins: Enantiodifferentiating Photocyclodimerization of 2-Anthracenecarboxylate. *Chem. Commun.* **2013**, *49*, 7433–7435.

(256) Ishida, Y.; Matsuoka, Y.; Kai, Y.; Yamada, K.; Nakagawa, K.; Asahi, T.; Saigo, K. Metastable Liquid Crystal as Time-Responsive Reaction Medium: Aging-Induced Dual Enantioselective Control. *J. Am. Chem. Soc.* **2013**, *135*, 6407–6410.

(257) Fukuhara, G.; Chiappe, C.; Mele, A.; Melai, B.; Bellina, F.; Inoue, Y. Photochirogenesis in Chiral Ionic Liquid: Enantiodifferentiating [4+4] Photocyclodimerization of 2-Anthracenecarboxylic Acid in (R)-1-Methyl-3-(2,3- Dihydroxypropyl)Imidazolium Bistriflimide. *Chem. Commun.* **2010**, *46*, 3472–3474.

(258) Fukuhara, G.; Okazaki, T.; Lessi, M.; Nishijima, M.; Yang, C.; Mori, T.; Mele, A.; Bellina, F.; Chiappe, C.; Inoue, Y. Chiral Ionic Liquid-Mediated Photochirogenesis. Enantiodifferentiating Photocyclodimerization of 2-Anthracenecarboxylic Acid. *Org. Biomol. Chem.* **2011**, *9*, 7105–7112.

(259) Wei, X.; Liu, J.; Xia, G.-J.; Deng, J.; Sun, P.; Chruma, J. J.; Wu, W.; Yang, C.; Wang, Y.-G.; Huang, Z. Enantioselective Photoinduced Cyclodimerization of a Prochiral Anthracene Derivative Adsorbed on Helical Metal Nanostructures. *Nat. Chem.* **2020**, *12*, 551–559.

(260) Kawanami, Y.; Umehara, H.; Mizoguchi, J. I.; Nishijima, M.; Fukuhara, G.; Yang, C.; Mori, T.; Inoue, Y. Cross- versus Homo-Photocyclodimerization of Anthracene and 2-Anthracenecarboxylic Acid Mediated by a Chiral Hydrogen-Bonding Template. Factors Controlling the Cross-/Homo-Selectivity and Enantioselectivity. *J. Org. Chem.* **2013**, *78*, 3073–3085.

(261) Maturi, M. M.; Fukuhara, G.; Tanaka, K.; Kawanami, Y.; Mori, T.; Inoue, Y.; Bach, T. Enantioselective [4+4] Photodimerization of Anthracene-2,6-Dicarboxylic Acid Mediated by a C2-Symmetric Chiral Template. *Chem. Commun.* **2016**, *52*, 1032–1035.

(262) Kawanami, Y.; Pace, T. C. S.; Mizoguchi, J. I.; Yanagi, T.; Nishijima, M.; Mori, T.; Wada, T.; Bohne, C.; Inoue, Y. Supramolecular Complexation and Enantiodifferentiating Photocyclodimerization of 2-Anthracenecarboxylic Acid with 4-Aminoprolinol Derivatives as Chiral Hydrogen-Bonding Templates. *J. Org. Chem.* **2009**, *74*, 7908–7921.

(263) Kawanami, Y.; Katsumata, S. Y.; Nishijima, M.; Fukuhara, G.; Asano, K.; Suzuki, T.; Yang, C.; Nakamura, A.; Mori, T.; Inoue, Y. Supramolecular Photochirogenesis with a Higher-Order Complex: Highly Accelerated Exclusively Head-to-Head Photocyclodimerization of 2-Anthracenecarboxylic Acid via 2:2 Complexation with Prolinol. *J. Am. Chem. Soc.* **2016**, *138*, 12187–12201.

(264) Fukuhara, G.; Nakamura, T.; Kawanami, Y.; Yang, C.; Mori, T.; Hiramatsu, H.; Dan-Oh, Y.; Tsujimoto, K.; Inoue, Y. Strictly Diastereocontrolled Photocyclodimerization of 2-

Anthracenecarboxylates Tethered to Cyclic Tetrasaccharides. *Chem. Commun.* **2012**, *48*, 9156–9158.

(265) Fukuhara, G.; Nakamura, T.; Kawanami, Y.; Yang, C.; Mori, T.; Hiramatsu, H.; Dan-Oh, Y.; Nishimoto, T.; Tsujimoto, K.; Inoue, Y. Diastereodifferentiating Photocyclodimerization of 2-Anthracenecarboxylates Tethered to a Cyclic Tetrasaccharide Scaffold: Critical Control of Photoreactivity and Stereoselectivity. *J. Org. Chem.* **2013**, *78*, 10996–11006.

(266) Fukuhara, G.; Iida, K.; Kawanami, Y.; Tanaka, H.; Mori, T.; Inoue, Y. Excited-State Dynamics Achieved Ultimate Stereocontrol of Photocyclodimerization of Anthracenecarboxylates on a Glucose Scaffold. *J. Am. Chem. Soc.* **2015**, *137*, 15007–15014.

(267) Fukuhara, G.; Iida, K.; Mori, T.; Inoue, Y. Critical Control by Scaffold Flexibility Achieved in Diastereodifferentiating Photocyclodimerization of 2-Anthracenecarboxylate. *J. Photochem. Photobiol. A Chem.* **2016**, *331*, 76–83.

(268) Dawn, A.; Fujita, N.; Haraguchi, S.; Sada, K.; Shinkai, S. An Organogel System Can Control the Stereochemical Course of Anthracene Photodimerization. *Chem. Commun.* **2009**, *7345*, 2100–2102.

(269) Tanabe, J.; Taura, D.; Ousaka, N.; Yashima, E. Chiral Template-Directed Regio-, Diastereo-, and Enantioselective Photodimerization of an Anthracene Derivative Assisted by Complementary Amidinium-Carboxylate Salt Bridge Formation. *J. Am. Chem. Soc.* **2017**, *139*, 7388–7398.

(270) Urushima, A.; Taura, D.; Tanaka, M.; Horimoto, N.; Tanabe, J.; Ousaka, N.; Mori, T.; Yashima, E. Enantiodifferentiating Photodimerization of a 2,6-Disubstituted Anthracene Assisted by Supramolecular Double-Helix Formation with Chiral Amines. *Angew. Chemie - Int. Ed.* **2020**, *59*, 7478–7486.

(271) Nishijima, M.; Tanaka, H.; Yang, C.; Fukuhara, G.; Mori, T.; Babenko, V.; Dzwolak, W.; Inoue, Y. Supramolecular Photochirogenesis with Functional Amyloid Superstructures. *Chem. Commun.* **2013**, *49*, 8916–8918.

(272) Bando, K.; Zako, T.; Sakono, M.; Maeda, M.; Wada, T.; Nishijima, M.; Fukuhara, G.; Yang, C.; Mori, T.; Pace, T. C. S.; Bohne, C.; Inoue, Y. Bio-Supramolecular Photochirogenesis with Molecular Chaperone: Enantiodifferentiating Photocyclodimerization of 2-Anthracenecarboxylate Mediated by Prefoldin. *Photochem. Photobiol. Sci.* **2010**, *9*, 655–660.

(273) Fukuhara, G.; Nakamura, T.; Yang, C.; Mori, T.; Inoue, Y. Dual Chiral, Dual Supramolecular Diastereodifferentiating Photocyclodimerization of 2-Anthracenecarboxylate Tethered to Amylose Scaffold. *Org. Lett.* **2010**, *12*, 3510–3513.

(274) Tung, C. H.; Guan, J. Q. Regioselectivity in the Photocycloaddition of 9-Substituted Anthracenes Incorporated within Nafion Membranes. *J. Org. Chem.* **1998**, *63*, 5857–5862.

(275) Schütz, A.; Wolff, T. Regioselectivity in the Photodimerization of 9-Hydroxy-Methylanthracene and 9-Anthracene Carboxylic Acid Esters in Surfactant Systems. *J. Photochem. Photobiol. A Chem.* **1997**, *109*, 251–258.

(276) Ryu, N.; Kawaguchi, T.; Yanagita, H.; Okazaki, Y.; Buffeteau, T.; Yoshida, K.; Shirosaki, T.; Nagaoka, S.; Takafuji, M.; Ihara, H.; Oda, R. Chirality Induction on Non-Chiral Dye-Linked Polysilsesquioxane in Nanohelical Structures. *Chem. Commun.* **2020**.

(277) Graaff, R.; Aarnoudse, J. G.; Zijp, J. R.; Sloot, P. M. A.; de Mul, F. F. M.; Greve, J.; Koelink, M. H. Reduced Light-Scattering Properties for Mixtures of Spherical Particles: A Simple Approximation Derived from Mie Calculations. *Appl. Opt.* **1992**, *31*, 1370.

(278) Ryu, N.; Okazaki, Y.; Hirai, K.; Takafuji, M.; Nagaoka, S.; Pouget, E.; Ihara, H.; Oda, R. Memorized Chiral Arrangement of Gemini Surfactant Assemblies in Nanometric Hybrid Organic-Silica Helices. *Chem. Commun.* **2016**, *52*, 5800–5803.

(279) Pathan, S.; Noguchi, H.; Yamada, N.; Kuwahara, Y.; Takafuji, M.; Oda, R.; Ihara, H. Fabrication of Fluorescent One-Dimensional-Nanocomposites through One-Pot Self-Assembling Polymerization on Nano-Helical Silica. *Chem. Lett.* **2019**, *48*, 1088–1091.

(280) Würthner, F.; Kaiser, T. E.; Saha-Möller, C. R. J-Aggregates: From Serendipitous Discovery to Supramolecular Engineering of Functional Dye Materials. *Angew. Chemie - Int. Ed.* **2011**, *50*, 3376–3410.

(281) Hinoue, T.; Shigenoi, Y.; Sugino, M.; Mizobe, Y.; Hisaki, I.; Miyata, M.; Tohnai, N. Regulation of π-Stacked Anthracene Arrangement for Fluorescence Modulation of Organic Solid from Monomer to Excited Oligomer Emission. *Chem. - A Eur. J.* **2012**, *18*, 4634–4643.

(282) Jones, R. N. The Ultraviolet Absorption Spectra of Anthracene Derivatives. *Chem. Rev.* **1947**, *41*, 353–371.

(283) Suzuki, S.; Fujii, T.; Yamanaka, S.; Yoshiike, N.; Hayashi, Z. Absorption and Fluorescence Spectra of Anthracenecarboxylic Acids. II. 1- and 2-Anthroic Acids. *Bull. Chem. Soc. Jpn.* **1979**, *52*, 742–746.

(284) Radziszewski, J. G.; Michl, J. Symmetry Assignment of Vibrations in Anthracene, Phenazine, and Acridine from Infrared Dichroism in Stretched Polyethylene. *J. Chem. Phys.* **1985**, *82*, 3527–3533.

(285) Cataldo, F.; García-Hernández, D. A.; Manchado, A. Sonochemical Synthesis of Fullerene C 60/Anthracene Diels-Alder Mono and Bis-Adducts. *Fullerenes Nanotub. Carbon Nanostructures* **2014**, *22*, 565–574.

(286) Nishijima, M.; Wada, T.; Nagamori, K.; Inoue, Y. High-Sensitivity HPLC Quantification of Nonfluorescent but Photolabile Analyte through Photoreversion in Fluorescence Detector. *Chem. Lett.* **2009**, *38*, 726–727.

(287) Corbett, J. F. Pseudo First-Order Kinetics. *J. Chem. Educ.* **1972**, *49*, 663.

(288) Williams, D. E.; Xiao, Y. Benzene, Naphthalene and Anthracene Dimers and Their Relation to the Observed Crystal Structures. *Acta Crystallogr. Sect. A* **1993**, *49*, 1–10.

(289) Dean, J. A. *Lange's Handbook Of Chemistry, 15th Ed.*; 1999.

(290) Schue, L.; Jean-Baptiste, P.-M.; Du, Y.; Jintoku, H.; Ihara, H.; Oda, R.; Nlate, S. Electrostatic Immobilization of Substrate and Polyoxotungstate Catalyst at the Surface of Micelles for Enhanced Reaction Efficiency in Water. *Catal. Commun.* **2015**, *59*, 65–68.

(291) Buffeteau, T.; Lagugné-Labarthet, F.; Sourisseau, C. Vibrational Circular Dichroism in General Anisotropic Thin Solid Films: Measurement and Theoretical Approach. *Appl. Spectrosc.* **2005**, *59*, 732–745.

(292) Nafie, L. A.; Vidrine, D. W. Fourier Transform Infrared Spectroscopy. In *Fourier Transform Infrared Spectroscopy*; Ferraro, J. ., Basile, L. J., Eds.; Academic Press: New York, 1982; pp 83–123.

(293) Saphier, S.; Piran, R.; Keinan, E. Photoenzymes and Photoabzymes. *Catalytic Antibodies*. October 7, 2004, pp 350–369.

(294) Staros, J. V.; Wright, R. W.; Swingle, D. M. Enhancement by N-Hydroxysulfosuccinimide of Water-Soluble Carbodiimide-Mediated Coupling Reactions. *Anal. Biochem.* **1986**, *156*, 220–222.

(295) GODING, J. W. 7 - Introduction to Monoclonal Antibodies; GODING, J. W. B. T.-M. A. (Third E., Ed.; Academic Press: London, 1996; pp 116–140.

(296) Krupanidhi, S. Therapeutic Proteins through Phage Display- a Brilliant Technique for Its Simplicity. *Indian J. Pharm. Educ. Res.* **2019**, *53*, S481–S486.

(297) Zielonka, S.; Krah, S. Genotype Phenotype Coupling. In *Methods in Molecular Biology*; Springer US, 2020; Vol. 2070.

(298) Wu, Y.; Li, C.; Xia, S.; Lu, L.; Jiang, S.; Ying, T.; Wu, Y.; Li, C.; Xia, S.; Tian, X.; Kong, Y.; Wang, Z.; Gu, C.; Zhang, R.; Tu, C. Short Article Identification of Human Single-Domain Antibodies against SARS-CoV-2 Short Article Identification of Human Single-Domain Antibodies against SARS-CoV-2. **2020**, 1–8.

(299) Smith, G. P.; Petrenko, V. A. Phage Display. *Chem. Rev.* **1997**, *97*, 391–410.

(300) Carpino, L. A. 1-Hydroxy-7-Azabenzotriazole. An Efficient Peptide Coupling Additive. *J. Am. Chem. Soc.* **1993**, *115*, 4397–4398.

(301) Hoogenboom, H. R. Selecting and Screening Recombinant Antibody Libraries. *Nat. Biotechnol.* **2005**, *23*, 1105–1116.

(302) Carmen, S.; Jermutus, L. Concepts in Antibody Phage Display. *Briefings Funct. Genomics Proteomics* **2002**, *1*, 189–203.

(303) Haque, A.; Tonks, N. K. The Use of Phage Display to Generate Conformation-Sensor Recombinant Antibodies. *Nat. Protoc.* **2012**, *7*, 2127–2143.

(304) Engvall, E.; Perlmann, P. Enzyme-Linked Immunosorbent Assay (ELISA) Quantitative Assay of Immunoglobulin G. *Mol. Immunol.* **1971**, *8*, 871–874.

(305) Engvall, E.; Perlmann, P. Enzyme-Linked Immunosorbent Assay, Elisa. 3. Quantitation of Specific Antibodies by Enzyme-Labeled Anti-Immunoglobulin in Antigen-Coated Tubes. *J. Immunol.* **1972**, *109*, 129–135.

(306) Yu, C.-M.; Peng, H.-P.; Chen, I.-C.; Lee, Y.-C.; Chen, J.-B.; Tsai, K.-C.; Chen, C.-T.; Chang, J.-Y.; Yang, E.-W.; Hsu, P.-C.; Jian, J.-W.; Hsu, H.-J.; Chang, H.-J.; Hsu, W.-L.; Huang, K.-F.; Ma, A. C.; Yang, A.-S. Rationalization and Design of the Complementarity Determining Region Sequences in an Antibody-Antigen Recognition Interface. *PLoS One* **2012**, *7*, e33340.

(307) De Wildt, R. M. T.; Mundy, C. R.; Gorick, B. D.; Tomlinson, I. M. Antibody Arrays for High-Throughput Screening of Antibody-Antigen Interactions. *Nat. Biotechnol.* **2000**, *18*, 989–994.

(308) Uba, A. .; Abdulazeez, M. .; Usman, S. .; Tabakolu, H. .; Abubakar, H. Phage Display Technology as a Strong Alternative to Hybridoma Technology for Monoclonal Antibody Production. *Int. J. Sci. Technol.* **2015**, *4*, 125–131.

(309) Hunkapiller, T.; Kaiser, R. J.; Koop, B. F.; Hood, L. Large-Scale and Automated DNA Sequence Determination. *Science (80-.).* **1991**, *254*, 59–67.

(310) Lee, L. G.; Connell, C. R.; Woo, S. L.; Cheng, R. D.; Mcardle, B. F.; Fuller, C. W.; Halloran, N. D.; Wilson, R. K. DNA Sequencing with Dye-Labeled Terminators and T7 DNA Polymerase: Effect of Dyes and DNTPs on Incorporation of Dye-Terminators and Probability Analysis of Termination Fragments. *Nucleic Acids Res.* **1992**, *20*, 2471–2483.

(311) Mardis, E. R. High-Throughput Detergent Extraction of M13 Subclones for Fluorescent DNA Sequencing. *Nucleic Acids Res.* **1994**, *22*, 2173–2175.

(312) Marcus, W. D.; Lindsay, S. M.; Sierks, M. R. Identification and Repair of Positive Binding Antibodies Containing Randomly Generated Amber Codons from Synthetic Phage Display Libraries. *Biotechnol. Prog.* **2006**, *22*, 919–922.

(313) Ho, S. N.; Hunt, H. D.; Horton, R. M.; Pullen, J. K.; Pease, L. R. Site-Directed Mutagenesis by Overlap Extension Using the Polymerase Chain Reaction. *Gene* **1989**, *77*, 51–59.

(314) Garfin, D. E. Chapter 29 One-Dimensional Gel Electrophoresis1. *Methods Enzymol.* **2009**, *463*, 497–513.

(315) Gasteiger, E.; Hoogland, C.; Gattiker, A.; Duvaud, S.; Wilkins, M. R.; Appel, R. D.; Bairoch, A. The Proteomics Protocols Handbook. *Proteomics Protoc. Handb.* **2005**, 571–608.

(316) Micsonai, A.; Wien, F.; Kernya, L.; Lee, Y. H.; Goto, Y.; Réfrégiers, M.; Kardos, J. Accurate Secondary Structure Prediction and Fold Recognition for Circular Dichroism Spectroscopy. *Proc. Natl. Acad. Sci. U. S. A.* **2015**, *112*, E3095–E3103.

(317) Micsonai, A.; Wien, F.; Bulyáki, É.; Kun, J.; Moussong, É.; Lee, Y. H.; Goto, Y.; Réfrégiers, M.; Kardos, J. BeStSel: A Web Server for Accurate Protein Secondary Structure Prediction and Fold Recognition from the Circular Dichroism Spectra. *Nucleic Acids Res.* **2018**, *46*, W315–W322.

(318) Coulter, C. B.; Stone, F. M.; Kabat, E. A. THE STRUCTURE OF THE ULTRAVIOLET ABSORPTION SPECTRA OF CERTAIN PROTEINS AND AMINO ACIDS. *J. Gen. Physiol.* **1936**, *19*, 739–752.

(319) Beychok, S. Circular Dichroism of Biological Macromolecules Circular Dichroism Spectra of Proteins and Nucleic Acids. *Science (80-.).* **1966**, *154*, 1288–1299.

(320) Inoue, Y.; Ikeda, H.; Kaneda, M.; Sumimura, T.; Everitt, S. R. L.; Wada, T. Entropy-Controlled Asymmetric Photochemistry: Switching of Product Chirality by Solvent. *J. Am. Chem. Soc.* **2000**, *122*, 406–407.

(321) Bjellqvist, B.; Basse, B.; Olsen, E.; Celis, J. E. Reference Points for Comparisons of Two-Dimensional Maps of Proteins from Different Human Cell Types Defined in a PH Scale Where Isoelectric Points Correlate with Polypeptide Compositions. *Electrophoresis* **1994**, *15*, 529–539.

(322) Bjellqvist, B.; Hughes, G. J.; Pasquali, C.; Paquet, N.; Ravier, F.; Sanchez, J. -C; Frutiger, S.; Hochstrasser, D. The Focusing Positions of Polypeptides in Immobilized PH Gradients Can Be Predicted from Their Amino Acid Sequences. *Electrophoresis* **1993**, *14*, 1023–1031.

(323) Mentzel, M.; Hoffmann, H. M. R. N-Methoxy-N-Methylamides (Weinreb Amides) in Modern Organic Synthesis. *J. Prakt. Chemie/Chemiker-Zeitung* **1997**, *339*, 517–524.

(324) Kalia, J.; Raines, R. T. Hydrolytic Stability of Hydrazones and Oximes. *Angew. Chemie - Int. Ed.* **2008**, *47*, 7523–7526.

(325) Zhang, N.; Yu, Q.; Chen, R.; Huang, J.; Xia, Y.; Zhao, K. Synthesis of Biaryl Imino/Keto Carboxylic Acids via Aryl Amide Directed C-H Activation Reaction. *Chem. Commun.* **2013**, *49*, 9464–9466.

(326) Liang, Y. F.; Wang, X.; Yuan, Y.; Liang, Y.; Li, X.; Jiao, N. Ligand-Promoted Pd-Catalyzed Oxime Ether Directed C-H Hydroxylation of Arenes. *ACS Catal.* **2015**, *5*, 6148–6152.

(327) Mayr, H.; Dogan, B. Selectivities in Ionic Reductions of Alcohols and Ketones with Triethylsilane/Trifluoroacetic Acid. *Tetrahedron Lett.* **1997**, *38*, 1013–1016.

(328) Mirza-Aghayan, M.; Boukherroub, R.; Rahimifard, M. Efficient Method for the Reduction of

Carbonyl Compounds by Triethylsilane Catalyzed by PdCl2. *J. Organomet. Chem.* **2008**, *693*, 3567–3570.

(329) Horning, E. C.; Reisner, D. B. Catalytic Reduction of Aromatic Ketones. *J. Am. Chem. Soc.* **1949**, *71*, 1036–1037.

(330) Ihmels, H. Synthesis, Fluorescence Properties, and Head-to-Tail Regioselectivity in the Photodimerization of a Donor-Acceptor-Substituted Anthracene. *European J. Org. Chem.* **1999**, No. 7, 1595–1600.

(331) Koo, J. Studies in Polyphosphoric Acid Cyclizations. *J. Am. Chem. Soc.* **1953**, *75*, 1891–1895.

(332) So, Y. H.; Heeschen, J. P. Mechanism of Polyphosphoric Acid and Phosphorus Pentoxide-Methanesulfonic Acid as Synthetic Reagents for Benzoxazole Formation. *J. Org. Chem.* **1997**, *62*, 3552–3561.

(333) Marquardt, D. J.; McCormick, F. A. An Efficient Reduction of Anthrones to Anthracenes. *Tetrahedron Lett.* **1994**, *35*, 1131–1134.

(334) Van Damme, J.; van den Berg, O.; Brancart, J.; Van Assche, G.; Du Prez, F. A Novel Donor-π-Acceptor Anthracene Monomer: Towards Faster and Milder Reversible Dimerization. *Tetrahedron* **2019**, *75*, 912–920.

(335) Kihara, H.; Yoshida, M. Reversible Phase Change of New Anthracene Compounds Triggered by the Action of Light and Heat. *IOP Conf. Ser. Mater. Sci. Eng.* **2014**, *54*, 012020.

(336) Khurana, J. M.; Chauhan, S.; Bansal, G. Facile Hydrolysis of Esters with KOH-Methanol at Ambient Temperature. *Monatshefte fur Chemie* **2004**, *135*, 83–87.

(337) Ahlrichs, R.; Bär, M.; Häser, M.; Horn, H.; Kölmel, C. Electronic Structure Calculations on Workstation Computers: The Program System Turbomole. *Chem. Phys. Lett.* **1989**, *162*, 165–169.

(338) Weigend, F.; Ahlrichs, R. Balanced Basis Sets of Split Valence, Triple Zeta Valence and Quadruple Zeta Valence Quality for H to Rn: Design and Assessment of Accuracy. *Phys. Chem. Chem. Phys.* **2005**, *7*, 3297–3305.

(339) Bursch, M.; Caldeweyher, E.; Hansen, A.; Neugebauer, H.; Ehlert, S.; Grimme, S. Understanding and Quantifying London Dispersion Effects in Organometallic Complexes. *Acc. Chem. Res.* **2019**, *52*, 258–266.

(340) Christiansen, O.; Koch, H.; Jørgensen, P. The Second-Order Approximate Coupled Cluster Singles and Doubles Model CC2. *Chem. Phys. Lett.* **1995**, *243*, 409–418.

(341) Zhang, I. Y.; Grüneis, A. Coupled Cluster Theory in Materials Science. *Front. Mater.* **2019**, *6*.

MATERIAL AND EQUIPMENT

Material

All the chemicals used were ordered from FUJIFILM Wako Pure Chemical Corporation (Osaka, Japan), Tokyo Chemical Industry Co., Ltd. (Tokyo, Japan) and Sigma-Aldrich, Inc. (St. Louis, Missouri, USA) unless stated otherwise. The water mentioned in this document was deionized water purified by Milli-Q® Ultrapure Water System with electrical resistance of 18.2 MΩ·cm. Tomlinson I and J phage libraries were purchased from Danaform (Yokohama, Japan). Amino acid derivatives and reagents for solid-phase peptide synthesis were purchased from Novabiochem (Darmstadt, Germany) or Watanabe Chemical Co. (Hiroshima, Japan). The reagents for plasmid purification and PCRs were purchased from Novagen (Darmstadt, Germany) and QIAGEN (Hilden, Germany). The Br-PEG5-COOH was ordered from BioPharm (China).

Equipment

1 High Performance Liquid Chromatography 1 (Shimadzu)
Pump: SHIMADZU LC-10ACvp Pump
Detector: Shimadzu-SPD10A UV-Vis Detector
Column: Cosmosil 5C18-AR-II column (10ID × 250 mm) for purifying of ACD3-PEG5-Lys(Bio) ligand
Cosmosil 5C18-AR-II column (4.6ID × 150 mm) for analysis of ACD3-PEG5-Lys(Bio) ligand
(Nacalai Tesque, Kyoto, Japan)

2 High Performance Liquid Chromatography 2 (JASCO)
Pump: JASCO PU-2080 Plus Intelligent Pump
Detector: JASCO UV-2075 Plus UV/Vis Intelligent Detector
JASCO FP-2025 Plus Intelligent Fluorescence Detector
Column: GPC Superdex 75 10/300 GL for analysis of antibody
Cosmosil 5C18-MS-II column (4.6ID × 150 mm) and CHIRALCEL OJ-RH column (2.1ID × 120 mm) for analysis of photochemical reaction products
(Nacalai Tesque, Kyoto, Japan)

3 High Performance Liquid Chromatography 3 (JASCO)
Pump: JASCO PU-2080 Plus Intelligent Pump
Detector: JASCO UV-2075 Plus Intelligent UV/Vis Detector
JASCO MD-2018 Plus Photodiode Array Detector
Column: CHIRALPAK® IA (20ID × 250 mm)
(Daicel Corporation, Osaka, Japan)

4 Microplate Reader: CORONA ELECCTRIC MTP-880 Lab

5 UV-Vis Absorption Spectrometer: JASCO V-560, JASCO V-570, JASCO V-670 JASCO V-770 and Varian Cary 300

6 Fluorescence Spectrometer: JASCO FP-6500

7 Circular Dichroism Spectrometer: JASCO J-820 and JASCO J-815

8 Circularly Polarized Luminescence Spectrometer: JASCO CPL-300

9 Thermal Cycler: Applied Biosystems 2720

10 Autoclave: TOMY ES-215

11 Centrifuge: KUBOTA 5500, HITACHI CT 15RE, TOMY CAPSULFUGE PMC-060

12 Incubator: TAITEC BioShaker BR-23FP

13 Cool Water Circulator: SIBATA CoolMan C-580

14 Photoirradiation

Photocyclodimerization of AC with synthetic antibody: USHIO Optical ModuleX 500-watt Xe short arc lamp with 340 nm long-pass filter

Photocyclodimerization of AC with hybrid nanoribbons or helices: USHIO F8T5BL (8 W 352 nm)

Photocyclodimerization of AC-Chd-MAC: THORLABS LED M365L2 (365 nm) DC2200 power supply

15 DNA Sequencer: Applied Biosystems / HITACHI 3500 Genetic Analyzer

16 Freeze Dryer: EYELA FDU-120 (Tokyo Rikakikai, Tokyo, Japan)

17 Fluorescence Lifetime Measurement

Laser: Ti:sapphire Second Harmonic Generation (388 nm) fwhm 150 fs, Spectra-Physics, Tsunami 3950-L2S

Detector: Streak Scope C4334-01Shimadzu-SPD10A, Hamamatsu Photonics

18 Fourier-Transform Infrared Spectrometer: ThermoNicolet Nexus 670 FTIR spectrometer equipped with a VCD optical bench

19 Transmission Electron Microscope: Philips CM-120 (FEI Company, USA) and LVEM5 (Delong Instrument, Austria)

20 Nuclear Magnetic Resonance Spectrometer: Bruker Avance II 300 MHz spectrometer, Bruker Avance III 400 MHz spectrometer, Bruker Avance III 500 MHz spectrometer, Bruker Avance III 600 MHz spectrometer

21 Mass Spectrometer: JEOL AccuTOF LC-plus JMS-T100LP ESI-TOF Mass Spectrometer, Bruker Daltonics micrOTOF-Q II-S1 ESI-QTOF Mass Spectrometer, Bruker AutoFlex Speed-S1 MALDI-TOF Mass Spectrometer

22 Probe sonicator: VCX 130 PB Sonicator with 3 mm Microtip

ACKNOWLEDGEMENT

This study has been carried out under the guidance of Professor Takehiko Wada at The Institute of Multidisciplinary Research for Advanced Materials and Department of Chemistry, Graduate School of Science, Tohoku University, Japan, and Professor Reiko Oda at The Institute of Chemistry and Biology of Membranes and Nano-objects, University of Bordeaux, France.

The author would like to express his sincerest gratitude to Professor Takehiko Wada for his kind guidance, valuable suggestions, inspiration and encouragement through this work. Even when the author had a tough time, he has always been the most important encouragement. His belief in the author since the undergraduate study is the most appreciated and will never be forgotten.

The author would like to also express his sincerest gratitude to Professor Reiko Oda for accepting the author as her student at the University of Bordeaux. The author had learned many different topics under her supervision. Professor Reiko Oda also encouraged the author to establish more connections with researchers in Europe and Japan. Professor Reiko Oda also helped the author with his life in France. Working with her is one of the most memorable memories during his PhD study.

In particular, the author is deeply grateful to Associate Professor Yasuyuki Araki at The Institute of Multidisciplinary Research for Advanced Materials for helpful advice and fruitful discussion on the chirality, interactions studies, photochemistry and physical chemistry-base analysis on this work. He also gave essential advice in the details and the direction of this research.

The author is grateful to Assistant Professor Masaki Nishijima at The Institute of Multidisciplinary Research for Advanced Materials for his help in analysis of HPLC while the author was in Bordeaux. He also helped the author in many steps of organic synthesis.

The author is grateful to Dr. Emilie Pouget at The Institute of Chemistry and Biology of Membranes and Nano-objects for her advice in different techniques about nano-chemistry and life in France, and Dr. Sylvain Nlate from the same institute for his help in French translation, advice in organic chemistry and knowledge of French education.

The author sincerely appreciates Assistance Professor Seiji Sakamoto at The Department of Synthetic Chemistry and Biological Chemistry, Graduate School of Engineering, Kyoto University for his advice in biochemistry and biotechnology.

The author is indebted to Professor Thierry Buffeteau at l'Institut des Sciences Moléculaires, University of Bordeaux in the collaboration of VCD and IR measurement, Professor Dario Bassani from the same institute for his advice in photochemistry, Associate Professor Tadashi Mori at The Department of Applied Chemistry, Graduate School of Engineering, Osaka University for the CD calculation and preparative HPLC chiral column, and Ms. Estelle Morvan at The Institute of European Chemistry and Biology, University of Bordeaux for the collaboration of NMR.

The author is greatly thankful to all member of Wada Laboratory from the year of 2012 to 2020, especially Dr. Ryohei Uematsu, Dr. Hiroka Sugai, Dr. Masahito Inagaki, Dr. Makoto Kuronuma, Mr. Takehito Sato, Mr. Yuya Fujishiro, Mr. Tomonori Kakizaki and Mr. Akira Yano, and Oda Team from the year of 2018 to 2020, especially Dr. Jie Gao, Dr. Antoine Amestoy, Dr. Antoine Scalabre, Dr. Shaheen Pathan, Dr. Jian-Qiao Jiang, Dr. Kyohei Yoshida, Dr. Balamurugan Kuppan, and Mr. Peizhao Liu for their friendship, interesting discussion, support and assistance.

The author would like to express his gratitude to The Sato-Yo International Scholarship Foundation and The Tohoku University President Fellowship for financial support during his study from undergraduate degree. The author also would like to express his gratitude to KAKENHI and LIA from CNRS for the financial support on this research, and also Tohoku University and University of Bordeaux for invaluable education.

The author truly appreciates Ms. Yoko Goto for her support related to administration, life and Japanese language, and Ms. Yumi Hayashi for her coordination to The Sato-Yo International Scholarship Foundation. He is also greatly thankful to his colleagues, Ms. Farsai Taemaitree and Mr. Yuto Kato for their motivation and unshakable friendship since undergraduate.

The author wishes to thank to his family, his father Mr. Wachira Yospanya, his mother Mrs. Jarinee Yospanya, his cousin Ms. Araya Chatchawan and all the family members for their encouragement, understanding, and support. The author will never be able to finish his PhD without their helps.

Wijak YOSPANYA

Department of Chemistry, Graduate School of Science

Tohoku University, Sendai, Japan

Doctoral School of Chemical Science

University of Bordeaux, Bordeaux, France

August 2020

APPENDIX

A1 UV-Vis, CD and Fluorescence Spectroscopy

Chapter 2

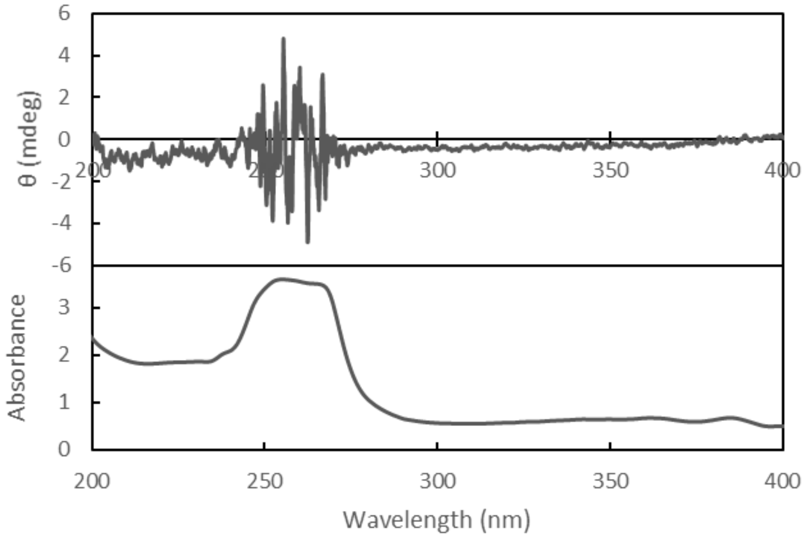

Figure A1-2-1. CD and UV-Vis absorption spectrum of AC 50 µM and L-silica nanoribbons 0.1 g / L in aqueous solution.

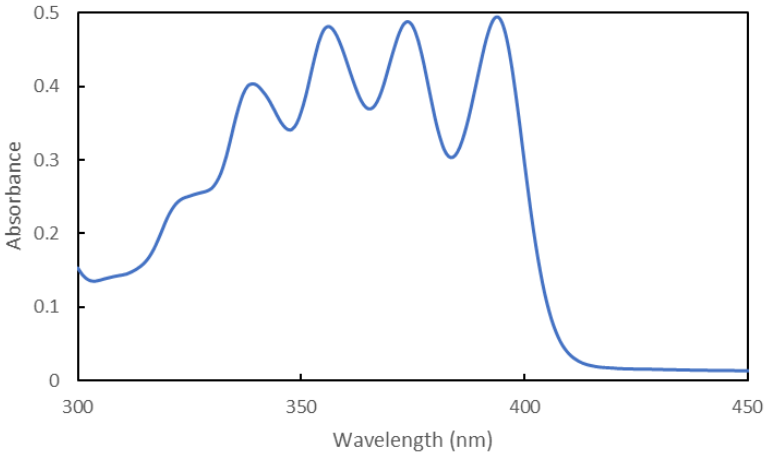

Figure A1-2-2. UV-Vis absorption spectrum of AC 0.1 mM in tetrahydrofuran.

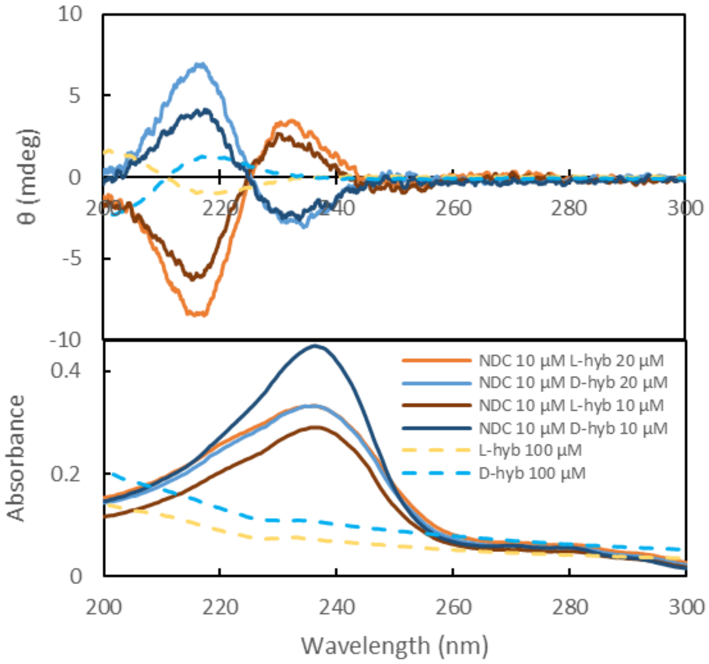

Figure A1-2-3. CD and UV-Vis absorption spectra of NDC 10 µM with hybrid nanoribbons 20 µM and 10 µM.

Chapter 3

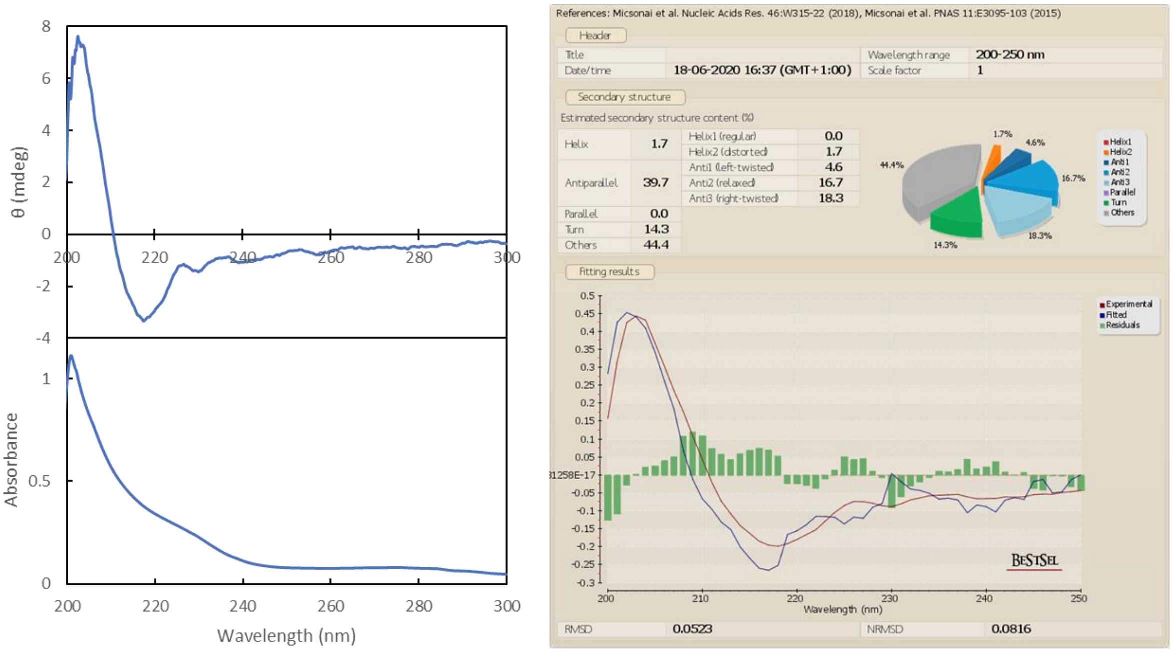

References: Micsonai et al. Nucleic Acids Res. 46:W315-22 (2018), Micsonai et al. PNAS 11:E3095-103 (2015)

Title		Wavelength range	200-250 nm
Date/time	18-06-2020 16:37 (GMT+1:00)	Scale factor	1

Estimated secondary structure content (%)

Helix	1.7	Helix1 (regular)	0.0
		Helix2 (distorted)	1.7
Antiparallel	39.7	Anti1 (left-twisted)	4.6
		Anti2 (relaxed)	16.7
		Anti3 (right-twisted)	18.3
Parallel	0.0		
Turn	14.3		
Others	44.4		

RMSD	0.0523	NRMSD	0.0816

Figure A1-3-1 (a) CD and UV-Vis absorption spectra of scFv J-20 antibody 2 µM and (b) calculated result from the BeStSel protein secondary structure estimation.

A2 NMR Spectroscopy

Chapter 2

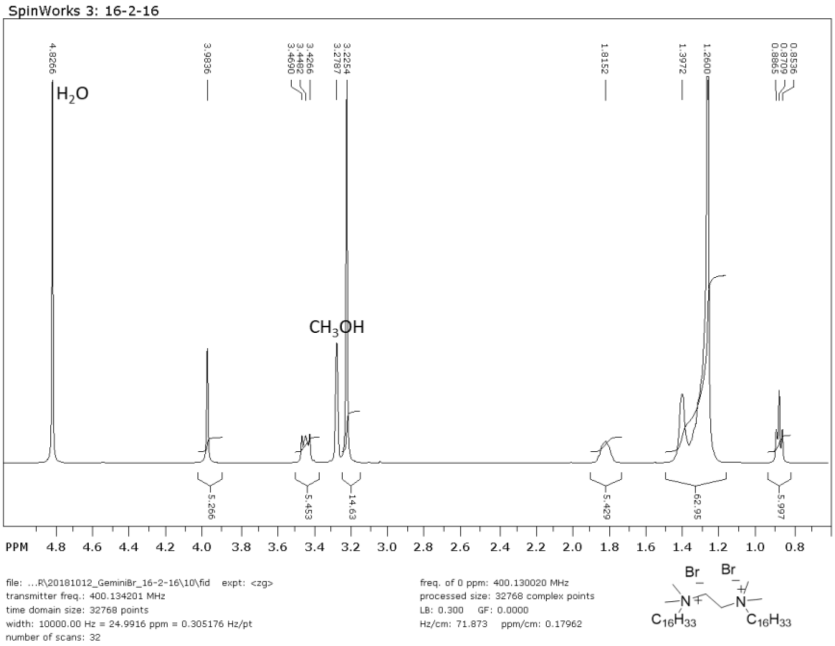

```
file: ...R\20181012_GeminiBr_16-2-16\10\fid   expt: <zg>
transmitter freq.: 400.134201 MHz
time domain size: 32768 points
width: 10000.00 Hz = 24.9916 ppm = 0.305176 Hz/pt
number of scans: 32
```

```
freq. of 0 ppm: 400.130020 MHz
processed size: 32768 complex points
LB: 0.300    GF: 0.0000
Hz/cm: 71.873    ppm/cm: 0.17962
```

Figure A2-2-1. ^{1}H NMR spectrum of *N,N′*-dihexadecyl-*N,N,N′,N′*-tetramethylethylene diammonium bromide.

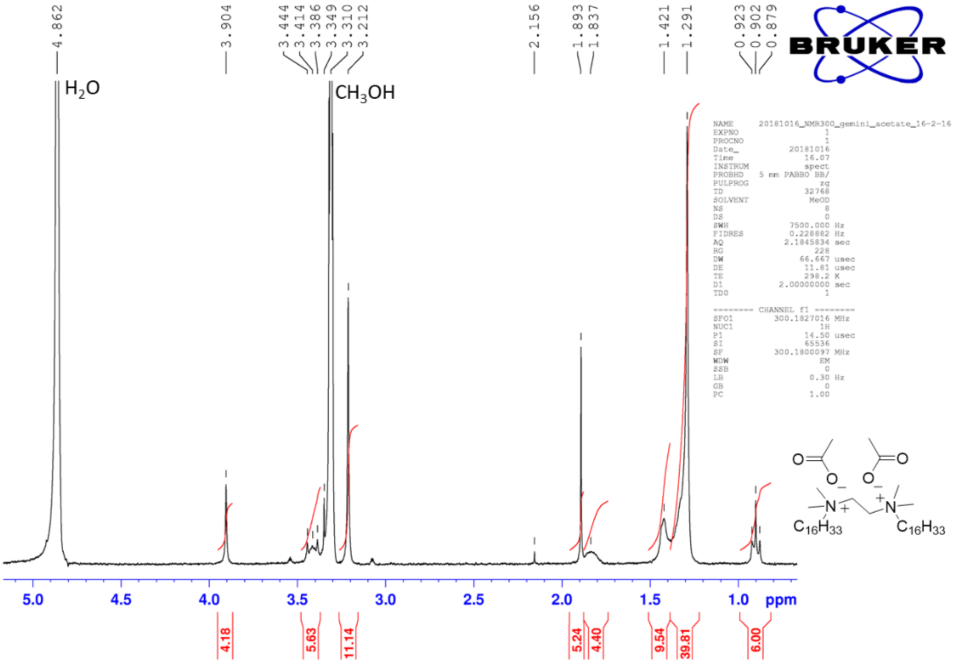

```
NAME      20181016_NMR300_gemini_acetate_16-2-16
EXPNO                  1
PROCNO                 1
Date_           20181016
Time               16.07
INSTRUM            spect
PROBHD    5 mm PABBO BB/
PULPROG               zg
TD                 32768
SOLVENT             MeOD
NS                     8
DS                     0
SWH             7500.000 Hz
FIDRES          0.228882 Hz
AQ             2.1845834 sec
RG                   228
DW                66.667 usec
DE                 11.81 usec
TE                 298.2 K
D1            2.00000000 sec
TD0                    1

======== CHANNEL f1 ========
SFO1         300.1827016 MHz
NUC1                  1H
P1                 14.50 usec
SI                 65536
SF           300.1800097 MHz
WDW                   EM
SSB                    0
LB                  0.30 Hz
GB                     0
PC                  1.00
```

Figure A2-2-2. ^{1}H NMR spectrum of *N,N′*-dihexadecyl-*N,N,N′,N′*-tetramethylethylene diammonium acetate.

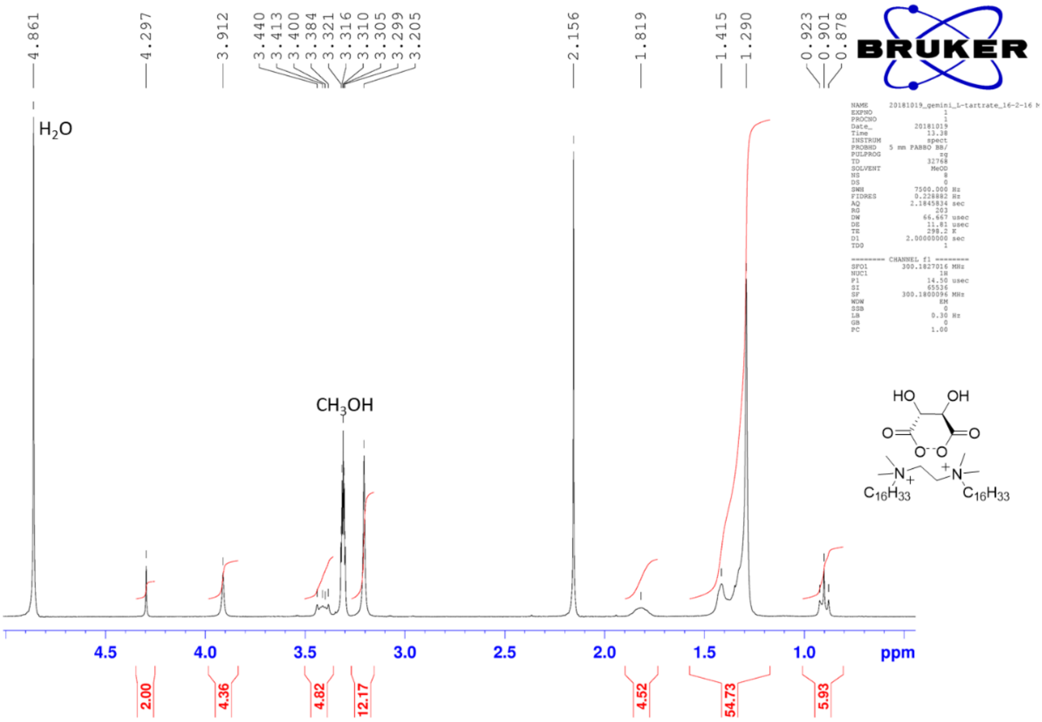

Figure A2-2-3. ^{1}H NMR spectrum of *N,N′*-dihexadecyl-*N,N,N′,N′*-tetramethylethylene diammonium L-tartrate.

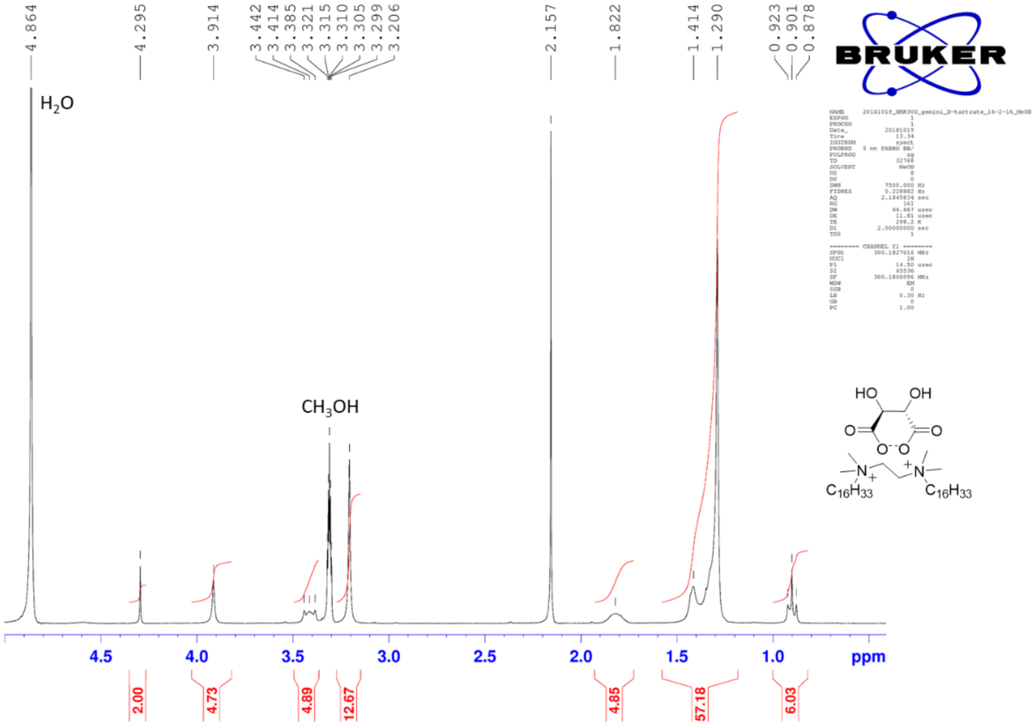

Figure A2-2-4. ^{1}H NMR spectrum of *N,N′*-dihexadecyl-*N,N,N′,N′*-tetramethylethylene diammonium D-tartrate.

Quantitative NMR for AC-Exchanged Hybrid Nanoribbons

The 10 mL suspension of AC 100 µM mixed with D-hybrid nanoribbons 100 µM was incubated overnight at 4 °C on the roller mixer. The suspension was centrifuged at 3893 × g and 4 °C for 12 min. The gel was washed twice by water 4 °C, and lyophilized. The deuterated methanol 1 mL was added to the dried nanoribbons. The suspension was heated at 50 °C for 10 min, sonicated for 10 min, and centrifuged at 3893 × g and 20 °C for 12 min. The supernatant 0.5 mL was measured the NMR (^{1}H, 400 MHz, D1 = 60 s).

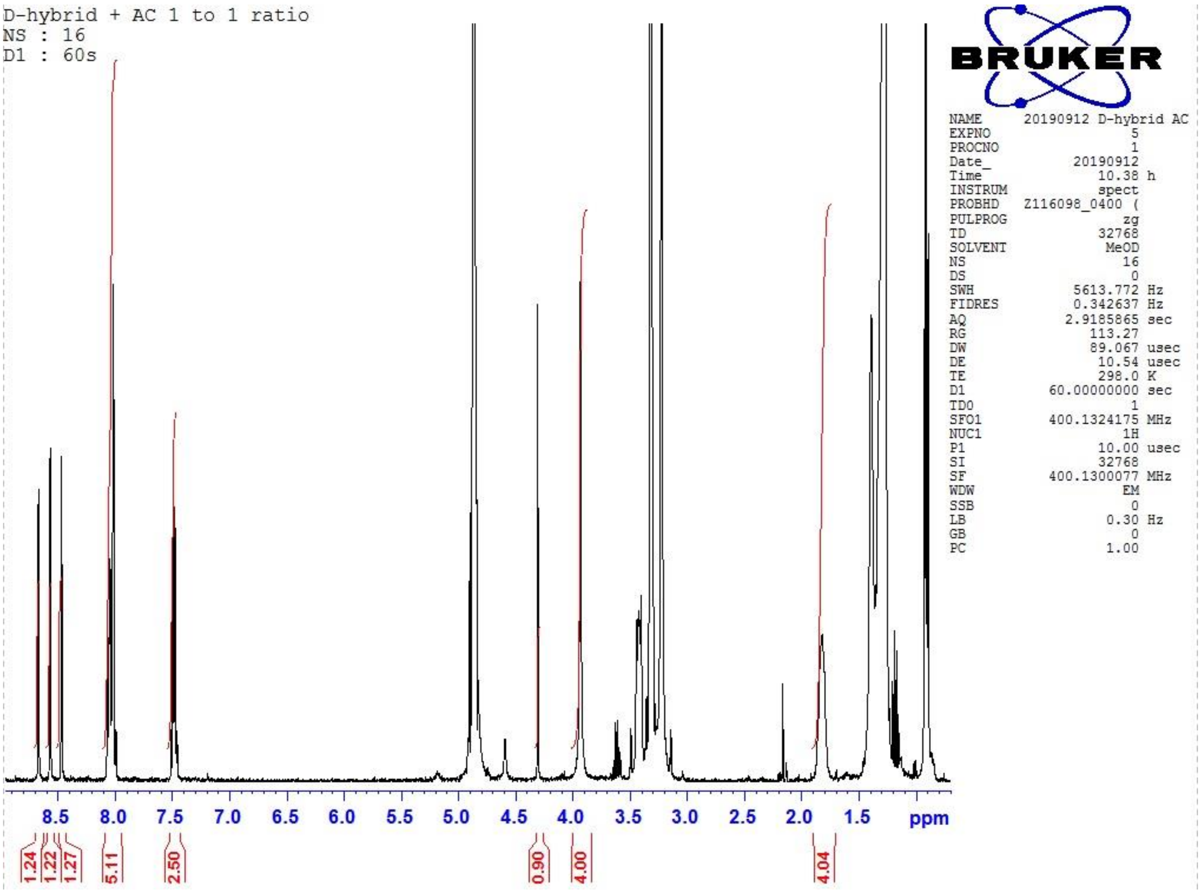

```
D-hybrid + AC 1 to 1 ratio
NS : 16
D1 : 60s
```

```
NAME       20190912 D-hybrid AC
EXPNO                         5
PROCNO                        1
Date_                  20190912
Time                    10.38 h
INSTRUM                   spect
PROBHD     Z116098_0400 (
PULPROG                      zg
TD                        32768
SOLVENT                    MeOD
NS                           16
DS                            0
SWH                5613.772 Hz
FIDRES             0.342637 Hz
AQ                2.9185865 sec
RG                       113.27
DW                  89.067 usec
DE                   10.54 usec
TE                      298.0 K
D1             60.00000000 sec
TD0                           1
SFO1          400.1324175 MHz
NUC1                         1H
P1                   10.00 usec
SI                        32768
SF            400.1300077 MHz
WDW                          EM
SSB                           0
LB                      0.30 Hz
GB                            0
PC                         1.00
```

Figure A2-2-5. ^{1}H NMR spectrum of AC-exchanged D-hybrid nanoribbons (1 : 1).

The ratio of AC was calculated from average integrations of the peaks 8.46 (s, 1H, Ar-H), 8.56 (s, 1H, Ar-H) and 8.66 ppm (s, 1H, Ar-H). The ratio of tartrate was calculated from the integration of the peak 4.30 ppm (s, 2H, CH), and the ratio of gemini was calculated from the average integrations of the peaks 1.81 (s, 4H, CH_2) and 3.92 ppm (s, 4H, N-CH_2). As a result, the ratio of [AC] : [tartrate] : [gemini] is 1.2 : 0.45 : 1.0, correlating to the 1 : 1 exchanged ratios.

Chapter 4

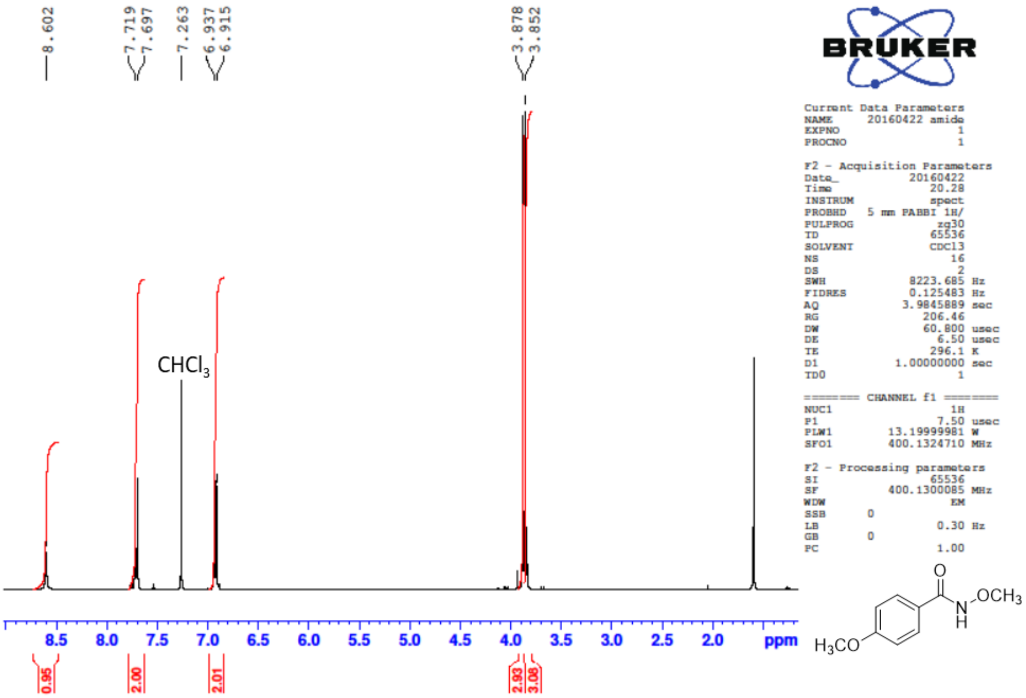

```
Current Data Parameters
NAME       20160422 amide
EXPNO                   1
PROCNO                  1

F2 - Acquisition Parameters
Date_            20160422
Time                20.28
INSTRUM             spect
PROBHD   5 mm PABBI 1H/
PULPROG              zg30
TD                  65536
SOLVENT             CDCl3
NS                     16
DS                      2
SWH              8223.685 Hz
FIDRES           0.125483 Hz
AQ              3.9845889 sec
RG                 206.46
DW                 60.800 usec
DE                   6.50 usec
TE                  296.1 K
D1             1.00000000 sec
TD0                     1

======== CHANNEL f1 ========
NUC1                   1H
P1                   7.50 usec
PLW1          13.19999981 W
SFO1          400.1324710 MHz

F2 - Processing parameters
SI                  65536
SF            400.1300085 MHz
WDW                    EM
SSB      0
LB                   0.30 Hz
GB       0
PC                   1.00
```

Figure A2-4-1. ^{1}H NMR of *N*,4-Dimethoxybenzamide.

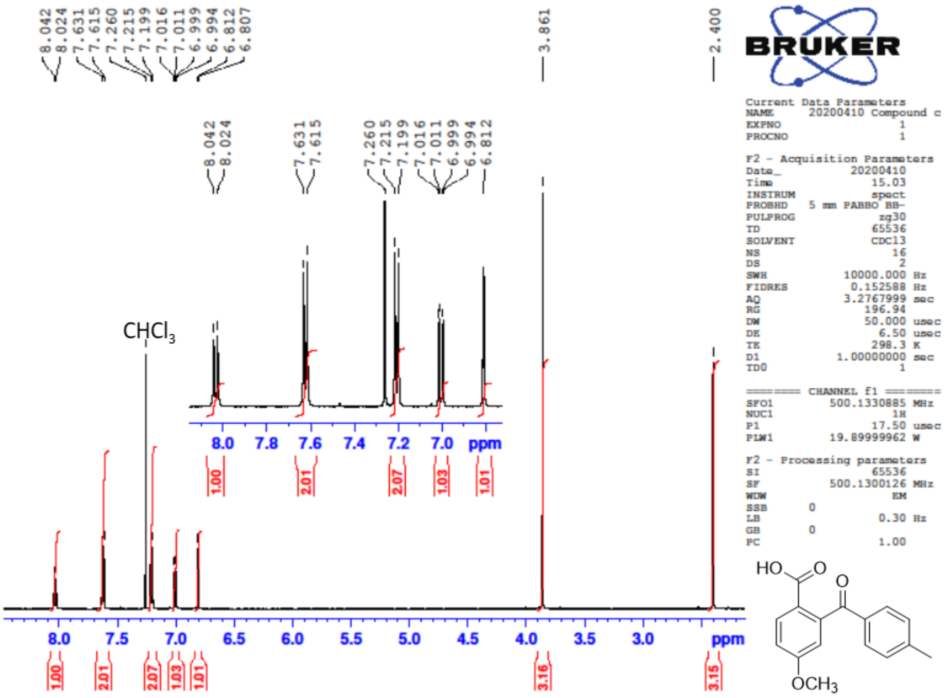

```
Current Data Parameters
NAME       20200410 Compound c
EXPNO                   1
PROCNO                  1

F2 - Acquisition Parameters
Date_            20200410
Time                15.03
INSTRUM             spect
PROBHD   5 mm PABBO BB-
PULPROG              zg30
TD                  65536
SOLVENT             CDCl3
NS                     16
DS                      2
SWH             10000.000 Hz
FIDRES           0.152588 Hz
AQ              3.2767999 sec
RG                 196.94
DW                 50.000 usec
DE                   6.50 usec
TE                  298.3 K
D1             1.00000000 sec
TD0                     1

======== CHANNEL f1 ========
SFO1          500.1330885 MHz
NUC1                   1H
P1                  17.50 usec
PLW1          19.89999962 W

F2 - Processing parameters
SI                  65536
SF            500.1300126 MHz
WDW                    EM
SSB      0
LB                   0.30 Hz
GB       0
PC                   1.00
```

Figure A2-4-2. ^{1}H NMR of 4-methoxy-2-(4-methylbenzoyl)benzoic acid.

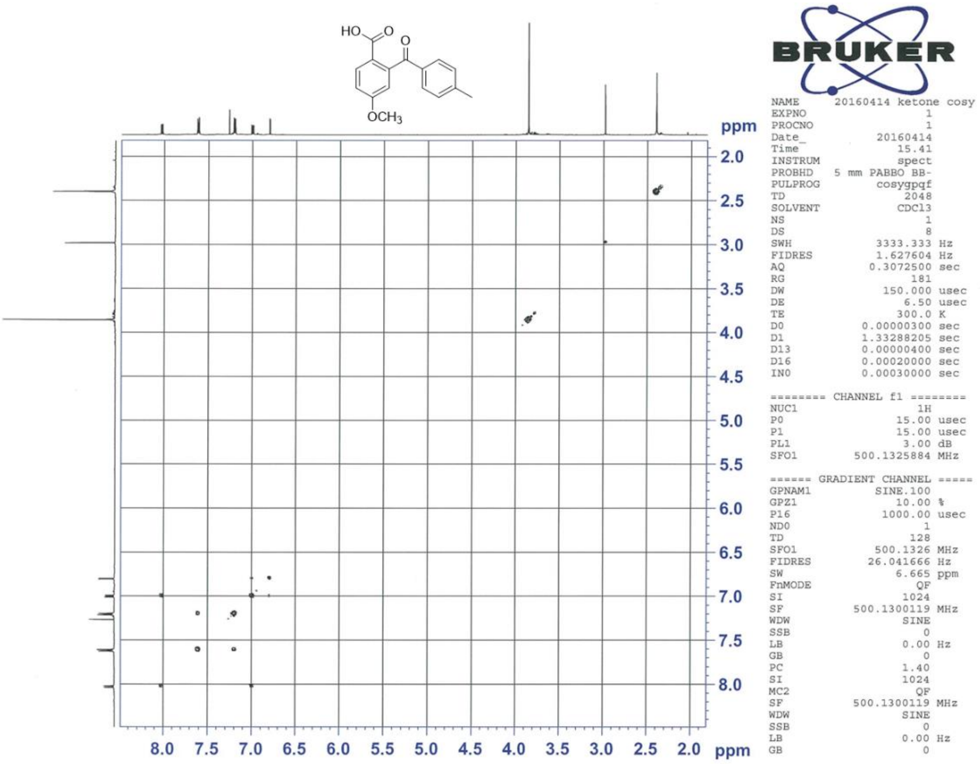

```
NAME       20160414 ketone cosy
EXPNO                     1
PROCNO                    1
Date_              20160414
Time                  15.41
INSTRUM               spect
PROBHD   5 mm PABBO BB-
PULPROG           cosygpqf
TD                     2048
SOLVENT               CDCl3
NS                        1
DS                        8
SWH                3333.333 Hz
FIDRES             1.627604 Hz
AQ                0.3072500 sec
RG                      181
DW                  150.000 usec
DE                     6.50 usec
TE                    300.0 K
D0               0.00000300 sec
D1               1.33288205 sec
D13              0.00000400 sec
D16              0.00020000 sec
IN0              0.00030000 sec

======== CHANNEL f1 ========
NUC1                     1H
P0                    15.00 usec
P1                    15.00 usec
PL1                    3.00 dB
SFO1            500.1325884 MHz

====== GRADIENT CHANNEL =====
GPNAM1             SINE.100
GPZ1                  10.00 %
P16                 1000.00 usec
ND0                       1
TD                      128
SFO1               500.1326 MHz
FIDRES            26.041666 Hz
SW                    6.665 ppm
FnMODE                   QF
SI                     1024
SF              500.1300119 MHz
WDW                    SINE
SSB                       0
LB                     0.00 Hz
GB                        0
PC                     1.40
SI                     1024
MC2                      QF
SF              500.1300119 MHz
WDW                    SINE
SSB                       0
LB                     0.00 Hz
GB                        0
```

Figure A2-4-3. ^{1}H-^{1}H COSY NMR of 4-methoxy-2-(4-methylbenzoyl)benzoic acid.

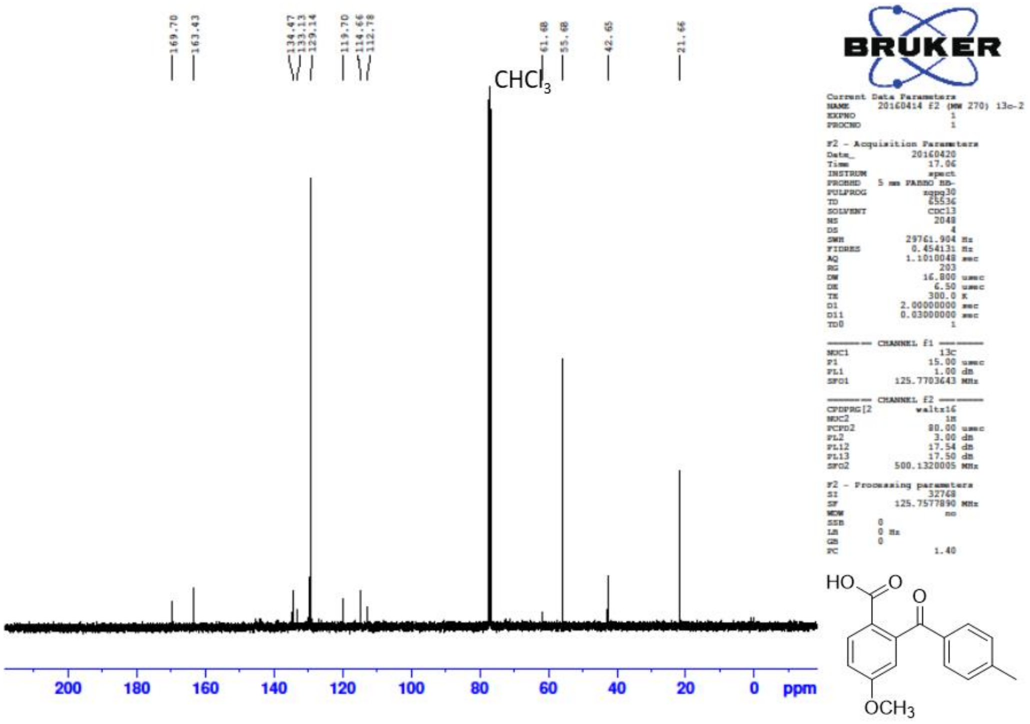

```
Current Data Parameters
NAME      20160414 f2 (mw 270) 13c-2
EXPNO                     1
PROCNO                    1

F2 - Acquisition Parameters
Date_              20160420
Time                  17.06
INSTRUM               spect
PROBHD   5 mm PABBO BB-
PULPROG             zgpg30
TD                    65536
SOLVENT               CDCl3
NS                     2048
DS                        4
SWH               29761.904 Hz
FIDRES             0.454131 Hz
AQ                1.1010048 sec
RG                      203
DW                   16.800 usec
DE                     6.50 usec
TE                    300.0 K
D1               2.00000000 sec
D11              0.03000000 sec
TD0                       1

======== CHANNEL f1 ========
NUC1                    13C
P1                    15.00 usec
PL1                    1.00 dB
SFO1            125.7703643 MHz

======== CHANNEL f2 ========
CPDPRG[2            waltz16
NUC2                     1H
PCPD2                 80.00 usec
PL2                    3.00 dB
PL12                  17.54 dB
PL13                  17.50 dB
SFO2            500.1320005 MHz

F2 - Processing parameters
SI                    32768
SF              125.7577890 MHz
WDW                      no
SSB        0
LB         0 Hz
GB         0
PC                     1.40
```

Figure A2-4-4. ^{13}C NMR of 4-methoxy-2-(4-methylbenzoyl)benzoic acid.

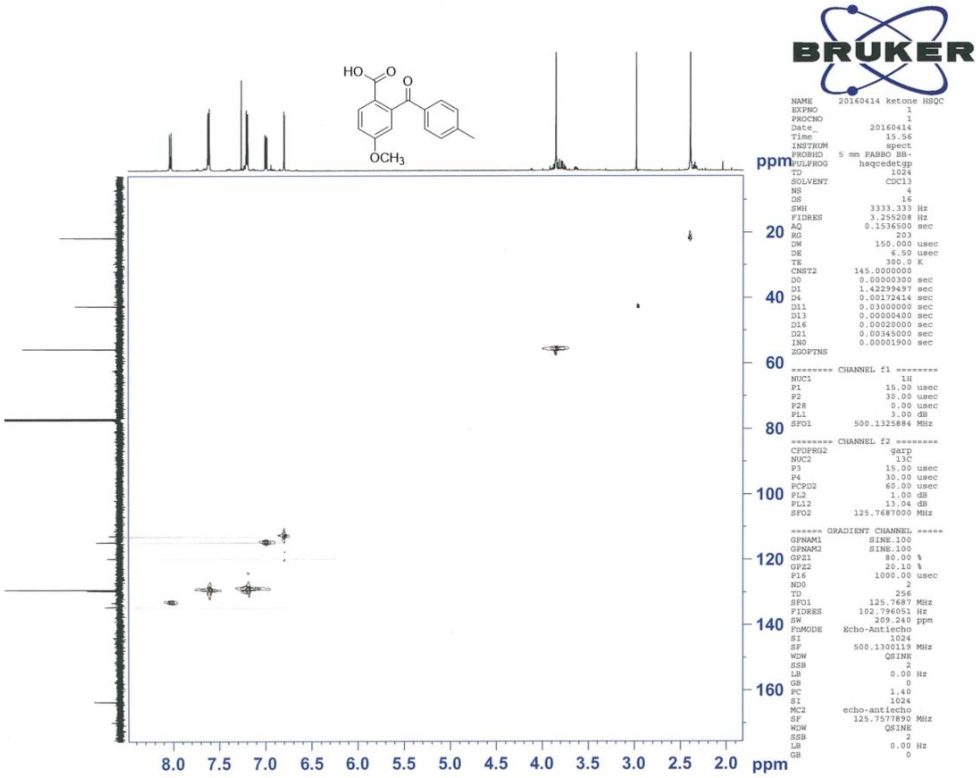

```
NAME       20160414 ketone HSQC
EXPNO                  1
PROCNO                 1
Date_           20160414
Time               15.56
INSTRUM            spect
PROBHD     5 mm PABBO BB-
PULPROG       hsqcedetgp
TD                  1024
SOLVENT            CDCl3
NS                     4
DS                    16
SWH             3333.333 Hz
FIDRES          3.255208 Hz
AQ             0.1536500 sec
RG                   203
DW               150.000 usec
DE                  6.50 usec
TE                 300.0 K
CNST2        145.0000000
D0            0.00000300 sec
D1            1.42299497 sec
D4            0.00172414 sec
D11           0.03000000 sec
D13           0.00000400 sec
D16           0.00020000 sec
D21           0.00345000 sec
IN0           0.00001900 sec
ZGOPTNS

======== CHANNEL f1 ========
NUC1                  1H
P1                 15.00 usec
P2                 30.00 usec
P28                 0.00 usec
PL1                 3.00 dB
SFO1         500.1325884 MHz

======== CHANNEL f2 ========
CPDPRG2             garp
NUC2                 13C
P3                 15.00 usec
P4                 30.00 usec
PCPD2              60.00 usec
PL2                 1.00 dB
PL12               13.04 dB
SFO2         125.7687000 MHz

====== GRADIENT CHANNEL =====
GPNAM1          SINE.100
GPNAM2          SINE.100
GPZ1               80.00 %
GPZ2               20.10 %
P16              1000.00 usec
ND0                    2
TD                   256
SFO1            125.7687 MHz
FIDRES        102.796051 Hz
SW               209.240 ppm
FnMODE     Echo-Antiecho
SI                  1024
SF           500.1300119 MHz
WDW                QSINE
SSB                    2
LB                  0.00 Hz
GB                     0
PC                  1.40
SI                  1024
MC2        echo-antiecho
SF           125.7577890 MHz
WDW                QSINE
SSB                    2
LB                  0.00 Hz
GB                     0
```

Figure A2-4-5. HSQC NMR of 4-methoxy-2-(4-methylbenzoyl)benzoic acid.

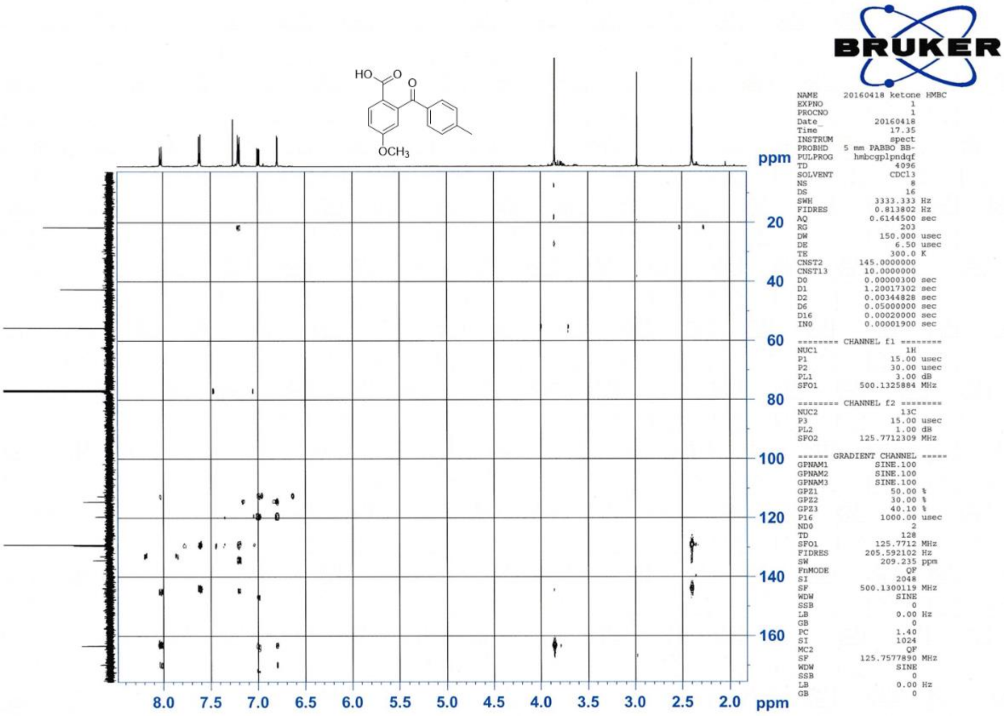

```
NAME       20160418 ketone HMBC
EXPNO                  1
PROCNO                 1
Date_           20160418
Time               17.35
INSTRUM            spect
PROBHD     5 mm PABBO BB-
PULPROG      hmbcgplpndqf
TD                  4096
SOLVENT            CDCl3
NS                     8
DS                    16
SWH             3333.333 Hz
FIDRES          0.813802 Hz
AQ             0.6144500 sec
RG                   203
DW               150.000 usec
DE                  6.50 usec
TE                 300.0 K
CNST2        145.0000000
CNST13        10.0000000
D0            0.00000300 sec
D1            1.20017302 sec
D2            0.00344828 sec
D6            0.05000000 sec
D16           0.00020000 sec
IN0           0.00001900 sec

======== CHANNEL f1 ========
NUC1                  1H
P1                 15.00 usec
P2                 30.00 usec
PL1                 3.00 dB
SFO1         500.1325884 MHz

======== CHANNEL f2 ========
NUC2                 13C
P3                 15.00 usec
PL2                 1.00 dB
SFO2         125.7712309 MHz

====== GRADIENT CHANNEL =====
GPNAM1          SINE.100
GPNAM2          SINE.100
GPNAM3          SINE.100
GPZ1               50.00 %
GPZ2               30.00 %
GPZ3               40.10 %
P16              1000.00 usec
ND0                    2
TD                   128
SFO1            125.7712 MHz
FIDRES        205.592102 Hz
SW               209.235 ppm
FnMODE                QF
SI                  2048
SF           500.1300119 MHz
WDW                 SINE
SSB                    0
LB                  0.00 Hz
GB                     0
PC                  1.40
SI                  1024
MC2                   QF
SF           125.7577890 MHz
WDW                 SINE
SSB                    0
LB                  0.00 Hz
GB                     0
```

Figure A2-4-6. HMBC NMR of 4-methoxy-2-(4-methylbenzoyl)benzoic acid.

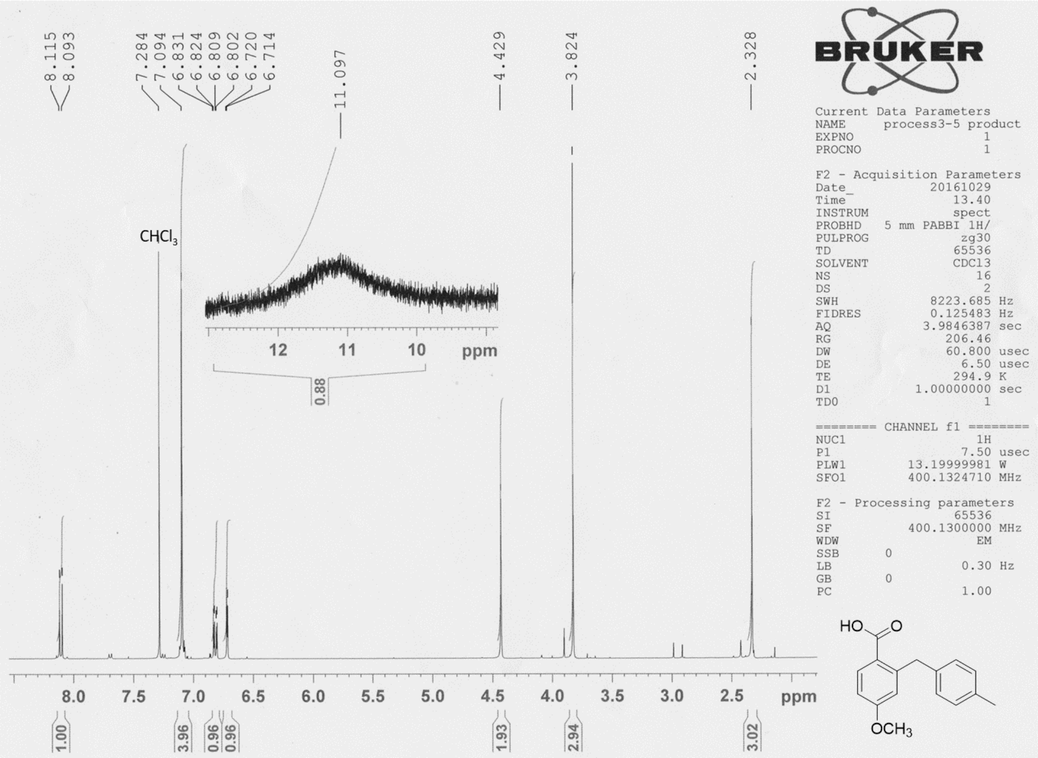

```
Current Data Parameters
NAME      process3-5 product
EXPNO                    1
PROCNO                   1

F2 - Acquisition Parameters
Date_             20161029
Time                 13.40
INSTRUM              spect
PROBHD   5 mm PABBI 1H/
PULPROG               zg30
TD                   65536
SOLVENT              CDCl3
NS                      16
DS                       2
SWH               8223.685 Hz
FIDRES            0.125483 Hz
AQ               3.9846387 sec
RG                  206.46
DW                  60.800 usec
DE                    6.50 usec
TE                   294.9 K
D1              1.00000000 sec
TD0                      1

======== CHANNEL f1 ========
NUC1                    1H
P1                    7.50 usec
PLW1           13.19999981 W
SFO1           400.1324710 MHz

F2 - Processing parameters
SI                   65536
SF             400.1300000 MHz
WDW                     EM
SSB       0
LB                    0.30 Hz
GB        0
PC                    1.00
```

Figure A2-4-7. ^{1}H NMR of 4-methoxy-2-[(4-methylphenyl)methyl]benzoic acid.

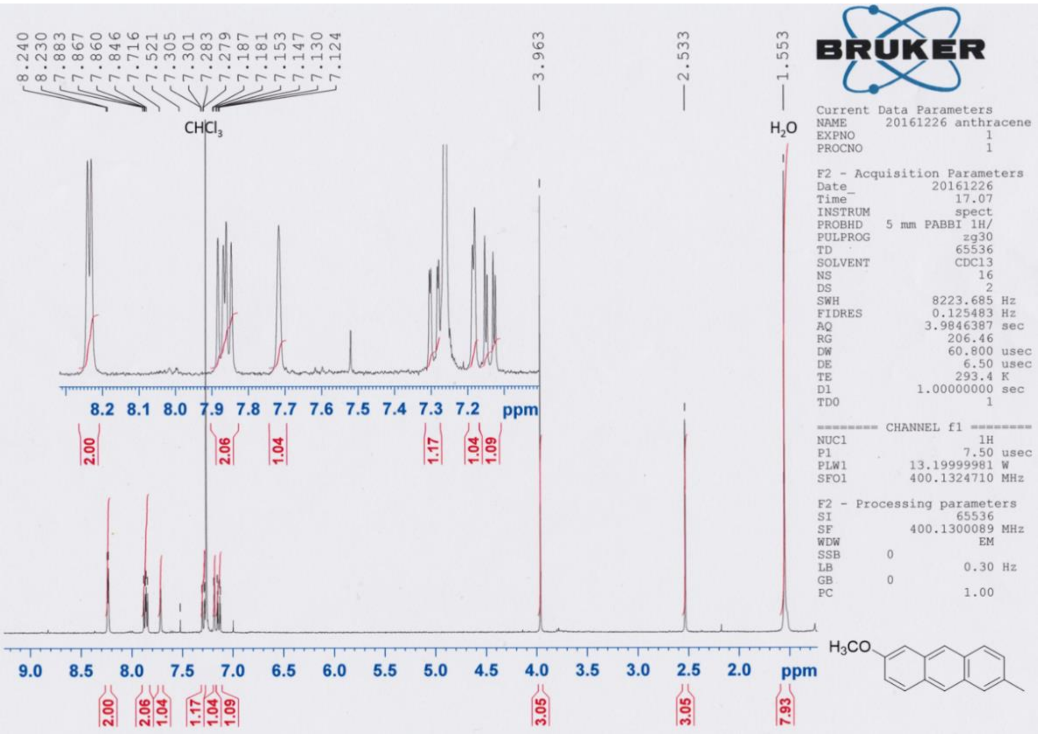

```
Current Data Parameters
NAME      20161226 anthracene
EXPNO                    1
PROCNO                   1

F2 - Acquisition Parameters
Date_             20161226
Time                 17.07
INSTRUM              spect
PROBHD   5 mm PABBI 1H/
PULPROG               zg30
TD                   65536
SOLVENT              CDCl3
NS                      16
DS                       2
SWH               8223.685 Hz
FIDRES            0.125483 Hz
AQ               3.9846387 sec
RG                  206.46
DW                  60.800 usec
DE                    6.50 usec
TE                   293.4 K
D1              1.00000000 sec
TD0                      1

======== CHANNEL f1 ========
NUC1                    1H
P1                    7.50 usec
PLW1           13.19999981 W
SFO1           400.1324710 MHz

F2 - Processing parameters
SI                   65536
SF             400.1300089 MHz
WDW                     EM
SSB       0
LB                    0.30 Hz
GB        0
PC                    1.00
```

Figure A2-4-8. ^{1}H NMR of 2-methoxy-6-methylanthracene.

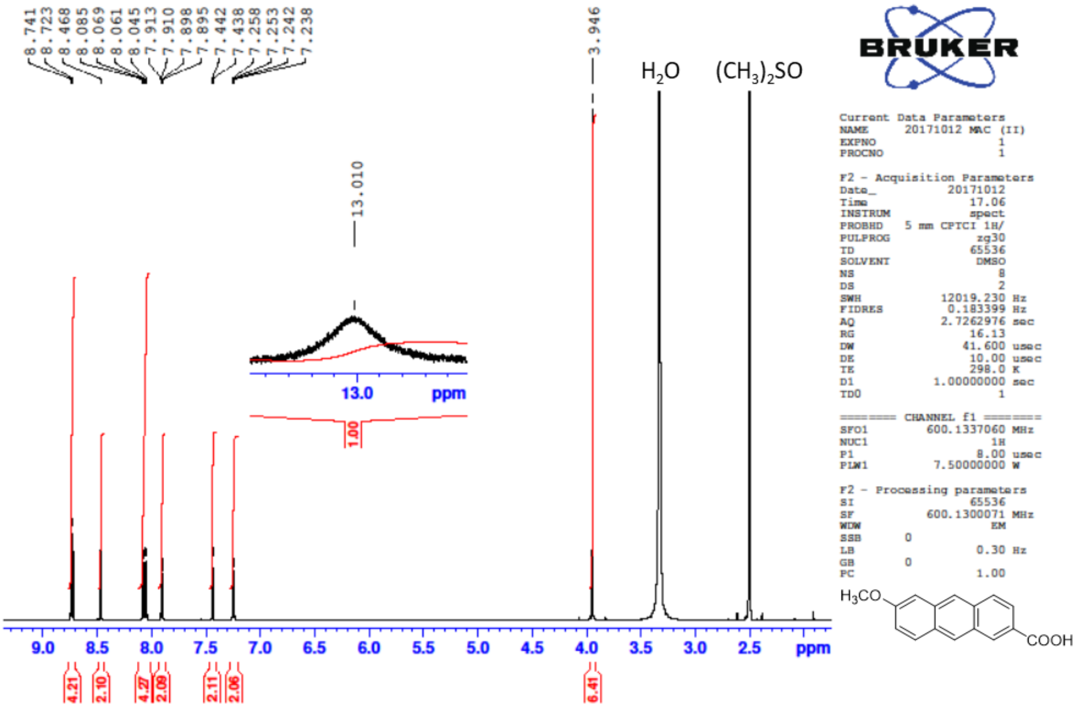

Figure A2-4-9. ^{1}H NMR of 6-methoxy-2-anthracenecarboxylic acid.

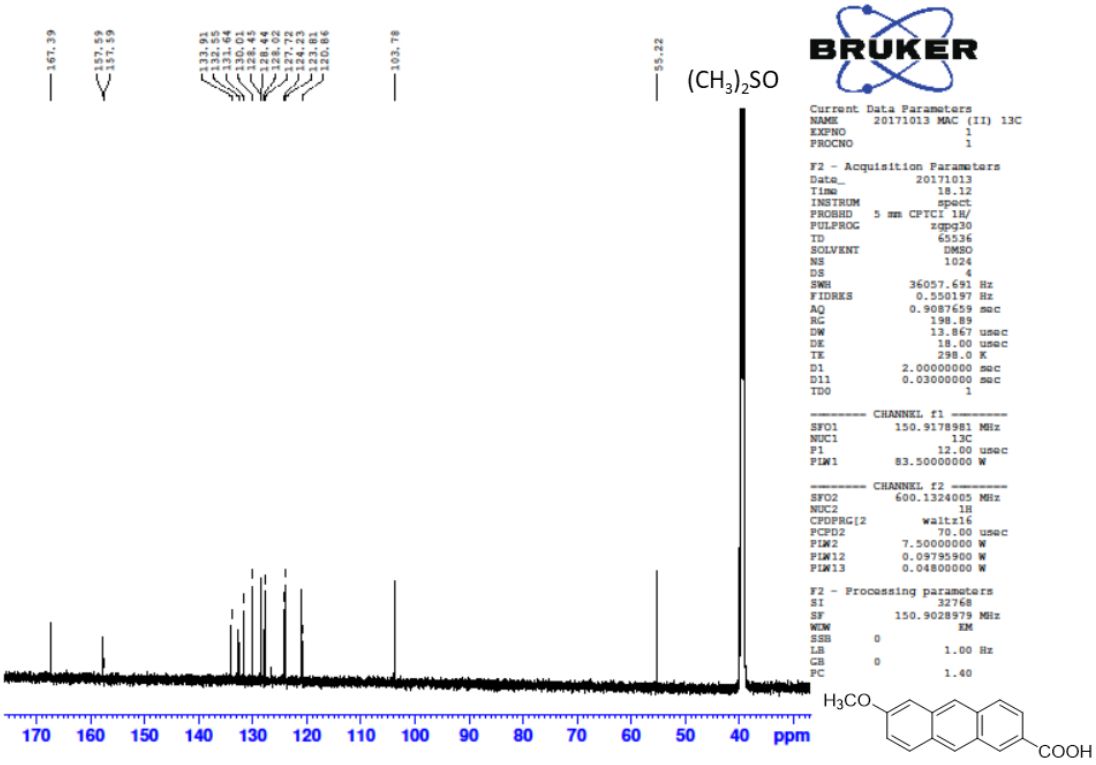

Figure A2-4-10. ^{13}C NMR of 6-methoxy-2-anthracenecarboxylic acid.

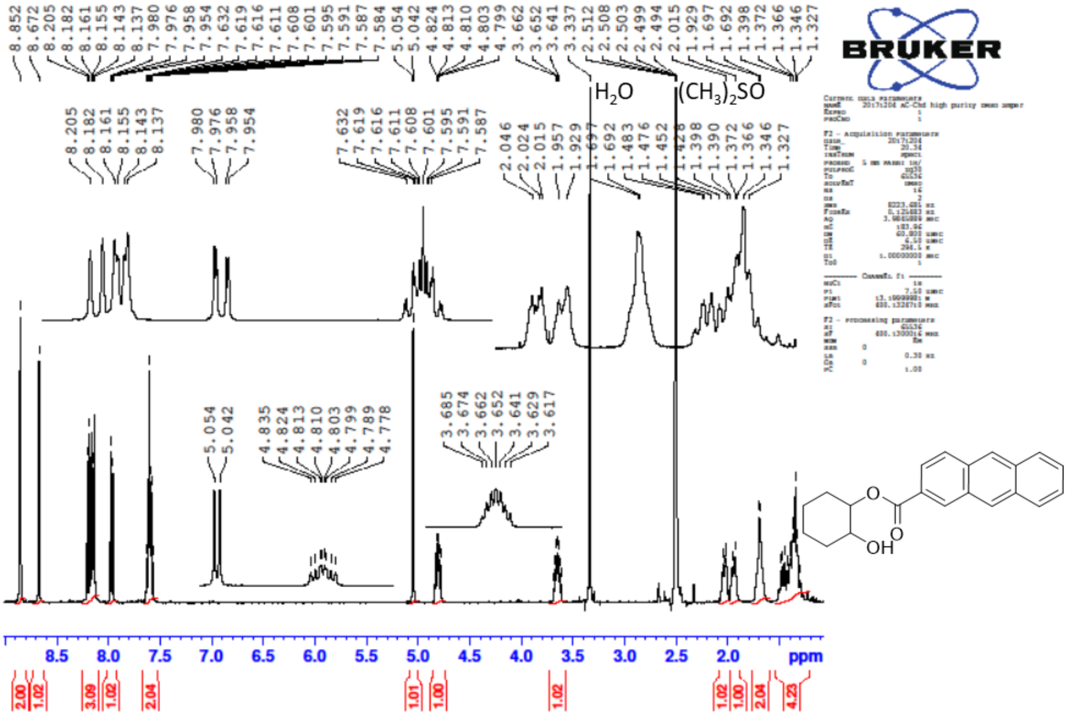

Figure A2-4-11. ^{1}H NMR of (2-*trans*-hydroxycyclohexyl)-2-anthroate.

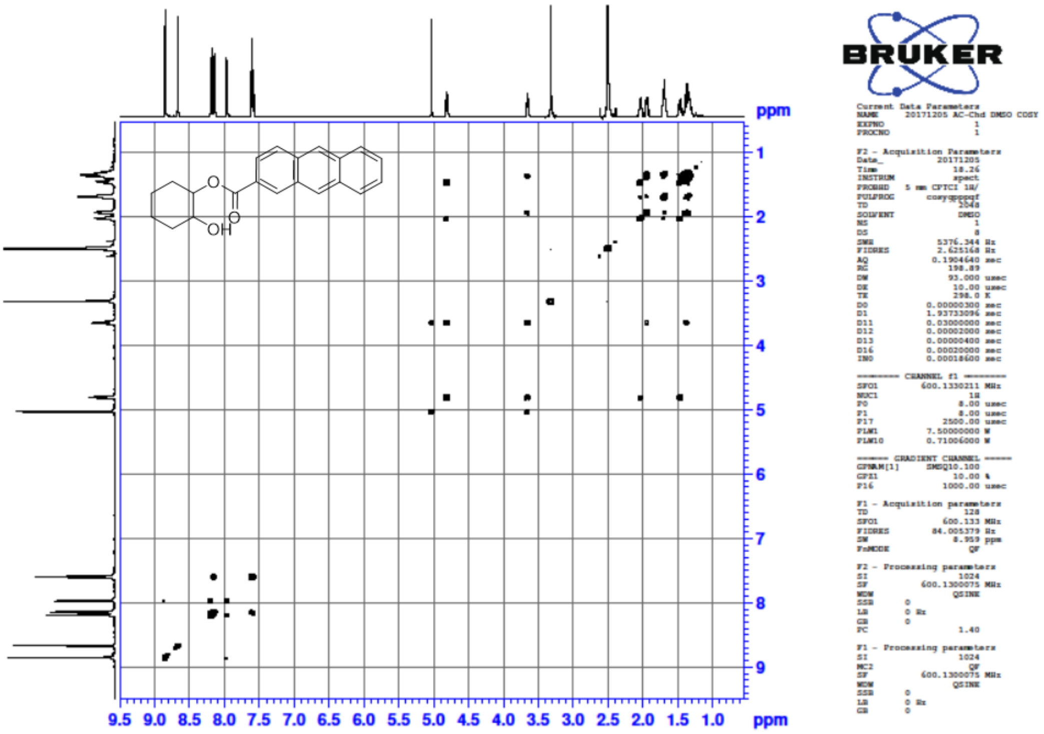

Figure A2-4-12. ^{1}H-^{1}H COSY NMR of (2-*trans*-hydroxycyclohexyl)-2-anthroate.

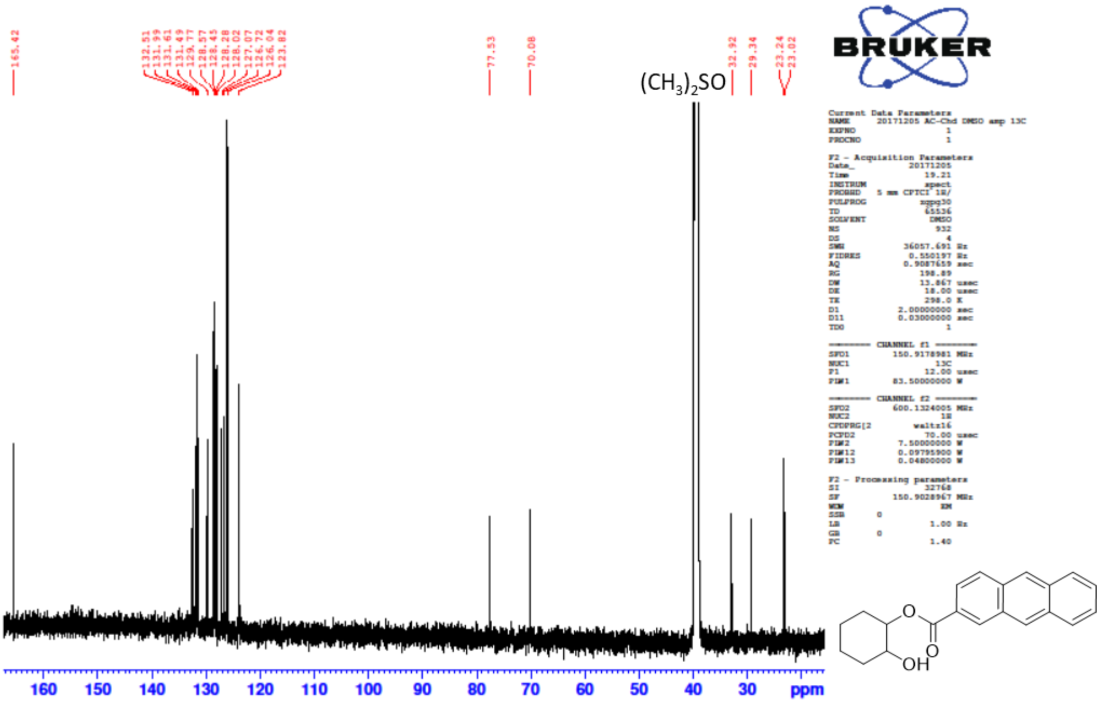

Figure A2-4-13. ^{13}C NMR of (2-*trans*-hydroxycyclohexyl)-2-anthroate.

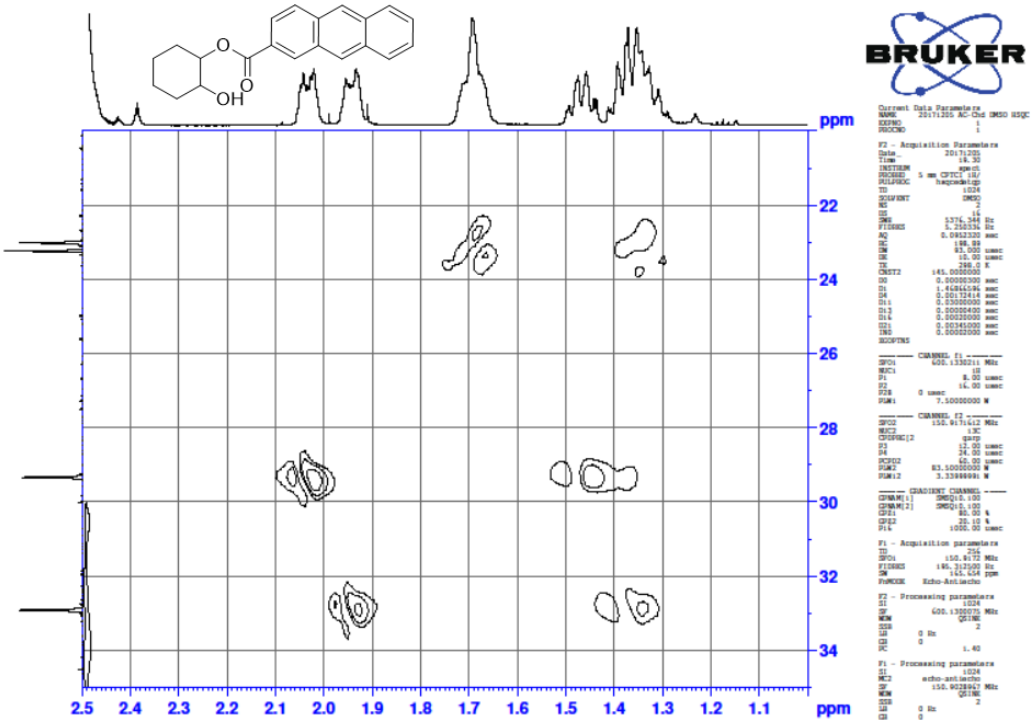

Figure A2-4-14. HSQC NMR (high field) of (2-*trans*-hydroxycyclohexyl)-2-anthroate.

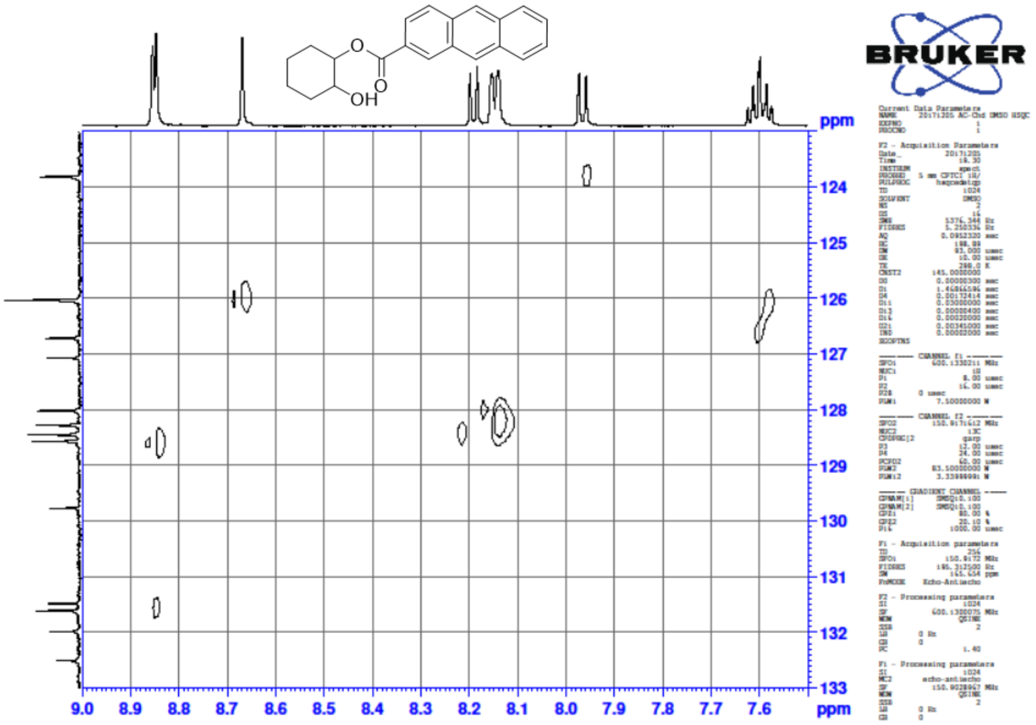

Figure A2-4-15. HSQC NMR (low field) of (2-*trans*-hydroxycyclohexyl)-2-anthroate.

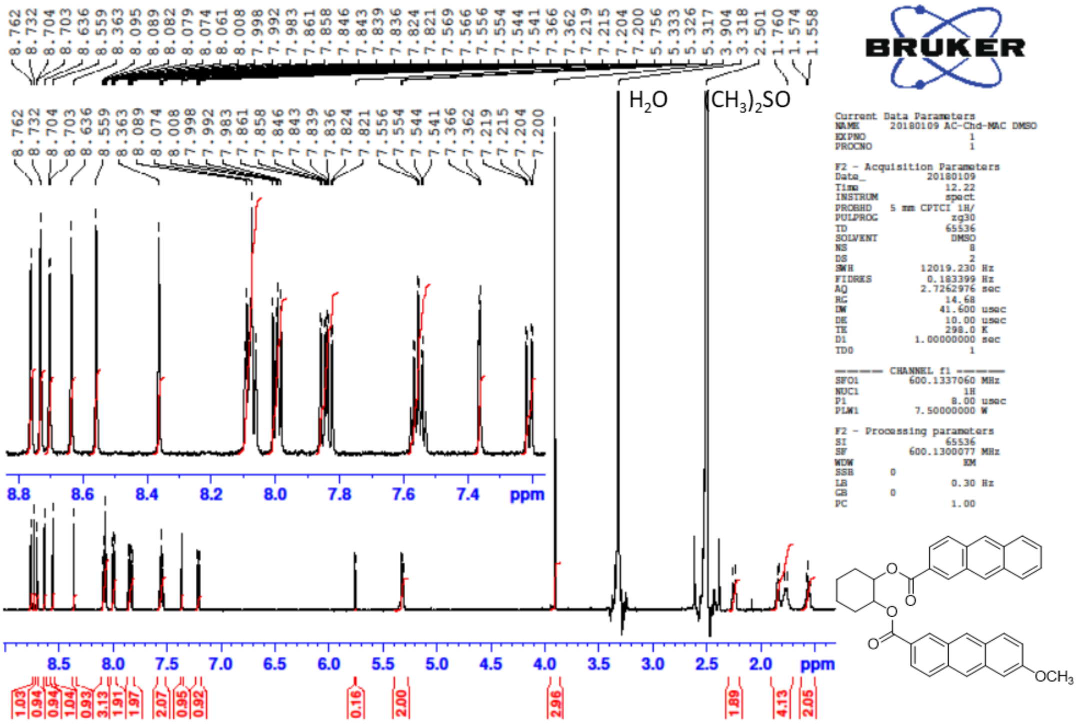

Figure A2-4-16. ^{1}H NMR of *trans*-1,2-cyclohexanediyl 1-(6-methoxy-2-anthroate)-2-(2-anthroate).

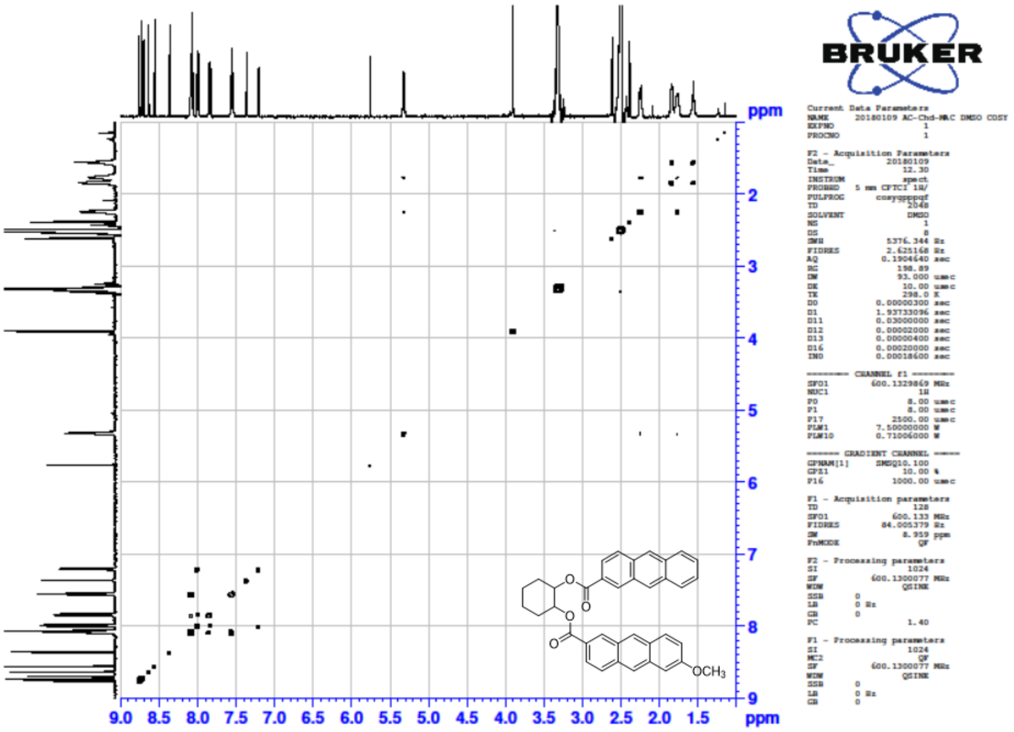

Figure A2-4-17. ^{1}H-^{1}H COSY NMR of *trans*-1,2-cyclohexanediyl 1-(6-methoxy-2-anthroate)-2-(2-anthroate).

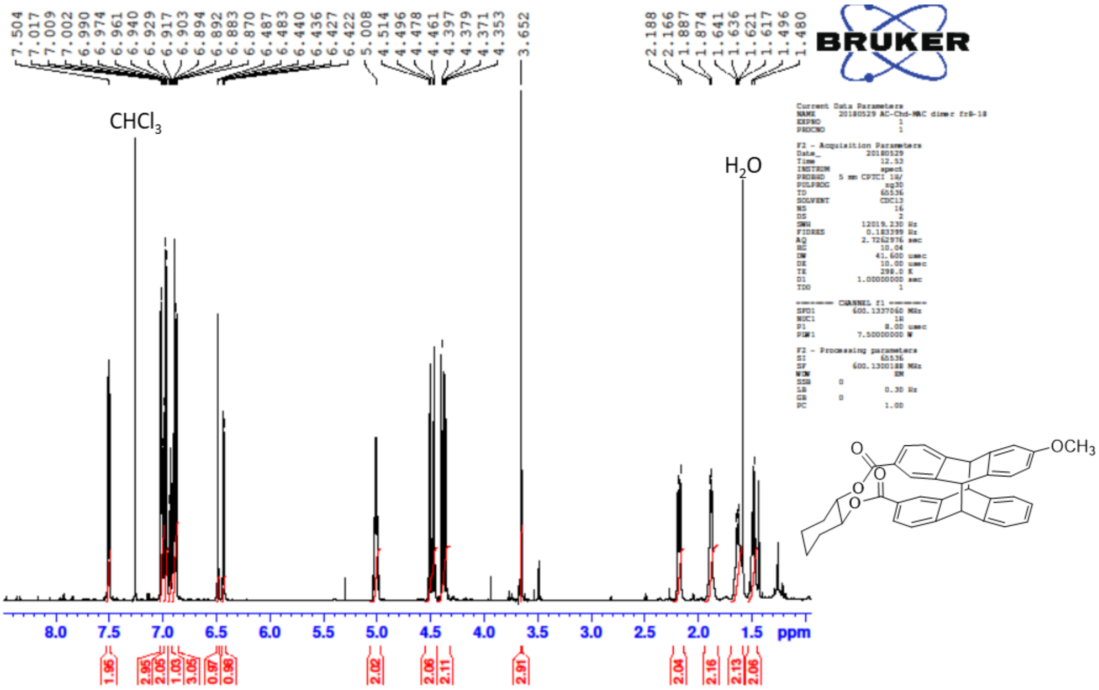

Figure A2-4-18. ^{1}H NMR of *trans*-1,2-cyclohexanediyl 6-methoxy-2-anthroate 2-anthroate *anti-head-to-head* heterodimer.

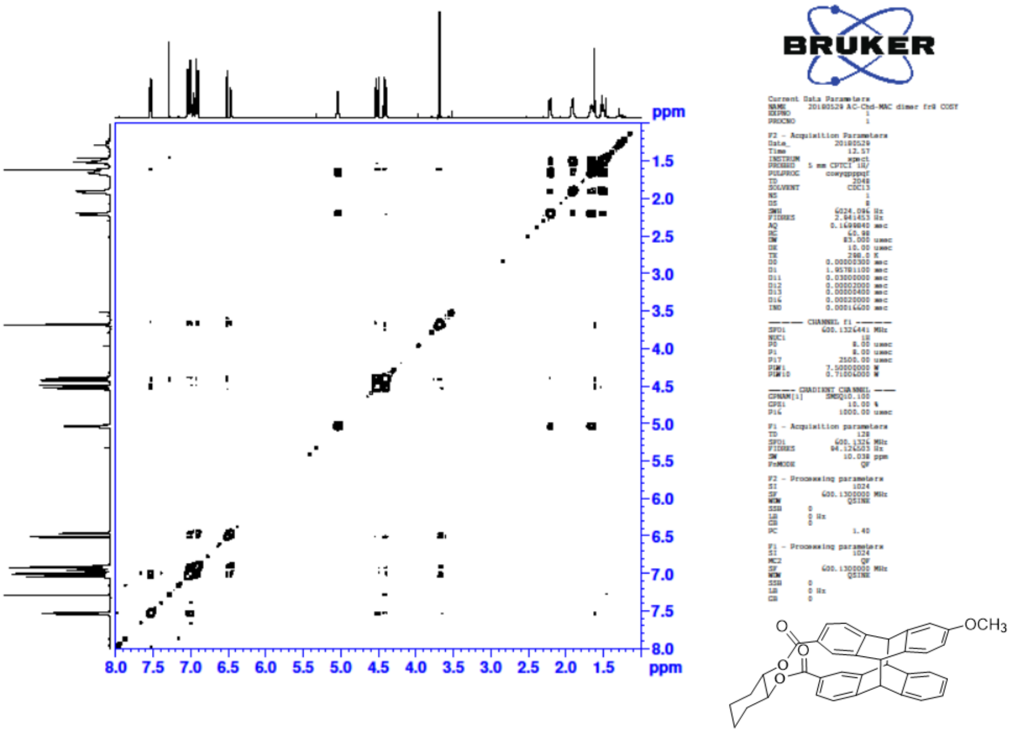

Figure A2-4-19. ^{1}H-^{1}H COSY NMR of *trans*-1,2-cyclohexanediyl 6-methoxy-2-anthroate 2-anthroate *anti-head-to-head* heterodimer.

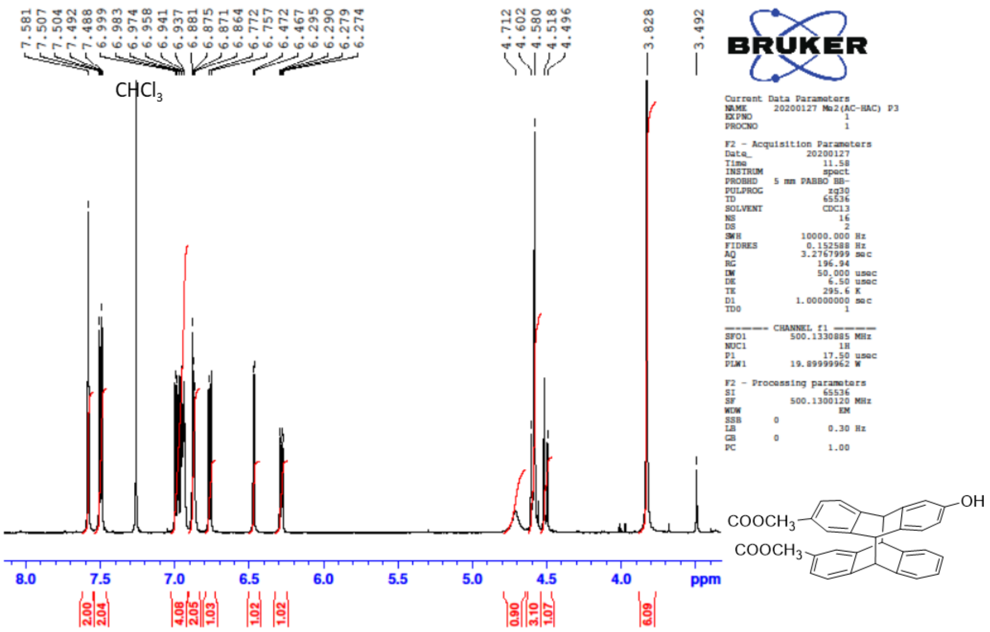

Figure A2-4-20. ^{1}H NMR of methyl 6-hydroxy-2-anthroate methyl 2-anthroate *anti-head-to-head* heterodimer (*P*-isomer).

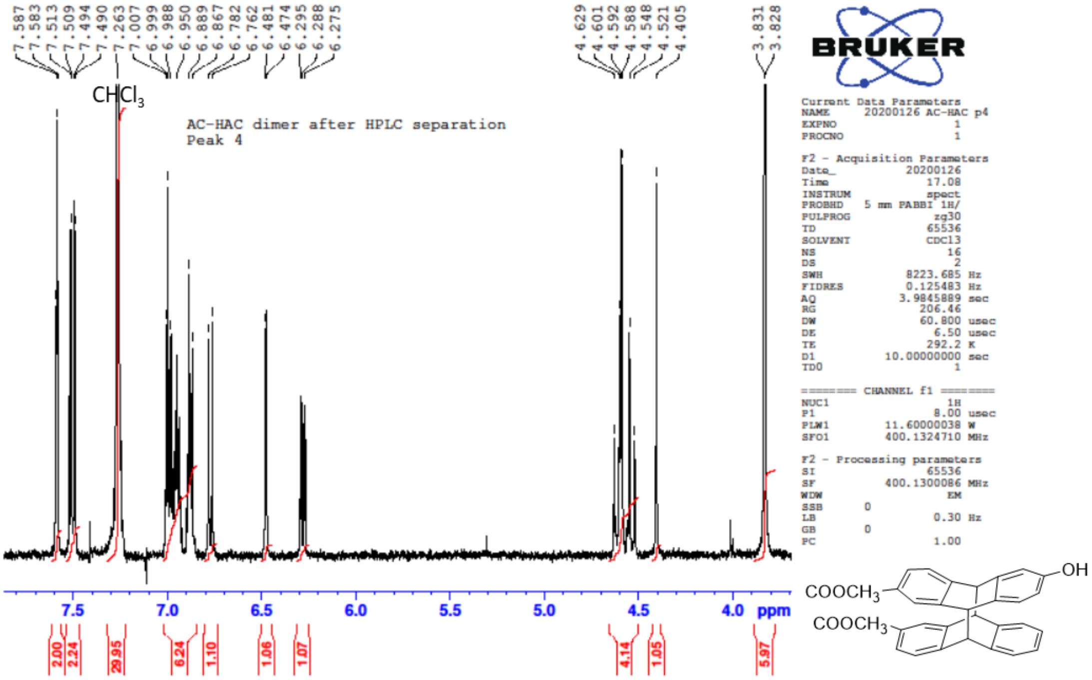

Figure A2-4-21. ^{1}H NMR of methyl 6-hydroxy-2-anthroate methyl 2-anthroate *anti-head-to-head* heterodimer (*M*-isomer).

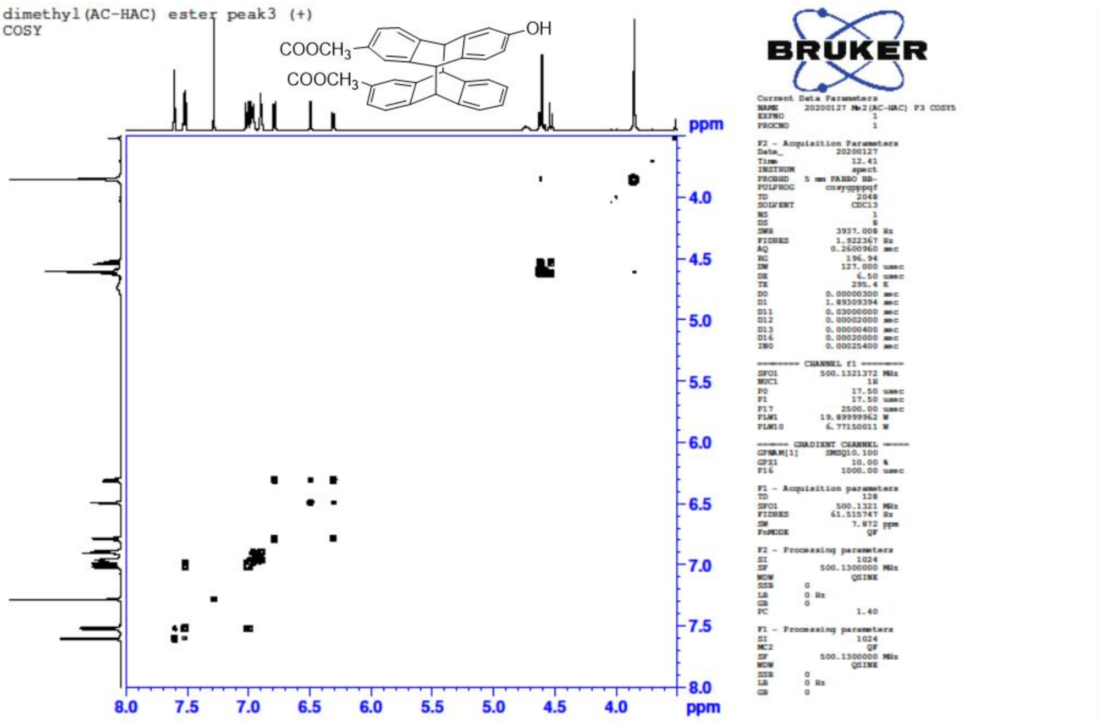

Figure A2-4-22. ^{1}H-^{1}H COSY NMR of methyl 6-hydroxy-2-anthroate methyl 2-anthroate *anti-head-to-head* heterodimer.

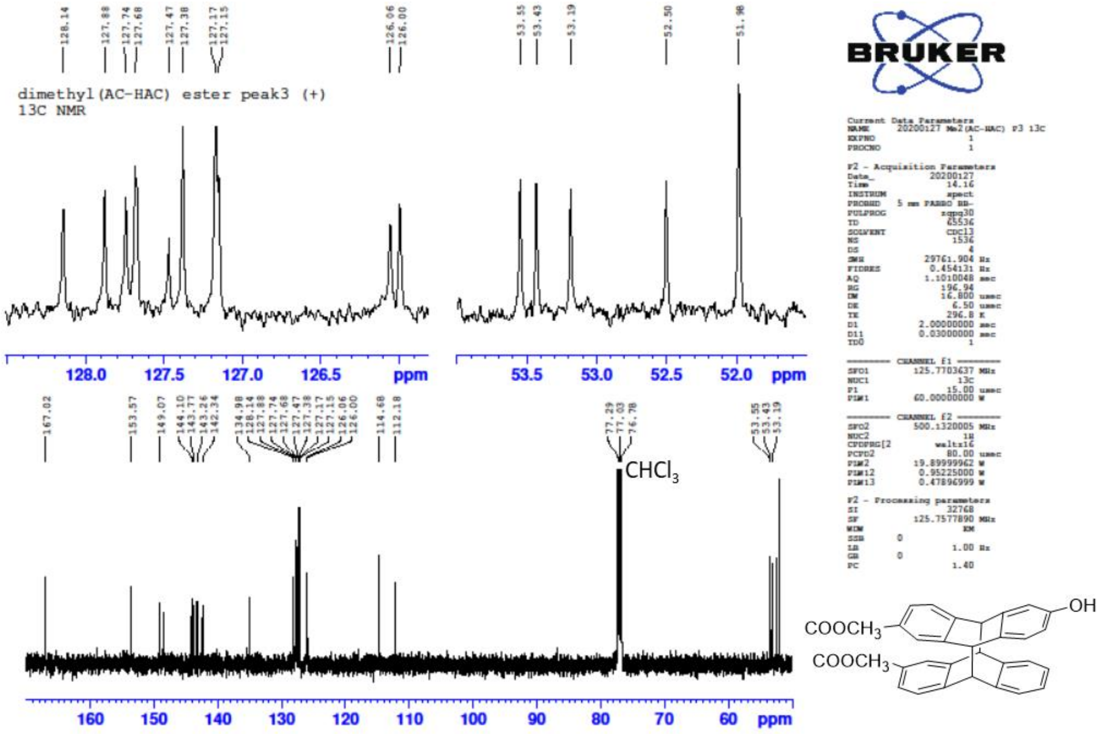

Figure A2-4-23. ^{13}C NMR of methyl 6-hydroxy-2-anthroate methyl 2-anthroate *anti-head-to-head* heterodimer.

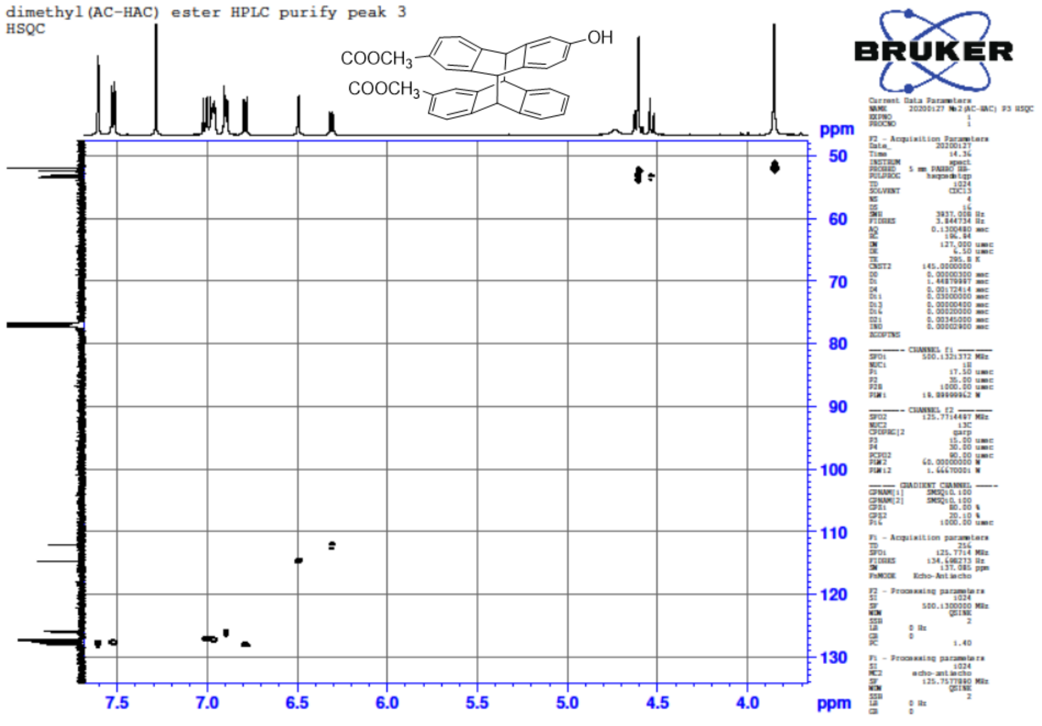

Figure A2-4-24. HSQC NMR of methyl 6-hydroxy-2-anthroate methyl 2-anthroate *anti-head-to-head* heterodimer.

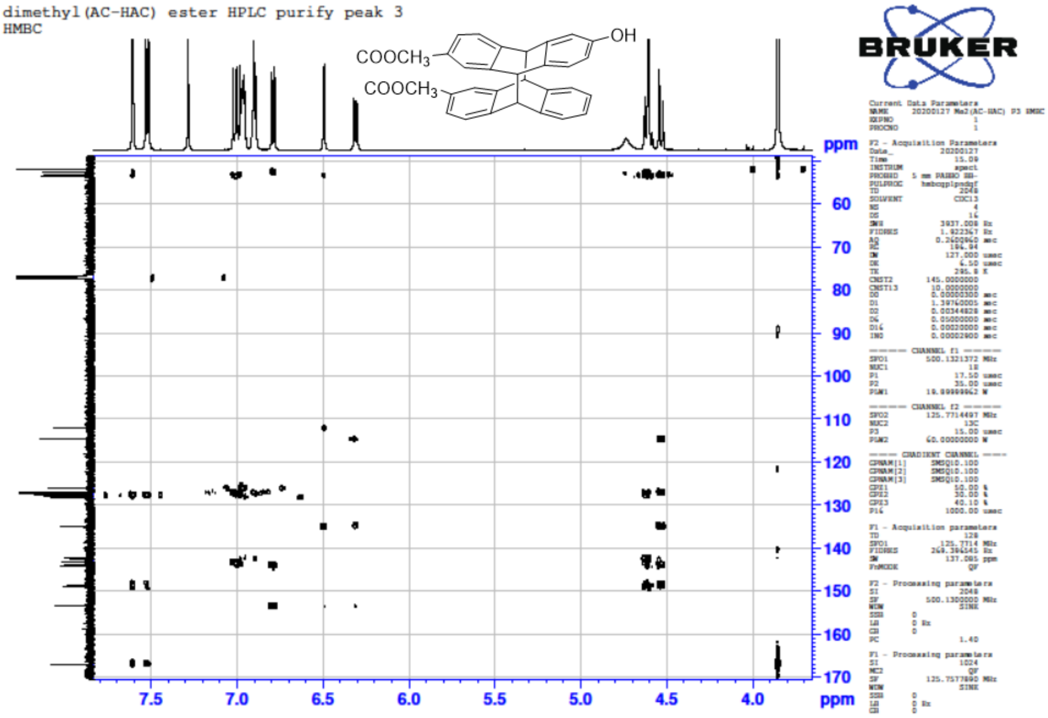

Figure A2-4-25. HMBC NMR of methyl 6-hydroxy-2-anthroate methyl 2-anthroate *anti-head-to-head* heterodimer.

A3 Mass Spectroscopy

Chapter 3

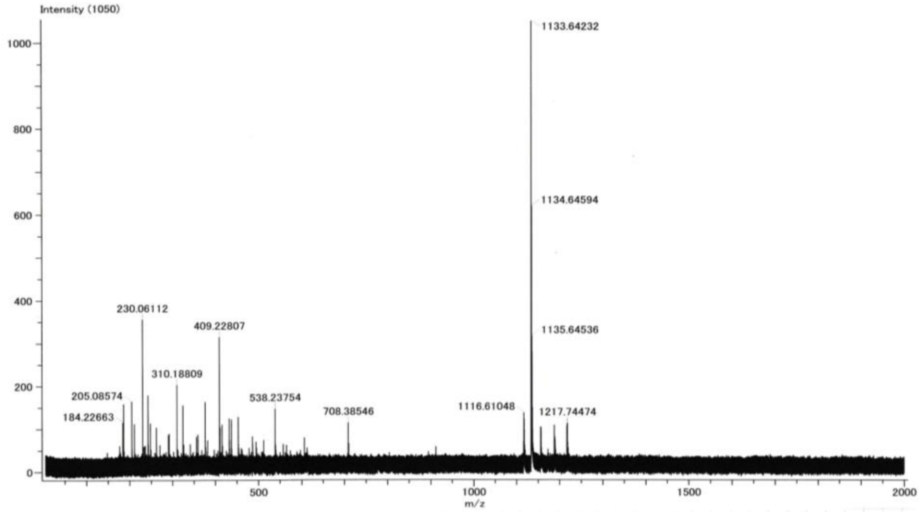

Figure A3-3-1. ESI-TOFMS spectrum of purified ACD3-PEG5-Lys(Biotin) ligand

Chapter 4

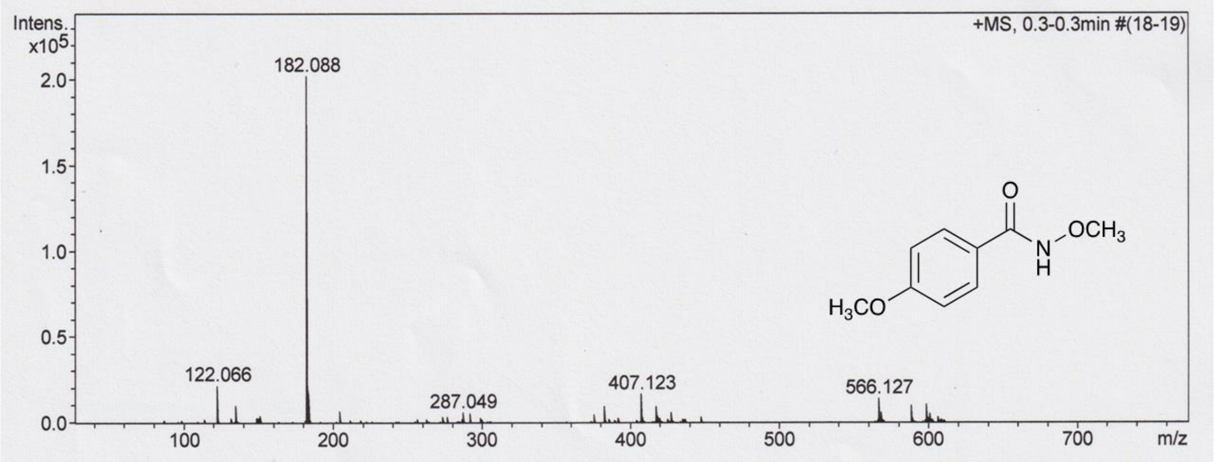

Figure A3-3-2. ESI-QTOFMS spectrum of *N*,4-Dimethoxybenzamide; m/z: $[M + H]^+$ Calcd for $C_9H_{12}NO_3$ 182.08; Found 182.09.

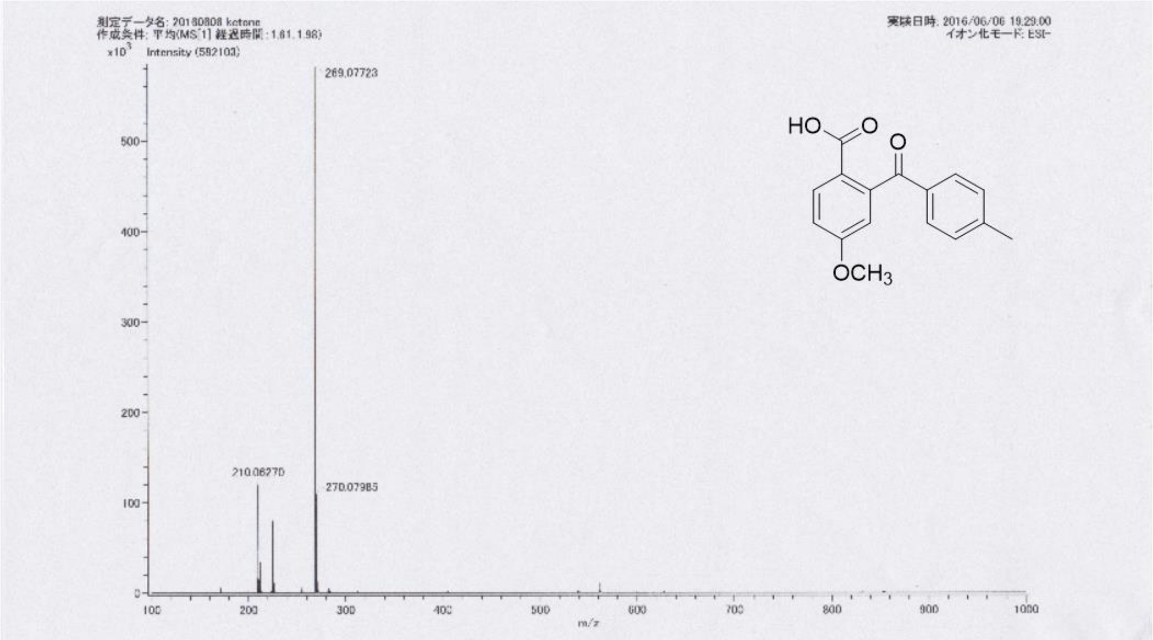

Figure A3-3-3. ESI-TOFMS spectrum of 4-methoxy-2-(4-methylbenzoyl)benzoic acid; m/z: $[M - H]^-$ Calcd for $C_{16}H_{13}O_4$ 269.08; Found 269.09.

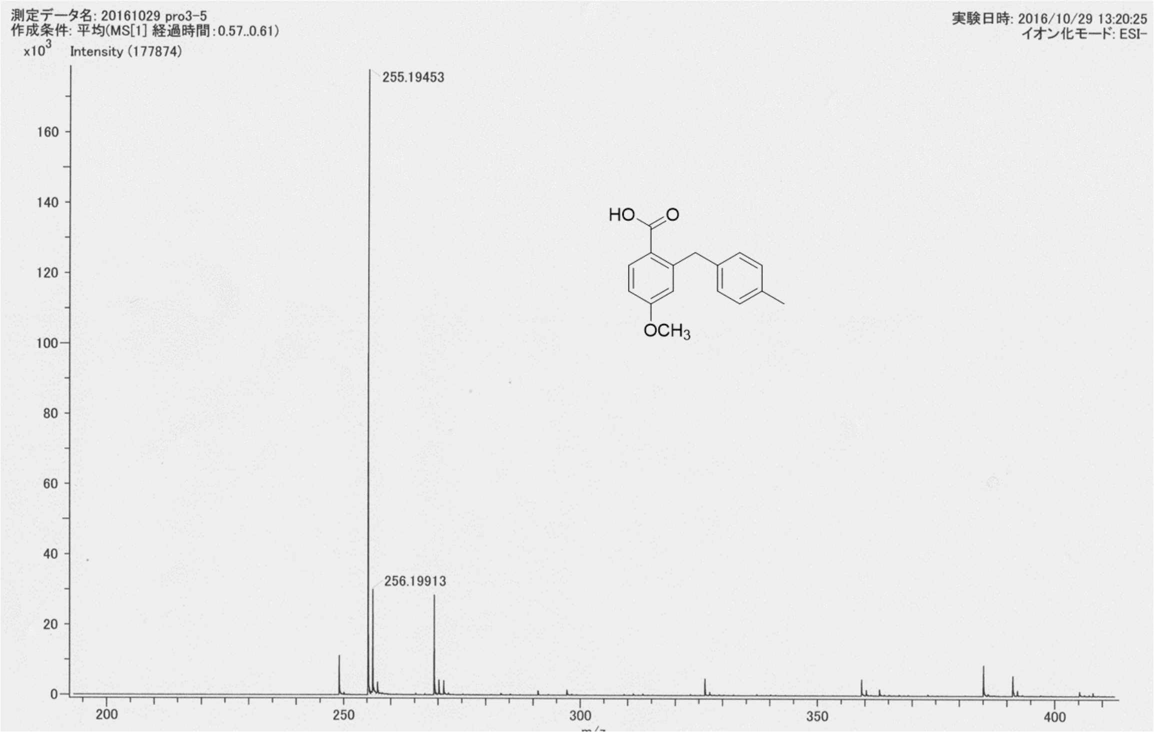

Figure A3-3-4. ESI-TOFMS spectrum of 4-methoxy-2-[(4-methylphenyl)methyl]benzoic acid; m/z: [M − H]⁻ Calcd for $C_{16}H_{15}O_3$: 255.10; Found 255.19.

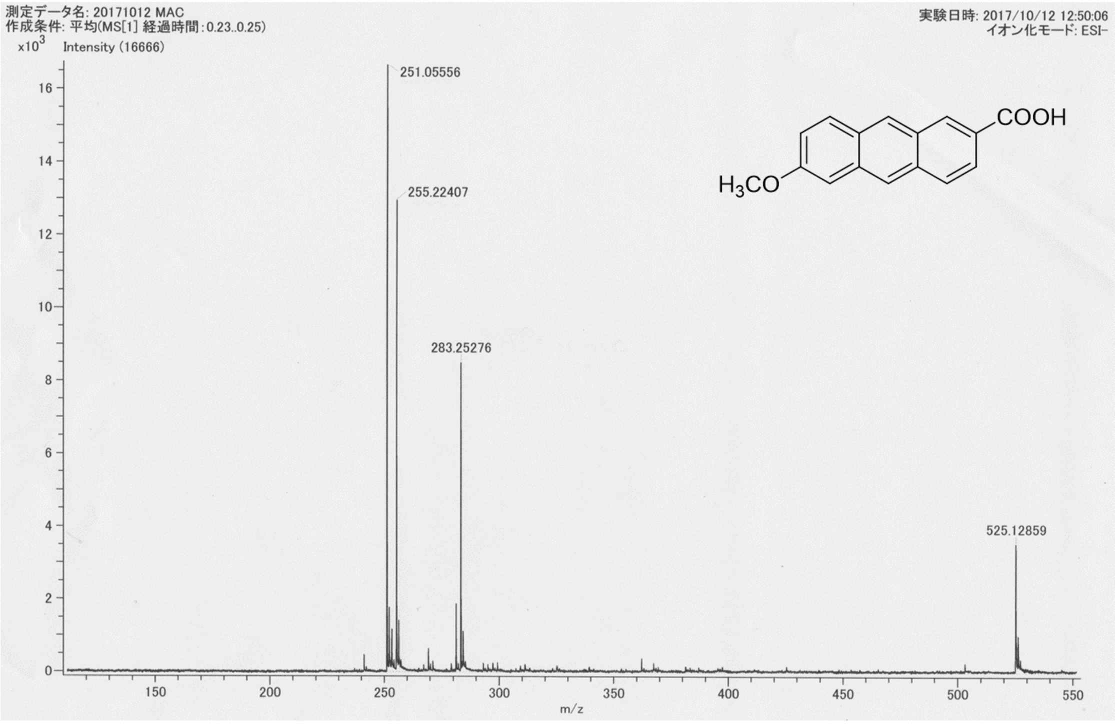

Figure A3-3-5. ESI-TOFMS spectrum of 6-methoxy-2-anthracenecarboxylic acid; m/z: [M − H]⁻ Calcd for $C_{16}H_{11}O_3$: 251.07; Found 251.06.

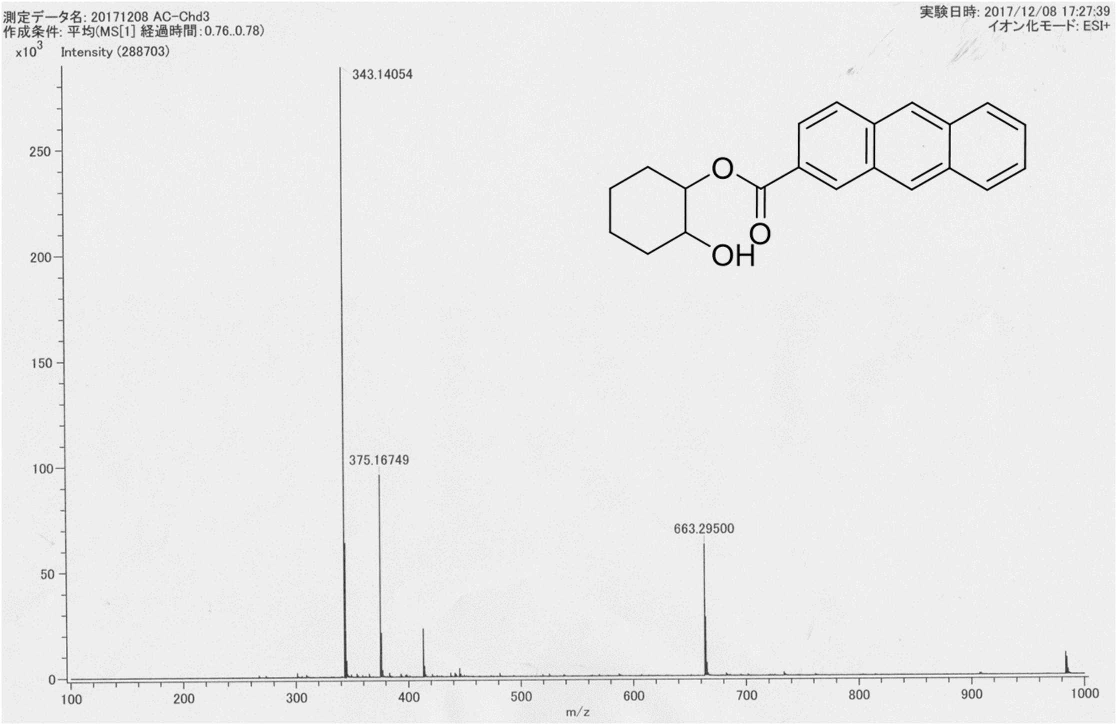

Figure A3-3-6. ESI-TOFMS spectrum of (2-*trans*-hydroxycyclohexyl)-2-anthroate; m/z: [M + Na]$^+$ Calcd for $C_{21}H_{20}O_3Na$ 343.13; Found 343.15.

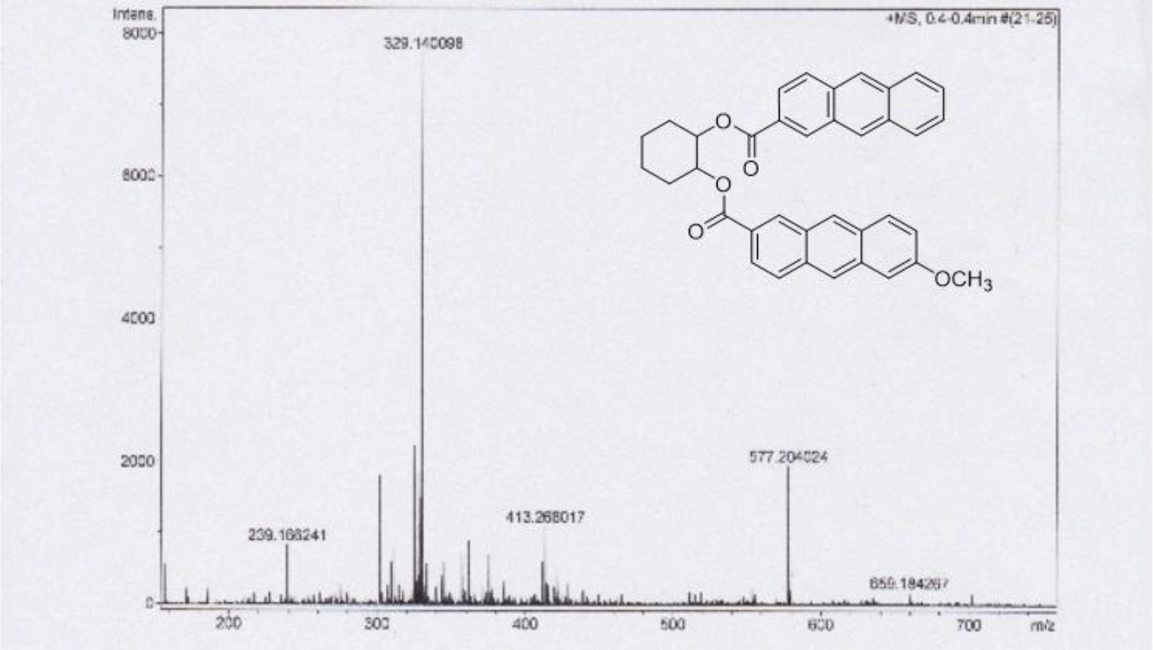

Figure A3-3-7. ESI-TOFMS spectrum of *trans*-1,2-cyclohexanediyl 1-(6-methoxy-2-anthroate)-2-(2-anthroate); m/z: [M + Na]$^+$ Calcd for $C_{37}H_{30}O_5Na$ 577.20; Found 577.20.

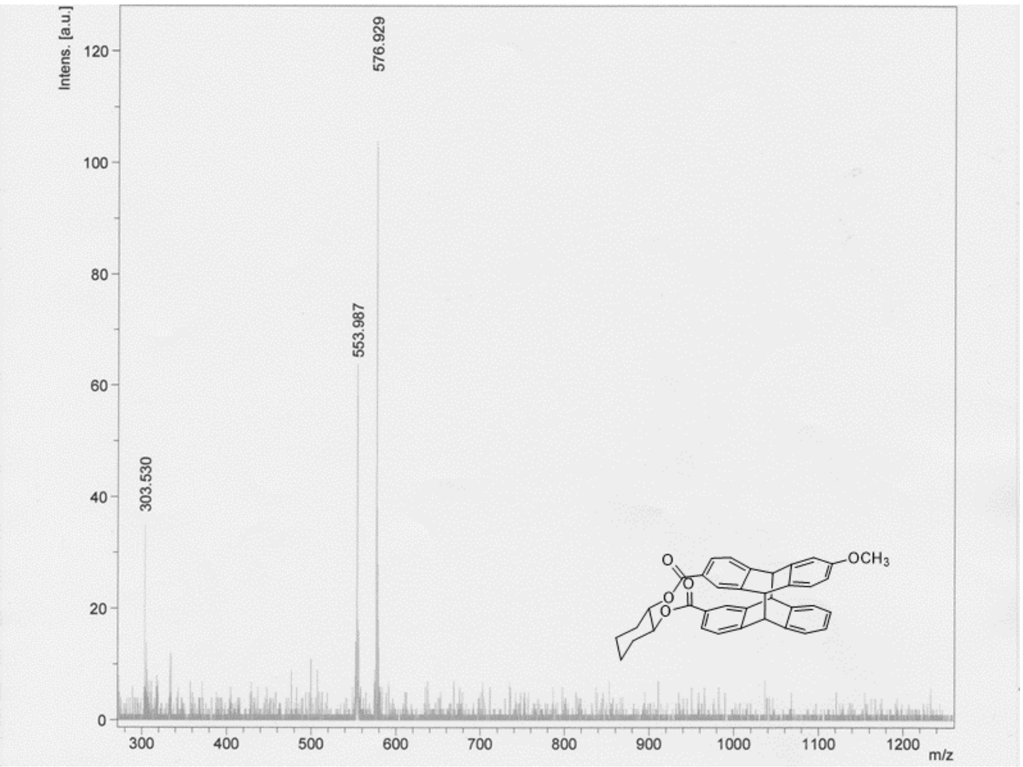

Figure A3-3-8. MALDI-TOF (tetracyanoquinodimethane as matrix) spectrum of *trans*-1,2-cyclohexanediyl 6-methoxy-2-anthroate 2-anthroate *anti-head-to-head* heterodimer; $[M]^+$ Calcd for $C_{37}H_{30}O_5$ 554.21; Found 553.99, $[M + Na]^+$ Calcd for $C_{37}H_{30}O_5Na$ 577.20; Found 576.93.

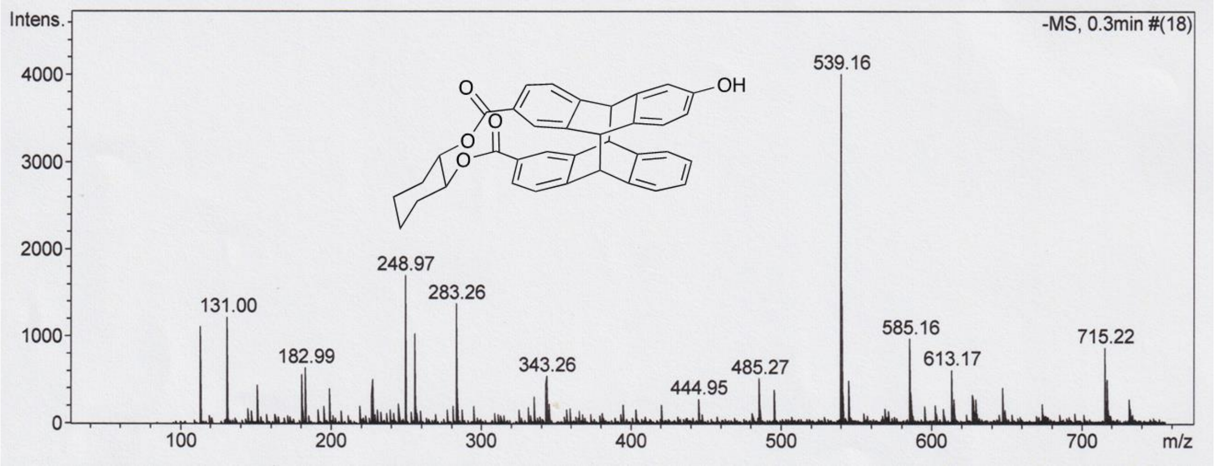

Figure A3-3-9. ESI-QTOFMS spectrum of *trans*-1,2-cyclohexanediyl 6-hydroxy-2-anthroate 2-anthroate *anti-head-to-head* heterodimer; m/z: $[M - H]^-$ Calcd for $C_{36}H_{27}O_5$ 539.19; Found 539.16.

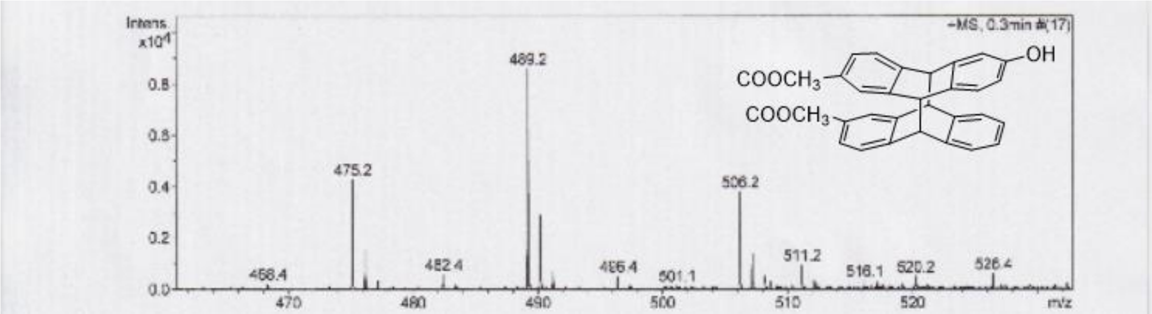

Figure A3-3-10. ESI-QTOFMS spectrum of methyl 6-hydroxy-2-anthroate methyl 2-anthroate *anti-head-to-head* heterodimer; m/z: $[M + H]^+$ Calcd for $C_{32}H_{25}O_5$ 489.2; Found 489.2.

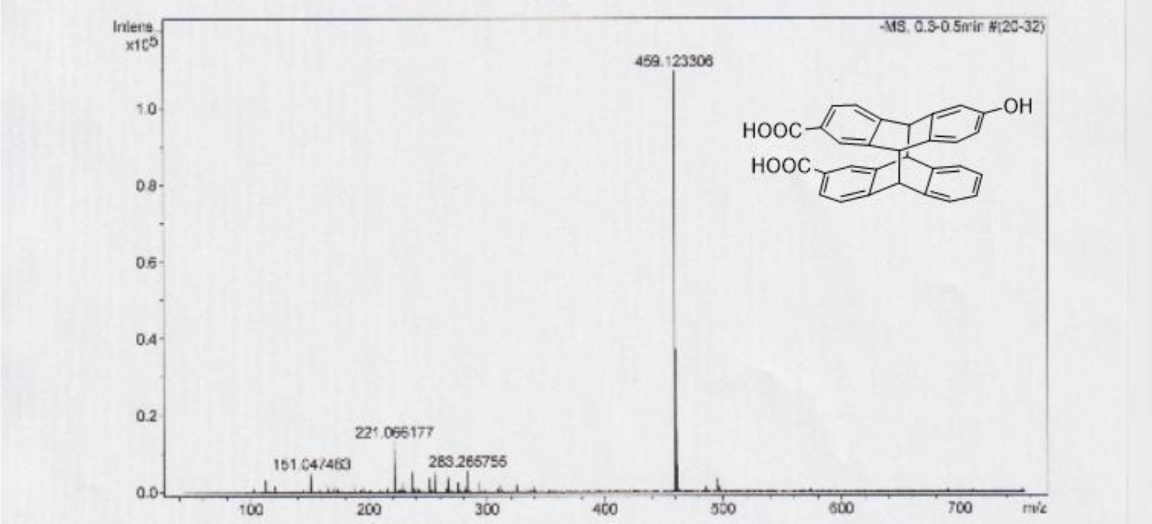

Figure A3-3-11. ESI-QTOFMS spectrum of 6-hydroxy-2-anthracenecarboxylic acid 2-anthracenecarboxylic acid *anti-head-to-head* heterodimer; m/z: $[M - H]^-$ Calcd for $C_{30}H_{19}O_5$ 459.12; Found 459.12.

A4 HPLC Chromatography

Chapter 3

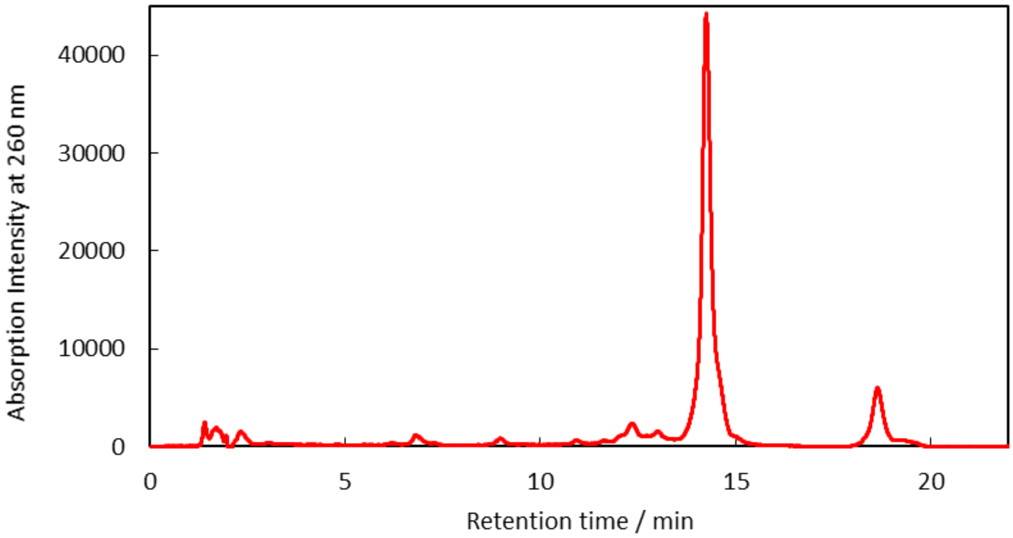

Figure A4-3-1. Analytical HPLC of purified ACD3-PEG5-Lys(Biotin) ligand.

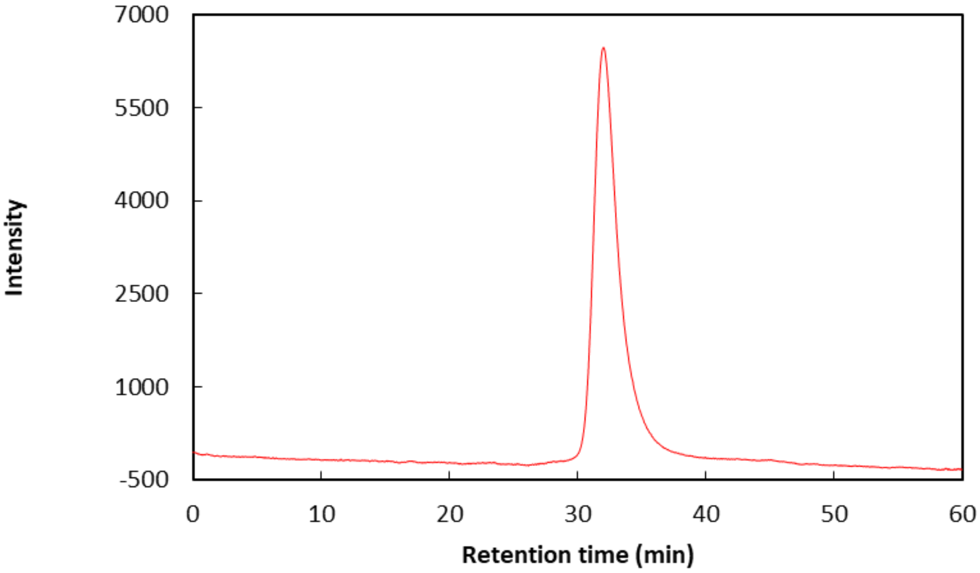

Figure A4-3-2. Gel-permeable HPLC of scFv J-20 antibody.

A5 Image

Chapter 2

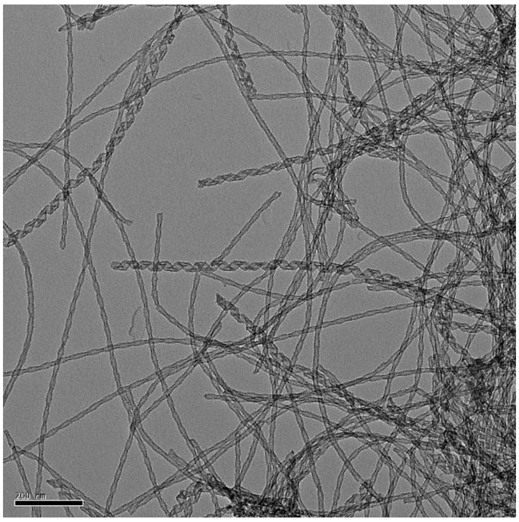

Figure A5-2-1. Example of TEM Imgage of hybrid nanohelices stock. The stock having pure nanohelices is rare.

Chapter 3

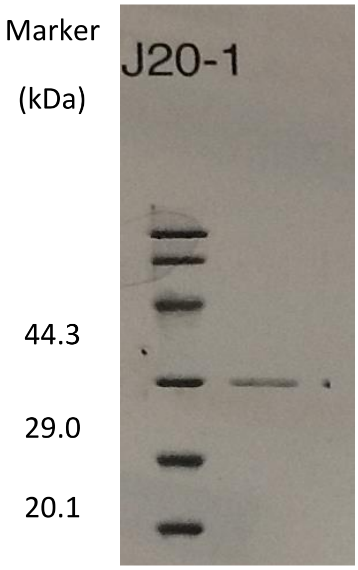

Figure A5-3-1. SDS-PAGE of scFv J-20 antibody with marker. The calculated molecular weight is 26.9 kDa.

A6 Calculation

Chapter 2

Calculation of AC molar extinction coefficient in aqueous solution

AC stocks were prepared in NaOH 1 mM solution. However, it is difficult to completely dissolve AC at this NaOH concentration, and using too high basic concentration will dissolve silica. Therefore, the concentration of AC was determined by UV absorption spectrum.

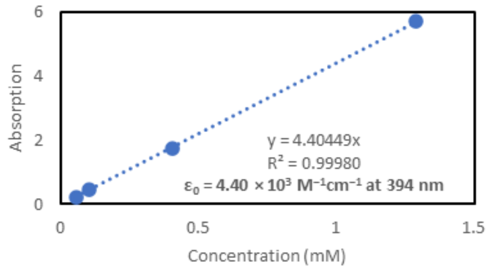

Concentration (mM)	Absorption 394 nm
1.29	5.7*
0.403	1.725*
0.102	0.431
0.0543	0.212

*The absorption was calculated from 2 mm multiplied by 5.

Figure A6-2-1. Calibration curve of AC in tetrahydrofuran.

First, the molar extinction coefficient in tetrahydrofuran, the solvent that AC can dissolve well, was determined from 4 separately prepared samples to be 4.40×10^3 $M^{-1}cm^{-1}$ at 394 nm (lowest-energy λ_{max}). (Figure A6-2-1) This data shows precision of sample preparation procedure.

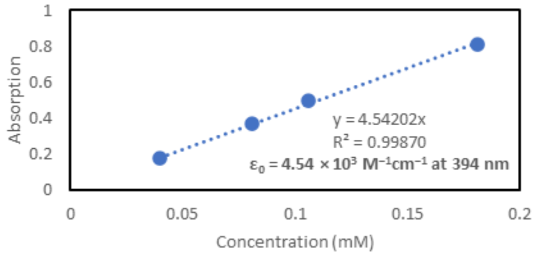

Concentration (mM)	Absorption 386 nm
0.181	0.813
0.106	0.495
0.0808	0.37
0.0398	0.18

Figure A6-2-2. Calibration curve of AC in 60 % THF and 40 % NaOH 1 mM (aq).

Then, AC was dissolved in the mixture of THF (60 %) and NaOH 1 mM (aq) (40 %). AC was first dissolved by THF, and NaOH 1 mM (aq) (40 %) was slowly added, avoiding any precipitation. The calibration curve was plotted from 4 separately prepared samples to be 4.54×10^3 $M^{-1}cm^{-1}$ at 386 nm. (Figure A6-2-2)

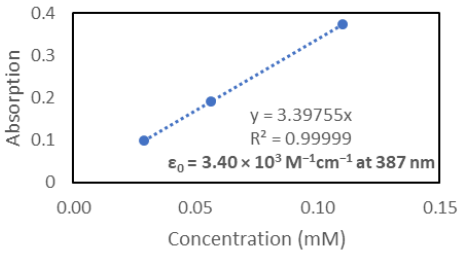

Dilution	Absorption 386 nm (THF 60 % NaOH aq 40 %)	Concentration* (μM)	Absorption 387 nm (NaOH aq)
40%	0.5	0.1101	0.374
20%	0.256	0.0564	0.192
10%	0.131	0.0289	0.0979

*Concentration was calculated from absorption at 386 nm in 60 % THF 40 % NaOH (aq).

Figure A6-2-3. Calibration curve of AC in in NaOH 1 mM (aq). Concentration was determined by absorption spectrum in THF 60 % and NaOH 1 mM (aq) 40 %.

Finally, AC was prepared by dissolving in NaOH 1 mM (aq) and filtering, the same method used for every preparation of AC stock. This solution was diluted to 10 %, 20 % and 40 % in NaOH 1 mM (aq), and the absorption of each sample was measured. The similar procedure was performed but using tetrahydrofuran and NaOH 1 mM (aq) mixture for dilution to give the final ratio of THF 60 % and NaOH 1 mM (aq) 40%. With this method, the concentration of AC can be calculated from molar extinction coefficient in THF 60 % (4.54×10^3 $M^{-1}cm^{-1}$), which was plotted against absorption diluted by only NaOH 1 mM (aq). (Figure A6-2-3) As a result, the molar extinction coefficient of AC in NaOH 1 mM (aq) is 3.40×10^3 $M^{-1}cm^{-1}$.

Calculation of excited AC concentration in CPL-300 spectrometer

It is difficult to get exact concentration of AC* because many unknown factors are involved. By assuming that AC solution completely absorb photons (which was less in this experiment), the maximum possible concentration can be estimated. First, the number of photons / s is estimated. The wavelength used in the experiments was 350 nm.

$$\begin{aligned}\text{Photon Energy} &= \frac{\mathrm{hc}}{\lambda}\\ &= \frac{(6.63\times10^{-34}\ \mathrm{J\cdot s})(3\times10^{8}\ \mathrm{m\cdot s^{-1}})}{350\times10^{-9}\ \mathrm{m}}\\ &= 5.68\times10^{-19}\ \mathrm{J\ \cdot photon^{-1}}\end{aligned}$$

In the case of laser, the number of photons can be calculated by dividing total energy with the energy of each photon with high accuracy. However, the light source in spectrometer is Xe arc lamp 150 W, so most of the photons are removed by excitation slit. Therefore, inequation is used instead.

$$\begin{aligned}\text{Number of Photon} &< \frac{\text{Energy of Light Source}}{\text{Energy of Photon}}\\ &< \frac{150\ \mathrm{J\cdot s^{-1}}}{5.68\times10^{-19}\ \mathrm{J\cdot photon^{-1}}}\\ &< 2.64\times10^{20}\ \mathrm{photon\cdot s^{-1}}\end{aligned}$$

Next, the concentration of AC* at any time t can be calculated using lifetime equation (3-1).

$$[\mathrm{AC}^*] = [\mathrm{AC}^*]_0 e^{-t/\tau}$$

From this equation and the fact that the fluorescence lifetime of AC in aqueous solution is 18 ns, concentration of AC* will reduce to 1 % of the original concentration at 83 ns. For 83 ns, less than 2.19×10^{11} photons are emitted from Xe lamp (calculated by above inequation).

Here, the calculation is complicated because the decay and excitation are happened simultaneously and continuously. So, the situation is simplified. Instead of Xe lamp, the femtosecond-pulse laser is considered as a light source. At the beginning, 2.19×10^{11} photons were irradiated from pulse laser excited simultaneously with negligible fluorescence decay. With continuous excitation from Xe lamp (2.19×10^{11} in 83 ns), the fluorescence decay is involved causing the amount of AC* to be always less than 2.19 × 10^{11} molecules. With this estimation, the inequation is maintained.

The concentration of AC used in this experiment is 10 μM, and the volume is 2 mL, meaning 1.2 × 10^{16} molecules (2.0 × 10^{-8} mol) exist. We can conclude that the amount of AC* is much less than AC. Moreover, this assumption based on the extreme approximation that photons are completely absorbed (They were partially absorbed in the experiments.), 150 W power of light source is completely converted to 350-nm light (Most of the photons of the lamp with different wavelength was removed by emission slit.), the excitation was not disturbed by fluorescence decay for 83 ns, and the lifetime of AC in hybrid nanoribbons is 18 ns (It should be reduced).

Therefore, the concentration of AC* in reality is much less than the approximation, more support to the approximation that [AC*] << [AC].

Chapter 4

AC-HAC dimer3 Atomic Coordinates for Calculations

atomic coordinate			atom	charge	isotope
-1.52310666	0.28869285	2.71136348	C	6	0
-0.25468088	-2.43053628	2.08724567	C	6	0
-4.05014013	0.58605448	1.41462532	C	6	0
-4.01559642	1.17086635	-1.17150962	C	6	0
-6.292847	1.43369688	-2.45623611	C	6	0
-8.59056095	1.11452824	-1.20367776	C	6	0
-8.60183187	0.53028159	1.36835106	C	6	0
-6.32567041	0.27429553	2.68387703	C	6	0
0.16796318	2.43319683	1.88537442	C	6	0
0.20138205	3.02117414	-0.70400437	C	6	0
-1.46486329	1.45807291	-2.41744866	C	6	0
1.68419871	3.78693745	3.55861118	C	6	0
3.25003686	5.71064344	2.68006025	C	6	0
3.28918799	6.29414898	0.1010901	C	6	0
1.75084432	4.94357003	-1.58003524	C	6	0
2.30234161	-2.12668424	0.85233612	C	6	0
2.33821799	-1.53628161	-1.73645433	C	6	0
4.638558	-1.20064882	-2.97281278	C	6	0
6.90514184	-1.42760137	-1.65601999	C	6	0
6.87088325	-2.01002993	0.92345895	C	6	0
4.55772814	-2.36615397	2.1637575	C	6	0
-1.90573766	-4.00037321	0.36556362	C	6	0
-1.86143449	-3.41750402	-2.21924992	C	6	0
-0.18382412	-1.25814588	-3.03994498	C	6	0
-3.43680449	-5.9530959	1.23967058	C	6	0

-4.93035514	-7.32741267	-0.44537679	C	6	0
-4.88159828	-6.75173548	-3.01508314	C	6	0
-3.34183687	-4.80002054	-3.89787206	C	6	0
-10.79529161	0.19103722	2.71796832	O	8	0
9.21098159	-2.26332057	2.43362882	C	6	0
-1.77623786	0.35494124	4.75927802	H	1	0
-0.03325103	-3.39099971	3.90131532	H	1	0
-6.29046297	1.88916298	-4.4590229	H	1	0
-10.36470733	1.32653255	-2.21999017	H	1	0
-6.37167088	-0.17718039	4.68500941	H	1	0
-1.67961791	2.42088539	-4.23128187	H	1	0
1.65402565	3.3253463	5.55926488	H	1	0
4.43856021	6.75853051	3.97722084	H	1	0
1.8138494	5.43036337	-3.57241301	H	1	0
4.65930102	-0.74275227	-4.97445398	H	1	0
8.69541525	-1.15665461	-2.6125185	H	1	0
4.57843296	-2.8175331	4.16532512	H	1	0
0.08342087	-1.32069234	-5.08674617	H	1	0
-3.46624662	-6.40240832	3.24395193	H	1	0
-6.12030359	-8.84860289	0.2474207	H	1	0
-6.0322362	-7.82423159	-4.33282657	H	1	0
-3.29729926	-4.3488647	-5.90169048	H	1	0
-12.22006315	0.42309038	1.5915172	H	1	0
4.91935633	8.30615546	-0.95520194	C	6	0
6.32980774	9.510957	0.84651275	O	8	0
5.04818466	8.88099727	-3.17965592	O	8	0
7.31572244	10.77130822	-0.06356726	H	1	0
11.35658706	-1.89393722	1.03810153	O	8	0
9.29571696	-2.74265397	4.68263284	O	8	0
12.75243101	-2.09941199	2.22056157	H	1	0